

**Particle Physics in the Sky and Astrophysics Underground:
Connecting the Universe's Largest and Smallest Scales**

by

Molly E. C. Swanson

BS Physics
California Institute of Technology (2002)

Submitted to the Department of Physics
in partial fulfillment of the requirements for the degree of

Doctor of Philosophy in Physics

at the

MASSACHUSETTS INSTITUTE OF TECHNOLOGY

June 2008

© Molly E. C. Swanson, MMVIII. All rights reserved.

The author hereby grants to MIT permission to reproduce and distribute publicly
paper and electronic copies of this thesis document in whole or in part in any
medium now known or hereafter created.

Author
Department of Physics
May 1, 2008

Certified by
Max Erik Tegmark
Associate Professor of Physics
Thesis Supervisor

Accepted by
Thomas J. Greytak
Professor of Physics
Associate Department Head for Education

arXiv:0808.0002v1 [astro-ph] 1 Aug 2008

Particle Physics in the Sky and Astrophysics Underground: Connecting the Universe's Largest and Smallest Scales

by
Molly E. C. Swanson

Submitted to the Department of Physics
on May 1, 2008, in partial fulfillment of the
requirements for the degree of
Doctor of Philosophy in Physics

Abstract

Particles have tremendous potential as astronomical messengers, and conversely, studying the universe as a whole also teaches us about particle physics. This thesis encompasses both of these research directions.

Many models predict a diffuse flux of high energy neutrinos from active galactic nuclei and other astrophysical sources. The “Astrophysics Underground” portion of this thesis describes a search for this neutrino flux performed by looking for extremely high energy upward-going muons using the Super-Kamiokande detector, and comparing the observed flux to the expected background. We use our results to set an upper limit on the diffuse neutrino flux from astrophysical sources.

In addition to using particles to do astronomy, we can also use the universe itself as a particle physics lab. Cosmology provides new insights that could never be observed in terrestrial laboratories. The “Particle Physics in the Sky” portion of this thesis focuses on extracting cosmological information from galaxy surveys.

To overcome technical challenges faced by the latest galaxy surveys, we produced a comprehensive upgrade to MANGLE, a software package that processes the angular masks defining the survey area on the sky. We added dramatically faster algorithms and new useful features to this software that are necessary for managing complex masks of the Sloan Digital Sky Survey (SDSS) and will be invaluable for future surveys as well.

With this software in hand, we utilized galaxy clustering data from SDSS to investigate the relation between galaxies and dark matter by studying relative bias, i.e., the relation between different types of galaxies. If all galaxies were perfect tracers of dark matter, different subpopulations would trace each other perfectly as well. However, separating galaxies by their luminosities and colors reveals a complicated picture: red galaxies are clustered more strongly than blue galaxies, with both the brightest and the faintest red galaxies showing the strongest clustering. Furthermore, red and blue galaxies tend to occupy different regions of space, effectively introducing an element of stochasticity (randomness) when modeling their relative distributions. In order to make precise measurements from the next generation of galaxy surveys, it will be essential to account for this complexity.

Thesis Supervisor: Max Erik Tegmark
Title: Associate Professor of Physics

Acknowledgments

I would like to extend my heartfelt thanks:

To my first teachers, my parents Barb and Rick Swanson. To my dad for everything from counting Cheerios to help with calculus homework, and for teaching me that physicists answer questions in the language of math, even when their 8-year-old daughters can't bear to see another equation scribbled on a napkin, and to my mom for her endlessly enthusiastic support of everything I've ever done.

To my most recent teachers, my advisors Max Tegmark and Kate Scholberg, for being such great role models, for always sticking up for me, and for showing me two such vastly different yet equally inspiring ways to be a scientist.

To all the great teachers I've had in between.

To my late grandmother Helen Hage – it was worth it, even though I'm not a boy.

To all of the Dr. Swanson physicists before me – my dad, my uncle Charlie Swanson, and my grandfather Bob Swanson, thanks to whom I always thought getting a PhD in physics was a common thing to do.

To the rest of the Swanson(/Olson/McLaughlin) clan, for doing other things so that we are not *all* huge nerds.

To the Crosby/Newman/Allen/etc. clan, especially to my grandfather-in-law Da (known to the rest of the world as Bob Newman) for taking a genuine interest in what I do and for my favorite definition of a neutrino ever.

To the Techer-Boston crew and various other dear friends in the area, including Wedge Cheung, Robin Friedman, Mike Fuerstman, Todd Schuman, Dave Guskin, Mick Garvey, Marlena Fecho, Brian and Sarah Bairstow, Craig Chu, Charley Mills, Pat Codd, Dave and Jess Tytell, Kate Jensen, and Dan Recht. The Thursday-night-dinners-on-Tuesdays-on-Wednesdays-on-Thursdays are among my fondest memories of my time in Boston.

To all my fellow astrograds, and everyone else I've had the pleasure of knowing at MIT, especially Miriam Krauss, Jake Hartman, Judd and Cassie Bowman, Ed Boyce, Robyn Sanderson, Ben Cain, Mike Stevens, Yi Mao, Bonna Newman, Julie Millane, Jessie Shelton, Tom and Liz Pasquini, Will Fox, and Sarah-Jane White. Having such awesome people with whom to share the pain made grad school infinitely more fun.

To my fellow 37-602 denizens, most especially Josh Carter and Ryan Lang, who were in it with me for the long haul, but also to Judd Bowman, Sam Conner, Chris Williams, Leslie Rogers, and (albeit briefly) Sarah Vigeland. It wouldn't have been the same without dodging Nerf footballs, green tea, Penzey's spice rub, indoor paper baseball, cutthroat games of Facebook Scrabble and World Traveler, multiwing bats, SoftLips pranks, paper airplane contests, and countless other diversions, not to mention the constant support.

To Gideon Koekoek, virtual officemate extraordinaire, who, thanks to the magic of teh intarnets, was just as distracting and just as inspiring as his real-life counterparts all the way from Amsterdam. Words can't do it justice, so here are some **doctoral hugs** instead.

To all of Walking Fish and Blacker Hovse, for being the most amazing friends a nerdy girl could ask for, especially to Katie Romportl, my first partner-in-crime, to Mike Borchert and Matt Kuzma for throwing pennies at my window late at night in order to sneak into my room to chat about quantum mechanics, to Mike Jorgenson for fractals and ensanguination, to Joe Carroll for frisbee and folk songs, to Nate Austin for castles and zeppelins, and to Katharina Kohler for always understanding exactly what I'm going through.

And most of all, to my husband Tim Crosby, for being the reason I come home every night, and for being the home I'll always come home to. Swarling swar swar, swarling swar.

The work presented in chapters 3, 5, 6 and §4.3 was all done in collaborations – here I would like to acknowledge my co-authors and detail my own role in each of these projects.

For chapter 3, I did the analysis and write-up primarily by myself, with valuable guidance from Kate Scholberg, Alec Habis, Shantanu Desai, and Jodi Cooley. The other members of the Super-Kamiokande collaboration helped via building the detector, keeping it running, and providing insightful comments on drafts of the paper. I also gratefully acknowledge the cooperation of the Kamioka Mining and Smelting Company. The Super-Kamiokande experiment has been built and operated from funding by the Japanese Ministry of Education, Culture, Sports, Science and Technology, the United States Department of Energy, and the US National Science Foundation.

For chapter 5, I added the new pixelization algorithms described here to the MANGLE software which was originally written by Andrew Hamilton, and did the bulk of the write-up as well. The *HEALPix* algorithms were done primarily by UROP student Colin Hill. Colin and I also worked together to create the new MANGLE website – Colin deserves a special thank you for pulling an all-nighter with me the night before the website went live. I also thank Michael Blanton for providing the SDSS DR6 VAGC mask, Krzysztof Górski and collaborators for creating the *HEALPix* package, and the WMAP team for making their data public via the Legacy Archive for Microwave Background Data Analysis (LAMBDA; <http://lambda.gsfc.nasa.gov>). Support for LAMBDA is provided by the NASA Office of Space Science.

For §4.3, which summarizes Tegmark et al. (2006), I contributed primarily by using my new version of MANGLE to create angular masks for each of the angular subsamples used in the analysis. I also helped with proofreading and editing the original paper.

For chapter 6, I did the analysis and write-up, with guidance from Max Tegmark. Idit Zehavi provided careful editing and insightful suggestions, and Michael Blanton provided the SDSS VAGC-DR5 data. I also wish to thank Daniel Eisenstein, David Hogg, Taka Matsubara, Ryan Scranton, Ramin Skibba, and Simon White for helpful comments. Funding for the SDSS has been provided by the Alfred P. Sloan Foundation, the Participating Institutions, the National Science Foundation, the U.S. Department of Energy, the National Aeronautics and Space Administration, the Japanese Monbukagakusho, the Max Planck Society, and the Higher Education Funding Council for England. The SDSS Web Site is <http://www.sdss.org>. The SDSS is managed by the Astrophysical Research Consortium for the Participating Institutions. The Participating Institutions are the American Museum of Natural History, Astrophysical Institute Potsdam, University of Basel, Cambridge University, Case Western Reserve University, University of Chicago, Drexel University, Fermilab, the Institute for Advanced Study, the Japan Participation Group, Johns Hopkins University, the Joint Institute for Nuclear Astrophysics, the Kavli Institute for Particle Astrophysics and Cosmology, the Korean Scientist Group, the Chinese Academy of Sciences (LAMOST), Los Alamos National Laboratory, the Max-Planck-Institute for Astronomy (MPIA), the Max-Planck-Institute for Astrophysics (MPA), New Mexico State University, Ohio State University, University of Pittsburgh, University of Portsmouth, Princeton University, the United States Naval Observatory, and the University of Washington.

This work was supported by a National Defense Science and Engineering Graduate Fellowship, a Bruno Rossi Fellowship, NASA grant NNG06GC55G, NSF grants AST-0134999, 0607597 and 0708534, the Kavli Foundation, and fellowships from the David and Lucile Packard Foundation and the Research Corporation.

Contents

List of Figures	12
List of Tables	13
1 Connecting particle physics and astrophysics	15
I Astrophysics Underground	19
2 Neutrino astronomy	21
2.1 History of multi-messenger astronomy	21
2.2 Neutrinos as astronomical messengers	21
2.3 Astrophysical production mechanisms	22
2.3.1 Diffusive shock acceleration	22
2.3.2 Active galactic nuclei	26
2.3.3 Other sources	27
2.4 Neutrino telescopes	28
2.4.1 How can we detect the astrophysical neutrino flux?	28
2.4.2 Super-K as a neutrino telescope	28
3 Search for diffuse astrophysical neutrino flux using ultra-high energy upward-going muons in Super-Kamiokande I	31
3.1 Introduction	31
3.2 The Super-Kamiokande Detector	32
3.3 Event Selection	32
3.3.1 Outer Detector Linear Fit	34
3.3.2 Selection Cuts	35
3.4 High-Energy Isotropic Monte Carlo	36
3.4.1 Resolution and Efficiency of Event Selection	37
3.4.2 Ultra-High-Energy Fraction	40
3.5 Flux Calculation	42
3.6 Expected Atmospheric Background from Monte Carlo	43
3.7 Analytical Estimate of Expected Muon Flux	45
3.7.1 Method for Calculating Muon Flux	45
3.7.2 Analytical Estimate of Expected Background	47
3.8 Upper Limit for Muon Flux from Cosmic Neutrinos	49
3.9 Conclusions	53

II	Particle Physics in the Sky	55
4	Doing cosmology with galaxies	57
4.1	Cosmology Basics	57
4.1.1	What is cosmology?	57
4.1.2	The standard cosmological model	57
4.1.3	Zeroth order cosmology	58
4.1.4	First order cosmology	62
4.1.5	Higher order cosmology	66
4.1.6	What does this teach us about particle physics?	71
4.2	Tools of cosmology	73
4.2.1	Combining cosmological probes	73
4.2.2	Galaxy surveys	73
4.2.3	Cosmic microwave background	78
4.2.4	Other probes	80
4.3	Example: combining WMAP and SDSS	82
4.3.1	Power spectrum estimation	82
4.3.2	Cosmological parameter estimation	84
4.4	Issues with using galaxies as cosmic tracers	87
4.4.1	Managing angular masks of galaxy surveys	87
4.4.2	Relative galaxy bias	88
5	Methods for rapidly processing angular masks of next-generation galaxy surveys	89
5.1	Introduction	89
5.2	MANGLE terminology	92
5.3	Speedup: pixelization	95
5.3.1	Pixelization concept	95
5.3.2	Pixelization schemes	96
5.3.3	Pixelization algorithm	99
5.3.4	Speed trials	99
5.4	Unification with <i>HEALPix</i> and other pixelized tools	102
5.4.1	Importing <i>HEALPix</i> maps into MANGLE	103
5.4.2	Exporting polygon files as <i>HEALPix</i> maps	104
5.5	Summary	105
6	SDSS galaxy clustering: luminosity & color dependence and stochasticity	109
6.1	Introduction	109
6.2	SDSS Galaxy Data	111
6.3	Analysis Methods	112
6.3.1	Overlapping Volume-Limited Samples	112
6.3.2	Counts-in-Cells Methodology	115
6.3.3	Relative Bias Framework	117
6.3.4	The Null-buster Test	123
6.3.5	Maximum Likelihood Method	124
6.4	Results	126
6.4.1	Null-buster Results	126
6.4.2	Likelihood Results	134

6.5	Conclusions	137
6.5.1	Biasing results	137
6.5.2	Implications for galaxy formation	138
6.A	Consistency Checks	139
6.A.1	Alternate null-buster analyses	139
6.B	Uncertainty Calculations	141
6.B.1	Jackknife uncertainties for null-buster analysis	141
6.B.2	Likelihood uncertainties	143
7	Conclusions	149
	Bibliography	151

List of Figures

1-1	Flow diagram of connections between particle physics and astrophysics. . .	16
2-1	Geometry of diffusive shock acceleration.	24
3-1	Schematic drawing of the Super-K detector.	33
3-2	OD-based muon trajectory fit applied to example MC muon events.	34
3-3	Resolution of OD-based fit on determining track parameters for events from the high energy isotropic MC.	38
3-4	Angular resolution of OD-based fit for events from the high energy isotropic MC.	39
3-5	Distribution of the time difference between OD entry and ID entry clusters for UHE downgoing muon events from data, compared to the distribution for the UHE events in the high-energy isotropic MC.	39
3-6	Efficiency of our data reduction on upward, throughgoing, $\geq 1.75 \times 10^6$ pe muons.	41
3-7	Fraction of events $k(E_\mu)$ that deposit $\geq 1.75 \times 10^6$ pe in the ID for the 100 yr atmospheric MC, the high-energy isotropic MC, and a power-law fit to the results from the latter.	48
3-8	The number of upward-going muon events above energy threshold E_μ^{\min} induced by atmospheric neutrinos, from our analytical calculatoin and from the 100 year atmospheric MC.	48
3-9	Upper limits from this analysis on muon ($\mu^+ + \mu^-$) flux above energy threshold E_μ^{\min} , compared to various model fluxes.	50
3-10	Approximate upper limits from SK-I on astrophysical neutrinos ($\nu_\mu + \bar{\nu}_\mu$). .	52
4-1	The curvature of space illustrated for two-dimensional universes.	59
4-2	A slice through the CfA redshift survey.	75
4-3	A slice through 2dFGRS.	76
4-4	A slice through SDSS.	77
4-5	Temperature anisotropies in the CMB from WMAP5.	79
4-6	CMB angular power spectrum from WMAP5.	80
4-7	The angular distribution of the SDSS DR4 luminous red galaxies showing the seven angular subsamples analyzed.	83
4-8	Measured power spectra for the full LRG and main galaxy samples.	86
4-9	95% constraints in the (ω_d, f_ν) plane.	87
5-1	Speed trials for a series of portions of the SDSS DR5 mask with and without pixelization.	91
5-2	A portion of the SDSS DR5 angular mask.	93

5-3	A cartoon illustrating the process of balkanization (a) with no pixelization, (b) with pixelization.	94
5-4	The full sky pixelized with the simple pixelization scheme.	97
5-5	The full sky pixelized with the SDSSPix pixelization scheme.	97
5-6	Left: portion of SDSS mask from Fig. 5-2 pixelized to a fixed resolution with the simple pixelization scheme. Right: the same mask pixelized with the simple pixelization scheme using the adaptive resolution method.	100
5-7	Time required to process the full SDSS DR5 mask with different choices of pixelization schemes and methods.	101
5-8	Left: Portion of SDSS mask as shown in Fig. 5-2. Right: Portion of SDSS mask from Fig. 5-2 as approximated by <i>HEALPix</i> pixels.	105
5-9	Top: The SDSS DR5 completeness mask, rasterized and plotted using <i>HEALPix</i> routines. Middle: The final 2dFGRS completeness mask, rasterized and plotted using <i>HEALPix</i> routines. Bottom: CMB temperature difference map measured by WMAP channel 4.	106
6-1	Histogram of the comoving number density of the volume-limited samples.	113
6-2	Color-magnitude diagram showing the number density distribution of the galaxies in the volume-limited samples.	115
6-3	Galaxy distributions plotted in comoving spatial coordinates for a radial slice, showing the four different types of pairwise comparisons made.	116
6-4	The SDSS DR5 angular mask pixelized at the four different resolutions used to partition the survey into cells.	118
6-5	A radial slice of the SDSS survey volume divided into cells.	118
6-6	Null-buster results for pairwise comparisons.	128
6-7	Relative bias b_{rel} between pairwise samples.	129
6-8	Luminosity dependence of bias for all, red, and blue galaxies.	131
6-9	Comparison to previous results for the luminosity dependence of bias for all, red, and blue galaxies.	132
6-10	The best-fitting values of the relative cross-correlation coefficient r_{rel} between pairwise samples.	135
6-11	Comparison of relative cross-correlation coefficient r_{rel} between red and blue galaxies as measured with different techniques.	136
6-12	Null-buster results for randomly split samples.	139
6-13	Comparison of jackknife and generalized χ^2 uncertainties on b_{rel} from the null-buster analysis.	142
6-14	Typical contour plots of $\Delta(2 \ln \mathcal{L})$ for volume V5 for three different resolutions.	143

List of Tables

3.1	Visual scan of candidate upward-going muon events	36
3.2	Fraction of high-pe events $k(E_\mu)$ in high energy isotropic MC	41
3.3	The flux of ultra-high energy upward-going muons as observed by SK-I. . .	42
3.4	Systematic uncertainties in atmospheric neutrino background	44
3.5	Confidence intervals for the upward-going muon flux due to neutrinos from astrophysical sources.	49
3.6	Approximate upper limits from SK-I on astrophysical neutrinos $(\nu_\mu + \bar{\nu}_\mu)$. .	51
4.1	Cosmological parameters measured from WMAP and SDSS LRG data. . . .	85
5.1	Definitions of Terms, in Alphabetical Order	93
6.1	Summary of cuts used to create luminosity-binned volume-limited samples.	114
6.2	Overlapping volumes in which neighboring luminosity bins are compared. .	114
6.3	Number of galaxies in each sample being compared.	117

Chapter 1

Connecting particle physics and astrophysics

Meg looked about. Ahead of her was a tremendous rhythmic swirl of wind and flame, but it was wind and flame quite different from the cherubim's; this was a dance, a dance ordered and graceful, and yet giving an impression of complete and utter freedom, of ineffable joy. As the dance progressed, the movement accelerated, and the pattern became clearer, closer, wind and fire moving together, and there was joy, and song, melody soaring, gathering together as wind and fire united.

And then wind, flame, dance, song, cohered in a great swirling, leaping, dancing, single sphere.

Meg heard Mr. Jenkins's incredulous, "What was that?"

Blajeny replied, "The birth of a star."

Mr. Jenkins protested, "But it's so small I can hold it in the palm of my hand." And then an indignant snort, "How big am I?"

"You must stop thinking about size, you know. It is both relative and irrelevant."

— Madeleine L'Engle, *A Wind in the Door*

One of the most remarkable things about physics is that it can be applied over such a vast range of size scales. Some physicists focus on understanding our world on almost inconceivably tiny scales, studying theories of fundamental building blocks of matter as small as 10^{-35} meters, a factor of 10^{-20} smaller than the diameter of a proton. Other physicists study our world at equally inconceivably huge scales, looking at the most distant parts of our universe that it is possible to see, over 10^{26} meters away. These largest and smallest scales in physics are separated by over 60 orders of magnitude.

Perhaps even more astounding is the fact that these two extreme regimes of physics are deeply connected: learning about how our universe behaves on the very largest scales can teach us things about elementary particles that could never be discovered in a terrestrial laboratory, and studying particles coming from space can also teach us about properties of distant astronomical objects. Over the past several decades, physicists have gained many great insights about both the macroscopic and microscopic regimes by taking advantage of this connection. The link between particle physics and astrophysics, which is the focus of this thesis, is but one example of a fruitful interaction between traditionally separate fields of science – there is a tremendous amount of exciting work being done at interfaces between

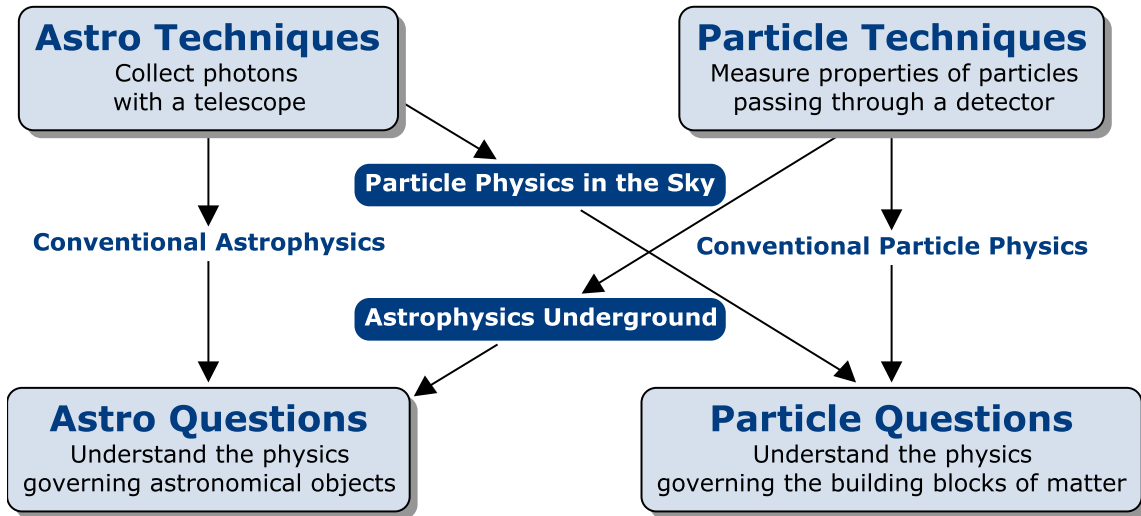


Figure 1-1 Flow diagram of connections between particle physics and astrophysics.

other fields as well. Some examples include applying statistical physics to biological systems, quantum computation research that aims to use quantum physics principles to revolutionize computer science, and neuroscience research integrating biology, psychology, and computer science.

Doing science at these interfaces is no easy task – integrating expertise across different fields generally leads to certain challenges. Scientists on either side of the fence will have different academic cultures, traditions, and methodologies, and they frequently do not mix well. For example, concerns have been raised that the trend towards using astronomy to study fundamental physics could ultimately be damaging to the astronomical community: White (2007) notes that “By uncritically adopting the values of an alien system [of high-energy physics traditions], astronomers risk undermining the foundations of their own current success and endangering the future vitality of their field.” However, the scientific potential of the crossover is large enough that such obstacles are well worth overcoming. As Kolb (2007) says, the ties between astronomy and particle physics “can either encourage or choke creativity ... It is up to us to choose wisely.” If these two scientific communities intelligently navigate the cultural interface, the science of both fields will be greatly enriched.

The nature of the particle-physics–astrophysics connection used in this thesis is illustrated in Fig. 1-1. The traditional means of doing astrophysics is to look at the light emitted from distant astronomical objects with a telescope and use this to infer the physics of these objects. On the other hand, traditional particle physics is done by measuring the properties of particles passing through a detector and using this to infer the nature of the particles themselves or the interactions that produced them.

One means of connecting astrophysics and particle physics is to use particles as astronomical messengers, i.e. to look for particles other than photons coming from astronomical objects to get a more complete picture of the physical system. We dub this “Astrophysics Underground” because when the particle messenger is a neutrino, the “telescopes” used for this endeavor are typically large particle detectors located deep underground to shield from background radiation. Essentially this is using the tools of particle physics to do astronomy.

We can also turn this connection in the other direction and use the tools of astronomy to

do particle physics, which we dub “Particle Physics in the Sky.” One particularly exciting area in which this can be applied is cosmology, the study of our universe as a whole. By doing astronomical observations cosmologists have built up a consistent theory of how our universe has evolved that turns out to depend on the properties of elementary particles and has also provided evidence for physics beyond the standard model of particle physics. Thus by studying the our universe at the largest scales we can also learn about the smallest.

The rest of this thesis is organized as follows: an exploration into doing “Astrophysics Underground” using neutrinos is given in chapters 2 and 3. Chapter 2 provides an overview of the field of neutrino astronomy, and chapter 3 describes a search for high energy neutrinos coming from astrophysical sources using the Super-Kamiokande neutrino detector. The following three chapters turn the connection arrow in the other direction and focus on “Particle Physics in the Sky” by doing cosmology with galaxy surveys. Chapter 4 gives a general introduction to the field of cosmology with a particular focus on the tool of galaxy surveys and what this can tell us about particle physics. In chapter 5, we describe a set of computational techniques for managing the complex data of modern galaxy surveys, and in chapter 6 we use data from the Sloan Digital Sky Survey to study how the clustering of galaxies depends on and their luminosities and colors and the implications of this for using galaxies as cosmological tools. Finally, we conclude in chapter 7 with a summary of what we have learned, some ideas for future research directions, and reflections on the nature of doing science at this fascinating interface between astrophysics and particle physics.

Part I

Astrophysics Underground

Chapter 2

Neutrino astronomy

2.1 History of multi-messenger astronomy

Historically, the study of astronomy has been the study of photons coming from the sky. Early astronomers learned a tremendous amount observing only the visible-wavelength photons that could be seen with the naked eye. Since then, revolutions in astronomy have come about through expanding our ability to detect different types of astronomical messengers.

The invention of the telescope in the early seventeenth century enabled the collection of much larger numbers of photons, opening a window on fainter sources. The twentieth century saw an explosion of astronomical information as techniques were developed to observe photons all across the electromagnetic spectrum from radio waves to gamma rays, leading to the discovery of remarkable astrophysical phenomena such as pulsars and gamma ray bursts.

Detecting particles other than photons from astrophysical sources provides yet another window on the universe. The discovery of cosmic rays in 1912 was the first step in this endeavor. Cosmic rays are charged particles – protons, electrons, and atomic nuclei – originating from cosmic sources. Studies of cosmic rays have led to insights about astrophysical processes such as the evolution of galactic magnetic fields and particle acceleration within remnants of supernova explosions. High-energy cosmic rays penetrating the atmosphere also provide a natural particle collider – this was an instrumental tool in particle physics as well: for example, positrons, muons, and pions were all discovered in cosmic ray studies. Today the astrophysical origin and acceleration mechanisms of the highest energy cosmic rays is one of the primary open questions in particle astronomy.

2.2 Neutrinos as astronomical messengers

Another exciting step towards using particles as astronomical messengers is to look for neutrinos coming from cosmic sources. In terms of providing astrophysical information, neutrinos have some advantages over photons and charged particles. Firstly, they are not readily absorbed by intervening matter, so they can act as probes of extremely high-density environments such as the central cores of stars, active galactic nuclei, or supernovae from which photons could never escape. Secondly, they are not deflected by cosmic magnetic fields, so unlike charged particles, they always point directly back to their source.

The advantage of low absorption, however, is the biggest disadvantage as well – they tend to pass through our detectors unseen just as readily as they pass through dense ma-

terial at the source. Thus neutrino astronomy demands sophisticated detection techniques, and as such, this field is still in its infancy. So far, neutrinos have only been detected from two astrophysical sources: the sun (Davis 2003; Koshiba 2003) and supernova 1987a (Hirata et al. 1987; Bionta et al. 1987). However, the insights gained into both astronomy and particle physics from just these two neutrino sources have been tremendous.

The work of Raymond Davis and others on detecting neutrinos from the sun generated the famous “solar neutrino problem”, whereby the observed flux of solar neutrinos was only about a third of what was expected based on astrophysical models of energy production in the sun (Davis 1996). This called both the experimental measurements and the standard solar models into question, and remained a controversy for decades. Its ultimate resolution actually came from a revolution in particle physics: measurements from the Super-Kamiokande neutrino detector (Super-K; Fukuda et al. 1998) provided conclusive evidence that neutrinos oscillate from one type to another and therefore must have mass, in conflict with the standard model of particle physics which treats them as massless. This explained the solar neutrino problem via some fraction of electron neutrinos produced in the sun oscillating to muon or tau neutrinos by the time they reach the Earth and thus going undetected. Ultimately, observations of solar neutrinos have both solidified our understanding of astrophysical processes in the sun and provided the first concrete evidence for physics beyond the standard model.

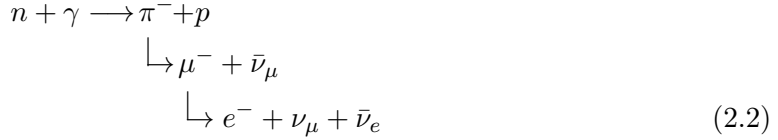
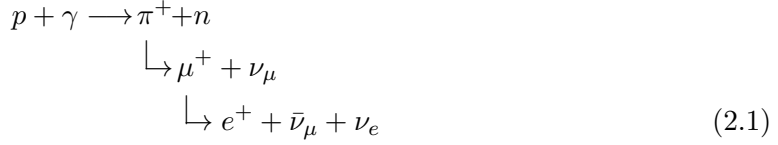
The 20 neutrinos detected from supernova 1987a by the Kamiokande-II and IMB detectors (Hirata et al. 1987; Bionta et al. 1987) similarly provided insights into both particle physics and astrophysics. The flux observed is consistent with astrophysical models of core-collapse supernovae in which nearly all of energy from the collapse is emitted in neutrinos. Additionally, the observation that neutrinos of different energies all arrived nearly simultaneously provides a clue to the nature of the neutrinos themselves: it means that the neutrinos of different energies all travel at nearly the speed of light, which implies that the electron neutrino rest mass must be quite small. Thus the neutrinos observed from the supernova can be used to set an upper limit on the mass of the electron neutrino (Kernan and Krauss 1995).

The next frontier of neutrino astronomy is to detect astrophysical neutrinos at high energies (GeV-PeV) – several experimental efforts to do this are currently underway. Such high-energy neutrinos will open yet another new window on the universe – they will shed light on astrophysical processes in extreme environments and will also provide clues to the origins of the highest energy cosmic rays. (See Halzen and Hooper 2002 for more details.)

2.3 Astrophysical production mechanisms

2.3.1 Diffusive shock acceleration

The general mechanism for producing high-energy neutrinos is the following: first, protons or other nuclei are accelerated by shocks in an astrophysical plasma. Then the accelerated hadrons interact with photons in a surrounding radiation field and produce charged pions that decay into high-energy neutrinos:



These interactions can also produce neutral pions, which generate high-energy gamma rays:



The proton acceleration mechanism at work here is known as diffusive shock acceleration, also known as the first-order Fermi mechanism (Fermi 1949). The difference in velocities on either side of a shock in a magnetized plasma can transfer kinetic energy to particles as they cross the shock multiple times. The basic geometry of a plane shock is illustrated in Fig. 2-1. This mechanism generically predicts a power-law spectrum of particle energies with $dN/dE \propto E^{-\alpha}$ where $\alpha \approx 2$. We give a rough derivation of this below following Gaisser (1990); for a more detailed treatment see Schlickeiser (2002).

The basic equations governing the behavior of shocks can be derived from conservation of mass, momentum, and energy across the shock boundary. For a non-relativistic hydrodynamic plane shock, these conditions are given by

$$\rho_2 u_2 - \rho_1 u_1 = 0, \tag{2.4}$$

$$\rho_2 u_2^2 - \rho_1 u_1^2 = P_1 - P_2, \tag{2.5}$$

$$\rho_2 u_2 \left(w_2 - \frac{1}{2} u_2^2 \right) - \rho_1 u_1 \left(w_1 - \frac{1}{2} u_1^2 \right) = 0, \tag{2.6}$$

where 1 subscripts denote conditions upstream of the shock and 2 subscripts denote downstream conditions. u is the component of the velocity normal to the shock front in the rest frame of the shock, ρ is the density, P is the pressure, and w is the specific enthalpy, given by $w = c_p T$ for temperature T and specific heat at constant pressure c_p . For an ideal gas, $w = \gamma P / ((\gamma - 1) \rho)$ where γ is the ratio of specific heats at constant pressure and constant volume; $\gamma = 5/3$ for a monatomic ideal gas. In a magnetized plasma the magnetic fields will also contribute to these conditions – here we assume either that the magnetic field is parallel to the normal of the shock plane or that the magnetic fields are small enough to be negligible for the continuity conditions.

In order for a shock to form, u_1 must be greater than the sound speed $c_{s1} = \sqrt{\gamma P_1 / \rho_1}$.

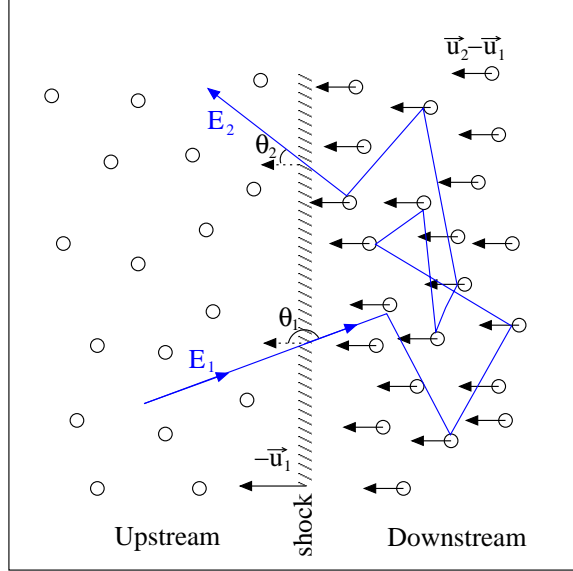


Figure 2-1 Geometry of diffusive shock acceleration, shown in the rest frame of the material upstream of the shock. The trajectory of an accelerated particle is shown in blue/grey. Scattering centers (i.e. magnetic field irregularities) are represented as circles.

The Mach number M of the shock is defined as $M = u_1/c_{s1}$, and by using equations (2.4), (2.5), and (2.6), and much clever algebra, the ratio of the upstream to downstream velocities is given by

$$\frac{u_1}{u_2} = \frac{M^2(\gamma + 1)}{M^2(\gamma - 1) + 2}. \quad (2.7)$$

The energy of a charged particle will increase as it diffuses across the shock from the upstream medium to the downstream medium and back, as illustrated by the trajectory in Fig. 2-1. To calculate the energy change, we start with a relativistic ($E \approx pc$) population of particles with velocities that are isotropic in the frame of the upstream medium. A particle with energy E_1 that crosses the shock at an angle θ_1 in the upstream frame will have an energy

$$E'_1 = \Gamma E_1 (1 - \beta \cos \theta_1) \quad (2.8)$$

in the downstream frame, where $\beta = (u_1 - u_2)/c$ and Γ is the corresponding Lorentz factor. Primes denote quantities in the downstream frame; unprimed quantities are in the upstream frame. Averaging over an isotropic population gives $\langle \cos \theta_1 \rangle = -2/3$ for particles crossing the shock.

In the downstream medium, the particle undergoes elastic scattering off of irregularities in the magnetic field generated by low-frequency magnetohydrodynamic waves. As the particle diffuses, its average motion will coincide with that of the downstream medium, so we now have an isotropic population in the downstream frame. To a first approximation, these scatterings do not cause the particle to lose energy, so a particle that is scattered back into the upstream medium at an angle θ'_2 will have energy $E'_2 = E'_1$. Transforming back into the upstream frame gives

$$E_2 = \Gamma E'_2 (1 + \beta \cos \theta'_2), \quad (2.9)$$

and since the particles have isotropized relative to the downstream medium, $\langle \cos \theta'_2 \rangle$ can be obtained by averaging over an isotropic population as well, yielding $\langle \cos \theta'_2 \rangle = 2/3$. Plugging equation (2.8) in for E'_2 in equation (2.9) and averaging over the angular factors yields the following formula for the fractional energy change in one “encounter” (diffusing from upstream to downstream and back):

$$\begin{aligned} \epsilon \equiv \frac{E_2 - E_1}{E_1} &= \frac{1 + \frac{4}{3}\beta + \frac{4}{9}\beta^2}{1 - \beta^2} \\ &\approx \frac{4}{3}\beta, \end{aligned} \tag{2.10}$$

where the last approximation holds for a non-relativistic shock with $\beta \ll 1$.

Once in the downstream medium, the particles have some probability to escape rather than get scattered back into the upstream medium. We can estimate this probability by considering the flux of particles through an imaginary plane one scattering length away from the shock in the downstream medium. Particles that pass through this plane back in the upstream direction will get swept up by the shock, and particles that pass through towards the downstream direction can escape. Working in the frame of the downstream medium, particles will pass back through the shock if $c \cos \theta < -u_2$. Thus the flux upstream is

$$\begin{aligned} F_u &\propto \int_{-1}^{-u_2/c} (c \cos \theta + u_2) d \cos \theta \\ &= -\frac{(c - u_2)^2}{2c} \end{aligned}$$

and the flux downstream is

$$\begin{aligned} F_d &\propto \int_{-u_2/c}^1 (c \cos \theta + u_2) d \cos \theta \\ &= \frac{(c + u_2)^2}{2c}. \end{aligned}$$

The probability for a particle to escape is then

$$\begin{aligned} P_{\text{esc}} &= 1 - \left| \frac{F_u}{F_d} \right| \\ &= 1 - \frac{(c - u_2)^2}{(c + u_2)^2} \\ &\approx \frac{4u_2}{c} \end{aligned} \tag{2.11}$$

for $u_2 \ll c$.

The energy spectrum produced in this scenario – where a particle gains fractional energy ϵ and has a probability P_{esc} of escaping with each encounter – can be calculated as follows: if particles initially have energy E_0 , the energy after m encounters is $E_n = E_0 (1 + \epsilon)^m$, so

the number of encounters n needed to reach energy E is

$$n = \frac{\log \frac{E}{E_0}}{\log(1 + \epsilon)}.$$

The probability of remaining after m encounters is $(1 - P_{\text{esc}})^m$, so the number of particles with energy greater than E is thus

$$\begin{aligned} N(> E) &\propto \sum_{m=n}^{\infty} (1 - P_{\text{esc}})^m \\ &= \frac{(1 - P_{\text{esc}})^n}{P_{\text{esc}}} \\ &= \frac{1}{P_{\text{esc}}} \left(\frac{E}{E_0} \right)^{-(\alpha-1)}, \end{aligned}$$

where

$$\alpha - 1 = \frac{\log \frac{1}{1 - P_{\text{esc}}}}{\log(1 + \epsilon)}. \quad (2.12)$$

The differential energy flux is thus $dN/dE \propto E^{-\alpha}$. Plugging in the results of equations (2.10) and (2.11) into equation (2.12) and using the approximations that u_1 and $u_2 \ll c$,

$$\alpha \approx 1 + \frac{3}{\frac{u_1}{u_2} - 1}.$$

Now we can insert equation (2.7) for u_1/u_2 , use $\gamma = 5/3$ for a monatomic ideal gas, and take the limit of a strong shock where $M \gg 1$, yielding

$$\alpha \approx 2 + \frac{4}{M^2}. \quad (2.13)$$

Thus, $dN/dE \sim E^{-2}$ for first order Fermi acceleration.

Calculating the details of the high-energy neutrino spectrum of a particular type of astrophysical source requires a more sophisticated treatment that relaxes some of the assumptions we have made here and accounts for appropriate energy loss mechanisms as well as how the pion energy is distributed among the decay products in a particular context. However, since most astrophysical models invoke this first-order Fermi mechanism, the prediction of a spectrum roughly proportional to E^{-2} is a generic feature. As such, $d\Phi_\nu/dE_\nu \propto E_\nu^{-2}$ is frequently used as a fiducial model for an astrophysical neutrino flux – we make use of this convention in chapter 3.

2.3.2 Active galactic nuclei

Astrophysical systems that produce high energy neutrinos via the mechanism outlined in the previous section must have two features: a shocked, magnetized plasma that can accelerate protons to very high energies, and a sufficiently intense radiation field to allow for photopion production. These conditions are expected to be present in a number of astrophysical systems, including gamma ray bursts and active galactic nuclei (AGNs). The expected signal from AGNs is the strongest for the energy range to which Super-K is sensitive, so they are the primary astrophysics target for the study discussed in chapter 3.

AGNs are supermassive black holes accreting matter at the centers of galaxies. They are the most luminous persistent sources in the universe and emit radiation over a vast range of the electromagnetic spectrum, from radio waves to gamma rays. There are two locations where an AGN could produce neutrinos: in the core or in the jets. We give a rough outline of these processes here; further details can be found in Gaisser et al. (1995).

In models of neutrino production within AGN cores, a shock is formed in an approximately spherical shell around the black hole, where the ram pressure of the infalling material is balanced by the radiation pressure of the emission. The region inside the shock is optically thick and provides ample radiation density for $p\gamma$ collisions. This process generates high-energy neutrinos from quite close to the black hole, thus probing a region from which photons cannot escape. A detailed model of neutrino production in AGN cores can be found in Stecker and Salamon (1996), along with a prediction for the diffuse flux of neutrinos expected from integrating the contributions from all AGN cores over the history of the universe.

Neutrinos can also be produced within AGN jets. Jets are relativistic outflows of charged particles collimated along the black hole’s rotation axis. The mechanism that powers the jets is not yet well-understood in detail, but the basic idea is that a varying magnetic field linked to the rotation of the black hole or the accretion disk generates an electric field that can accelerate charged particles. In the case of jets, the shocks needed for first-order Fermi acceleration to extremely high energies are formed by inhomogeneities in the matter traveling along the jet. The required photon field is provided by synchrotron radiation from electrons spiraling around magnetic field lines. A model of the predicted diffuse neutrino flux from AGN jets can be found in Mannheim et al. (2001).

It is not known whether jets consist mainly of electrons and positrons or if there is a hadronic component as well. The observed gamma rays coming from jets could be explained by either leptonic or hadronic processes. In the leptonic process, gamma rays are produced via low-energy synchrotron photons gaining energy via inverse Compton scattering with the accelerated electrons – this is known as synchrotron-self-Compton radiation. Alternatively, accelerated hadrons could produce gamma rays via the decay of neutral pions, as in equation (2.3). Since neutrinos are only produced in hadronic processes, observation of a neutrino flux from these sources would help distinguish between these models. The question of whether hadrons are accelerated to extremely high energies by AGNs is also an important question for determining the origin of ultra-high energy cosmic rays. Recent results from the Auger Observatory (Abraham et al. 2007) indicate that the arrival directions of the highest energy cosmic rays are statistically correlated with the locations of nearby AGNs – this is a tantalizing hint that AGNs could be the answer to the long-standing puzzle of ultra-high energy cosmic rays. A definitive observation of a neutrino flux associated with AGNs would lend strong support to this picture (Halzen and O’Murchadha 2008).

2.3.3 Other sources

In addition to AGNs, there are many other possible astrophysical sources of neutrinos. For example, gamma ray bursts (GRBs) – the highest-energy explosions in the universe – are likely to provide the conditions needed for diffusive shock acceleration and photopion production as well (Waxman and Bahcall 1999). There are also a number of more exotic phenomena that could produce high-energy neutrinos, including decays of topological defects such as cosmic strings or magnetic monopoles and self-annihilation of weakly interacting dark matter particles (WIMPs) (Staśto 2004).

Another source of high-energy neutrinos is linked to the propagation of ultra-high energy cosmic rays through the universe: protons with energies above $\sim 10^{20}$ eV will undergo photo-pion production as in equation (2.3) via collisions with cosmic microwave background (CMB) photons (see §4.2.3 for more about the CMB). This is known as the GZK cutoff (Greisen 1966; Zatsepin and Kuzmin 1966), and recent cosmic ray experiments (Sokolsky and Thomson 2007) claim to have observed the predicted break in the cosmic ray spectrum due to this effect. Thus there should be a corresponding neutrino flux from the decay of the pions produced – experiments such as ANITA (Barwick et al. 2006) are attempting to detect these neutrinos.

2.4 Neutrino telescopes

2.4.1 How can we detect the astrophysical neutrino flux?

The flux of high-energy neutrinos from active galactic nuclei is quite small and the probability of a neutrino interacting with material in a detector is also quite low. These two basic facts point to the need for an extremely large collecting area. Modern neutrino “telescopes” are thus actually large naturally-occurring volumes of ice or water instrumented with photomultiplier tubes (PMTs). Neutrinos that interact in or near the detector volume produce charged particles that emit Cerenkov light as they pass through the water or ice; this light is then recorded by the PMTs.

In order to make a significant observation of astrophysical neutrino flux, it is expected that we will need a detector with a volume on the order of 1 km^3 (Halzen and Hooper 2002). There are two main efforts underway aiming towards this goal: IceCube, a detector currently under construction at the South Pole which uses the Antarctic ice shelf as its detection medium that is expected to be completed in 2011 (IceCube Collaboration 2007), and KM3NeT, a detector to be built in the Mediterranean Sea (Katz 2006; Kappes et al. 2007) with the combined efforts of the ANTARES (Katz 2004), NEMO (Sapienza 2006), and NESTOR (Aggouras et al. 2005) collaborations. Additionally, the AMANDA detector (Ahrens et al. 2004), a pathfinder for IceCube covering a volume of 0.015 km^3 of Antarctic ice that was completed in 2000, has already produced a number of interesting results (Berghaus et al. 2007).

2.4.2 Super-K as a neutrino telescope

The Super-K volume is a large tank of water with a volume of $5 \times 10^{-5} \text{ km}^3$. It was designed primarily to detect neutrinos from the sun, supernovae, and particle accelerators – its volume is quite small compared to the neutrino telescopes currently being built whose primary science target is the high-energy astrophysical neutrino flux. Thus the chances of actually seeing this signal in Super-K are not very high.

Nonetheless, it is still an interesting exercise to look for it in the Super-K data: it provides an important consistency check, and Super-K can complement IceCube and KM3NeT in terms of sky coverage and livetime. Furthermore, observing a high-energy neutrino event in Super-K would provide much more detailed directional information than the more sparsely instrumented kilometer-scale detectors.

To this end, a number of neutrino astronomy studies have been undertaken by the Super-K collaboration, including searches for neutrino point sources (Abe et al. 2006; Desai et al. 2008), supernova bursts (Ikeda et al. 2007), and annihilations of WIMPs in the Sun, Earth,

and galactic center (Desai et al. 2008). Here we focus on one such study: chapter 3 describes a search for a diffuse neutrino flux from unresolved sources performed by looking for extremely high energy events in 1679.6 live days of Super-K data and comparing the observed flux to the expected atmospheric neutrino background. We use Super-Kamiokande's highest energy data sample to set an upper limit on the diffuse flux of neutrinos from astrophysical sources.

Chapter 3

Search for diffuse astrophysical neutrino flux using ultra-high energy upward-going muons in Super-Kamiokande I

This chapter is adapted from the paper “Search for diffuse astrophysical neutrino flux using ultra-high energy upward-going muons in Super-Kamiokande I” by Molly E. C. Swanson et al. (the Super-Kamiokande Collaboration), which was previously published in the *Astrophysical Journal* 652, pp. 206-215 (Swanson et al. 2006).

3.1 Introduction

Neutrinos have great potential as astronomical messengers. The detection of neutrinos from astronomical sources has led to many significant discoveries. Two sources of extraterrestrial neutrinos in the MeV energy range have been detected so far: the Sun (Davis 2003; Koshiba 2003) and supernova 1987a (Hirata et al. 1987; Bionta et al. 1987). The next step for neutrino astronomy is to detect neutrinos in the GeV-PeV energy range, which will open a new window on the high energy universe. A wide variety of astrophysical phenomena are expected to produce extremely high energy neutrinos, ranging from active galactic nuclei (AGNs) and gamma-ray bursts (GRBs; Halzen and Hooper 2002; Gaisser et al. 1995) to more exotic sources such as dark matter annihilation or decays of topological defects (Stasto 2004).

The flux of neutrinos at such high energies is quite small; therefore, large-scale detectors are required. One effective technique for observing high-energy neutrinos with an underground detector is to look for muons produced by ν_μ or $\bar{\nu}_\mu$ interacting in the surrounding rock. (Throughout this chapter, “muons” will refer to both μ^+ and μ^- .) The muon range in rock increases with muon energy, which expands the effective interaction volume for high-energy events. Downward-going neutrino-induced muons cannot be distinguished from the much larger flux of downward cosmic-ray muons, but since cosmic ray muons cannot travel through the entire Earth, upward-going muons are almost always neutrino-induced. Thus, upward-going muons provide a suitable high-energy neutrino signal.

At muon energies above 1 – 10 TeV, the upward-going muon flux due to neutrinos from AGNs is expected to exceed the upward-going muon flux due to atmospheric neutrinos (Stecker and Salamon 1996; Mannheim et al. 2001). This cosmic neutrino flux could be detected either by searching for point sources of high-energy neutrinos or by detecting a diffuse, isotropic flux of neutrinos from unresolved astrophysical sources. A diffuse cosmic neutrino flux would be observed as an excess to the expected atmospheric neutrino flux at high energies. In this analysis, we focus on searching for a diffuse flux of upward-going muons due to neutrinos from astrophysical sources using the highest energy data sample in Super-Kamiokande (Super-K).

This study complements other Super-K searches for astrophysical point sources of high energy neutrinos that use data over a larger energy range (Abe et al. 2006). In this chapter we describe a search for evidence of a high energy astrophysical neutrino flux in Super-K’s highest energy upward-going muon sample. In §3.2 we describe the Super-Kamiokande detector, and in §3.3 we give the details of how we selected candidate events from Super-K’s ultra-high-energy sample. We evaluate our selection process with Monte Carlo in §3.4 and calculate the observed upward-going muon flux in §3.5. Section 3.6 and §3.7 discuss the background due to the atmospheric neutrino flux. Based on the results, we set an upper limit in §3.8 and conclude in §3.9. Any necessary estimates and approximations have been made so that they lead to a conservative result for this upper limit.

3.2 The Super-Kamiokande Detector

The Super-K detector, shown in Figure 3-1, is a cylindrical 50 kiloton water Cerenkov detector, located in the Kamioka-Mozumi mine in Japan. It is 41.4 m tall and 39.3 m in diameter. The detector was constructed under the peak of Mount Ikenoyama, which provides an average rock overburden of 1000 m (2700 m water equivalent). Its geodetic location is at 36.4° north, 137.3° east, and altitude 370 m.

Super-K consists of two concentric, optically separated detectors. Until 2001 July the inner detector (ID) was instrumented with 11,146 inward-facing 50 cm diameter photomultiplier tubes (PMTs). The outer detector (OD) is a cylindrical shell of water surrounding the ID and is instrumented with 1885 outward-facing 20 cm diameter PMTs. Between the ID and the OD, there is a 50 cm thick shell. Photons coming from this region will not be detected by either the OD or the ID, so we refer to it as the insensitive region.

More details about the detector can be found in Fukuda et al. (2003). The data sample used in this analysis was taken from 1996 April to 2001 July, corresponding to 1679.6 days of detector livetime. This data run is referred to as SK-I.

Super-K is primarily designed to detect lower energy neutrinos from the Sun, the atmosphere, and particle accelerators but can potentially detect the extremely high energy neutrinos expected from astrophysical sources as well. This chapter focuses on the events at the highest energy end of Super-K’s detection range.

3.3 Event Selection

The ultra-high-energy sample in SK-I consists of events that deposit $\geq 1.75 \times 10^6$ photoelectrons (pe) in the ID. In the low-energy regime, on average about 9 pe are recorded by the ID PMTs for each MeV of energy deposited in the tank; the electronics for the ID PMTs saturate at about 300 pe. Thus an event with $\geq 1.75 \times 10^6$ pe in the ID corresponds to a

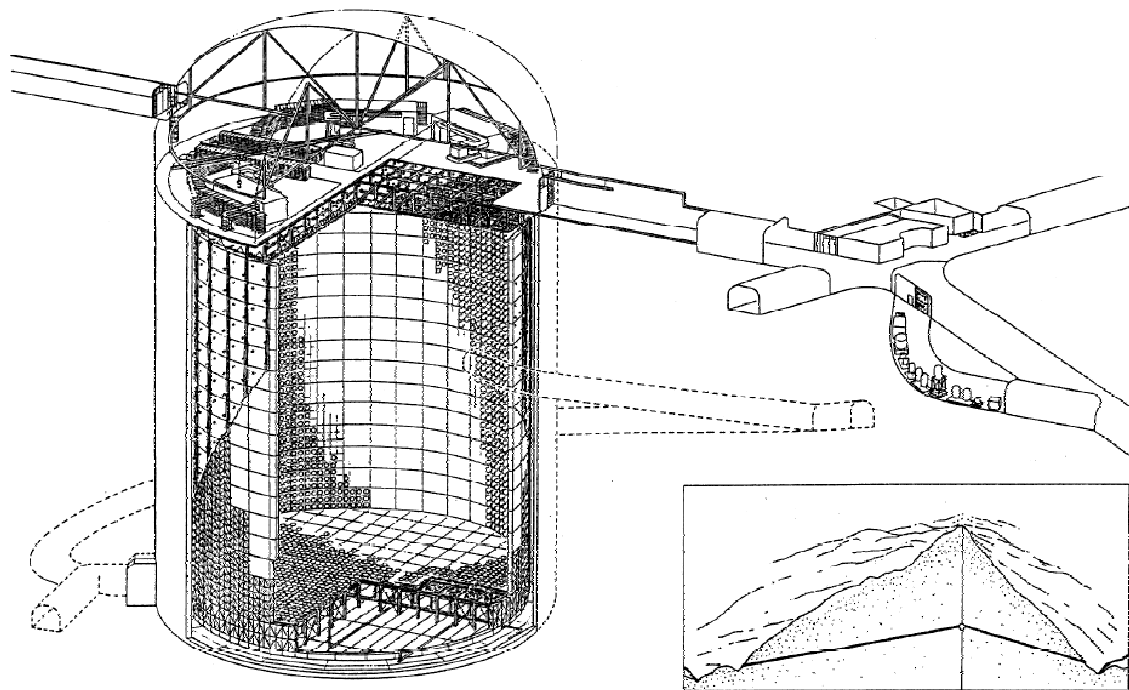


Figure 3-1 Schematic drawing of the Super-K detector. Inset at bottom right shows the location of the detector within Mount Ikenoyama (cutaway view).

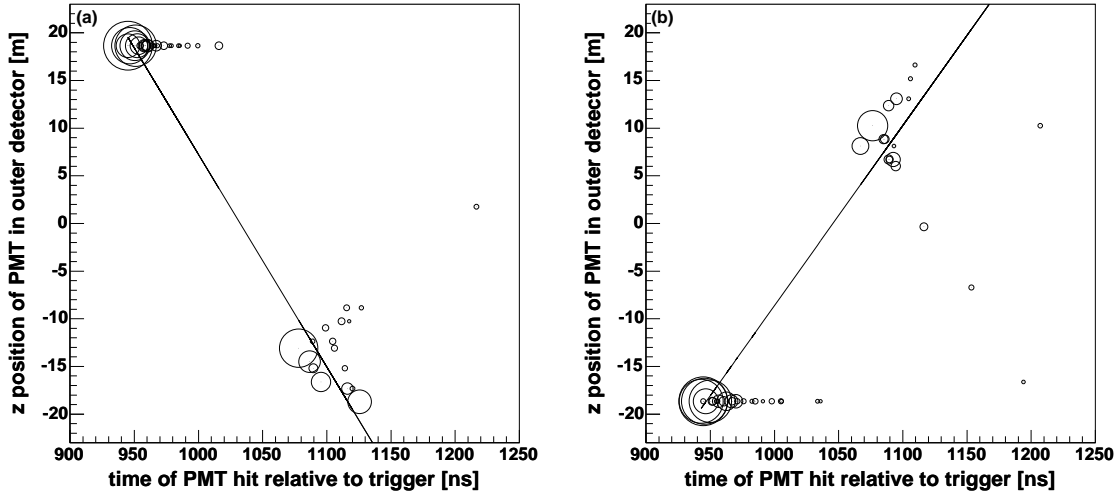


Figure 3-2 (a) OD-based muon trajectory fit applied to an example MC downward-going muon event. (b) OD-based fit applied to an example MC upward-going muon event. The size of the circle around each point is proportional to the charge detected in the PMT.

minimum energy deposition of approximately 200 GeV, but the actual energy deposition could be much higher, since the saturation effect prevents all of the produced pe from being recorded.

At high energies, muons have some probability to lose energy through radiative processes such as bremsstrahlung, resulting in an electromagnetic shower that deposits large quantities of pe in the detector. For comparison, a muon that traverses the maximum path length through the ID (50 m) but does not produce any electromagnetic showers will deposit approximately 11 GeV via ionization energy loss, corresponding to $\sim 10^5$ pe deposited in the ID. Thus a high-pe cutoff offers a means of selecting high energy events.

At the high-pe threshold of $\geq 1.75 \times 10^6$ pe, the high level of saturation in the ID PMT electronics can cause Super-K's precision muon fitting algorithms to fail. Therefore, these extremely energetic events are not included in other studies of upward-going muons in SK-I (Desai et al. 2004; Fukuda et al. 1999; Ashie et al. 2005). In this study we analyzed this ultra-high-energy data sample separately using a different fitting method based on information from the OD.

3.3.1 Outer Detector Linear Fit

SK-I's ultra-high-energy data sample contains a total of 52214 events. Most of these are either very energetic downward-going cosmic-ray muons or multiple muon events where two or more downward-going muons hit the detector simultaneously. In order to select candidate upward-going muons from this sample, we applied a simple linear fit to the OD data for each event. A linear fit was done on the z -position of each OD PMT versus the time it fired, weighted by the total charge in the PMT. Example fits of simulated downward-going and upward-going muon events are shown in Figure 3-2. The slope of this fitted line is an estimate of $-\cos \Theta$, where Θ is the zenith angle of the incoming muon. A positive fitted slope indicates that the muon is upward-going. A similar linear fit was done on the x - and

y -positions to determine the full muon trajectory through the detector.

Since this fitting method is based on the OD (which has a lower resolution than the ID), it is not as precise as the muon fitting algorithms used in the lower energy upward-going muon analysis. However, it works even when the ID PMT electronics are completely saturated and the precision ID-based algorithms fail.

3.3.2 Selection Cuts

To select candidate upward-going muons, we applied the OD-based fit to all 52214 events in the ultra-high-energy data sample. A cut of $\cos \Theta \leq 0.1$ was used to eliminate the bulk of the downward-going single and multiple muon events. In addition, the fitted trajectory was required to have a path length of > 7 m in the ID.

To ensure high-quality fit results, we looked at the number of OD PMTs hit near the projected entry and exit points. For a true throughgoing muon, there will be a cluster of hit PMTs around the entry and exit points. If the fit is accurate, the projected path should pass through both of these clusters, so we made an additional cut on the number of OD PMTs hit within 10 m of the projected OD entry and exit points, N_{ODentry} and N_{ODexit} . We required both N_{ODentry} and N_{ODexit} to be 10 or greater, indicating significant clusters of OD PMTs that were hit near the entry and exit points of the fitted trajectory.

Events that do not have N_{ODentry} and $N_{\text{ODexit}} \geq 10$ are generally either stopping muons, partially contained events, or poorly fitted throughgoing muons. Stopping muons are muons that stop in the detector and only form an OD entry cluster. They typically have energies of 1-10 GeV, well below the range of the expected astrophysical signal, so it is appropriate to discard events that look like stopping muons. Partially-contained events are neutrino interactions that take place inside the detector and only form an OD exit cluster — they are not part of the upward-going muon flux incident on the detector, so we want to discard these as well. This cut also occasionally eliminates inaccurately fitted throughgoing muon events, which reduces the efficiency somewhat but improves the accuracy of the fit results.

Another possible type of event that can masquerade as a throughgoing muon is a partially-contained event with multiple exiting particles. Such an event will create two (or more) clusters of hit PMTs in the OD, which could be mistaken as the entry and exit points of a throughgoing muon. In order to eliminate such events, we looked at the timing between the OD and ID entry points. If the event is truly a throughgoing muon, the OD PMTs near the entry point should fire before the ID PMTs. We determined OD and ID entry clusters via a simple time-based clustering method and evaluated the mean time of hits within 6 m of the OD and ID entry points, t_{IDentry} and t_{ODentry} .

In an ideal measurement, $t_{\text{IDentry}} < t_{\text{ODentry}}$ would indicate that the perceived entry cluster is actually caused by an exiting particle. However, the timing determination is complicated by an effect known as prepulsing. Prepulsing occurs when there are so many photons incident on the PMT that they are not all converted to photoelectrons at the photocathode - some photons hit the first dynode instead and are converted to photoelectrons there. When this happens in an ID PMT, the time it was hit appears earlier than it actually was, which will artificially reduce t_{IDentry} , making the ID light appear earlier compared to the OD light. If this occurs for an ultra-high energy throughgoing muon event, it could cause $t_{\text{IDentry}} - t_{\text{ODentry}}$ to be negative. To allow for this effect, we used a fairly loose cut of -40 ns: if $t_{\text{IDentry}} - t_{\text{ODentry}} < -40$ ns, indicating very early ID light, then the event was rejected as a likely neutrino interaction in the ID.

After these cuts on $\cos \Theta$, path length, N_{ODentry} , N_{ODexit} , and $t_{\text{IDentry}} - t_{\text{ODentry}}$ were

Table 3.1 Visual scan of candidate upward-going muon events

Visual scan classification	Number of events
Multiple muon events	164
PMT “flashers” (malfunctioning PMTs)	5
Other noise events	2
Downgoing muons (manual fit $\cos \Theta \geq 0$)	171
Upgoing muons (manual fit $\cos \Theta < 0$)	1
Total	343

applied to the 52214 events in the sample, 343 candidate events remained. These remaining events were then evaluated by a visual scan and a manual direction fit by two independent researchers to select events with $\cos \Theta < 0$.

The visual scan eliminates events that can pass the automatic reduction but are obvious to the trained human eye as noise, i.e., mainly downward-going multiple muon events and “flashers.” Multiple muon background events occur when two or more downward-going muons from an atmospheric shower pass through the detector simultaneously. They have extra energy deposition (and thus are expected to be more common in the ultra-high-energy sample) and typically give poor OD fit results due to multiple OD clusters, but they are easy to identify visually. Flashers are events caused by malfunctioning PMTs that emit light and create characteristic patterns. After the multiple muon events and flashers are removed, the manual direction fit separates truly upward-going muons from mis-fitted downward-going muons.

From the 343 candidates, only one event passed the visual scan and manual direction fit selection as being truly upward-going. The breakdown of the visual scan and manual fit classifications is shown in Table 3.1.

This upward-going muon event selected from the $\geq 1.75 \times 10^6$ pe sample is the ultra-high energy upward-going muon signal observed by SK-I. This event occurred on 2000 May 12 at 12:28:07 UT and deposited 1,804,716 pe in the ID. Based on the manual fit results, the path length through the ID was 40 m, and the zenith angle was $\cos \Theta = -0.63$, corresponding to a direction of origin of (R.A., decl.) = $20^{\text{h}}38^{\text{m}}, -37^{\circ}18'$.

3.4 High-Energy Isotropic Monte Carlo

In order to calculate the observed muon flux, we need to determine the resolution and efficiency of the OD-based fit and other cuts on high-energy muons, and we need to estimate the probability that a muon of a given energy will deposit $\geq 1.75 \times 10^6$ pe in the ID.

To determine these quantities, we generated a high-energy isotropic Monte Carlo (MC) sample. This MC consists of an isotropic flux of muons in monoenergetic bins impinging on the Super-K detector, representing a flux of muons from neutrino interactions in the surrounding rock. The MC simulates the detector response – i.e., the time hit and charge deposited for each PMT.

Seven monoenergetic bins were used, with muon energies ranging from 100 GeV to 100 TeV, and 10000 events with a path length in the ID of > 7 m were generated in each bin. The simulation was performed using a GEANT-based detector simulation. GEANT’s muon propagation has been shown to agree with theoretical predictions up to muon energies of

100 TeV (Bottai and Perrone 2001; Desai et al. 2003).

3.4.1 Resolution and Efficiency of Event Selection

The muon trajectory fitting algorithm discussed in §3.3.1 was applied to the high-energy isotropic MC, and the fitted values for $\cos \Theta$, path length, number of OD PMTs hit near the entry and exit points, and direction of trajectory were compared with the true MC values. These plots are shown in Fig. 3-3. A plot illustrating the angular resolution of the fit is shown in Fig. 3-4. The resolution of $5\text{--}12^\circ$ is poor compared to the typical 1° resolution of precision ID fitting algorithms, but those algorithms do not work well on these high-energy saturated events.

The efficiency of the upward-going cuts was estimated by considering all of the MC events with true values of $\cos \Theta < 0$ and ID path length > 7 m and then determining the fraction of these events that pass the selection cuts described in §3.3.2. This was done using isotropic MC events with $> 10^5$ pe since there were relatively few events in the MC with $\geq 1.75 \times 10^6$ pe. (Above 10^5 pe the efficiency and resolution do not depend strongly on the number of ID pe deposited.) Also, as discussed in §3.4.2, only the energy bins in the range 3.16 – 100 TeV were considered. The efficiency was calculated as a function of muon energy and $\cos \Theta$.

Statistical uncertainties on the efficiency determination were calculated using the Bayesian method discussed by Conway (2002). Systematic uncertainties due to uncertainties in the fitted values of the zenith angle, path length, and number of OD PMTs hit near the entry and exit points were calculated using the resolution histograms for $\cos \Theta$, path length, $N_{\text{OD entry}}$ and $N_{\text{OD exit}}$ shown in Fig. 3-3. First, a 1σ acceptance region containing 68.27% of the total area was selected for each resolution histogram. Then the cuts on these parameters were varied by 1σ in either direction to determine the effect on the efficiency.

Another source of systematic uncertainty on the efficiency is prepulsing, which is not included in the MC simulation and must be estimated separately. To do this, we compared the results from the high-energy isotropic MC to a sample of 627 ultra-high-energy downward-going muon data events with $\geq 1.75 \times 10^6$ pe in the ID selected by a visual scan. For many of these data events, the time difference $t_{\text{ID entry}} - t_{\text{OD entry}}$ is negative, showing evidence of prepulsing not seen in the MC sample.

Histograms of the time difference $t_{\text{ID entry}} - t_{\text{OD entry}}$ for the data events and the MC events are shown in Fig. 3-5.

Note that for the MC events, the histogram is sharply peaked around a time difference slightly above zero, and has very few events with negative time differences. In contrast, the histogram for the data events has a wider spread, and has several events with negative time differences. The difference between the data and the MC distributions is expected to be due mainly to prepulsing.

To adjust for this, we derive a heuristic correction for prepulsing by drawing a random value from the distribution defined by the data histogram and another random value from the distribution defined by the MC histogram, and then subtracting the data value from the MC value. By repeating this process several thousand times, we build up a distribution of the expected difference between the data and MC values of $t_{\text{ID entry}} - t_{\text{OD entry}}$. Then for each event in the MC sample, a random value is drawn from the distribution of the expected difference between data and MC, and then adding it to $t_{\text{ID entry}} - t_{\text{OD entry}}$ for the MC event. The result is a rough approximation of what the time difference might be if the MC simulation included prepulsing.

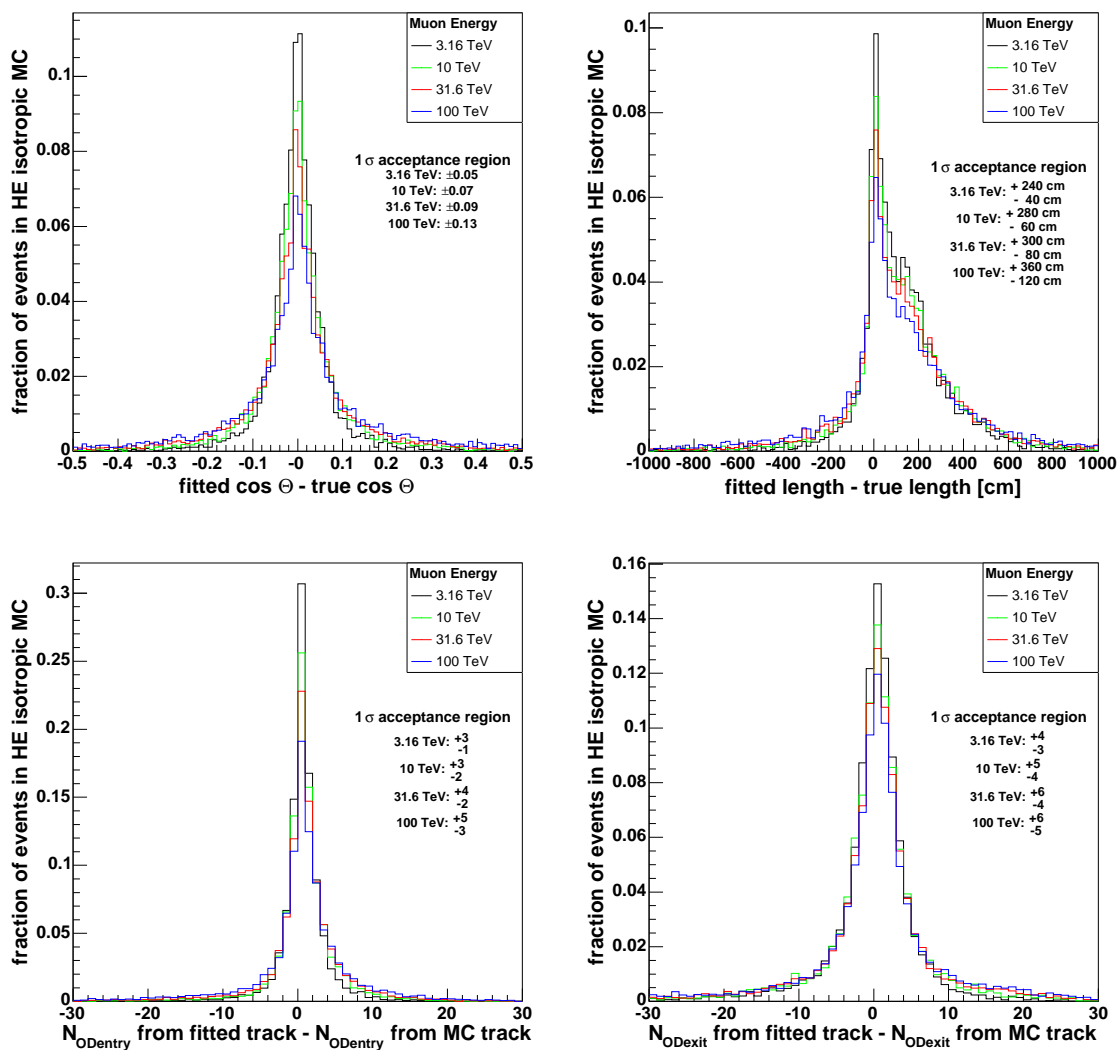


Figure 3-3 Resolution of OD-based fit on determining track parameters for events from the high energy isotropic MC with $> 10^5$ pe in the inner detector. Parameters shown are $\cos \Theta$, path length, and the number of OD PMTs hit within 8 meters of the OD entry and exit points. The 1σ acceptance regions contain 68.27% of the total area under each histogram in each plot.

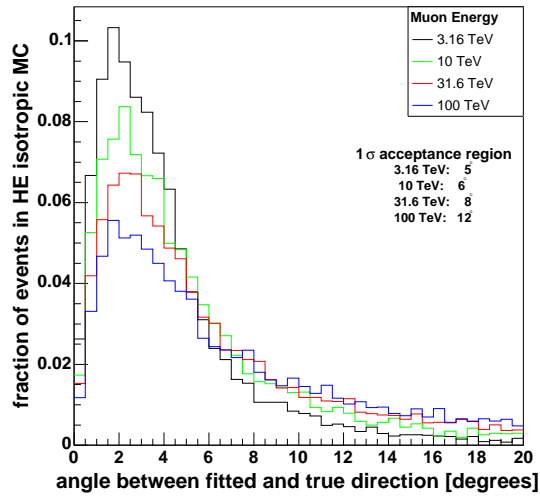


Figure 3-4 Angular resolution of OD-based fit for events from the high energy isotropic MC with $> 10^5$ pe in the ID.

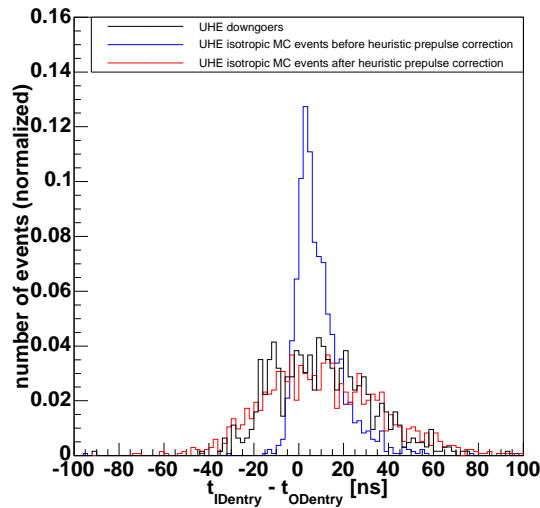


Figure 3-5 Distribution of the time difference between OD entry and ID entry clusters for UHE downgoing muon events from data, compared to the distribution for the UHE events in the high-energy isotropic MC. After applying a heuristic correction to account for prepulsing, the MC distribution looks similar to the data distribution.

The histogram of the heuristically-corrected ultra-high energy MC events is also shown in Fig. 3-5 — the distribution looks similar to the data events, as expected. To estimate the systematic uncertainty on the efficiency calculation due to prepulsing, we applied this adjustment to the events in the MC sample and found that an additional 1% of the MC events would be cut after accounting for prepulsing, which lengthens the negative-side error bars on the efficiency estimates by approximately 0.01.

Finally, one additional correction must be made: the efficiency has been estimated *at* different values for E_μ , but the flux calculation is for the flux *above* a threshold energy E_μ^{\min} . Since the efficiency decreases with energy, $\varepsilon(E_\mu, \Theta)$ is an overestimate for $\varepsilon(\geq E_\mu^{\min}, \Theta)$. This does *not* lead to a conservative upper limit for the flux, so a correction must be made. This requires knowledge of the energy spectrum of the expected signal, so we modeled the signal as an isotropic flux of neutrinos with $d\Phi_\nu(E_\nu)/dE_\nu \propto E_\nu^{-2}$ (a plausible astrophysical spectrum Gaisser 1990), used the method of §3.7 to estimate the muon flux $\Phi_\mu(\geq E_\mu^{\min})$, and used this muon flux to extrapolate our efficiency calculations to find $\varepsilon(\geq E_\mu^{\min}, \Theta)$.

The efficiency as a function of energy was estimated using a linear fit on $\varepsilon(E_\mu, \Theta)$ vs. $\log E_\mu$ in each angular bin, using the MC results from the energy bins in the range 3.16 – 100 TeV. This gives an estimator $\hat{\varepsilon}(E_\mu, \Theta)$ for the efficiency:

$$\hat{\varepsilon}(E_\mu, \Theta) = A(\Theta) + B(\Theta) \log E_\mu, \quad (3.1)$$

where A and B are the fit parameters.

Then $\varepsilon(\geq E_\mu^{\min}, \Theta)$ is estimated by weighting the fitted efficiency $\hat{\varepsilon}(E_\mu, \Theta)$ by the E_ν^{-2} model muon flux.

$$\varepsilon(\geq E_\mu^{\min}, \Theta) = \frac{\int_{E_\mu^{\min}}^{\infty} \hat{\varepsilon}(E_\mu, \Theta) \frac{d\Phi_\mu(\geq E_\mu)}{dE_\mu} dE_\mu}{\int_{E_\mu^{\min}}^{\infty} \frac{d\Phi_\mu(\geq E_\mu)}{dE_\mu} dE_\mu}. \quad (3.2)$$

This procedure yields small downward adjustments (0.6–9%) to the calculated efficiency in each angular bin.

Additionally, we must also account for the efficiency of the visual scan and manual fit procedure. To do this, we did a visual scan of the 605 events from the high-energy isotropic MC with true $\cos \Theta < 0$, true ID path length > 7 m, and $\geq 1.75 \times 10^6$ pe in the ID and found that 10 of these events were eliminated in the visual scan. This gives an efficiency of roughly 98%, so we adjust our efficiency results by a factor of 0.98.

The final results for the efficiency of our cuts on upward, throughgoing, $\geq 1.75 \times 10^6$ pe muons (including all corrections discussed above) are plotted in Figure 3-6.

3.4.2 Ultra-High-Energy Fraction

In order to set an upper limit on the flux of upward-going muons from cosmic neutrinos one must make an inference about the energies of the upward-going muons in the ultra-high-energy sample. Above energies of ~ 1 TeV, muon energy loss in water is dominated by radiative processes such as bremsstrahlung, so high-energy muons have some probability of depositing large numbers of photoelectrons in the Super-K detector and contributing to the ultra-high-energy sample. Since this energy loss is not continuous, it is not possible to estimate the muon energy for a single ultra-high-energy upward-going muon event. Rather, MC is used to make a statistical statement about the energies of the muons that make up the $\geq 1.75 \times 10^6$ pe sample.

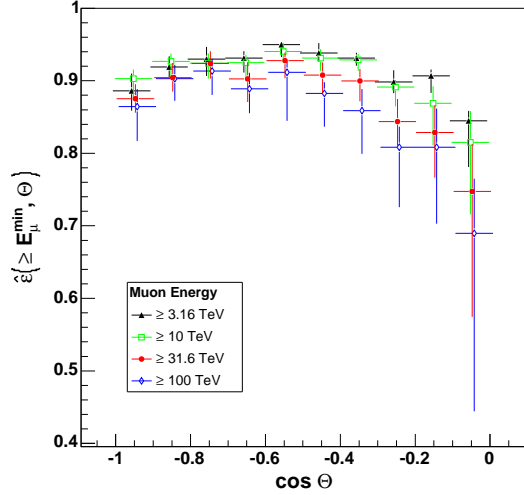


Figure 3-6 Efficiency of our data reduction on upward, throughgoing, $\geq 1.75 \times 10^6$ pe muons as determined by the high-energy isotropic MC. Error bars include statistical and systematic errors.

The high-energy isotropic MC has been used to determine the fraction $k(E_\mu)$ of muons with energy E_μ that will deposit $\geq 1.75 \times 10^6$ pe in the ID, thus contributing to the ultra-high-energy sample. Results are shown in Table 3.2. Statistical uncertainties were calculated using the Bayesian method discussed by Conway (2002). As can be seen in Table 3.2, the three lowest energy bins — from 100 GeV to 1 TeV — do not make a significant contribution to the $\geq 1.75 \times 10^6$ pe sample. Hence, the rest of this analysis was done using only the four highest energy bins — from 3.16 to 100 TeV.

These results for $k(E_\mu)$ are used in §3.5 to calculate the flux $\Phi_\mu(\geq E_\mu^{\min})$. Since $k(E_\mu)$ increases with energy, it is an underestimate for $k(\geq E_\mu^{\min})$, which leads to a conservative upper limit for $\Phi_\mu(\geq E_\mu^{\min})$.

Also, since this MC only simulates the muon and not the actual neutrino interaction,

Table 3.2 Fraction of high-pe events $k(E_\mu)$ in high energy isotropic MC

E_μ (TeV)	number of MC events (out of 10000) with $\geq 1.75 \times 10^6$ pe in ID	$k(E_\mu)$ (with statistical uncertainties)
0.1, 0.316, 1	0	0.0000 $+0.0001$ -0.0000
3.16	35	0.0035 ± 0.0006
10	113	0.0113 $+0.0011$ -0.0010
31.6	293	0.0293 ± 0.0017
100	879	0.0879 $+0.0029$ -0.0028

Table 3.3 The flux of ultra-high energy upward-going muons as observed by SK-I.

E_μ^{\min} (TeV)	$\Phi_\mu (\geq E_\mu^{\min})$ ($\text{cm}^{-2}\text{s}^{-1}\text{sr}^{-1}$)	
3.16	2.64×10^{-14}	+16.1%
		-17.9%
10	8.23×10^{-15}	+9.48%
		-9.73%
31.6	3.25×10^{-15}	+6.67%
		-6.40%
100	1.10×10^{-15}	+4.96%
		-4.09%

Note. — These fluxes include both atmospheric background and potential astrophysical signal at each threshold energy.

the effect of lower energy debris from deep inelastic scattering events that make it into the detector has been neglected, again leading to an underestimate of $k(E_\mu)$. This effect is expected to be small in the energy range considered here — above $E_\mu = 1$ TeV at the detector entry, over 80% of the neutrino-induced upward-going muons come from over 200 m away from the detector, so most of the debris is absorbed by the surrounding rock, as determined using the atmospheric neutrino MC discussed in §3.6.

3.5 Flux Calculation

The flux of upward-going muons above a threshold energy E_μ^{\min} is given by

$$\Phi_\mu (\geq E_\mu^{\min}) = \frac{1}{2\pi T k (\geq E_\mu^{\min})} \sum_{j=1}^n \frac{1}{\varepsilon (\geq E_\mu^{\min}, \Theta_j) A (\Theta_j)}, \quad (3.3)$$

where n is the total number of upward-going muon events observed and Θ_j is the zenith angle of the j th event. The efficiency $\varepsilon (\geq E_\mu^{\min}, \Theta_j)$ and the ultra-high-energy fraction $k (\geq E_\mu^{\min})$ are calculated in §3.4. T is the detector livetime, which is 1679.6 days for SK-I. $A (\Theta_j)$ is the effective area of the Super-K detector perpendicular to the direction of incidence for tracks with a path length of > 7 m in the ID. The average effective area of the detector is ~ 1200 m².

Equation (3.3) has been applied to the detected upward-going muon event discussed in §3.3.2 to calculate $\Phi_\mu (\geq E_\mu^{\min})$ for E_μ^{\min} in the range 3.16 – 100 TeV. Results are shown in Table 3.3. Systematic uncertainties include a 0.1% uncertainty on the live time T , a 0.3% uncertainty on the effective area A , the total efficiency uncertainties shown in Figure 3-6, and the statistical uncertainties on k shown in Table 3.2. This flux includes both the potential signal from astrophysical neutrinos and a background of atmospheric neutrinos.

3.6 Expected Atmospheric Background from Monte Carlo

When searching for neutrinos from astrophysical sources, the dominant background is the high-energy tail of the atmospheric neutrino spectrum. Atmospheric neutrinos are produced by decays of pions and kaons formed when cosmic rays interact with particles in the atmosphere. In order to set a limit on the flux of cosmic neutrinos, the expected flux of upward-going muons due to the atmospheric background must be carefully analyzed. To do this, we have used an atmospheric neutrino MC that is a 100 yr equivalent sample of events due to the atmospheric neutrino flux. The neutrino flux in Honda et al. (2004) was used up to neutrino energies of 1 TeV. At 1 TeV, the calculated flux in Volkova (1980) was rescaled to the Honda et al. flux. Above 1 TeV, the rescaled flux from Volkova was used up to 100 TeV. Neutrino interactions were modeled using the GRV94 parton distribution functions (Gluck et al. 1995), and muon propagation through the rock and water was modeled using GEANT. Further details on the atmospheric neutrino MC can be found in Ashie et al. (2005). No correction is made for neutrino oscillations, because based on the oscillation parameters determined in Ashie et al. (2005), the neutrino oscillation probability is negligible for neutrinos above 1 TeV.

The model flux is weighted to represent 3 years of solar minimum, 1 year of changing activity, and 1 year of solar maximum, which corresponds to the actual solar activity during the run of SK-I. This atmospheric MC is split into two parts: a partially-contained/fully-contained (PC/FC) sample, which consists of events with neutrino interaction points inside the ID plus a shell 50 cm thick surrounding the ID (the insensitive region), and an upward-going muon sample, which consists of events with neutrino interaction points outside the ID. Note that these two samples overlap because they both cover the 50 cm insensitive region.

The OD-based fit was applied to the events in the atmospheric MC, using the same cuts that were applied to the SK-I data. A total of 11 MC events passed the $\geq 1.75 \times 10^6$ pe, $\cos \Theta \leq 0.1$, path length > 7 m, N_{ODentry} and $N_{\text{ODexit}} \geq 10$, OD/ID timing, and manual fit cuts. Out of these 11, 2 are from the PC/FC sample, both with interaction points inside the ID. The remaining 9 events are from the upward-going muon sample: 3 events with interaction points in the 50 cm insensitive region, 1 event in the water of the OD, and 5 events in the rock surrounding the detector.

All of these background events are deep inelastic scattering (DIS) events where an interaction between a muon neutrino and a nucleon produces a muon plus a spray of lower energy particles. The 6 events with interaction points within the detector (ID or OD) have muon energies of 0.1 – 0.8 TeV, and the 5 events occurring in the rock have muon energies of 1 – 20 TeV. This difference in the energy range can be understood as follows: For DIS events occurring a long distance (> 2 m or so) from the detector, only the muon will reach the detector since the lower energy debris will be absorbed by the surrounding rock, but for nearby events or events occurring in the water of the OD, some of these lower energy particles will enter the detector as well. This means that nearby events can be included in the $\geq 1.75 \times 10^6$ pe sample with lower muon energies than more distant events.

Since the insensitive region is covered by both the PC/FC and the upward-going muon MC samples, we divided the 3 events originating from this region in half, for a total of 1.5 events in the insensitive region. This gives a total of 9.5 MC events in 100 yr of simulated live time. Scaling the 100 yr MC to SK-I's live time of 1679.6 days gives an expected background of 0.44 events due to atmospheric neutrinos during the operation of SK-I.

Table 3.4 Systematic uncertainties in atmospheric neutrino background

Source of Uncertainty	Uncertainty
Statistical	31%
Absolute normalization of atm ν flux	10%
Primary spectral index	37%
Neutrino cross-section uncertainty	10%
Total uncertainty in background flux	50%

The statistical uncertainty in this background measurement of the MC events is

$$\frac{1}{9.5} \sqrt{(\sqrt{8})^2 + \left(\frac{\sqrt{3}}{2}\right)^2} = 31\%. \quad (3.4)$$

There are also significant systematic uncertainties: the normalization of the atmospheric neutrino flux has a theoretical uncertainty of $\pm 10\%$ at neutrino energies below 10 GeV (Ashie et al. 2005). In order to extend this to the energy range of the expected background, we must also account for the uncertainty of 0.05 in the spectral index of the primary cosmic ray spectrum above 100 GeV, which leads to a 0.05 uncertainty in the spectral index for atmospheric neutrinos above 10 GeV (Ashie et al. 2005).

To determine how much this uncertainty affects our result for the background, we consider the spectral index γ to be known at $E_\nu^{\text{pivot}} = 10$ GeV, and we calculate the uncertainty of the total flux Φ_ν above a threshold energy $E_\nu^{\text{min}} = 10.6$ TeV, the average neutrino energy of the 100 year MC events passing our cuts. For a differential flux of $d\Phi_\nu/dE_\nu \propto E_\nu^{-\gamma}$, the uncertainty in Φ_ν due to the uncertainty in γ is given by

$$\frac{\delta\Phi_\nu}{\Phi_\nu} = \left(\frac{1}{-\gamma + 1} - \ln \left(\frac{E_\nu^{\text{min}}}{E_\nu^{\text{pivot}}} \right) \right) \delta\gamma. \quad (3.5)$$

With $\gamma = 3.7$, $\delta\gamma = 0.05$, $E_\nu^{\text{min}} = 10.6$ TeV, and $E_\nu^{\text{pivot}} = 10$ GeV, this formula yields $\delta\Phi_\nu/\Phi_\nu = 0.37$. Thus the primary spectral index uncertainty gives us an additional $\pm 37\%$ uncertainty on the atmospheric neutrino flux Φ_ν .

Finally, the neutrino cross-section at high energies is thought to be known to within 10% or less, so we include an additional 10% uncertainty to account for this. These uncertainties are summarized in Table 3.4 and lead to a total uncertainty on the background of 50%.

The atmospheric MC does not include neutrino oscillations, so this is another potential systematic uncertainty. However, for neutrinos above 1 TeV, the neutrino oscillation probability is negligible, so it does not make a significant contribution for this analysis. Other potential errors (uncertainties in the simulation of the SK detector and varying hadron multiplicities in different deep inelastic scattering models) were tested and shown to not make a significant contribution to the systematic uncertainty.

Another potential background source of high-energy neutrinos not included in the 100 yr atmospheric MC is the prompt atmospheric neutrino flux, which arises from decays of short-lived charmed particles produced when cosmic rays interact with particles in the atmosphere. This flux is not as well-understood as the conventional atmospheric neutrino flux from decays of pions and kaons, but it is expected to have a harder spectrum and

therefore is expected to become more important as we push towards higher energy scales.

Based on the 100 yr atmospheric MC, we calculate an expected background for this analysis of 0.44 ± 0.22 events, compared to the 1 event observed. However, there are three effects that this MC does not take into account: it does not include neutrinos over 100 TeV, it does not include the prompt atmospheric neutrino flux, and it does not account for attenuation of neutrinos passing through the Earth. We account for these issues by making corrections based on an analytical calculation discussed in §3.7.

Also, it is important to note that the atmospheric background — both conventional and prompt — comes from a lower energy range than that for which we expect to observe the possible signal of neutrinos from astrophysical sources. Roughly speaking, the peak 90% of the expected upward-going muon events come from muons with energies in the range $E_\mu = 0.02 - 10$ TeV for conventional atmospheric neutrinos, and $E_\mu = 0.2 - 200$ TeV for prompt neutrinos. As we learned from the 11 background events in the 100 yr atmospheric MC, muons with energies $E_\mu < 1$ TeV contribute to the 1.75×10^6 pe sample mainly via debris from DIS events very close to the detector rather than from catastrophic energy loss of the muon.

Since there are many more low-energy events in the atmospheric spectrum, they will dominate even though each one only has a tiny probability of depositing a large amount of energy in the detector. In contrast, the peak 90% of the expected muon events from a harder spectrum — a hypothetical E_ν^{-2} astrophysical flux — come from the range $E_\mu = 7 - 6000$ TeV. Thus, even though the atmospheric flux is very small in the energy range $E_\mu = 3 - 100$ TeV and above where we are setting our limit, the high-pe tails of the distribution from lower energy events dominate our background simply because of the much larger flux of lower energy atmospheric events.

3.7 Analytical Estimate of Expected Muon Flux

3.7.1 Method for Calculating Muon Flux

In order to better understand our observed flux of high-energy upward-going muons, we developed a method to calculate the expected upward-going muon event rate due to a predicted flux of neutrinos. We have used this to plot curves for theoretical muon fluxes in Figure 3-9 and also to adjust the atmospheric background calculated with MC in §3.6 by correcting for effects not included in the simulation.

To convert a model neutrino flux into an expected upward-going muon event rate, we follow the calculation detailed in Gaisser et al. (1995) and Gandhi et al. (1996). The flux of muons $\Phi_\mu (\geq E_\mu^{\min})$ above an energy threshold E_μ^{\min} is given by

$$\Phi_\mu (\geq E_\mu^{\min}) = \int_{E_\mu^{\min}}^{\infty} dE_\nu P_\mu (E_\nu, E_\mu^{\min}) \frac{d\Phi_\nu^{\text{av}} (E_\nu)}{dE_\nu}, \quad (3.6)$$

where $P_\mu (E_\nu, E_\mu^{\min})$ is the probability that an incoming neutrino with energy E_ν will produce a muon with energy above the threshold E_μ^{\min} at the detector, and $d\Phi_\nu^{\text{av}} (E_\nu)/dE_\nu$ is the differential neutrino flux averaged over solid angle and reduced by an exponential factor due to attenuation of the neutrinos as they pass through the Earth.

given by

$$\frac{d\Phi_\nu^{\text{av}}(E_\nu)}{dE_\nu} = \frac{\int_{-1}^0 d\cos(\Theta) \int_0^{2\pi} d\phi A(\Theta) e^{(-z(\Theta)\sigma(E_\nu)N_A)} \frac{d^2\Phi_\nu(E_\nu, \Theta, \phi)}{d\Omega dE_\nu}}{2\pi A_{\text{av}}}. \quad (3.7)$$

Here, the integral over solid angle extends over $\cos\Theta < 0$, $[d^2\Phi_\nu(E_\nu, \Theta, \phi)] / [d\Omega dE_\nu]$ is the angle-dependent neutrino flux, $A(\Theta)$ is the effective area of the SK detector at a zenith angle Θ , and A_{av} is the average effective area $\int_{-1}^0 d\cos(\Theta) A(\Theta)$. The exponential factor accounts for attenuation of neutrinos as they pass through the Earth, which becomes important at higher energies.

$N_A = 6.022 \times 10^{23} \text{ mol}^{-1} = 6.022 \times 10^{23} \text{ cm}^{-3}$ (water equivalent) is Avogadro's number, $\sigma(E_\nu)$ is the total neutrino-nucleon cross-section, and $z(\Theta)$ is the column depth through the Earth at a zenith angle Θ . The column depth has been calculated in Gandhi et al. (1996) using the Preliminary Earth Model (Dziewonski 1989) — we adopt this column depth here.

As discussed in Gandhi et al. (1996), there is an uncertainty in choosing a value for the cross-section $\sigma(E_\nu)$ to use in the neutrino attenuation factor. Neutrinos interacting in the Earth via charged-current (CC) interactions will disappear from the incoming neutrino beam. However, neutrinos interacting via neutral current (NC) interactions will only be scattered and reduced in energy, so they may still contribute to the overall neutrino flux. Thus, we can put upper and lower limits on the appropriate value of σ to use in Eq. 3.7: $\sigma_{CC} < \sigma < \sigma_{CC} + \sigma_{NC}$. Here we calculate the angle-averaged flux using both the upper and lower limits to estimate the resulting uncertainty, and then average the resulting fluxes together.

If the model neutrino flux is isotropic, it can be taken out of the angular integral in equation (3.7), and we can derive a shadow factor $S(E_\nu)$ given by

$$S(E_\nu) = \frac{1}{A_{\text{av}}} \int_{-1}^0 d\cos(\Theta) A(\Theta) e^{(-z(\Theta)\sigma(E_\nu)N_A)}. \quad (3.8)$$

Thus, for an isotropic neutrino flux, equation (3.6) simplifies to

$$\Phi_\mu(\geq E_\mu^{\text{min}}) = \int_{E_\mu^{\text{min}}}^{\infty} dE_\nu P_\mu(E_\nu, E_\mu^{\text{min}}) S(E_\nu) \frac{d\Phi_\nu(E_\nu)}{dE_\nu}. \quad (3.9)$$

The probability $P_\mu(E_\nu, E_\mu^{\text{min}})$ depends on both the charged-current neutrino cross-section and the energy lost by the resulting muon as it propagates through the Earth. It is given by

$$P_\mu(E_\nu, E_\mu^{\text{min}}) = N_A \int_0^{E_\nu} dE_\mu \frac{d\sigma_{CC}}{dE_\mu}(E_\mu, E_\nu) R(E_\mu, E_\mu^{\text{min}}), \quad (3.10)$$

where $d\sigma_{CC}/dE_\mu$ is the differential (with respect to muon energy) charged-current neutrino cross section and $R(E_\mu, E_\mu^{\text{min}})$ is the average range that a muon with energy E_μ will travel before its energy is reduced to E_μ^{min} .

In our calculation, we calculate the cross-section using the GRV94 parton distribution functions (Gluck et al. 1995) applied with the code used in Gandhi et al. (1996) provided by M. Reno (2005, private communication), and we use an effective muon range calculated using MC methods (Lipari and Stanev 1991).

We integrated equation (3.6) numerically using various predicted models of the neutrino flux $d\Phi_\nu/dE_\nu$ to calculate theoretical $\Phi_\mu(\geq E_\mu^{\text{min}})$ curves. These are shown in Figure 3-9

for comparison to our experimental limits.

3.7.2 Analytical Estimate of Expected Background

Of particular interest here are the model fluxes of the background due to atmospheric neutrinos, both conventional and prompt. We use the method discussed in §3.7.1 to correct for the omissions in the 100 yr atmospheric MC discussed in §3.6 by accounting for neutrinos over 100 TeV, attenuation of neutrinos in the Earth, and the flux of prompt neutrinos.

To estimate the number of expected background events with our analytical calculation, we need to factor in the number of muons at each energy that will make it above the $\geq 1.75 \times 10^6$ pe cutoff. The expected number of events N seen by Super-K in livetime T is given by

$$N = 2\pi T A_{\text{av}} \int_0^\infty dE_\mu^{\text{min}} \frac{d\Phi_\mu(\geq E_\mu^{\text{min}})}{dE_\mu^{\text{min}}} k(E_\mu^{\text{min}}), \quad (3.11)$$

where $d\Phi_\mu(\geq E_\mu^{\text{min}})/dE_\mu^{\text{min}}$ is the derivative of the curve calculated by the method in §3.7.1 and $k(E_\mu^{\text{min}})$ is the fraction of muons with energy above E_μ^{min} that will deposit $\geq 1.75 \times 10^6$ pe in the ID. We estimated $k(E_\mu^{\text{min}})$ using the results of the high-energy isotropic MC discussed in §3.4.2. The four non-zero values of $k(E_\mu)$ shown in Table 3.2 are used to find an estimator \hat{k}_{PL} by fitting with a simple power law: $\log[\hat{k}_{\text{PL}}(E_\mu)] = A + B \log[E_\mu]$. Additionally, we impose a physically motivated high-energy cutoff: since k represents a probability, it should never exceed 1. Thus our estimator for $k(E_\mu^{\text{min}})$ is given by

$$\hat{k}(E_\mu^{\text{min}}) = \max(\hat{k}_{\text{PL}}(E_\mu^{\text{min}}), 1) \quad (3.12)$$

The energy at which \hat{k}_{PL} crosses 1 is approximately 1.5×10^6 GeV, well above the energy range that produces most of the flux. Figure 3-7 compares this power-law fit to results from 100 yr atmospheric MC, illustrating that the power law is reasonable in the energy range we are considering.

We analytically estimated the expected number of events in the 100 yr atmospheric MC by starting with the same input neutrino flux, applying equation (3.6) *without* the exponential neutrino attenuation factor and integrating up to a maximum neutrino energy of $E_\nu^{\text{max}} = 100$ TeV.

As a cross-check on the analytical calculation, we compared the resulting angle-averaged muon flux with the data from the 100 year atmospheric MC. Figure 3-8 shows that the analytical calculation predicts the shape of the flux curve accurately, but has a slightly lower normalization. Since we only use the analytical calculation to derive relative scalings, we consider it to be in good agreement with the MC.

We then used this muon flux in equation (3.11) to find the expected number of background events in 100 yr and obtained $N_{100} = 7.39$ expected events. (The 100 subscript denotes 100 yr of exposure.) This matches our results from the 100 yr atmospheric MC to within statistical uncertainties.

To estimate the effects of neutrinos above 100 TeV, we repeated the above calculation without the $E_\nu^{\text{max}} = 100$ TeV cutoff and obtained $N_{100} = 7.47$ events, an increase of 1.1%. Including the neutrino attenuation factor as well, we obtained $N = 7.32$ events for $\sigma = \sigma_{CC}$ and $N = 7.27$ events for $\sigma = \sigma_{CC} + \sigma_{NC}$, corresponding to an average of $N_{100} = 7.29 \pm 0.02$ events, a decrease of $2.4\% \pm 0.3\%$.

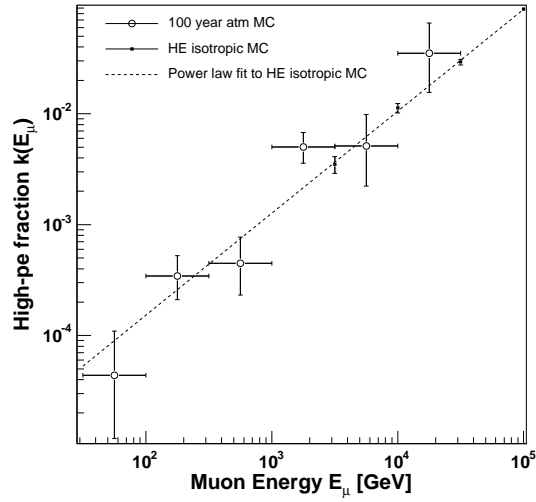


Figure 3-7 Fraction of events $k(E_\mu)$ that deposit $\geq 1.75 \times 10^6$ pe in the ID for the 100 yr atmospheric MC (*open circles*), the high-energy isotropic MC (*filled squares*), and a power-law fit to the results from high-energy isotropic MC. The power law is a reasonable approximation for the dominant energy range of the atmospheric flux ($E_\mu = 100$ GeV – 30 TeV).

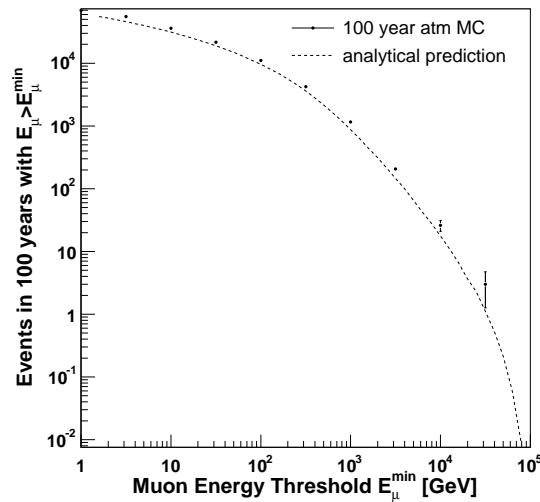


Figure 3-8 The number of upward-going muon events above energy threshold E_μ^{\min} induced by atmospheric neutrinos. Predictions from our analytical calculation are compared with the results from the 100 year atmospheric MC.

Table 3.5 Confidence intervals for the upward-going muon flux due to neutrinos from astrophysical sources.

E_{μ}^{min} (TeV)	90% C.L. range ($\text{cm}^{-2}\text{s}^{-1}\text{sr}^{-1}$)
3.16	$0 - 1.03 \times 10^{-13}$
10	$0 - 3.19 \times 10^{-14}$
31.6	$0 - 1.26 \times 10^{-14}$
100	$0 - 4.28 \times 10^{-15}$

We also used this calculation to correct for the prompt atmospheric neutrino flux. To account for the theoretical uncertainty in the prompt flux due to differences between various flux models, we defined a high model and a low model for the prompt flux that bracket the models shown in Figure 1 of Gelmini et al. (2003) that are not ruled out by experimental limits. The models used are discussed in more detail in Thunman et al. (1996), Zas et al. (1993), Ryazhskaya et al. (2002), Bugaev et al. (1989), Pasquali et al. (1999), and Gelmini et al. (2000a,b). Our analytical calculation gives $N_{100} = 0.033$ events for the low model and $N_{100} = 0.94$ events for the high model, corresponding to a prompt flux that is $6.7\% \pm 6.2\%$ of the flux of conventional atmospheric neutrinos.

Based on these results, we correct the background estimate made using the 100 yr atmospheric MC in §3.6 by applying these relative scalings to the result of 0.44 events in the SK-I livetime from §3.6. This gives us a final result for the background of 0.46 ± 0.23 events for the SK-I exposure.

3.8 Upper Limit for Muon Flux from Cosmic Neutrinos

Using the observed ultra-high-energy upward-going muon signal of 1 event and the expected atmospheric neutrino background of 0.46 ± 0.23 events, we have calculated 90% confidence upper limits for the upward-going muon flux in the 3.16 – 100 TeV range due to neutrinos from astrophysical sources (or any other non-atmospheric sources).

This was done using the method of Feldman and Cousins (1998), with the systematic uncertainties incorporated using the method of Cousins and Highland (1992), as implemented by Conrad et al. (2003) and improved by Hill (2003). This method incorporates both uncertainties in the background flux and uncertainties in the flux factor f relating the observed number of events n to the observed flux Φ : $\Phi = f n$. The uncertainty in f includes systematic errors in the livetime, effective area, efficiency, and ultra-high-energy fraction. For the confidence interval calculation, the largest percent error for each energy bin from Table 3.3 was used as the percent uncertainty in f . The uncertainties in both the background and the flux factor were assumed to have a Gaussian distribution.

The final results are shown in Table 3.5 and plotted in Figure 3-9, along with models of various possible signals from AGNs (Stecker and Salamon 1996; Mannheim et al. 2001) and GRBs (Waxman and Bahcall 1999), as well as the backgrounds due to atmospheric neutrinos (Honda et al. 2004; Volkova 1980) and prompt neutrinos (Gelmini et al. 2003).

The upper limits calculated here are consistent with the models of astrophysical signals. Also shown are limits on a hypothetical E_{ν}^{-2} isotropic neutrino flux set by MACRO (Ambrosio et al. 2003) and AMANDA-II (Achterberg et al. 2007). The model neutrino

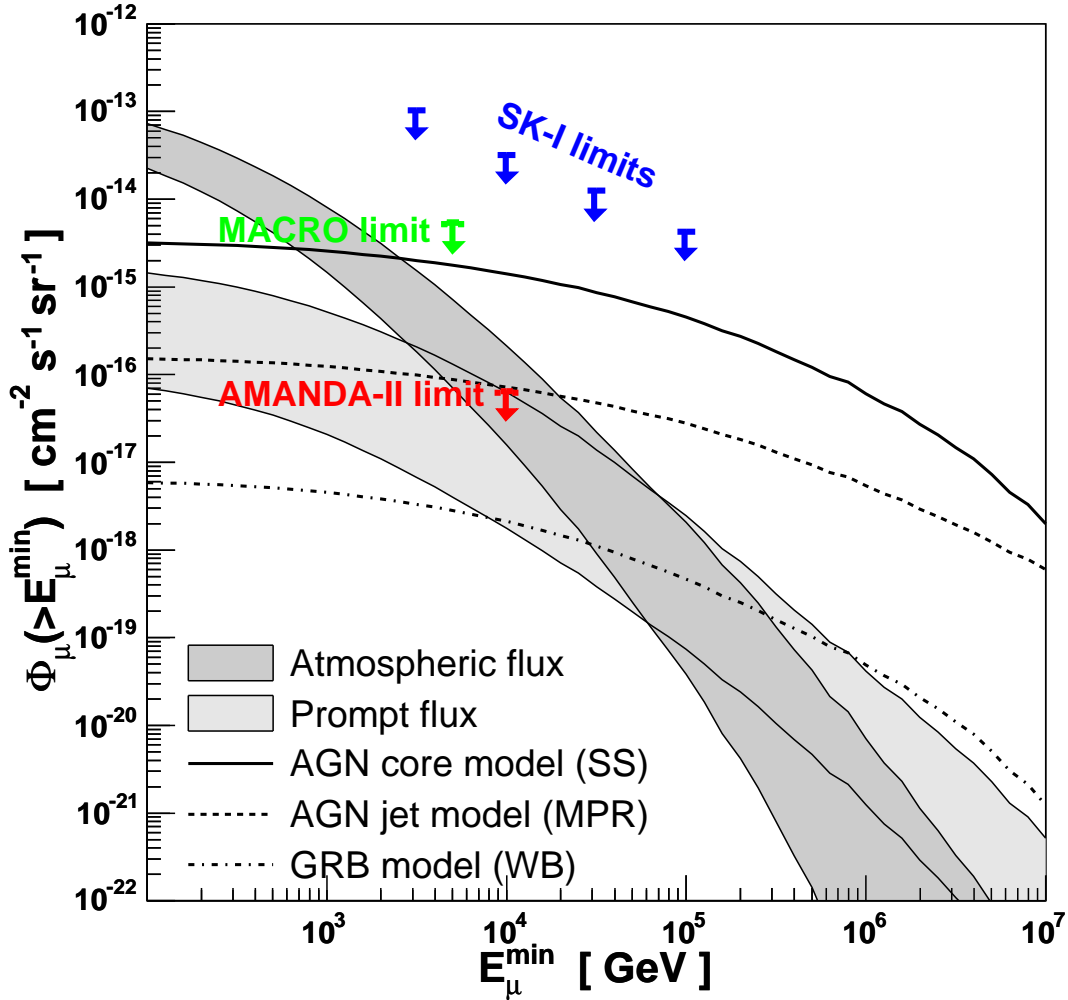


Figure 3-9 Upper limits from this analysis on muon ($\mu^+ + \mu^-$) flux above energy threshold E_{μ}^{\min} , compared to various model fluxes. Models shown for muon flux due to astrophysical neutrinos are AGN models from SS (Stecker and Salamon 1996) and MPR (Mannheim et al. 2001), and a GRB model from WB (Waxman and Bahcall 1999). Also shown is the atmospheric background, as modeled by Honda et al. (2004) below $E_{\nu} = 1$ TeV and by Volkova (1980) rescaled to match the Honda model above $E_{\nu} = 1$ TeV. The upper edge of the atmospheric band represents the horizontal flux, and the lower edge represents the vertical flux. The background due to muons from prompt atmospheric neutrinos (assumed to be isotropic) is shown for a range of possible models as summarized in Gelmini et al. (2003). Finally, we also show limits on a hypothetical E_{ν}^{-2} isotropic neutrino flux set by MACRO (Ambrosio et al. 2003) and AMANDA-II (Achterberg et al. 2007). The models of the neutrino flux have been converted to a muon flux with equation (3.6) using the GRV94 parton distributions (Gluck et al. 1995) and the effective muon range from Lipari and Stanev (1991).

Table 3.6 Approximate upper limits from SK-I on astrophysical neutrinos ($\nu_\mu + \bar{\nu}_\mu$).

E_μ^{\min} (TeV)	90% C.L. upper limit (GeV cm ⁻² s ⁻¹ sr ⁻¹)	Neutrino energy range (GeV)
3.16	6.0×10^{-5}	$6.3 \times 10^3 - 1.4 \times 10^6$
10	3.7×10^{-5}	$1.7 \times 10^4 - 2.4 \times 10^6$
31.6	3.2×10^{-5}	$4.7 \times 10^4 - 5.1 \times 10^6$
100	2.6×10^{-5}	$1.4 \times 10^5 - 1.1 \times 10^7$

Note. — Upper limits on $E_\nu^2 (d\Phi_\nu/dE_\nu)$. Note that converting from a muon flux limit to a neutrino flux limit requires additional assumptions — our limits on the muon flux are shown in Table 3.5.

fluxes were converted into muon fluxes using equation (3.6) as discussed in §3.7.

To facilitate easier comparison with other experiments, we also convert our limits on the muon flux into approximate limits on the neutrino flux. In order to do this, we assume a model neutrino flux that is isotropic and proportional to E_ν^{-2} . To get an approximate neutrino limit, we find normalization factors for an E_ν^{-2} muon flux curve such that the curve passes through each of our four limit points in Figure 3-9, and we use these factors to find the implied limits on E_ν^{-2} flux.

In order to determine the approximate neutrino energy range in which these limits are valid, we use equation (3.6) to determine the neutrino energy range that produces the bulk of the muon signal for a given value of the muon energy threshold E_μ^{\min} . We define the energy range as the range that (1) produces 90% of the muon flux above E_μ^{\min} and (2) has a higher value of the integrand of equation (3.6) within the range than anywhere outside the range. This definition is based on the definition of highest posterior density intervals as described by Conway (2002).

Explicitly, the energy range is (E_a, E_b) , where

$$.9 = \frac{\int_{E_a}^{E_b} dE_\nu I(E_\nu)}{\int_{E_\mu^{\min}}^{\infty} dE_\nu I(E_\nu)}, \quad (3.13)$$

with the integrand defined as

$$I(E_\nu) = P(E_\nu, E_\mu^{\min}) S(E_\nu) \frac{d\Phi_\nu(E_\nu)}{dE_\nu} \quad (3.14)$$

as in equation (3.9), with

$$\frac{d\Phi_\nu(E_\nu)}{dE_\nu} \propto E_\nu^{-2}. \quad (3.15)$$

Since this requirement alone does not define a unique range, we also require that the value of $I(E_\nu)$ at any $E_\nu \in (E_a, E_b)$ be greater than the value of $I(E_\nu)$ at any $E_\nu \notin (E_a, E_b)$.

The results of these approximations for neutrino limits and energy ranges are shown in Table 3.6 and are also plotted in Figure 3-10, with the same models and experimental limits as shown in Figure 3-9. To draw our limits on this plot, we chose to draw only the most sensitive limit in each energy range.

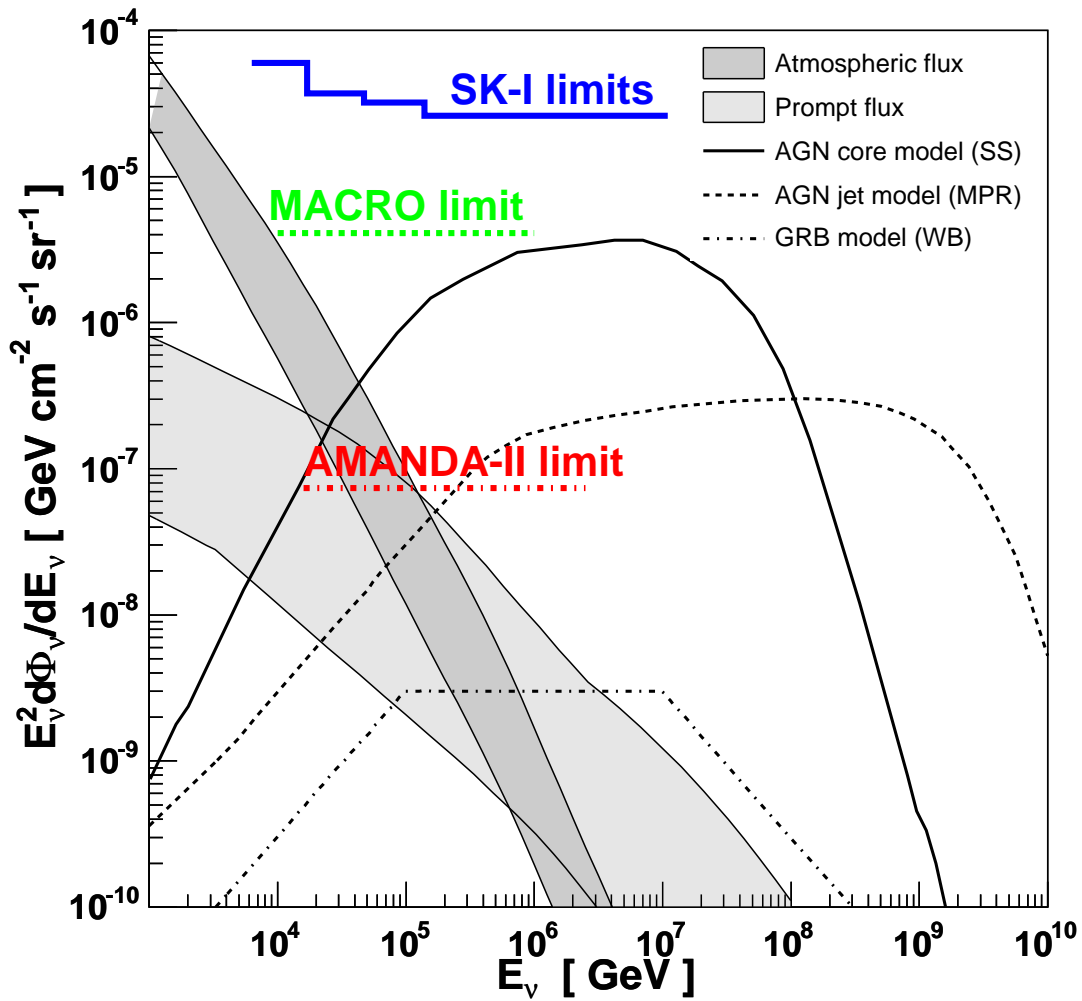


Figure 3-10 Approximate upper limits from SK-I on astrophysical neutrinos ($\nu_\mu + \bar{\nu}_\mu$). Models shown are the same as in Figure 3-9. Note that converting from a muon flux limit to a neutrino flux limit requires additional assumptions - our limits on the muon flux are shown in Figure 3-9.

Note that these results for the limits on the neutrino flux are only approximations made to facilitate comparison to other experiments — our primary results are the limits on the muon flux shown in Table 3.5 and Figure 3-9.

3.9 Conclusions

In conclusion, we have developed a method for analyzing Super-K's highest energy data to search for evidence of high-energy neutrino flux from astrophysical sources. We have done a thorough study of the efficiency and the expected backgrounds from this method and applied our method to the SK-I data sample. Our study of the highest energy events in SK-I does not show evidence of a high-energy cosmic neutrino signal.

We have set upper limits on the muon flux due to cosmic neutrino sources. These limits are consistent with the results of other experiments (Ambrosio et al. 2003; Achterberg et al. 2007). It is possible that an astrophysical neutrino signal could be within the grasp of the next generation of neutrino detectors such as IceCube (IceCube Collaboration 2007) and KM3NeT (Katz 2006; Kappes et al. 2007).

Part II

Particle Physics in the Sky

Chapter 4

Doing cosmology with galaxies

4.1 Cosmology Basics

4.1.1 What is cosmology?

Cosmology is the study of our universe as a whole, and thus focuses on the largest scales accessible to science. It strives to answer a number of “big questions”: What is our universe made of? How did it begin? How did the matter assemble into the structures we see today? What is its ultimate fate? In order to address these questions, cosmologists use a wide variety of astronomical observations and draw on theory from across essentially all fields of physics, ranging from general relativity to quantum field theory.

One remarkable feature of the study of cosmology is that it provides insights into particle physics – i.e., the study of the smallest scales in physics – that could never be observed in a terrestrial laboratory. The tremendous energy in the hot, early universe shortly after the Big Bang far exceeds the energies that could ever be produced by the most sophisticated particle accelerators on Earth. Now that cosmology is becoming a precision science, particle physicists are turning to cosmology as a tool, using the study of the largest scales in physics to learn more about the smallest.

4.1.2 The standard cosmological model

Over the past few decades, cosmology has evolved from a highly speculative field dubbed “A search for two numbers” by Sandage (1970) into a full-fledged observational science, with vast quantities of data supporting a detailed theoretical model that is now well-established enough to be known as the “standard cosmological model”. We are commonly said to be living in the age of precision cosmology. However, many aspects of the standard cosmological model are quite surprising, and have led to more questions than answers.

The basic premises of the standard cosmological model are as follows:

- Our universe is expanding – the gravitationally bound structures in our universe (e.g. clusters of galaxies) are all moving away from each other.
- Our universe used to be much hotter, denser, and smoother than it is today - the early universe was a hot soup of quarks and elementary particles.
- The large-scale structures in our universe grew through gravitational instabilities seeded by quantum fluctuations in the early universe.

- These quantum fluctuations were stretched to macroscopic size during a phase of rapidly accelerating expansion of the early universe called *inflation*.
- Ordinary matter (protons and neutrons, a.k.a. baryons) only make up 4% of the mass density in our universe.
- About 21% is made of *dark matter*, a mysterious substance that is gravitationally attractive but does not interact with light.
- About 75% is made of *dark energy*, an even more mysterious substance that effectively gives rise to a repulsive gravitational force and is causing the current expansion of our universe to accelerate.

This basic picture is consistent with a wide variety of different types of measurements, ranging from the tiny fluctuations in the microwave radiation produced by the early universe to the rates at which distant supernovae are moving away from us to the clustering patterns observed in the distribution of galaxies today. The agreement between all of these different measurements is quite remarkable, and has forced scientists to take seriously these seemingly preposterous concepts of dark matter, dark energy, and inflation.

Today the study of cosmology is focused on gaining a deeper understanding of the physics behind these concepts. What triggered inflation and how did it stop? What is the nature of dark matter? How much of the dark matter might be neutrinos? What sort of substance could have such bizarre properties as dark energy? Is dark energy a substance at all, or is the observed acceleration really due to a breakdown of general relativity at cosmological distance scales? These are the types of questions currently being investigated.

4.1.3 Zeroth order cosmology

As a first approximation, our universe can be treated as being homogenous and isotropic – that is, the matter in our universe is distributed uniformly and it looks the same in every direction. Looking around our neighborhood might lead us to believe that this is not a very good assumption: matter is packed together much more densely within the Earth than a thousand kilometers above its surface, for example.

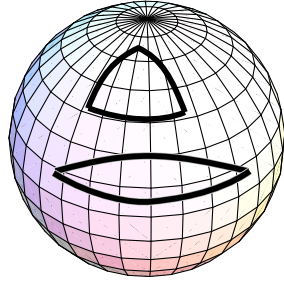
However, cosmologists think on much larger scales: if we average over scales of several hundred Mpc (i.e. about a billion light years – that’s 100 trillion times the distance from the Earth to the Sun), we will smooth out structures as small as a solar system, a galaxy, or even a galaxy cluster, and the matter in our universe begins to look quite uniform. Historically, the homogeneity and isotropy of our universe on large scales has been a fundamental assumption of cosmology, but in recent years our surveys of our universe have gotten large enough to confirm this directly (see, e.g., Yadav et al. 2005).

The physics of a homogenous and isotropic universe can be described in Einstein’s theory of general relativity (or more generally, any metric theory of gravity) using the Friedmann-Robertson-Walker (FRW) spacetime metric:

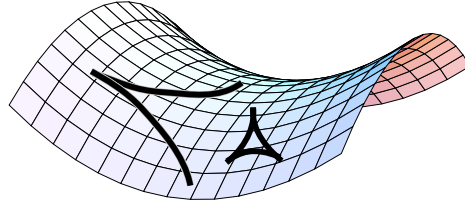
$$ds^2 = -c^2 dt^2 + a(t) \left[\frac{dr^2}{1 - Kr^2} + r^2 (d\theta^2 + \sin^2 \theta d\phi^2) \right]. \quad (4.1)$$

This resembles the more familiar Minkowski metric used in special relativity, given by

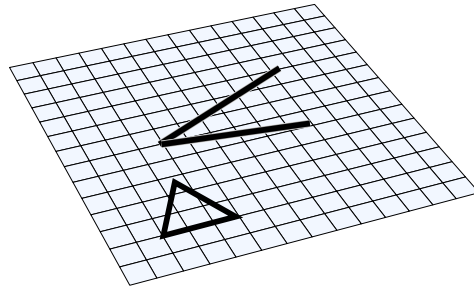
$$ds^2 = -c^2 dt^2 + dr^2 + r^2 (d\theta^2 + \sin^2 \theta d\phi^2) \quad (4.2)$$



Universe with *positive* curvature. Diverging lines converge at great distances. Triangle angles add to more than 180° .



Universe with *negative* curvature. Lines diverge at ever increasing angles. Triangle angles add to less than 180° .



Universe with no curvature. Lines diverge at constant angle. Triangle angles add to 180° .

Figure 4-1 The curvature of space illustrated for two-dimensional universes. Figure copyright Nick Strobel, <http://www.astronomynotes.com>. Used with permission.

with two additional pieces: a constant factor K describing the global curvature of space, and an arbitrary function of time $a(t)$. The curvature of space is defined by the behavior of parallel lines: in flat space ($K = 0$), parallel lines always remain parallel, in a space with negative curvature ($K < 0$), they diverge, and in a space with positive curvature ($K > 0$), they converge. An illustration of this is shown for two-dimensional spaces in Fig. 4-1; our universe is a three-dimensional analog of this. The function $a(t)$ is known as the scale factor, which allows space itself to expand or contract as our universe evolves. Here we normalize $a(t)$ such that $a(t_0) = 1$ at the present time t_0 . Doing cosmology at zeroth order fundamentally boils down to determining K and $a(t)$.

By applying the Einstein field equations for a homogeneous, isotropic universe to the FRW metric (see, e.g., Dodelson 2003), K and $a(t)$ can be linked to the composition of our universe via the Friedmann equation:

$$H^2 \equiv \left(\frac{\dot{a}}{a}\right)^2 = \frac{8\pi G}{3}\rho(t) - \frac{Kc^2}{a^2}. \quad (4.3)$$

We will discuss each term in this equation in turn. The factor \dot{a}/a is the expansion rate of our universe. It is called the Hubble parameter and denoted by H . The value of H today is known as the Hubble constant $H_0 \equiv \dot{a}(t_0)/a(t_0)$. This is the parameter that Edwin Hubble measured in his initial observations of the expansion of our universe (Hubble and Humason 1931). He observed that the further away a galaxy was, the faster

it appeared to be moving away from us:

$$v = H_0 d \quad (4.4)$$

where v is a galaxy's recession velocity and d is its distance from us. Hubble's initial measurements gave $H_0 \sim 550 \text{ km s}^{-1} \text{ Mpc}^{-1}$; the modern accepted value is $H_0 = 73 \text{ km s}^{-1} \text{ Mpc}^{-1}$. It is often parameterized using the Hubble parameter h , where $h \equiv H_0 / [100 \text{ km s}^{-1} \text{ Mpc}^{-1}]$. Cosmological distances are conventionally written in units of $h^{-1} \text{ Mpc}$ – we use this convention in chapter 6.

The recession velocity v is inferred from the wavelength shift of the galaxy's spectral lines due to the Doppler effect:

$$\frac{v}{c} \approx \frac{\lambda_{\text{obs}} - \lambda_{\text{rest}}}{\lambda_{\text{rest}}} \equiv z. \quad (4.5)$$

where c is the speed of light, λ_{rest} is the wavelength of the spectral line in the rest frame of the emitter, λ_{obs} is the wavelength observed at Earth, and the quantity z is called the “redshift” since objects moving away from us appear redder. The approximation holds when $v \ll c$ and the galaxy is close enough that it is sensible to interpret the redshift as a recession velocity. However, it is more accurate to think of the redshift as being caused by the expansion of space as the light is propagating through our universe. The wavelength of the light will get stretched along with space, and thus the wavelength change can be directly related to the scale factor a :

$$\frac{\lambda_{\text{obs}}}{\lambda_{\text{rest}}} = \frac{a(t_e)}{a(t_0)} \quad (4.6)$$

where t_e is the time the light was emitted from the galaxy. Light from galaxies that are further away will take longer to reach us, so it will have a longer amount of time in which to get stretched and thus appears more redshifted. Using equations (4.5) and (4.6) along with the normalization convention $a(t_0) = 1$, we can relate z to a :

$$a = \frac{1}{1+z}. \quad (4.7)$$

Moving on to the first term on the left-hand side, we have the the matter-energy density of our universe $\rho(t)$. The time evolution of this quantity depends on the type of matter. For the case of a perfect isotropic fluid with density ρ and pressure P , the Einstein field equations and the FRW metric tell us that (see, e.g., Dodelson 2003)

$$\dot{\rho} + 3\frac{\dot{a}}{a} \left(\rho + \frac{P}{c^2} \right) = 0, \quad (4.8)$$

Determining the evolution of ρ requires a relation between P and ρ , known as the equation of state. Here we will consider three different types of contributions to ρ :

- Cold, pressureless matter ρ_m (includes baryons and dark matter): $P = 0$, so equation (4.8) yields $\rho_m \propto a^{-3}$. Physically this means that the number of particles stays constant while the volume expands as length³.
- Radiation or relativistic matter ρ_r (includes photons and neutrinos): $P = \rho/3$, so equation (4.8) yields $\rho_r \propto a^{-4}$. Again the number of particles stays constant and

the volume expands as length³, but we gain an additional factor of a^{-1} since the energy of each particle is $\hbar\omega \propto \lambda^{-1}$, so the energy per particle decreases as a^{-1} as the wavelength gets redshifted.

- Unknown equation of state, i.e. dark energy ρ_Λ : $P = w\rho$, so equation (4.8) yields $\rho_\Lambda \propto a^{-3(1+w)}$. Current observations of dark energy are consistent with a cosmological constant, i.e. an energy density that remains constant as our universe expands. This corresponds to $\rho_\Lambda \propto a^0$, so $w = -1$. In the above examples, pressureless matter has $w = 0$ and radiation has $w = 1/3$. More general parameterizations of the dark energy equation of state also allow w to vary in time.

Finally, the second term on the right-hand side of equation (4.3), which includes the parameter K defining the overall curvature of space in our universe. One important insight to be gained from this equation is that the global geometry of our universe is directly linked to its matter content. There is a special value of the matter density that corresponds to flat space (i.e. $K = 0$) that is known as the “critical density” ρ_{cr} . By plugging $K = 0$ into equation (4.3) we find that the present value of the critical density is given by

$$\rho_{\text{cr}0} = \frac{3H_0^2}{8\pi G}. \quad (4.9)$$

The Friedmann equation takes on a particularly elegant form if we express all densities as fractions of the critical density. We define

$$\Omega_m \equiv \frac{\rho_{m0}}{\rho_{\text{cr}0}}, \Omega_r \equiv \frac{\rho_{r0}}{\rho_{\text{cr}0}}, \Omega_\Lambda \equiv \frac{\rho_{\Lambda 0}}{\rho_{\text{cr}0}}, \quad (4.10)$$

where again the 0 subscript denotes the present-day value. Now the Friedmann equation evaluated at the present is

$$1 = \Omega_m + \Omega_r + \Omega_\Lambda - \frac{Kc^2}{H_0^2}.$$

Using this we can define an effective Ω for the curvature:

$$\Omega_K \equiv 1 - \Omega_m - \Omega_r - \Omega_\Lambda = -\frac{Kc^2}{H_0^2}. \quad (4.11)$$

Thus the curvature is determined by the total matter density: if $\Omega_m + \Omega_r + \Omega_\Lambda = 1$, i.e. the total density of matter is exactly equal to the critical density, then $\Omega_K = 0$ and our universe is flat. If the total density is less than the critical density, then $K < 0$ and our universe has negative curvature. If the total density is greater than the critical density, then $K > 0$ and our universe has positive.

To write our elegant Friedmann equation, we use the definitions in equations (4.10) and (4.11) and the scalings with a of different types of matter density determined by equation (4.8) to re-express equation (4.3) as

$$\left(\frac{\dot{a}}{a}\right)^2 = H_0^2 \left(\Omega_r a^{-4} + \Omega_m a^{-3} + \Omega_K a^{-2} + \Omega_\Lambda a^{-3(1+w)} \right) \quad (4.12)$$

This relatively simple differential equation for the scale factor $a(t)$ is the cornerstone of zeroth order cosmology. Given values for the parameters H_0 , Ω_m , Ω_r , Ω_Λ , and w , one can completely describe the evolution of a homogenous universe containing matter, radiation,

and dark energy. (Or to be more precise, a dark-energy-like component with an equation of state that can be parameterized by a constant w .)

4.1.4 First order cosmology

The next step in cosmology is to study the evolution of small deviations from homogeneity. The early universe was extremely smooth, with tiny perturbations in the density on the order of one part in 10^5 . As our universe evolved, these small fluctuations grew under the influence of gravity into the complex cosmic web we see today. The behavior of these fluctuations is properly understood by perturbing the Einstein equations of general relativity around the homogenous solution described in §4.1.3 – the details of this can be found in, e.g., Dodelson (2003). Here we go through a Newtonian approximation that elucidates much of the key physics governing cosmological perturbations, and then discuss the statistical measures used to analyze them.

Linear growth of structure

The equations governing the behavior of a non-relativistic, self-gravitating fluid are the continuity equation, Euler's equation, and the Poisson equation, respectively given by

$$\frac{\partial \rho}{\partial t} + \nabla_{\mathbf{r}} \cdot (\rho \mathbf{v}) = 0 \quad (4.13)$$

$$\frac{\partial \mathbf{v}}{\partial t} + (\mathbf{v} \cdot \nabla_{\mathbf{r}}) \mathbf{v} = -\frac{\nabla_{\mathbf{r}} P}{\rho} - \nabla_{\mathbf{r}} \Phi \quad (4.14)$$

$$\nabla_{\mathbf{r}}^2 \Phi = 4\pi G \rho \quad (4.15)$$

where $\rho(\mathbf{r}, t)$ is the density of the fluid, $P(\mathbf{r}, t)$ is the pressure, $\mathbf{v}(\mathbf{r}, t)$ is the velocity of a fluid element, $\Phi(\mathbf{r}, t)$ is the gravitational potential, and $\nabla_{\mathbf{r}}$ denotes the gradient with respect to \mathbf{r} . The spirit of first order cosmology is to start with a homogenous universe and then consider small perturbations to ρ , \mathbf{v} , Φ , and P . We will use

$$\begin{cases} \rho_0(\mathbf{r}, t) = \frac{\rho_C}{a(t)^3} \\ \mathbf{v}_0(\mathbf{r}, t) = \frac{\dot{a}(t)}{a(t)} \mathbf{r} \\ \Phi_0(\mathbf{r}, t) = \frac{2\pi G}{3} \rho_0(\mathbf{r}, t) r^2 \\ P_0(\mathbf{r}, t) = 0 \end{cases} \quad (4.16)$$

for our homogenous solution, which satisfies equations (4.13), (4.14), and (4.15) if $a(t)$ satisfies our zeroth order cosmology equations (4.3) and (4.8). This corresponds to a universe of pressureless matter (such as dark matter) undergoing Hubble expansion $\mathbf{v}_0 = H\mathbf{r}$.

Now we solve for the behavior of small perturbations:

$$\begin{cases} \rho(\mathbf{r}, t) = \rho_0(\mathbf{r}, t) + \rho_1(\mathbf{r}, t) \\ \mathbf{v}(\mathbf{r}, t) = \mathbf{v}_0(\mathbf{r}, t) + \mathbf{v}_1(\mathbf{r}, t) \\ \Phi(\mathbf{r}, t) = \Phi_0(\mathbf{r}, t) + \Phi_1(\mathbf{r}, t) \end{cases} \quad (4.17)$$

where quantities with 1 subscripts are small enough that we can ignore all but the linear terms. Inserting these into the continuity, Euler, and Poisson equations, subtracting the homogenous solution, and dropping higher order terms of the perturbations gives

$$\frac{\partial \rho_1}{\partial t} + (\mathbf{v}_0 \cdot \nabla_{\mathbf{r}}) \rho + \rho_0 \nabla_{\mathbf{r}} \cdot \mathbf{v}_1 + 3 \frac{\dot{a}}{a} \rho_1 = 0 \quad (4.18)$$

$$\frac{\partial \mathbf{v}_1}{\partial t} + (\mathbf{v}_0 \cdot \nabla_{\mathbf{r}}) \mathbf{v}_1 + \frac{\dot{a}}{a} \mathbf{v}_1 = -\nabla_{\mathbf{r}} \Phi_1 \quad (4.19)$$

$$\nabla_{\mathbf{r}}^2 \Phi_1 = 4\pi G \rho_1. \quad (4.20)$$

Cosmology is often best understood in *comoving* coordinates defined by $\mathbf{x} \equiv \mathbf{r}/a(t)$. Comoving coordinates are defined such that they remain fixed for observers moving along with the Hubble expansion in a homogenous universe. The comoving peculiar velocity is given by $\mathbf{u} \equiv \mathbf{v}_1/a(t)$, and we define the density contrast as $\delta \equiv \rho_1/\rho_0$. Re-writing the above equations in comoving coordinates gives

$$\dot{\delta} = -\nabla \cdot \mathbf{u} \quad (4.21)$$

$$\dot{\mathbf{u}} + \frac{\dot{a}}{a} \mathbf{u} = -\frac{1}{a^2} \nabla \Phi_1 \quad (4.22)$$

$$\nabla^2 \Phi_1 = 4\pi G a^2 \rho_0 \delta, \quad (4.23)$$

where $\nabla = a(t) \nabla_{\mathbf{r}}$ is the gradient with respect to the comoving coordinates \mathbf{x} , dots represent $d/dt \equiv \partial/\partial t + \mathbf{v}_0 \cdot \nabla_{\mathbf{r}}$, the time derivative for comoving observers, and $c_s \equiv (\partial P/\partial \rho)^{1/2}$ is the sound speed.

By taking the time derivative of equation (4.21) and the divergence of equation (4.22) we can derive a second order differential equation for δ :

$$\ddot{\delta} + 2 \frac{\dot{a}}{a} \dot{\delta} - 4\pi G \rho_0 \delta = 0. \quad (4.24)$$

This is the basic equation governing the growth of small density perturbations in a universe of pressureless matter, which is quite applicable to our universe since the bulk of large-scale structure formation in our universe occurs while dark matter is the dominant component.

Equation (4.24) has two linearly independent solutions:

$$\begin{aligned} \delta_G(t) &= \frac{\dot{a}}{a} \int_0^a \frac{1}{a^3} da && \text{(growing mode)} \\ \delta_d(t) &= \frac{\dot{a}}{a} && \text{(decaying mode)} \end{aligned} \quad (4.25)$$

where the growing mode increases with time and the decaying mode decreases. The general solution is a linear combination:

$$\delta(\mathbf{x}, t) = A(\mathbf{x}) \delta_G(t) + B(\mathbf{x}) \delta_d(t), \quad (4.26)$$

where A and B are arbitrary functions of \mathbf{x} . The decaying mode will eventually become negligible as the universe expands, and is thus not relevant to structure formation, so we focus on the growing mode. We can then write the density contrast as

$$\delta(\mathbf{x}, t) = \delta(\mathbf{x}, t_i) \frac{\delta_G(t)}{\delta_G(t_i)}, \quad (4.27)$$

where the perturbations are specified at some initial time t_i . Thus an initial perturbation field $\delta(\mathbf{x}, t_i)$ will retain its shape but increase in amplitude until $\delta \sim 1$ and our linear

approximation no longer holds. This is the basic picture of how small perturbations start growing into large structures through gravitational instability. For a more detailed, properly relativistic treatment, see Padmanabhan (1993); Dodelson (2003).

Statistics of random fields

A general theory of how structure formed in our universe could never hope to predict the value of the density contrast δ at a specific point \mathbf{x} . Instead the goal is to predict its statistical properties, which are typically described in the language of random fields. A random field is an infinite dimensional random variable that has some probability to take on a given value at every point in space. The function $\delta(\mathbf{x}, t_i)$ in equation (4.27), for example, is a realization of a random field.

The statistical properties of a random field δ are specified by a series of joint probability distributions $P_n(\delta_1, \delta_2, \dots, \delta_n)$ for its values $\delta_i \equiv \delta(\mathbf{x}_i)$ at n points $\mathbf{x}_1, \mathbf{x}_2, \dots, \mathbf{x}_n$ for $n = 1, 2, 3, \dots$. The most commonly used random field in cosmology is a zero-mean Gaussian random field, where the probability distribution is a multivariate Gaussian:

$$P_n(\delta_1, \delta_2, \dots, \delta_n) d\delta_1 d\delta_2 \dots d\delta_n = \frac{1}{\sqrt{(2\pi)^n \det(\mathbf{M})}} \exp(\delta^T \mathbf{M}^{-1} \delta) d\delta_1 d\delta_2 \dots d\delta_n, \quad (4.28)$$

where δ is a column vector of the δ_i 's and \mathbf{M} is a covariance matrix that defines the distribution. The expectation value of any function f of the δ_i 's is defined as

$$\langle f(\delta_1, \delta_2, \dots, \delta_n) \rangle \equiv \int f(\delta_1, \delta_2, \dots, \delta_n) P_n(\delta_1, \delta_2, \dots, \delta_n) d\delta_1 d\delta_2 \dots d\delta_n. \quad (4.29)$$

In typical cosmological applications, we try to infer the statistical properties of a random field, e.g. the density contrast, from observing the one realization of it provided by our universe. We do not have the luxury of observing multiple universes drawn from the ensemble defined by our model probability distribution, so we cannot really measure an ensemble average like equation (4.28) specifies. To connect our statistical model with what we can actually observe, we have to make an assumption that the random fields are *ergodic*, which means that averaging over a sufficiently large volume of space is equivalent to averaging over a statistical ensemble, so we can use

$$\langle f(\delta_1, \delta_2, \dots, \delta_n) \rangle = \lim_{V'_s \rightarrow \infty} \int_{V_1} \int_{V_2} \dots \int_{V_n} f(\delta(\mathbf{x}_1), \delta(\mathbf{x}_2), \dots, \delta(\mathbf{x}_n)) d^3x_1 d^3x_2 \dots d^3x_n \quad (4.30)$$

for a practical means of defining expectation values.

The most commonly used statistical measures of random fields are moments of the probability distribution, called n -point functions. The 1-point function, i.e. the mean, is given by $\langle \delta_i \rangle$, the 2-point function is given by $\langle \delta_i \delta_j \rangle$, and so forth. For example, a zero-mean Gaussian random field with P_n given by equation (4.28) has $\langle \delta_i \rangle = 0$ (hence the “zero-mean”), $\langle \delta_i \delta_j \rangle = \mathbf{M}_{ij}$, and $\langle \delta_1 \delta_2 \dots \delta_n \rangle = 0$ for $n > 2$.

The 2-point function is the most basic statistical measure of inhomogeneities in a random field and thus plays an important role in first-order cosmology. It is known as the correlation

function $\xi(\mathbf{x}_i, \mathbf{x}_j) \equiv \langle \delta_i \delta_j \rangle$, and for a universe that is statistically homogenous and isotropic, the correlation function will only depend on the distance between the two points \mathbf{x}_i and \mathbf{x}_j and not on their absolute position or orientation: $\xi(\mathbf{x}_i, \mathbf{x}_j) = \xi(|\mathbf{x}_i - \mathbf{x}_j|)$.

The 2-point function has some particularly convenient properties if we transform into Fourier space. Defining the Fourier transform as

$$\hat{\delta}(\mathbf{k}) \equiv \int e^{i\mathbf{k}\cdot\mathbf{x}} \delta(\mathbf{x}) d^3x, \quad (4.31)$$

the Fourier space version of the 2-point function is

$$\langle \hat{\delta}^*(\mathbf{k}_i) \hat{\delta}(\mathbf{k}_j) \rangle = \int e^{i\mathbf{k}_j\cdot\mathbf{x}_j - i\mathbf{k}_i\cdot\mathbf{x}_i} \xi(\mathbf{x}_i, \mathbf{x}_j) d^3x_i d^3x_j, \quad (4.32)$$

and if the correlation function depends only on the separation, i.e. $\xi(\mathbf{x}_i, \mathbf{x}_j) = \xi(\mathbf{x}_i - \mathbf{x}_j)$, then equation (4.32) reduces to

$$\langle \hat{\delta}^*(\mathbf{k}_i) \hat{\delta}(\mathbf{k}_j) \rangle = (2\pi)^3 \delta_D(\mathbf{k}_i - \mathbf{k}_j) P(\mathbf{k}_i), \quad (4.33)$$

where δ_D is the Dirac delta function and $P(\mathbf{k})$, called the *power spectrum*, is the Fourier transform of the correlation function:

$$P(\mathbf{k}) \equiv \int e^{i\mathbf{k}\cdot\mathbf{x}} \xi(\mathbf{x}) d^3x. \quad (4.34)$$

Furthermore, if the correlation function depends only on the magnitude of the separation, i.e. $\xi(\mathbf{x}_i, \mathbf{x}_j) = \xi(|\mathbf{x}_i - \mathbf{x}_j|)$, then the power spectrum will depend only on the magnitude $k \equiv |\mathbf{k}|$ of the wavevector \mathbf{k} : $P(\mathbf{k}) = P(k)$.

Equation (4.33) illustrates why theorists prefer to work with the power spectrum rather than the correlation function: the Dirac delta function indicates that for a random field that is homogenous in real space, its Fourier modes will be *uncorrelated* for different values of \mathbf{k} . In other words, its covariance matrix is diagonal: if $\delta(\mathbf{x})$ is a homogenous, zero-mean Gaussian random field described by the probability distribution in equation (4.28), then $\hat{\delta}(\mathbf{k})$ is a Gaussian random field as well, with the additional feature that the matrix \mathbf{M} in equation (4.28) is a diagonal matrix. This makes the power spectrum much more convenient for many theoretical calculations. For more details see Hamilton (1998) for an excellent discussion of correlation functions and power spectra.

The primary goal of first order cosmology is to predict the power spectrum $P(k, t)$ of the density contrast $\delta(\mathbf{x}, t)$ of matter in our universe as a function of cosmic time. This can be modeled as

$$P(k, t) = \left(\frac{\delta_G(t)}{\delta_G(t_i)} \right)^2 T^2(k) P(k, t_i),$$

where $\delta_g(t)$ is (an appropriately relativistic version of) the growing mode in equation (4.25) and $T(k)$, known as the transfer function, accounts for a bunch of physics we have ignored in the simple treatment here – interactions between matter and radiation, the behavior of modes with wavelengths larger than the horizon (the distance a photon can travel through the universe since time $t = 0$) and so forth. See Padmanabhan (1993) for a detailed discussion of the transfer function.

The function $P(k, t_i)$ is the spectrum of primordial fluctuations that seeds the growth of structure. Theories of inflation predict that this initial spectrum was produced by quantum

fluctuations that were stretched to macroscopic size by a period of exponential expansion in the very early universe. This process typically predicts that the initial fluctuations can be described by a Gaussian random field with a power-law power spectrum:

$$P(k, t_i) = A_s k^{n_s},$$

where A_s and n_s are the basic first order cosmological parameters that are included along with the zeroth order parameters H_0 , w , and various Ω 's in parameter estimation analyses such as the one discussed in §4.3. Most models of inflation predict that n_s to be slightly less than 1.

Theoretical predictions for $P(k, t)$ for matter in our universe given a set of cosmological parameters can be computed exactly in the linear regime and is typically done using the handy computer program CMBFAST (Seljak and Zaldarriaga 1996). With the first order approximation that $\delta \ll 1$, each Fourier mode evolves independently, so this makes the theoretical calculations much easier in Fourier space than in real space. However, there are two issues with comparing this predicted power spectrum with what we observe: first, for perturbations with $\delta \sim 1$ the linear theory no longer applies. Secondly, our observations rely on using galaxies to trace the overall matter distribution. The issue of nonlinear evolution is discussed in the next section, and the issue of galaxies as tracers is explored in depth in chapter 6. Here we merely note the usual assumption made when measuring the power spectrum from galaxy surveys: that the power spectrum of the galaxies has the same shape as that of the overall matter, but scaled by a normalization factor:

$$P_{\text{galaxy}}(k) = b^2 P_{\text{matter}}(k), \quad (4.35)$$

where the parameter b is called the bias. On scales larger than the size of the largest gravitationally bound structures in our universe ($k \lesssim 0.09h/\text{Mpc}$, or $\lambda \equiv 2\pi/k \gtrsim 70h^{-1}\text{Mpc}$), the simplifying assumptions of linear evolution and simple galaxy bias have been found to be quite reasonable (Tegmark et al. 2006).

4.1.5 Higher order cosmology

The zeroth and first order cosmology discussed in the previous sections can take us a long way, but a full theory of structure formation in our universe requires a nonlinear treatment of differential equations such as equations(4.13), (4.14), and (4.15) that can be applied to systems like galaxies and galaxy clusters that have $\delta \gg 1$. Unfortunately, this turns out to be quite challenging – the nonlinear versions of the equations couple together the evolution of different Fourier modes, so most of the techniques used in first order cosmology cannot be applied and exact solutions do not exist.

This difficult and unsolved problem has been tackled from a number of different angles: analytical models that apply under various simplified conditions, numerical simulations that attempt to include all of the relevant physics, empirical fitting formulas tuned to match simulations or observations, and various hybrid techniques that endeavor to combine analytical and numerical results to build up a complete picture. Numerical simulations are arguably the only way to obtain a complete solution, and much work has been done on both N -body simulations that model purely gravitational systems (e.g. Springel et al. 2005) and hydrodynamical simulations that include gas physics as well (see Dolag et al. 2008 for a recent review). However, such simulations are always subject to a variety of approximations and the results can be challenging to interpret (Tasitsiomi et al. 2004; Romeo et al. 2008),

so analytical and semi-analytical methods continue to play an important role. Here we outline perhaps the most widely-used analytical model for nonlinear structure evolution and discuss some of its extensions, and then we give an overview of a hybrid approach known as the halo model that has had much success in recent years.

Spherical collapse and Press-Schechter theory

The analytical model we will discuss here starts with a simple approximation for the collapse of a spherical overdensity. Consider a universe that contains only matter and has a density equal to the critical density ρ_{cr} such that $\Omega_m = 1$, except in a spherical region of comoving radius R_0 enclosing mass $M = 4\pi\Omega'_m\rho_{\text{cr}0}R_0^3/3$ in which the density is slightly higher than the critical density, with $\Omega'_m \gtrsim 1$. Equation (4.12) can be solved for the $\Omega_m = 1$ background universe to give

$$a_b(t) = \left(\frac{3}{2}H_0t\right)^{2/3}, \quad \rho_b(t) = \frac{1}{6\pi Gt}, \quad (4.36)$$

where the b subscript denotes the background universe. The perturbed region also evolves according to Equation (4.12), but with $\Omega'_m > 1$. A parametric solution is given by

$$\begin{cases} a_p(\eta) = \frac{1}{2}\frac{\Omega'_m}{\Omega'_m-1}(1 - \cos\eta) \\ t(\eta) = \frac{1}{2H_0}\frac{\Omega'_m}{(\Omega'_m-1)^{3/2}}(\eta - \sin\eta) \end{cases} \quad (4.37)$$

where the p subscript denotes the perturbation. The perturbation will expand until $\eta = \pi$, and then start to contract until $\eta = 2\pi$, at which point it will be fully collapsed.

In reality, the density will not become infinite – if the matter is baryonic, the collapse will eventually be stopped by gas pressure, and if it is dark matter, the particles will whiz past each other and get slowed down by gravitational forces. Either way, the system is roughly expected to reach an equilibrium state where its kinetic and potential energy should satisfy the virial theorem: $U + 2K = 0$. The virialized radius can be found by considering the energy at the turnaround point $\eta = \pi$ is purely potential. Since the gravitational potential energy of a sphere is proportional to R^{-1} , energy conservation and the virial theorem imply that the virialized radius is half the radius at turnaround, so the collapsed density will be

$$\begin{aligned} \rho_{\text{collapsed}} &= 8\rho_p(\eta = \pi) \\ &= 18\pi^2\rho_b(\eta = 2\pi). \end{aligned} \quad (4.38)$$

After the collapse, the virialized object will retain this physical density as the background universe continues to expand.

The density contrast between the perturbation and the background universe can be found from equations (4.36) and (4.37) to be

$$\begin{aligned} \delta \equiv \frac{\rho_p - \rho_b}{\rho_b} &= \frac{9(\eta - \sin\eta)^2}{2(1 - \cos\eta)^3} \\ &\approx \frac{3}{20}\eta^2 \text{ for } \eta \ll 1. \end{aligned} \quad (4.39)$$

How does this compare to the first order evolution of δ derived in §4.1.4? Equation 4.25 for a flat, matter-dominated universe gives $\delta_g \propto a$, so the linear theory prediction gives $\delta_{\text{lin}} \propto t^{2/3}$. Choosing the proportionality constant to match equation 4.39 for early times,

we have

$$\delta_{\text{lin}} = \frac{3}{20} [6(\eta - \sin \eta)]^{2/3}. \quad (4.40)$$

Equations (4.39) and (4.40) give us an important tool: a means of connecting an exact solution with linear theory predictions. We have done these calculations for a the simple model of a $\Omega_m = 1$ universe, but the same basic ideas apply for other cases – see Padmanabhan (1993) for more details. At the time of the collapse, we have $\delta_{\text{lin}}(\eta = 2\pi) = 3(12\pi)^{2/3}/20 \approx 1.686$. Based on this, we can construct a recipe for modeling nonlinear evolution: evolve δ using linear perturbation theory until it reaches a critical value of $\delta_c = 1.686$ in a given region, and then substitute in a spherically-collapsed, virialized object at that location.

Press and Schechter (1974) applied this idea to describe structure formation in our universe and produced a canonical formula for the mass function $n(M)$ giving the comoving number density of objects of mass M based on the following argument: consider a universe with mean comoving mass density $\bar{\rho}$ that has a matter distribution described by the linearly-evolved power spectrum $P_{\text{lin}}(k)$. To determine the properties of the population of mass M objects, smooth the linearly-evolved density field with a spherical top-hat filter $w(r, R) \equiv 3/(4\pi R^3)\Theta(R - r)$ with radius $R \equiv (3M/(4\pi\bar{\rho}))^{1/3}$. The smoothed density field is

$$\delta_M(\mathbf{x}) = \int w(|\mathbf{x} - \mathbf{x}'|, R) \delta(\mathbf{x}') d^3\mathbf{x}', \quad (4.41)$$

and the variance of the smoothed field is

$$\langle \delta_M(\mathbf{x})^2 \rangle \equiv \sigma^2(M) = \int \frac{dk}{k} \frac{k^3 P_{\text{lin}}(k)}{2\pi^2} |\hat{w}(k, R)|^2, \quad (4.42)$$

where $\hat{w}(k, R)$ is the Fourier transform of the top hat filter:

$$\hat{w}(k, R) = \frac{3}{(kR)^3} [\sin(kR) - kR \cos(kR)]. \quad (4.43)$$

Now consider any region that has $\delta_M(\mathbf{x}) > \delta_c$ to be a virialized object that has mass $\geq M$. By repeating this for all smoothing scales, we can build up a picture of the mass distribution of objects in our universe.

Assuming that the density contrast δ can be modeled as a Gaussian random field, the fraction of the mass in our universe contained in virialized objects with masses $\geq M$ is given in the Press-Schechter model by

$$\begin{aligned} F(> M) &= \frac{1}{\sqrt{2\pi}\sigma(M)} \int_{\delta_c}^{\infty} \exp\left(-\frac{\delta_M^2}{2\sigma^2(M)}\right) d\delta_M \\ &= \frac{1}{2} \text{erfc}\left(\sqrt{\frac{\nu}{2}}\right), \end{aligned} \quad (4.44)$$

where $\nu \equiv \delta_c^2/\sigma^2(M)$. This formula has a curious feature: it says that the maximum fraction of mass that can be contained in virialized objects is 1/2, not 1 – this is because we have ignored underdense regions that have $\delta < 0$. However, mass in underdense regions is likely to accrete onto the virialized objects eventually. To account for this omission, Press and Schechter simply multiply equation (4.44) by a “fudge factor” of 2 and find they get a sensible final answer.

We can find the mass function by differentiating equation (4.44) and multiplying by the

extra factor of 2 and by the number density $\bar{\rho}/M$ that would be expected if *all* of the mass in a universe with average mass density $\bar{\rho}$ were in mass M objects:

$$\begin{aligned} n(M) dM &= -2 \frac{\bar{\rho}}{M} \frac{dF}{dM} dM \\ &= \frac{\bar{\rho}}{M^2} \sqrt{\frac{\nu}{2\pi}} \exp\left(-\frac{\nu}{2}\right) \left(\frac{d(\ln \nu)}{d(\ln M)}\right) dM \end{aligned} \quad (4.45)$$

This is the famous Press-Schechter mass function. Although it is based on a rather heuristic argument, it has proven to be a remarkably valuable tool – it agrees well with numerical simulations (e.g. White et al. 1993) and has provided a launching point for further theoretical work, particularly the extended Press-Schechter theory based on the excursion set formalism (see Zentner (2007) for a recent review). Early applications of the excursion set formalism (Peacock and Heavens 1990; Bond et al. 1991) provided a more formal derivation of equation (4.45) that explains the factor of 2 and resolves other issues as well.

An updated version of the mass function that provides a better fit to the latest numerical simulations (Springel et al. 2005) is given by Sheth and Tormen (1999):

$$n(M) dM = \frac{A(p) \bar{\rho}}{m^2} \sqrt{\frac{q\nu}{2\pi}} \left(1 + \frac{1}{(q\nu)^p}\right) \exp\left(-\frac{q\nu}{2}\right) \left(\frac{d(\ln \nu)}{d(\ln M)}\right) dM, \quad (4.46)$$

with $q \approx 0.707$, $p \approx 0.3$, and $A(p) = (1 + 2^{-p}\Gamma(1/2 - p)/\sqrt{\pi})^{-1} \approx 0.3222$. Note that if $p = 0$ and $q = 1$ then This mass function can be derived using excursion set theory (Sheth et al. 2001) by considering ellipsoidal rather than spherical collapse.

The extended Press-Schechter theory also provides a way to make theoretical predictions for the clustering of halos and their merger histories – see Martínez and Saar (2002) for a good summary. For example, Bond et al. (1991) showed that the fraction of mass of a large object of mass M_0 with present linear density contrast δ_0 and variance σ_0 that is made up of merged-in smaller objects of mass M_1 , present linear density contrast δ_1 and variance σ_1 is given by

$$f(\sigma_1, \delta_1 | \sigma_0, \delta_0) \frac{d\sigma_1^2}{dM_1} dM_1 = \frac{1}{\sqrt{2\pi}} \frac{\delta_1 - \delta_0}{(\sigma_1^2 - \sigma_0^2)^{3/2}} \exp\left[-\frac{(\delta_1 - \delta_0)^2}{2(\sigma_1^2 - \sigma_0^2)}\right] \frac{d\sigma_1^2}{dM_1} dM_1 \quad (4.47)$$

Mo and White (1996) use equation (4.47) to calculate the bias factor b_M for halos of mass M using the extended Press-Schechter theory, where b_M is defined such that the power spectrum $P_M(k)$ of virialized objects of mass M is $b_M^2 P_{\text{lin}}(k)$, with $P_{\text{lin}}(k)$ being the linear theory matter power spectrum. They find that

$$b_M = 1 + \frac{\nu - 1}{\delta_c}. \quad (4.48)$$

The generalized version of this equation using the Sheth-Tormen mass function (equation (4.46)) was derived by Sheth and Tormen (1999):

$$b_M = 1 + \frac{q\nu - 1}{\delta_c} + \frac{2p/\delta_c}{1 + (q\nu)^p}. \quad (4.49)$$

These and other results from extended Press-Schechter theory are key ingredients in assem-

bling an analytical description of nonlinear structure formation.

Halo model

One particular model that has proven useful for describing both nonlinear clustering and galaxy bias is the known as the halo model, first formalized by Seljak (2000); Scoccimarro et al. (2001). (See Cooray and Sheth 2002 for a comprehensive review.) The basic idea is this: at late times, the matter distribution in our universe can be modeled using only virialized objects made of dark matter that are called *halos*, and the galaxy distribution can be modeled by an appropriate scheme for placing galaxies in these dark matter halos. The key assumption of the model is that the average properties of a halo – its density profile and its galaxy content – only depend on the halo mass.

Using this assumption, we can construct an analytical form for the nonlinear power spectrum by assembling components from first order cosmology, the extended Press-Schechter theory discussed above, and N -body simulation results. The halo model power spectrum is

$$P(k) = P^{1h}(k) + P^{2h}(k), \quad (4.50)$$

where $P^{1h}(k)$ is the 1-halo term arising from correlations between mass within the same halo and $P^{2h}(k)$ is the 2-halo term arising from correlations between mass in different halos.

To calculate these terms we need a description of how mass is distributed within a halo. This is usually modeled by an NFW profile (Navarro et al. 1996), which has been found to be an excellent fit to dark matter halos that form in N -body simulations. The normalized profile $u(r|M) \equiv \rho(r|M)/M$ is given by

$$u(r|M) = \frac{fc^3}{4\pi r_{\text{vir}}} \frac{1}{\left(\frac{cr}{r_{\text{vir}}}\right) \left(1 + \frac{cr}{r_{\text{vir}}}\right)^2} \quad (4.51)$$

where $f = 1/[\ln(1+c) - c/(1+c)]$ and the concentration parameter c is a function of the mass, typically approximated as (Bullock et al. 2001)

$$\bar{c}(M, z) = \frac{9}{1+z} \left(\frac{M}{M_*(z)}\right)^{-0.13} \quad (4.52)$$

with the characteristic mass scale M_* is defined as the point where $\nu = 1$: $\delta_c^2 \equiv \sigma^2(M_*)$. The virial radius r_{vir} is defined by the mass: $M = \Delta \bar{\rho} 4\pi r_{\text{vir}}^3/3$, where Δ is the typical overdensity of a virialized structure compared to the background density – we found in equation (4.38) that $\Delta = 18\pi^2 \approx 178$ for a $\Omega_m = 1$. Equation (4.51) is normalized such that the total mass within the virial radius is equal to M .

The 1- and 2-halo terms are then given by

$$P^{1h}(k) = \frac{1}{\bar{\rho}^2} \int dM n(M) |\hat{u}(k|M)|^2 \quad (4.53)$$

$$P^{2h}(k) = \frac{1}{\bar{\rho}^2} \int dM_1 n(M_1) \hat{u}(k|M_1) \int dM_2 n(M_2) \hat{u}(k|M_2) P^{hh}(k|M_1, M_2), \quad (4.54)$$

where $\hat{u}(k|M)$ is the Fourier transform of the NFW profile in equation (4.51) and $n(M)$ is the mass function given by equation (4.46). $P^{hh}(k|M_1, M_2)$ is the halo-halo power spectrum,

most simply modeled by

$$P^{hh}(k|M_1, M_2) = b_{M_1} b_{M_2} P_{\text{lin}}(k), \quad (4.55)$$

where b_M is bias for halos of mass M given in equation (4.49), although more sophisticated models have been used in recent work (Zehavi et al. 2005; Tinker et al. 2005).

In addition to modeling the dark matter distribution, the halo model is also a useful tool for modeling galaxy bias. The galaxy distribution then be modeled by first determining the halo distribution and then populating the halos with galaxies. The second step requires a model for $P(N|M, L, C, \dots)$, the probability that a halo of mass M will host N galaxies with luminosity L , color C , and any other galaxy properties the modelers wish to include. Multiple parameterizations for this probability distribution have been developed (Peacock and Smith 2000; Berlind and Weinberg 2002; Sefusatti and Scoccimarro 2005; Yang et al. 2003; van den Bosch et al. 2003). The algorithm used for placing the galaxies in halos encodes the physics of galaxy formation and can be used to compare semi-analytical galaxy formation models (Baugh 2006) with observational results such as those discussed in chapter (6). This procedure yields a model of galaxy bias that is more closely linked with the actual physical processes than the simple assumption of equation (4.35).

The halo model has been successfully used to model several different types of observations, such as galaxy correlation functions (Zehavi et al. 2005), void statistics (Tinker et al. 2007), and counts of galaxies in groups (Yang et al. 2008). However, as we will see in §4.3 it has yet to be incorporated into full cosmological parameter analyses – this could potentially be a promising direction for future work.

4.1.6 What does this teach us about particle physics?

What can we hope to learn about physics on at the sub-atomic level by studying our universe on such a grand scale? Quite a lot, as it turns out! One basic tenet of particle physics is that higher energies can probe shorter length scales. In order to examine extremely small length scales – the quarks within a proton, for example – particles are collided with each other at extremely high energies. The current generation of particle accelerators can achieve energies of 2 TeV, and the Large Hadron Collider, set to turn on in 2008, will push this up to 14 TeV (Feng 2008). However, the extremely hot, dense conditions in the first fraction of a second after the Big Bang provide a natural particle accelerator – a split-second after the Big Bang, the average thermal energy of particles could have been as high as 10^{13} TeV. Thus by studying cosmology, particle physicists can learn about phenomena that could not be created in a terrestrial experiment.

Of course, the problem with this plan is that after 14 billion years, much of the action has faded away – unstable particles created early on have long since decayed and the present-day density of any remaining stable particles has been so diluted by the expansion that they are no longer interacting with each other. Particle physicists who endeavor to use our early universe as a laboratory must find ways to predict detectable signatures left behind by the processes they hope to investigate. Particle physicists also work to develop models that can explain the bizarre features of the standard cosmological model described in §4.1.2. This is especially interesting because the ideas of dark matter and dark energy cannot be explained within the framework of the standard model of particle physics and thus hint at physics beyond our current understanding.

From cosmological and other astronomical observations, we know that some form of

non-baryonic dark matter that does not couple strongly to photons makes up most of the mass in our universe. Theorized particles that have properties similar to dark matter are actually well-motivated in a particle physics context. One class of proposed extensions to the standard model of particle physics, known as supersymmetry, postulate that every particle has a supersymmetric partner particle whose spin differs by $1/2$ (Peskin 2008). The supersymmetric partners of known particles are expected to have such high masses that we would not have been produced by the current generation of particle accelerators. Supersymmetry was proposed to explain a number of seemingly “unnatural” features of the standard model, such as why the masses of standard model particles are so much smaller than the natural energy scale of the theory. It also provides a candidate particle for dark matter: the lightest supersymmetric particle. At the extremely high temperatures and densities present in the early universe, an abundance of supersymmetric particles might have been created. Most of these will be unstable and decay quickly into lighter supersymmetric particles, but the lightest supersymmetric particle is predicted to be stable. If this is the case, it would be present in our universe today and act like dark matter – that is, like a weakly interacting massive particle, a.k.a. a WIMP. This is currently regarded as the most natural explanation for dark matter, but there are a number of other particle physics theories that can generate particles with dark-matter-like properties as well, such as axions, solitons, or WIMPZILLAS (Gondolo 2004).

One might ask why we need to resort to such exotic-sounding models to explain dark matter – after all, we know that neutrinos must have some mass, as discussed in §2, so could the dark matter simply be neutrinos? The answer comes from first order cosmology, considering the nature of the perturbations in the density field. The three types of neutrinos in the standard model, while we know they must have *some* mass, are still light enough that their average velocity is quite high at the time when structure is forming, so they are classified as *hot* dark matter. The main effect of hot dark matter is to wash out the formation of structure on small scales – heuristically, neutrinos will not collapse into a structure if their average velocity exceeds the escape velocity of the a given overdense clump. For small (i.e., galaxy-sized) clumps, the escape velocity is small enough that we would not expect neutrinos to collapse into structures of this size. See Lesgourgues and Pastor (2006) for a detailed explanation of this effect.

Such a picture is not consistent with the structure we see today, which implies that the dark matter must be *cold* – that is, massive enough to have very low average velocity at the time structure starts to form. In fact, measurements of the power spectrum can be used to set a strong upper limit on the sum of the masses of the three types of neutrinos – we discuss an example of this in §4.3. In fact, cosmology currently place stronger upper limits on the neutrino mass than current particle physics experiments (Elgarøy and Lahav 2006; Hannestad et al. 2008), and the next generation of cosmological measurements may be sensitive enough to detect masses as small as the mass differences seen by Super-K.

Another cosmological puzzle particle physicists have sought to tackle is that of dark energy. What kind of substance could lead to the bizarre repulsive gravitational effects that are driving the current acceleration of our universe’s expansion? The most basic possibility from the point of view of quantum field theory is that there is an inherent energy density associated with empty space called *vacuum energy*. The vacuum energy density would remain constant as the universe expands, which is consistent with the observed properties of dark energy. Theoretical predictions of what the value of the vacuum energy density should be are rather problematic – a basic quantum field theory calculation gives a divergence, predicting infinite vacuum energy density. Imposing a natural cutoff to this divergence

gives an estimate of $\sim 10^{110}$ erg/cm³ for the vacuum energy density. Prior to the discovery of dark energy, particle theorists devoted much effort to searching for natural ways this vacuum energy could cancel out to be exactly zero. Finding that there is indeed something that looks like vacuum energy in our universe made the problem even more difficult for the theorists, since the cosmological observations indicate that the density of dark energy is $\sim 10^{-10}$ erg/cm³, 120 orders of magnitude less than the estimated value! A theory where the vacuum energy is almost entirely canceled out except for a tiny fraction would be much more bizarre than perfect cancellation. Supersymmetry provides some help here, but not enough – it can reduce the discrepancy to “just” 60 orders of magnitude. Dark energy has proven to be a fascinating challenge from a particle theory perspective (see Frieman et al. 2008 for a review of possible models) and is particularly interesting from the point of view of connecting particle physics and astronomy because as far as we know, the *only* way to measure its properties is through cosmological observations (see Albrecht et al. 2006 for more details).

4.2 Tools of cosmology

4.2.1 Combining cosmological probes

The great strength of modern observational cosmology is that such a wide variety of different experimental measurements point to the same theoretical model. Some measurements, such as using supernovae as standard candles to trace the expansion history of our universe, target the zeroth order cosmology discussed in §4.1.3 – that is, they are effectively probing the function $a(t)$. Other measurements, such as studying the tiny fluctuations in the cosmic microwave background or the clustering patterns in the distribution of galaxies, are fundamentally probes of the first order cosmology discussed in §4.1.4: they measure variations on the power spectrum $P(k)$. Still others, such as measuring the abundances of elements formed by fusion in the hot, dense plasma of the early universe, target one particular cosmological parameter – in this case, the ratio of baryon density to photon density.

Combining all of these complementary probes is an extremely powerful way to study our universe. First of all, since different probes are sensitive to different combinations of cosmological parameters, combining two or more different measurements allows us to break the degeneracies between the parameters we want to measure. Furthermore, because each technique is subject to different systematic effects, we can use them as consistency checks. If two experiments disagree, it would be a sign that either there is some systematic effect that has not been accounted for or that our theoretical model is flawed. The fact that there is broad agreement over so many different experiments lends much stronger support to the standard cosmological model than any single experiment could ever do. In the following sections we describe two key probes – the cosmic microwave background and galaxy surveys – in some detail, and give a brief overview of other complementary techniques.

4.2.2 Galaxy surveys

The work in chapters 5 and 6 focuses on issues with using such surveys as cosmological tools, so we describe this particular cosmological probe in some detail here. The basic idea behind a galaxy survey is to map out the locations of galaxies over a large volume and use them as point tracers of the overall matter distribution in our universe. This provides a

way to observe the statistical properties of the large-scale structure predicted from the first order and higher order cosmological models discussed in §4.1.4 and §4.1.5.

Galaxy surveys come in two basic flavors: angular surveys and redshift surveys. Angular surveys identify galaxies over a large area of the sky, and thus only see the two-dimensional projection of the galaxy distribution. Redshift surveys, on the other hand, also measure spectra to obtain the redshift of each galaxy and thus its distance from us according to Hubble's law (equation (4.4)), which produces a three-dimensional map of galaxy locations. Recently a hybrid approach between these two types of surveys has become popular: photometric redshift surveys, whereby the redshift is estimated based on the photometric information from multiple wavelength bands of an angular survey. This provides rough measure of the distance that eliminates the need for time-consuming spectroscopy and the accuracy of the redshift estimation techniques is continuing to improve (Collister et al. 2007; Oyaizu et al. 2008; Banerji et al. 2007).

Furthermore, surveys can either be wide and shallow – covering a large area of the sky but only extending a modest distance from us, or narrow and deep – focusing on a small patch of sky for an extended time to find very faint and therefore extremely distant objects. Typical surveys strike a balance between these two choices that is optimal for a particular set of science goals.

Early observations

Astronomers have been interested in studying the distribution of galaxies since the time of Hubble (see, e.g., Hubble 1934; Carpenter 1938). The early angular catalogs studied were the Palomar (Abell 1959) and the Lick (Doughty et al. 1974) sky surveys, and redshifts of over 800 galaxies from various spectroscopic observations were collected in Humason et al. (1956). These early studies showed evidence for clumpiness in the overall distribution, although its exact nature was difficult to discern (see, e.g. Zwicky 1952; de Vaucouleurs 1958; Abell 1961). These observations inspired the theoretical work of Neyman and Scott (1952) which formed the seeds of the present-day halo model discussed in §4.1.5 as well as the first effort to compare observations with a simulated galaxy distribution (Scott et al. 1954).

The first true redshift survey was the Center for Astrophysics Redshift Survey (CfA; Huchra et al. 1983), which started in 1978 – prior to this only ~ 2000 galaxies had measured redshifts (da Costa 1999). This survey measured redshifts of the 2401 galaxies with an apparent Z -band magnitude brighter than $14.5 m_Z$. A slice through the CfA survey is shown in Fig. 4-2 This survey revealed that galaxies are distributed in a complex web of filaments, sheets, and voids.

Over the following decade a number of other surveys were undertaken, including the Southern Sky Redshift Survey (SSRS1; da Costa et al. 1991), surveys done by the Infrared Astronomy Satellite (IRAS; Strauss et al. 1992), the Automatic Plate Measurement angular survey (APM; Maddox et al. 1990a,b, 1996), and the Las Campanas Redshift Survey (LCRS; Shectman et al. 1996). Peacock and Dodds (1994) compiled power spectrum measurements from this generation of surveys and fit them with several cosmological models – they found that the data favored models with low matter density: $\Omega_M < 1$, in agreement with present day standard model. Further details on the history of this field can be found in da Costa (1999); Biviano (2000).

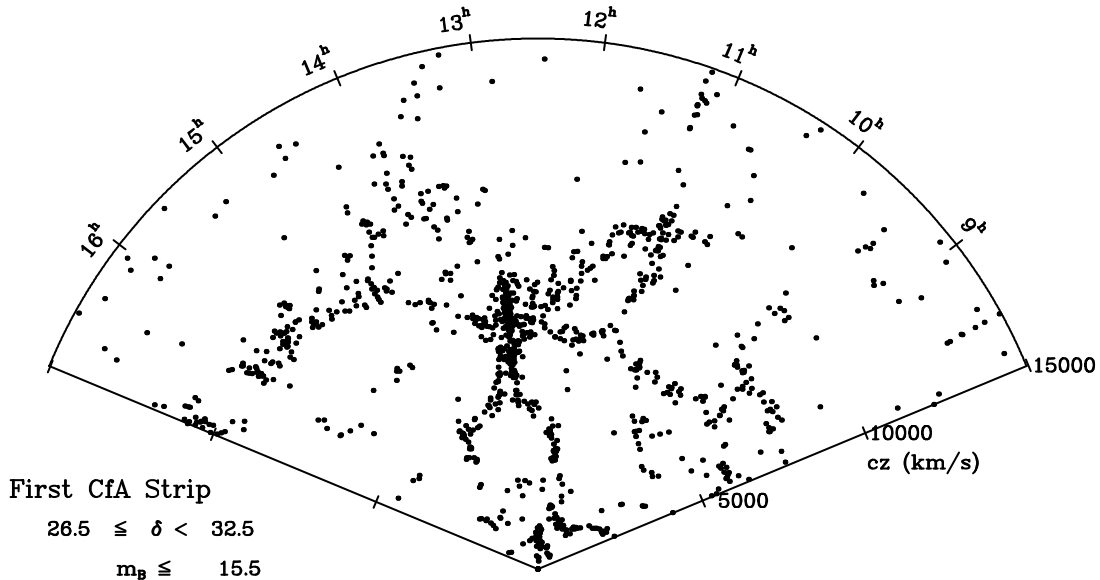


Figure 4-2 A slice through the CfA redshift survey (Huchra et al. 1983) done at the Smithsonian Astrophysical Observatory. Figure from <http://cfa-www.harvard.edu/~huchra/zcat/>.

Modern surveys

The current state of the art in galaxy survey cosmology is exemplified by two surveys: the Two Degree Field Galaxy Redshift Survey (2dFGRS; Colless et al. 2001, 2003) and the Sloan Digital Sky Survey (SDSS; York et al. 2000).

2dFGRS is a redshift survey that measured the redshifts of galaxies observed by the APM angular survey. Target galaxies with an apparent blue-band magnitude brighter than $b_J < 19.5$ were selected from APM's $5^\circ \times 5^\circ$ photographic plates and spectra were taken using the Two Degree Field system at the Anglo-Australian Telescope in New South Wales, Australia. This is a 4 meter telescope with a 2° field of view and a set of spectrographs which accept 400 optical fibers such that spectra of 400 objects in the field of view can be taken simultaneously. The redshift survey was completed in 2002 and took 272 nights over 5 years. It measured redshifts for 221,414 galaxies with a mean redshift of $z = 0.11$ and covered an area of about 1500 square degrees. A slice through the galaxy distribution measured by 2dFGRS is shown in Fig. 4-3.

SDSS, our source of data for the work in chapter 6, is the largest galaxy redshift survey to date, and is continuing to gather more data. It is being conducted using a dedicated 2.5 meter telescope at the Apache Point Observatory in New Mexico that has a 3° field of view and $\sim 1.4''$ (Gunn et al. 2006). The final SDSS data set will cover nearly 1/4 of the sky and have spectra of nearly 1 million galaxies and about 105,000 quasars (a.k.a. AGNs; see §2.3.2). The most recent data release, DR6, covers 17% of the sky and has 790,860 galaxies and 103,647 quasars.

The camera used for the photometric survey is a 5×6 array of CCDs arranged such that each of the 5 rows observes through a different filter, ranging from near-ultraviolet to near-infrared wavelengths (Fukugita et al. 1996; Gunn et al. 1998). The survey method used is known as drift-scanning: as the sky moves overhead due to the rotation of the Earth, points on the sky pass through each filter in succession. This produces a long strip of 6 scanlines

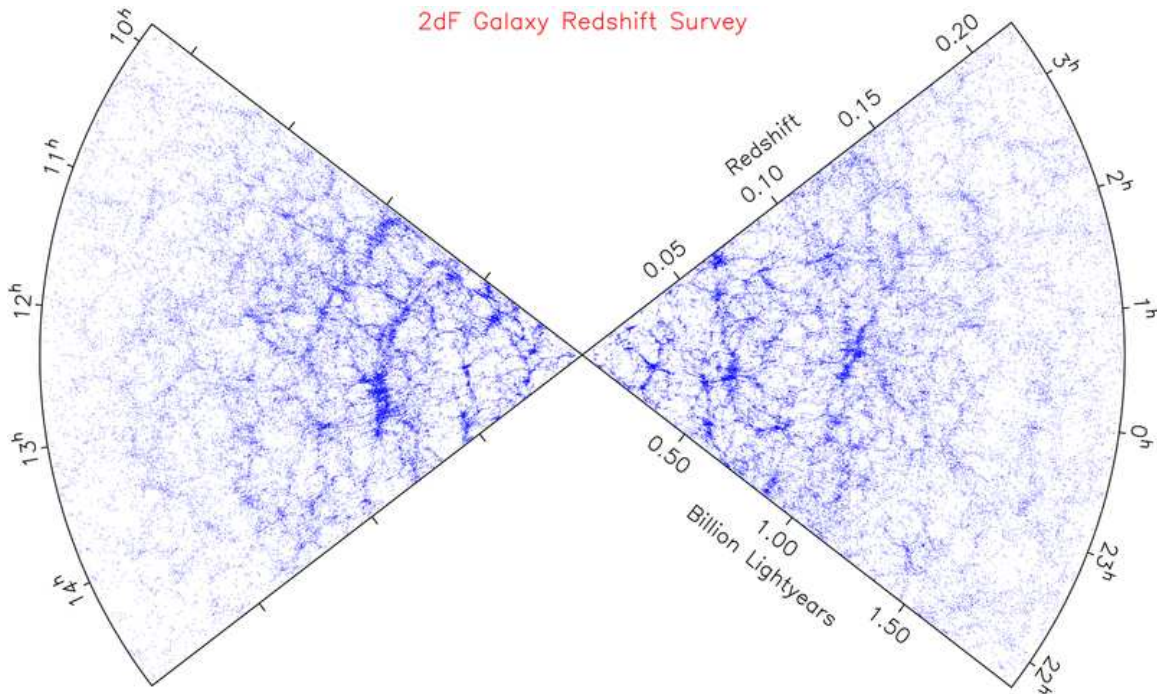


Figure 4-3 A slice through 2dFGRS (Colless et al. 2001, 2003). Figure from <http://www.mso.anu.edu.au/2dFGRS>.

across the sky with photometric data from all 5 filters simultaneously. It takes over 8 hours to scan a strip 130° long.

Based on this photometric information, targets are selected for the spectroscopic survey to obtain redshifts. There are several types of targets selected, including “main” galaxies, the luminous red galaxies (LRGs), quasars, and stars within our galaxy. The main galaxy sample includes all galaxies with an r -band apparent magnitude brighter than $r < 17.77$ – a typical galaxy at a redshift of $z = 0.1$ has $r = 17.5$. The brightest galaxies in the main sample can be seen out to a redshift of $z \sim 0.3$. This is the sample used in chapter 6. The LRG sample (Eisenstein et al. 2001) is a sparser sample extending to higher redshifts that contains only galaxies of a particular type: very luminous early-type elliptical galaxies. The LRGs is roughly volume-limited and extends to a redshift of $z \sim 0.5$. The properties of the LRG sample make it especially useful for certain types of cosmological measurements, such as the study discussed in §4.3.

SDSS spectroscopy is done using a pair of integral field spectrographs that can take up to 640 spectra simultaneously (Uomoto et al. 2004). This is done using 3° diameter aluminum plates drilled with holes at the locations of the targets and plugged with optical fiber cables which are fed into the spectrographs. Typically six to nine spectroscopic fields can be observed on a given night. Once a spectrum has been measured for a galaxy, its redshift can be determined by the positions of known spectral lines, and thus we know its three-dimensional location within the survey volume. A slice of the SDSS galaxy distribution is shown in Fig. 4-4.

Both 2dFGRS and SDSS have been extraordinarily valuable resources for the general scientific community, in large part because the data is made publicly available. The unprecedented volume mapped by these two surveys have revolutionized studies of large-scale

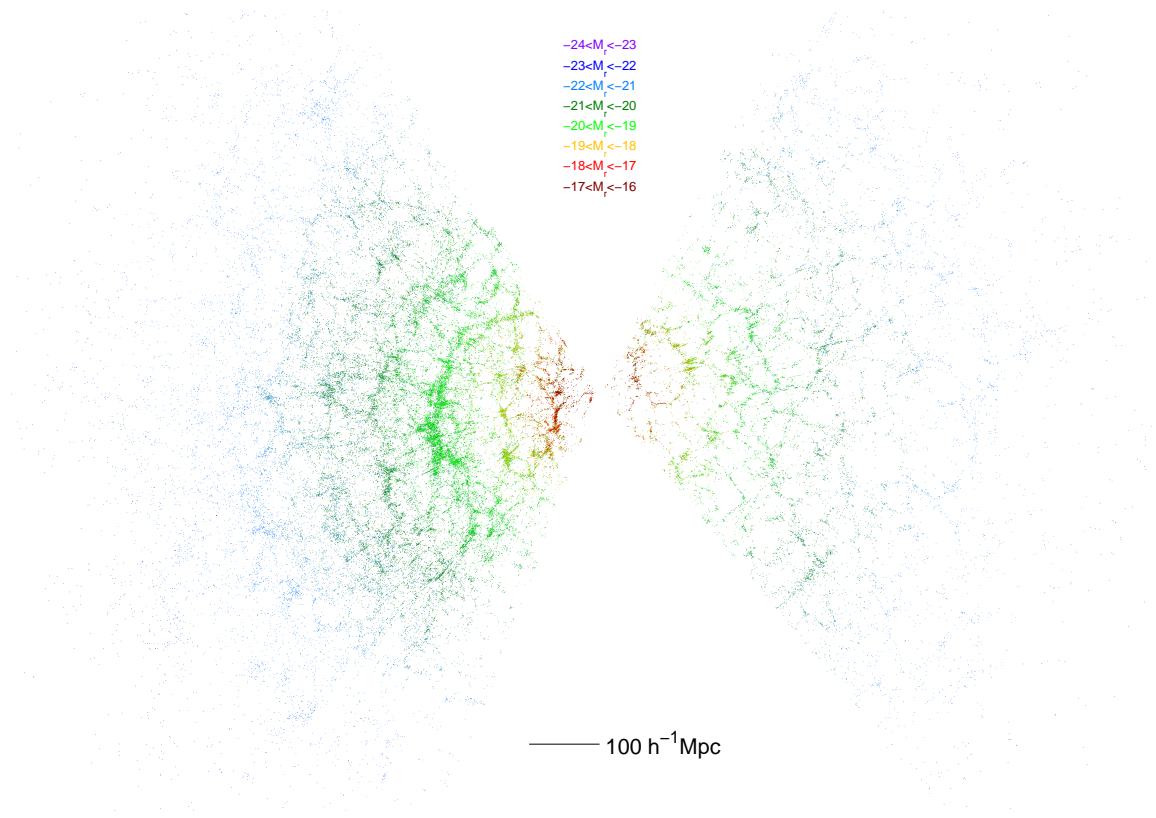


Figure 4-4 A slice through SDSS (York et al. 2000). The galaxies are colored according to their absolute r -band magnitude M_r , using the same luminosity bins as in chapter 6.

structure in our universe in many ways. One worth noting here is that the galaxy samples are now large enough that they can be reasonably divided up into subsets for more detailed analysis, as is done in chapter 6.

Other current surveys such as the 2-Micron All Sky Survey (2MASS; Huchra et al. 2005) and the second phase of the Deep Extragalactic Evolutionary Probe (DEEP2; Davis et al. 2003) have led to quite interesting cosmological results as well – we have focused on 2dFGRS and SDSS here because their balance on the wide and shallow versus narrow and deep spectrum is ideal for large-scale structure studies. However, the full-sky coverage of 2MASS provides of our nearby universe has been quite fruitful for matching local velocity flows to the mass density (Crook et al. 2007) and the high redshift data from DEEP2 allows us to measure the evolution of galaxy properties and clustering as well (Coil et al. 2008).

There are a number of upcoming surveys planned that will take this field another giant step forward. Starting in the next year or so, the Baryon Oscillation Spectroscopic Survey (BOSS; SDSS Collaboration 2007) will use the SDSS telescope with updated technology to target the baryon oscillation signal described in §4.2.4 and the Dark Energy Survey (DES; Dark Energy Survey Collaboration 2005) will perform a photometric redshift survey that will contain about 300 million galaxies. Further in the future are the Panoramic Survey Telescope and Rapid Response System (Pan-STARRS; Kaiser 2004) and the Large Synoptic Survey Telescope (LSST; Tyson 2002; Stubbs et al. 2004), which will operate with unprecedented speed, surveying the entire available sky several times each month, and the Wide-Field Multi-Object Spectrograph (WF MOS; Yamamoto et al. 2006), which will be able to take spectra of 20,000 galaxies every night.

On the theoretical side, it is important to be prepared for these upcoming surveys by understanding systematic effects such as nonlinear structure growth and galaxy bias so that we can extract as much cosmological information from them as possible. Galaxy surveys will continue to be an important probe as cosmology moves into a new era.

4.2.3 Cosmic microwave background

Galaxy surveys map out the present-day or relatively low redshift universe, so they are particularly well-complemented by probes of our universe’s early stages. Perhaps the richest source of information we have about the early universe comes from the leftover radiation from our universe’s hot and dense early phase, known as the cosmic microwave background (CMB). Measurements of the CMB are complementary to galaxy surveys that aim to map out our universe today because the CMB is essentially a snapshot of the early universe. Combining information from galaxy surveys and the CMB provides a way to break degeneracies between parameters and tighten the constraints on our theoretical model.

The basic physics behind this early universe snapshot is as follows: the early universe was filled with a plasma of protons and electrons coupled to photons in thermal equilibrium. The electrons were tightly coupled to the photons through Thomson scattering, and the protons are tightly coupled to the electrons through electromagnetic attraction, so these three components behave as a single fluid.

The dark matter, however, does not interact with baryons or light, so at this point it has already started to clump together under the influence of gravity around the seed fluctuations generated by inflation. The mass of the protons drags the baryon-photon fluid into the gravitational potential wells formed by the clumping dark matter, but the radiation pressure from the photons resists this infall. This process generates oscillations which propagate as sound waves through the baryon-photon plasma.

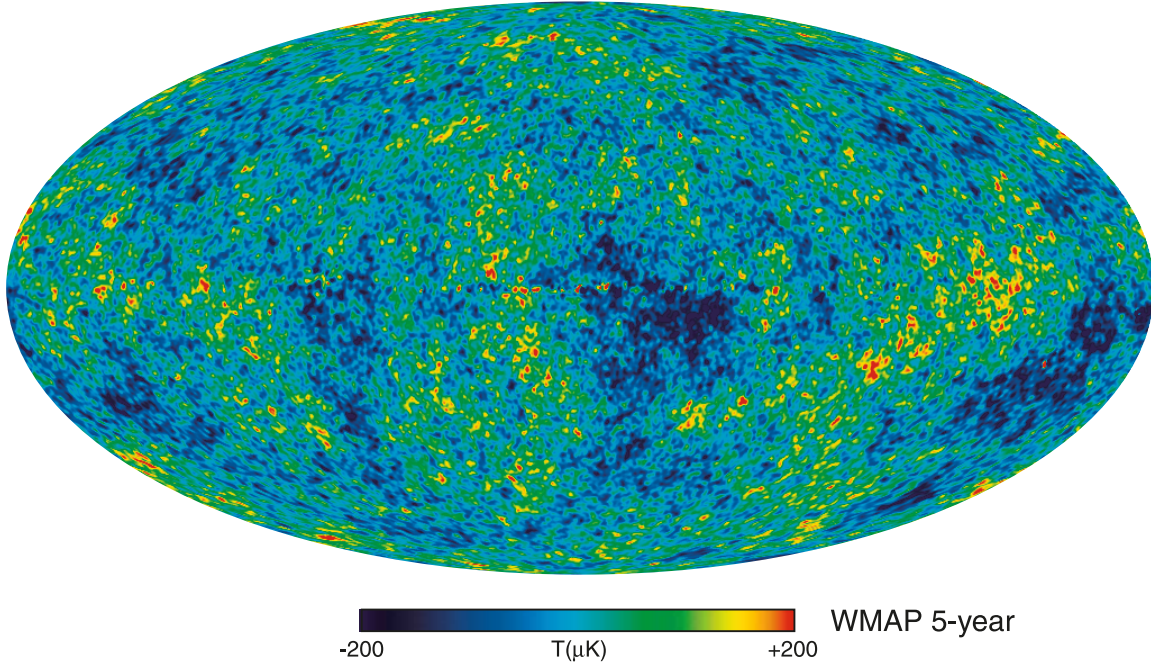


Figure 4-5 Temperature anisotropies in the CMB measured by the NASA/WMAP Science Team, shown in Hammer-Aitoff projection in Galactic coordinates. Reproduced from Hinshaw et al. (2008); used with permission.

As our universe continues to expand, it also cools, and when our universe is about 400,000 years old (0.003% of its current age), it became cool enough for the protons and electrons to combine into neutral hydrogen. At this point, the baryons and photons decouple from each other. The baryons are now free to collapse into the potential wells formed by the dark matter, and begin forming into stars and galaxies. The photons, on the other hand, free-stream through our universe and undergo (nearly) no further interactions from the time of decoupling until the present.

Today these CMB photons permeate our universe, and they have been redshifted to microwave wavelengths as our universe has expanded. Because they have traveled largely unimpeded since they decoupled, they provide a snapshot of the early universe at the moment of decoupling. This leftover glow from the hot and dense early universe has been observed to be essentially a perfect blackbody with a uniform temperature of 2.725K in all directions on the sky (Mather et al. 1994). This fact alone is extremely solid evidence for the basic picture of the standard cosmological model described in §4.1.2.

However, the true power of CMB observations lies in tiny deviations from this uniformity: the CMB anisotropies. The sound waves propagating through the plasma of the early universe create slight inhomogeneities in the density, which we can see as tiny variations in the CMB temperature at different points on the sky. Figure 4-5 shows the latest measurement of these anisotropies from the 5-year data release of the Wilkinson Microwave Anisotropy Probe(WMAP5; Hinshaw et al. 2008). Since the fluctuations at the time of decoupling are very small (1 part in 10^5), the first order cosmology described in §4.1.4 can provide extremely accurate predictions for the statistical properties of these anisotropies, namely their power spectrum.

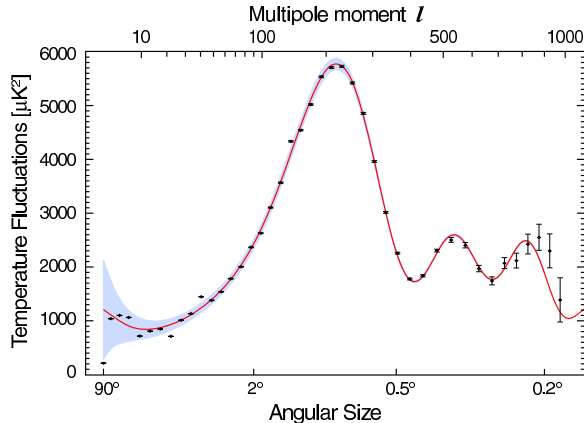


Figure 4-6 CMB angular power spectrum measured by the NASA/WMAP Science Team from the 5 year data release. This plot shows the average magnitude of the temperature deviations vs. their angular size on the sky. Reproduced from Hinshaw et al. (2008); used with permission.

To predict the power spectrum, we need only two basic physical assumptions: that we can apply general relativity to cosmological length scales and that our understanding of plasma physics is accurate under the conditions at the time of decoupling (a density of about 300 particles per cubic centimeter and temperature of about 3000K, within the range well-studied by solar physics). Figure 4-6 shows the prediction for the CMB power spectrum from the standard cosmological model to the power spectrum measured by WMAP5. The theoretical curve shown has only six free parameters defining its shape, and matches the data astonishingly well.

The six parameters describing the “vanilla” standard cosmological model are the baryon and cold dark matter fractions scaled by h^2 , i.e., $\Omega_b h^2$ and $\Omega_c h^2$, the dark energy fraction Ω_Λ , the power law parameters for the power spectrum of initial fluctuations A_s and n_s , and a nuisance parameter corresponding to the optical depth τ looking back through our universe to the point when the hydrogen atoms were reionized at a redshift of $z \sim 11$. In this simplest possible model that can match the data, neutrinos are assumed to be massless, dark energy is assumed to be a cosmological constant, our universe is assumed to be flat, and a handful of other assumptions are made as well. The measured shape of the CMB power spectrum provides tight constraints on the values of these parameters and also can be used to place limits on deviations from the vanilla model assumptions, e.g., massive neutrinos or dark energy with $w \neq -1$. Furthermore, measuring the polarization of the CMB provides another complementary source of information. (See de Oliveira-Costa 2005 for more details.)

4.2.4 Other probes

There are several other important cosmological probes that deserve mention here for completeness, although we will not focus on them in depth.

Perhaps the most important for the discovery of dark energy is the use of type Ia supernovae to trace the expansion of the universe. These stellar explosions are the result of a white dwarf star in a binary system accreting mass from its companion. Eventually the white dwarf will reach a critical mass, known as the Chandrasekhar limit, where that electron

degeneracy pressure can no longer support the stellar material. This triggers an extremely luminous explosion that can be seen at cosmological distances. Because the physics of these systems dictates that the explosion occurs at a particular mass, the resulting supernovae have sufficiently similar properties that they can be used as standard (or standardizable) candles: since we know their absolute brightness, measuring their apparent brightness tells us the distance. Thus by also measuring their redshift we can do zeroth order cosmology and effectively measure the scale factor $a(t)$ as a function of cosmic time. Cosmologists set out to do this expecting to measure the deceleration of the expansion rate due to gravity, but instead found that the expansion was accelerating (Riess et al. 1998; Perlmutter et al. 1999). This discovery provided the first evidence for dark energy and has induced a paradigm shift in cosmological thinking over the past decade.

Another key piece of evidence for the standard cosmological model comes from Big Bang nucleosynthesis studies. Our universe's hot dense early phase reached temperatures high enough to induce nuclear fusion of light elements, including deuterium, helium, and lithium. The fact that our universe is roughly 25% helium-4 by mass, too much to have been fused within stars, is by itself evidence that our universe was, in fact, once hot and dense. Furthermore, careful measurements of the abundances of deuterium, lithium, and helium-3 yield an estimate of the baryonic matter density that is both independent of the CMB results and in good agreement with them (Tytler et al. 1996; Steigman 2007).

Another class of cosmological probes focuses on tracing the present day (or low-redshift) matter distribution by means other than the galaxy redshift surveys discussed in §4.2.2. These include galaxy cluster surveys, gravitational lensing, and Lyman alpha absorption by cosmic gas clouds.

Galaxy cluster surveys aim to detect galaxy clusters – the largest gravitationally bound and equilibrated clumps of matter in our universe – via the X-ray emission of their hot gas (Haiman et al. 2005) their effect on the CMB (Hu et al. 2007), or other means, and measure their abundance as a function of mass. This provides a sensitive probe of nonlinear structure formation by is complicated by the difficulty of linking the cluster mass to its observable properties.

Gravitational lensing takes advantage of the general relativistic effect that mass bends light and aims to map out the mass distribution directly by studying the distortion of the light from distant objects. This has the advantage of dodging the issue of galaxy bias that plagues the interpretation of galaxy surveys, but is subject to other challenging systematic effects (Benabed and van Waerbeke 2004; Mandelbaum et al. 2005).

Measurements of Lyman alpha absorption study the light from distant AGNs that has passed through clumps of hydrogen along the way. Hydrogen at different redshifts will absorb light at the wavelength of the Lyman alpha spectral line of atomic hydrogen, creating a series of absorption lines known as the Lyman alpha forest which provides a one-dimensional map of the gas density along the line of sight. This probe of large-scale structure is sensitive to a somewhat higher redshift than current galaxy surveys, but it is constrained by the geometry of requiring an AGN backlight which makes it difficult to build up a true three-dimensional picture (Weinberg et al. 2003).

Finally, we mention two additional probes that are likely to be important in future cosmological pursuits: 21cm studies of the epoch of reionization and measuring baryon oscillations in the galaxy distribution. The epoch of reionization probes the time period partway between the time when the CMB was emitted and the time at which we observe the most distant astronomical objects. This era is known as the cosmological Dark Ages due to the lack of information we have about it. However, we do know that our universe went

through a phase of reionization when the first stars and galaxies began to shine, since most of the hydrogen is ionized today. There are several experiments currently in the construction or planning phases aiming to probe this era by detecting the 21cm emission line of neutral hydrogen redshifted to low radio frequencies (Terzian and Lazio 2006; Bowman et al. 2007; Falcke et al. 2007). These experiments will open a new window on our universe for cosmological studies.

We conclude our whirlwind tour of other cosmological probes by discussing baryon oscillations. The physics behind this probe is as follows: The overall matter distribution is determined primarily by dark matter, but the sound wave patterns of the baryon-photon plasma observed in the CMB leave an imprint of tiny wiggles in the matter power spectrum as well. These wiggles, called baryon oscillations, encode a characteristic length scale: the distance a sound wave traveled from the time of the Big Bang until decoupling. This length scale can be used as a standard ruler: since we know the physical size, measuring its apparent angular size on the sky tells us its distance from us. By measuring this length scale as a function of redshift using galaxy surveys, we can map out the expansion history of the universe and use it as a probe of zeroth order cosmology, which will hopefully provide insights about the nature of dark energy. Current measurements of the baryon oscillations at two redshifts (Eisenstein et al. 2005; Percival et al. 2007) have already proved to be a quite valuable constraint on cosmological parameters (Komatsu et al. 2008). However, the effects of nonlinear matter clustering and galaxy bias discussed in §4.1.5 complicate efforts to measure this standard ruler to high precision (Smith et al. 2007, 2008). Detailed studies of galaxy bias such as the one presented in chapter 6 can therefore help us more fully utilize this promising probe in the future.

4.3 Example: combining WMAP and SDSS

Combining CMB and galaxy survey data is a particularly powerful strategy: the early-universe snapshot of the CMB and the present-universe snapshot of the galaxy distribution provide complementary information that allows us to precisely constrain the parameters of the cosmological model describing the evolution from one state to the other. In this section we discuss one example of this: the combination of CMB data from the WMAP 3 year data release (WMAP3; Spergel et al. 2007) and the SDSS LRG sample from Data Release 4 (DR4; Adelman-McCarthy et al. 2006) analyzed in Tegmark et al. (2006). The goals of this analysis are twofold: first, measure the matter power spectrum $P(k)$ on scales large enough to avoid unfounded assumptions regarding nonlinear clustering and galaxy bias, and second, combine this $P(k)$ measurement with the CMB power spectrum measured by WMAP3 to constrain the parameters of the standard cosmological model.

4.3.1 Power spectrum estimation

The LRG galaxy sample has a number of features that make it ideal for measuring the galaxy power spectrum. First of all, its effective volume $V_{\text{eff}}(k)$ (as defined by Tegmark 1997) is larger by a factor of six than the SDSS main galaxy sample and over ten times larger than that of the 2dFGRS. The error bars on the power spectrum scale roughly as $\Delta P(k) \propto V_{\text{eff}}(k)^{-1/2}$, so the SDSS LRGs yield the smallest error bars. Additionally, since the LRGs are selected to be galaxies of a similar physical type, the effects of luminosity- and color-dependent bias explored in chapter 6 should not have a significant effect.

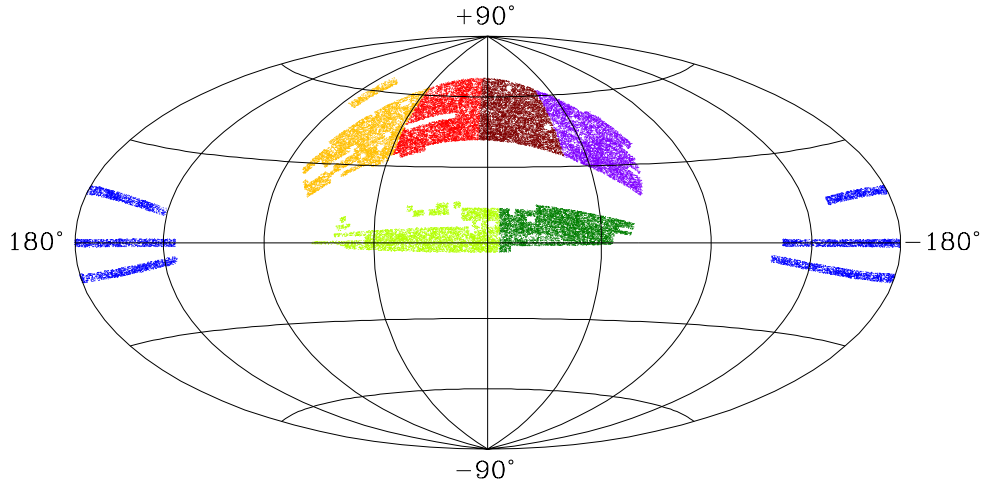


Figure 4-7 The angular distribution of the SDSS DR4 luminous red galaxies shown in Hammer-Aitoff projection in celestial coordinates, with the seven colors/greys indicating the seven angular subsamples analyzed in Tegmark et al. (2006) constructed with the MANGLE software discussed in chapter 5.

The angular distribution of the LRGs from DR4 is shown in Fig. 4-7. The regions of the sky containing the galaxies illustrate the area that has been covered by the SDSS spectroscopic survey at the time of DR4 – the task of managing such angular coverage masks is discussed in detail in chapter 5. Here we just note that the updated MANGLE software was used to create the masks for the angular subsamples shown in different colors in Fig. 4-7. The method used to calculate the power spectrum is the Pseudo Kahrunen-Loève (PKL) eigenmode method described in Tegmark et al. (2004b), which, among other advantages, produces uncorrelated error bars on the power spectrum. In order to speed up the computation time, the PKL method was applied separately on 21 subvolumes (the 7 angular subsets shown in Fig. 4-7 \times 3 radial subsets) and then combined with minimum variance weighting. Additionally, a global PKL analysis of the full data set was done to specifically target length scales larger than the individual subvolumes.

The measured power spectra for both the LRGs and the main sample galaxies are shown in Fig. 4-8. Theoretical predictions are also shown, both for linear theory (a.k.a. first order cosmology; see §4.1.4) and nonlinear theory (a.k.a. higher order cosmology; see §4.1.5). The particular flavor of nonlinear modeling used here is based on Eisenstein and Hu (1999); Cole et al. (2005); Eisenstein et al. (2007). The measured galaxy power spectrum is modeled as

$$P_g(k) = P_{\text{dewiggled}}(k) b^2 \frac{1 + Q_{\text{nl}} k^2}{1 + 1.4k}. \quad (4.56)$$

$P_{\text{dewiggled}}(k)$ models the damping of the baryon oscillations on small scales and is given by (Eisenstein et al. 2007)

$$P_{\text{dewiggled}}(k) = W(k) P(k) + [1 - W(k)] P_{\text{nowiggle}}(k), \quad (4.57)$$

where $P(k)$ is the linear theory power spectrum calculated using CMBFAST (Seljak and Zaldarriaga 1996), $P_{\text{nowiggle}}(k)$ is given by the baryon-free fitting formula in Eisenstein and Hu (1999), and $W(k) \equiv e^{-(k/k_*)^2/2}$ is a weighted averaging factor combining the two. This retains the wiggles on large scales and fades them out beginning around $k = k_*$. The wiggle suppression scale k_* is defined by $1/\sigma$, where $\sigma \equiv \sigma_{\perp}^{2/3} \sigma_{\parallel}^{1/3} (A_s/0.6841)^{1/2}$, σ_{\perp} and σ_{\parallel} are given by

equations (12) and (13) in Eisenstein et al. (2007), and A_s is the power law normalization for the primordial spectrum. The parameters b and Q_{nl} in equation (4.56) parameterize bias and nonlinear evolution respectively: b is the usual linear bias factor defined in §4.1.4, and increasing values of Q_{nl} indicate stronger nonlinear evolution. A_s is fixed by the CMB observations – b^2 characterizes the difference in normalization between what one predicts for the matter power spectrum given the CMB data and what is observed for the galaxy power spectrum.

The theoretical curves for linear theory shown as solid lines in Fig. 4-8 are calculated using the best-fit cosmological parameters from the WMAP3 CMB data alone (Spergel et al. 2007) plus a fit to the data for the normalization b^2 , giving $b = 1.9$ for the LRGs and $b = 1.1$ for the main galaxies relative to the predicted matter power spectrum. The nonlinear models shown as dashed lines again use the WMAP3 cosmological parameters, plus a fit for b and Q_{nl} , yielding $Q_{\text{nl}} = 4.6$ for the main galaxies and $Q_{\text{nl}} = 30$ for the LRGs. The models agree quite well with the data, which is a good indicator that the nonlinear modeling prescription outlined above captures the important effects, but also indicate that nonlinear evolution is quite strong for the LRGs and becomes important at larger scales. Tegmark et al. (2006) perform several tests to ensure that their cosmological results are not sensitive to the details of this largely empirically-based nonlinear modeling, but it is important to note that if we want to improve the precision with which future galaxy surveys can do cosmology, it will be essential to understand bias and nonlinear evolution on a deeper, more physics-based level – such work is currently underway (Smith et al. 2007; Nishimichi et al. 2007; Tinker et al. 2007; Zheng and Weinberg 2007; Taruya and Hiramatsu 2008; Crocce and Scoccimarro 2008; Smith et al. 2008).

4.3.2 Cosmological parameter estimation

With the galaxy power spectrum in hand, the next goal is to combine it with the WMAP3 CMB power spectrum to constrain cosmological parameters. For simplicity, only the LRG power spectrum on scales larger than $k \lesssim 0.2h/\text{Mpc}$ are used here.

The cosmological model is parameterized in terms of 12 standard parameters, plus the two nuisance parameters b and Q_{nl} from equation (4.56):

$$\mathbf{p} \equiv (\Omega_{\text{tot}}, \Omega_{\Lambda}, \omega_b, \omega_c, \omega_{\nu}, w, A_s, r, n_s, n_t, \alpha, \tau, b, Q_{\text{nl}}). \quad (4.58)$$

Table 4.1 defines these 14 parameters and another 45 that can be derived from them; in essence, $(\Omega_{\text{tot}}, \Omega_{\Lambda}, \omega_b, \omega_c, \omega_{\nu}, w)$ define the cosmic matter budget, $(A_s, n_s, \alpha, r, n_t)$ specify the seed fluctuations and (τ, b, Q_{nl}) are nuisance parameters. The “vanilla” model, i.e., the minimal model parametrized by $(\Omega_{\Lambda}, \omega_b, \omega_c, A_s, n_s, \tau, b, Q_{\text{nl}})$, setting $\omega_{\nu} = \alpha = r = n_t = 0$, $\Omega_{\text{tot}} = 1$ and $w = -1$, is the smallest subset of our parameters that provides a good fit to the WMAP plus LRG data – this is the same vanilla model discussed in §4.2.3 with the addition of b and Q_{nl} . Constraints on these parameters from the WMAP plus LRG data were computed using the Monte Carlo Markov Chain (MCMC) approach (Metropolis et al. 1953; Hastings 1970; Gilks et al. 1996; Christensen et al. 2001; Lewis and Bridle 2002; Slosar and Hobson 2003; Verde et al. 2003) as implemented in Tegmark et al. (2004a). The best-fit parameter values and their uncertainties are shown in Table 4.1 – more details about the assumptions that have gone into these parameter estimations as well as tests of how robust these constraints are to these assumptions can be found in Tegmark et al. (2006).

Table 4.1 Cosmological parameters measured from WMAP and SDSS LRG data, reproduced from Tegmark et al. (2006). References cited in the table are C05 (Cole et al. 2005), KT (Kolb and Turner 1990), H05 (Hu 2005), T94 (Tegmark et al. 1994), T98 (Tegmark and Rees 1998), T05 (Tegmark et al. 2005), and H01 (Hu et al. 2001).

Parameter	Value	Meaning	Definition
Matter budget parameters:			
Ω_{tot}	$1.003^{+0.010}_{-0.009}$	Total density/critical density	$\Omega_{\text{tot}} = \Omega_m + \Omega_\Lambda = 1 - \Omega_k$
Ω_Λ	$0.761^{+0.017}_{-0.018}$	Dark energy density parameter	$\Omega_\Lambda \approx h^{-2} \rho_\Lambda (1.88 \times 10^{-26} \text{ kg/m}^3)$
ω_b	$0.0222^{+0.0007}_{-0.0007}$	Baryon density	$\omega_b = \Omega_b h^2 \approx \rho_b / (1.88 \times 10^{-26} \text{ kg/m}^3)$
ω_c	$0.1050^{+0.0041}_{-0.0040}$	Cold dark matter density	$\omega_c = \Omega_c h^2 \approx \rho_c / (1.88 \times 10^{-26} \text{ kg/m}^3)$
ω_ν	< 0.010 (95%)	Massive neutrino density	$\omega_\nu = \Omega_\nu h^2 \approx \rho_\nu / (1.88 \times 10^{-26} \text{ kg/m}^3)$
w	$-0.941^{+0.087}_{-0.101}$	Dark energy equation of state	$\rho_\Lambda / \rho_\Lambda$ (approximated as constant)
Seed fluctuation parameters:			
A_s	$0.690^{+0.045}_{-0.044}$	Scalar fluctuation amplitude	Primordial scalar power at $k = 0.05/\text{Mpc}$
r	< 0.30 (95%)	Tensor-to-scalar ratio	Tensor-to-scalar power ratio at $k = 0.05/\text{Mpc}$
n_s	$0.953^{+0.016}_{-0.016}$	Scalar spectral index	Primordial scalar spectral index at $k = 0.05/\text{Mpc}$
$n_t + 1$	$0.9861^{+0.0096}_{-0.0142}$	Tensor spectral index	$n_t = -r/8$ assumed
α	$-0.040^{+0.027}_{-0.027}$	Running of spectral index	$\alpha = dn_s/d \ln k$ (approximated as constant)
Nuisance parameters:			
τ	$0.087^{+0.028}_{-0.030}$	Reionization optical depth	
b	$1.896^{+0.074}_{-0.069}$	Galaxy bias factor	$b = [P_{\text{gal}}(k)/P(k)]^{1/2}$ on large scales, where $P(k)$ refers to today.
Q_{nl}	$30.3^{+4.4}_{-4.1}$	Nonlinear correction parameter [C05]	$P_{\text{g}}(k) = P_{\text{dewiggled}}(k)b^2(1 + Q_{\text{nl}}k^2)/(1 + 1.7k)$
Other popular parameters (determined by those above):			
h	$0.730^{+0.019}_{-0.019}$	Hubble parameter	$h = \sqrt{(\omega_b + \omega_c + \omega_\nu)/(\Omega_{\text{tot}} - \Omega_\Lambda)}$
Ω_m	$0.239^{+0.018}_{-0.017}$	Matter density/critical density	$\Omega_m = \Omega_{\text{tot}} - \Omega_\Lambda$
Ω_b	$0.0416^{+0.0019}_{-0.0018}$	Baryon density/critical density	$\Omega_b = \omega_b/h^2$
Ω_c	$0.197^{+0.016}_{-0.015}$	CDM density/critical density	$\Omega_c = \omega_c/h^2$
Ω_ν	< 0.024 (95%)	Neutrino density/critical density	$\Omega_\nu = \omega_\nu/h^2$
Ω_k	$-0.0030^{+0.0095}_{-0.0102}$	Spatial curvature	$\Omega_k = 1 - \Omega_{\text{tot}}$
ω_m	$0.1272^{+0.0044}_{-0.0043}$	Matter density	$\omega_m = \omega_b + \omega_c + \omega_\nu = \Omega_m h^2$
f_ν	< 0.090 (95%)	Dark matter neutrino fraction	$f_\nu = \rho_\nu/\rho_d$
A_t	< 0.21 (95%)	Tensor fluctuation amplitude	$A_t = rA_s$
M_ν	< 0.94 (95%) eV	Sum of neutrino masses	$M_\nu \approx (94.4 \text{ eV}) \times \omega_\nu$ [KT]
$A_{.002}$	$0.801^{+0.042}_{-0.043}$	WMAP3 normalization parameter	A_s scaled to $k = 0.002/\text{Mpc}$: $A_{.002} = 25^{1-n_s} A_s$ if $\alpha = 0$
$r_{.002}$	< 0.33 (95%)	Tensor-to-scalar ratio (WMAP3)	Tensor-to-scalar power ratio at $k = 0.002/\text{Mpc}$
σ_8	$0.756^{+0.035}_{-0.035}$	Density fluctuation amplitude	$\sigma_8 = \{4\pi \int_0^\infty [\frac{3}{x^3} (\sin x - x \cos x)]^2 P(k) \frac{k^2 dk}{(2\pi)^3}\}^{1/2}$, $x \equiv k \times 8h^{-1} \text{ Mpc}$
$\sigma_8 \Omega_m^{0.6}$	$0.320^{+0.024}_{-0.023}$	Velocity fluctuation amplitude	
Cosmic history parameters:			
z_{eq}	3057^{+103}_{-102}	Matter-radiation Equality redshift	$z_{\text{eq}} \approx 24074\omega_m - 1$
z_{rec}	$1090.25^{+0.93}_{-0.91}$	Recombination redshift	$z_{\text{rec}}(\omega_m, \omega_b)$ given by eq. (18) of [H05]
z_{ion}	$11.1^{+2.2}_{-2.7}$	Reionization redshift (abrupt)	$z_{\text{ion}} \approx 92 \left(\frac{0.03h\tau}{\omega_b}\right)^{2/3} \Omega_m^{1/3}$ (assuming abrupt reionization [T94])
z_{acc}	$0.855^{+0.059}_{-0.059}$	Acceleration redshift	$z_{\text{acc}} = [(-3w - 1)\Omega_\Lambda/\Omega_m]^{-1/3} w - 1$ if $w < -1/3$
t_{eq}	$0.0634^{+0.0045}_{-0.0041}$ Myr	Matter-radiation Equality time	$t_{\text{eq}} \approx (9.778 \text{ Gyr}) \times h^{-1} \int_{z_{\text{eq}}}^\infty [H_0/H(z)(1+z)] dz$ [KT]
t_{rec}	$0.3856^{+0.0040}_{-0.0040}$ Myr	Recombination time	$t_{\text{rec}} \approx (9.778 \text{ Gyr}) \times h^{-1} \int_{z_{\text{rec}}}^\infty [H_0/H(z)(1+z)] dz$ [KT]
t_{ion}	$0.43^{+0.20}_{-0.10}$ Gyr	Reionization time	$t_{\text{ion}} \approx (9.778 \text{ Gyr}) \times h^{-1} \int_{z_{\text{ion}}}^\infty [H_0/H(z)(1+z)] dz$ [KT]
t_{acc}	$6.74^{+0.25}_{-0.24}$ Gyr	Acceleration time	$t_{\text{acc}} \approx (9.778 \text{ Gyr}) \times h^{-1} \int_{z_{\text{acc}}}^\infty [H_0/H(z)(1+z)] dz$ [KT]
t_{now}	$13.76^{+0.15}_{-0.15}$ Gyr	Age of Universe now	$t_{\text{now}} \approx (9.778 \text{ Gyr}) \times h^{-1} \int_0^\infty [H_0/H(z)(1+z)] dz$ [KT]
Fundamental parameters (independent of observing epoch):			
Q	$1.945^{+0.051}_{-0.053} \times 10^{-5}$	Primordial fluctuation amplitude	$Q = \delta_h \approx A_{.002}^{1/2} \times 59.2384 \mu\text{K}/T_{\text{CMB}}$
κ	$1.3^{+3.7}_{-4.3} \times 10^{-61}$	Dimensionless spatial curvature [T98]	$\kappa = (hc/k_B T_{\text{CMB}} \alpha)^2 k$
ρ_Λ	$1.48^{+0.11}_{-0.11} \times 10^{-123} \rho_{\text{Pl}}$	Dark energy density	$\rho_\Lambda \approx h^2 \Omega_\Lambda \times (1.88 \times 10^{-26} \text{ kg/m}^3)$
ρ_{halo}	$6.6^{+1.2}_{-1.0} \times 10^{-123} \rho_{\text{Pl}}$	Halo formation density	$\rho_{\text{halo}} = 18\pi^2 Q^3 \xi^4$
ξ	$3.26^{+0.11}_{-0.11}$ eV	Matter mass per photon	$\xi = \rho_m/n_\gamma$
ξ_b	$0.569^{+0.018}_{-0.018}$ eV	Baryon mass per photon	$\xi_b = \rho_b/n_\gamma$
ξ_c	$2.69^{+0.11}_{-0.10}$ eV	CDM mass per photon	$\xi_c = \rho_c/n_\gamma$
ξ_ν	< 0.26 (95%) eV	Neutrino mass per photon	$\xi_\nu = \rho_\nu/n_\gamma$
η	$6.06^{+0.20}_{-0.19} \times 10^{-10}$	Baryon/photon ratio	$\eta = n_b/n_\gamma = \xi_b/m_p$
A_Λ	2077^{+135}_{-125}	Expansion during matter domination	$(1 + z_{\text{eq}})(\Omega_m/\Omega_\Lambda)^{1/3}$ [T05]
σ_{gal}^*	$0.561^{+0.024}_{-0.023} \times 10^{-3}$	Seed amplitude on galaxy scale	Like σ_8 but on galactic ($M = 10^{12} M_\odot$) scale early on
CMB phenomenology parameters:			
A_{peak}	$0.579^{+0.013}_{-0.013}$	Amplitude on CMB peak scales	$A_{\text{peak}} = A_s e^{-2\tau}$
A_{pivot}	$0.595^{+0.012}_{-0.011}$	Amplitude at pivot point	A_{peak} scaled to $k = \frac{0.028}{\text{Mpc}}$. $A_{\text{pivot}} = 0.56^{n_s-1} A_{\text{peak}}$ if $\alpha = 0$
H_1	$4.88^{+0.37}_{-0.34}$	1st CMB peak ratio	$H_1(\Omega_{\text{tot}}, \Omega_\Lambda, \omega_b, \omega_m, w, n_s, \tau)$ given by [H01]
H_2	$0.4543^{+0.0051}_{-0.0051}$	2nd to 1st CMB peak ratio	$H_2 = \frac{(0.925\omega_m^{0.18} 2.4^{n_s-1})}{[1+(\omega_b/0.0164)12\omega_m^{0.32}]0.2}$ [H01]
H_3	$0.4226^{+0.0088}_{-0.0088}$	3rd to 1st CMB peak ratio	$H_3 = \frac{2.17[1+(\omega_b/0.044)^2] - 1 \omega_m^{0.59} 3.6^{n_s-1}}{1+1.63(1-\omega_b/0.071)\omega_m}$
$d_A(z_{\text{rec}})$	$14.30^{+0.17}_{-0.17}$ Gpc	Comoving ang. diam. dist. to CMB	$d_A(z_{\text{rec}}) = \frac{r_s}{H_0} \sinh \left[\Omega_k^{1/2} \int_0^{z_{\text{rec}}} [H_0/H(z)] dz \right] / \Omega_k^{1/2}$ [KT]
$r_s(z_{\text{rec}})$	$0.1486^{+0.0014}_{-0.0014}$ Gpc	Comoving sound horizon scale	$r_s(\omega_m, \omega_b)$ given by eq. (22) of [H05]
r_{damp}	$0.0672^{+0.0009}_{-0.0008}$ Gpc	Comoving acoustic damping scale	$r_{\text{damp}}(\omega_m, \omega_b)$ given by eq. (26) of [H05]
Θ_s	$0.5918^{+0.0020}_{-0.0020}$	CMB acoustic angular scale fit ($^\circ$)	$\Theta_s(\Omega_{\text{tot}}, \Omega_\Lambda, w, \omega_b, \omega_m)$ given by [H01]
ℓ_A	$302.2^{+1.0}_{-1.0}$	CMB acoustic angular scale	$\ell_A = \pi d_A(z_{\text{rec}})/r_s(z_{\text{rec}})$

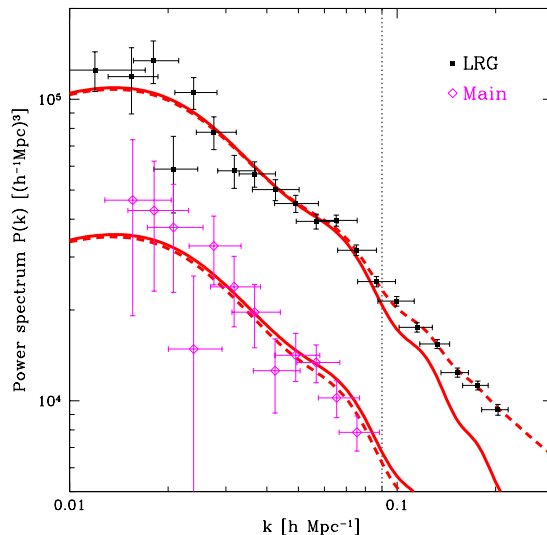


Figure 4-8 Measured power spectra for the full LRG and main galaxy samples, reproduced from Tegmark et al. (2006). The solid curves correspond to the linear theory cosmological model fits to WMAP3 alone from Table 5 of Spergel et al. (2007), normalized to galaxy bias $b = 1.9$ (top) and $b = 1.1$ (bottom) relative to the $z = 0$ matter power. The dashed curves include the nonlinear correction of Cole et al. (2005) for $A = 1.4$, with $Q_{\text{nl}} = 30$ for the LRGs and $Q_{\text{nl}} = 4.6$ for the main galaxies; see equation (4.56). The onset of nonlinear corrections is clearly visible for $k \gtrsim 0.09h/\text{Mpc}$ (vertical line).

The parameter constraints provided by any given experiment define an allowed region within the N -dimensional parameter space (where N is the number of parameters) that can be quite complicated and may have degeneracies between some parameters – for example, CMB data constrains $\omega_m \equiv \Omega_m h^2$ quite tightly but gives only weak constraints on Ω_m and h individually. A common way to illustrate this is to choose two parameters and plot the constraints in a two-dimensional plane. Such plots illustrate how combining different data sets breaks various parameter degeneracies, as discussed in depth in Tegmark et al. (2006).

As an example here, we show just one of these plots in Fig. 4-9 that is particularly relevant for particle physics: the constraints on the dark matter fraction ω_d and the fraction f_ν of the dark matter that is composed of neutrinos. This plot shows that the first year WMAP data (WMAP1; Spergel et al. 2003) only constrains ω_d without saying anything about neutrinos, and the WMAP3 data indicates that at most about 20% of the dark matter mass could be neutrinos. Adding the SDSS LRG data tightens the constraints still further, allowing only about 10% of the dark matter to be neutrinos. Assuming that there are no sterile neutrinos, this implies a constraint that the mass of any neutrino must be less than $\sim 0.3\text{eV}$. This is comparable to the sensitivity of the KATRIN particle physics experiment currently being conducted to measure the mass of the electron neutrino via tritium beta decay (Lobashev 2003). Thus by looking at distant galaxies and the radiation that fills our universe, we can do some extremely interesting and relevant particle physics.

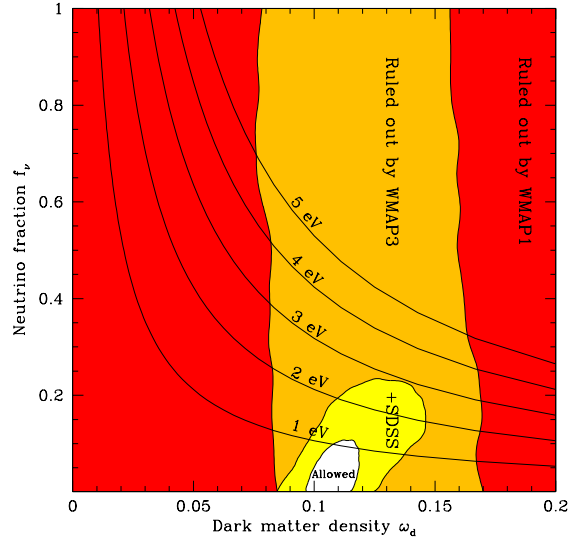


Figure 4-9 95% constraints in the (ω_d, f_ν) plane, reproduced from Tegmark et al. (2006). The large shaded regions are ruled out by WMAP1 (red/dark grey) and WMAP3 (orange/grey) when neutrino mass is added to the 6 vanilla parameters. The yellow/light grey region is ruled out when adding SDSS LRG information. The five curves correspond to M_ν , the sum of the neutrino masses, equaling 1, 2, 3, 4 and 5 eV respectively – barring sterile neutrinos, no neutrino can have a mass exceeding $\sim M_\nu/3 \approx 0.3$ eV (95%).

4.4 Issues with using galaxies as cosmic tracers

Measuring the distribution of galaxy clustering has proved to be an extremely powerful tool for measuring cosmological parameters. However, there are still issues, both practical and theoretical, that need to be addressed in order to optimally extract cosmological information from the next generation of galaxy surveys. The following two chapters focus on two of these issues: chapter 5 addresses the technical matter of managing angular masks defining the survey area on the sky, and chapter 6 addresses the more fundamental question of understanding how closely galaxies trace the underlying matter distribution.

4.4.1 Managing angular masks of galaxy surveys

As galaxy surveys become larger and more complex, keeping track of the completeness, magnitude limit, and other survey parameters as a function of direction on the sky becomes an increasingly challenging computational task. For example, typical angular masks of SDSS contain about $N = 300,000$ distinct spherical polygons. Managing masks with such large numbers of polygons becomes intractably slow, particularly for tasks that run in time $\mathcal{O}(N^2)$ with a naive algorithm, such as finding which polygons overlap each other. In chapter 5, we present a “divide-and-conquer” solution to this challenge: we first split the angular mask into predefined regions called “pixels,” such that each polygon is in only one pixel, and then perform further computations, such as checking for overlap, on the polygons within each pixel separately. This reduces $\mathcal{O}(N^2)$ tasks to $\mathcal{O}(N)$, and also reduces the important task of determining in which polygon(s) a point on the sky lies from $\mathcal{O}(N)$ to $\mathcal{O}(1)$, resulting in significant computational speedup.

Additionally, we present a method to efficiently convert any angular mask to and from the popular *HEALPix* format. This method can be generically applied to convert to and from any desired spherical pixelization. We have implemented these techniques in a new version of the MANGLE software package, which is freely available at <http://space.mit.edu/home/tegmark/mangle/>, along with complete documentation and example applications. These new methods should prove quite useful to the astronomical community, and since MANGLE is a generic tool for managing angular masks on a sphere, it has the potential to benefit terrestrial mapmaking applications as well.

4.4.2 Relative galaxy bias

Differences in clustering properties between galaxy subpopulations complicate the cosmological interpretation of the galaxy power spectrum, but can also provide insights about the physics underlying galaxy formation. Chapter 6 details a study of the nature of this relative clustering in which we perform a counts-in-cells analysis of galaxies in SDSS to measure the relative bias between pairs of galaxy subsamples of different luminosities and colors. We use a generalized χ^2 test to determine if the relative bias between each pair of subsamples is consistent with the simplest deterministic linear bias model, and we also use a maximum likelihood technique to further understand the nature of the relative bias between each pair.

We find that the simple, deterministic model is a good fit for the luminosity-dependent bias on scales above $\sim 2 h^{-1}\text{Mpc}$, which is good news for using magnitude-limited surveys for cosmology. However, the color-dependent bias shows evidence for stochasticity and/or non-linearity which increases in strength toward smaller scales, in agreement with previous studies of stochastic bias. Also, confirming hints seen in earlier work, the luminosity-dependent bias for red galaxies is significantly different from that of blue galaxies: both luminous and dim red galaxies have higher bias than moderately bright red galaxies, whereas the biasing of blue galaxies is not strongly luminosity-dependent. These results can be used to constrain galaxy formation models and also to quantify how the color and luminosity selection of a galaxy survey can impact measurements of the cosmological matter power spectrum.

Chapter 5

Methods for rapidly processing angular masks of next-generation galaxy surveys

This chapter is adapted from the paper “Methods for rapidly processing angular masks of next-generation galaxy surveys” by Molly E. C. Swanson, Max Tegmark, Andrew J. S. Hamilton, and J. Colin Hill, which has been accepted for publication in the *Monthly Notices of the Royal Astronomical Society* (Swanson et al. 2007).

5.1 Introduction

Over the past few decades, galaxy surveys have provided a wealth of information about the large-scale structure of our Universe, and the next generation of surveys currently being planned promises to provide even more insight. In order to realize the full potential of upcoming surveys, it is essential to avoid unnecessary errors and approximations in the way they are analyzed. The tremendous volumes of data produced by these new surveys will shrink statistical uncertainty to unprecedented levels, and in order to take advantage of this we must ensure that the systematic uncertainties can keep pace. The purpose of this chapter is to maximize the scientific utility of next-generation surveys by providing methods for processing angular masks as rapidly and accurately as possible.

Angular masks of a galaxy survey are functions of direction on the sky that model the survey completeness, magnitude limit, seeing, dust extinction, or other parameters that vary across the sky. The earliest galaxy redshift surveys – the first Center for Astrophysics redshift survey (CfA1; Huchra et al. 1983) and the first Southern Sky Redshift Survey (SSRS1; da Costa et al. 1991) – had simple angular masks defined by boundaries in declination and Galactic latitude. The next generation of surveys – IRAS (Strauss et al. 1992) and PCSz (Saunders et al. 2000) – had somewhat more complex masks, with some regions of high contamination excluded from the survey.

The present generation of surveys – the Two Degree Field Galaxy Redshift Survey (2dFGRS; Colless et al. 2001, 2003) and the Sloan Digital Sky Survey (SDSS; York et al. 2000) – consist of photometric surveys that identify galaxies and measure their angular positions combined with spectroscopic surveys that measure a redshift for each galaxy to determine its distance from us. Angular masks are useful for describing parameters for

both photometric and spectroscopic surveys – for example, seeing and magnitude limit are key parameters to model in photometric surveys, and the survey completeness – i.e., the fraction of photometrically selected target galaxies for which a spectrum has been measured – is vital for analyzing spectroscopic surveys.

The angular masks of SDSS and 2dFGRS consist of circular fields defined by the spectroscopic plates of the redshift survey superimposed on an angular mask of the parent photometric survey. 2dFGRS uses the Automatic Plate Measurement (APM) survey (Maddox et al. 1990a,b, 1996) as its parent photometric survey and covers approximately 1500 square degrees. The APM angular mask consists of 269 $5^\circ \times 5^\circ$ photographic plates which are drilled with numerous holes to avoid bright stars, satellite trails, plate defects, and so forth. Combining the photographic plates, holes, and spectroscopic fields gives a total of 3525 polygons that define the spectroscopic angular mask of 2dFGRS.

The SDSS covers a larger area on the sky – 5740 square degrees in Data Release 5 (DR5; Adelman-McCarthy et al. 2007) – and has a yet more complicated angular mask than 2dFGRS. The SDSS photometric survey is done by drift-scanning: each scan across the sky covers six long, narrow scanlines, and the gaps between these lines are filled in with a second scan slightly offset from the first, producing a “stripe” about 2.5° wide assembled from 12 scanlines. In addition to the fairly intricate pattern produced by this scanning strategy, there are nearly 250,000 holes masked out of the photometric survey for various reasons, plus the circular 3° spectroscopic fields. Combining all of these elements produces an angular mask for the spectroscopic survey that contains 340,351 polygons.

To accurately manage the 2dFGRS and SDSS angular masks, Hamilton and Tegmark (2004) developed a suite of general-purpose software called MANGLE, which performs several important procedures on angular masks using computational methods detailed in Hamilton (1993a,b). This software has proved to be a valuable resource to the astronomical community: it has been used in several analyses of galaxy survey data (Tegmark et al. 2002, 2004b; Mandelbaum et al. 2005; Hikage et al. 2005; Park et al. 2005; Conroy et al. 2005; Park et al. 2007; Nishimichi et al. 2007; Shen et al. 2007; Wang et al. 2007; Tinker et al. 2007). Additionally, it was used extensively in the preparation of the New York University Value-Added Galaxy Catalog (NYU-VAGC; Blanton et al. 2005b), which has been used as the basis for almost all publications on large-scale structure by the SDSS collaboration.

However, many of functions in the original version of MANGLE run in $\mathcal{O}(N^2)$ time, which becomes quite computationally challenging as the size and complexity of surveys continues to increase – computations involving the SDSS mask can take several months of CPU time. In this chapter we present new algorithms that can process complicated angular masks such as SDSS dramatically faster with no loss of accuracy. Our method is based on splitting an angular mask into pixels, reducing the processing time to $\mathcal{O}(N)$ by adding an $\mathcal{O}(N \log N)$ preprocessing step. Similar methods based on hierarchical spatial subdivisions have been found to be useful in the field of computational geometry (see, e.g., Goodman and O’Rourke 2004), but have not previously been applied to angular masks in an astronomy context.

This will be especially useful for next-generation surveys, such as the Dark Energy Survey (DES; Dark Energy Survey Collaboration 2005) and surveys done with the Wide-Field Multi-Object Spectrograph (WF MOS; Yamamoto et al. 2006; Glazebrook et al. 2006), the Panoramic Survey Telescope and Rapid Response System (Pan-STARRS; Kaiser 2004), and the Large Synoptic Survey Telescope (LSST; Tyson 2002; Stubbs et al. 2004; Tyson 2006; LSST Collaboration 2006). DES, Pan-STARRS, and LSST will perform photometric surveys and use techniques for estimating redshifts based on the photometric information; WF MOS will perform spectroscopic surveys using one of the upcoming photometric sur-

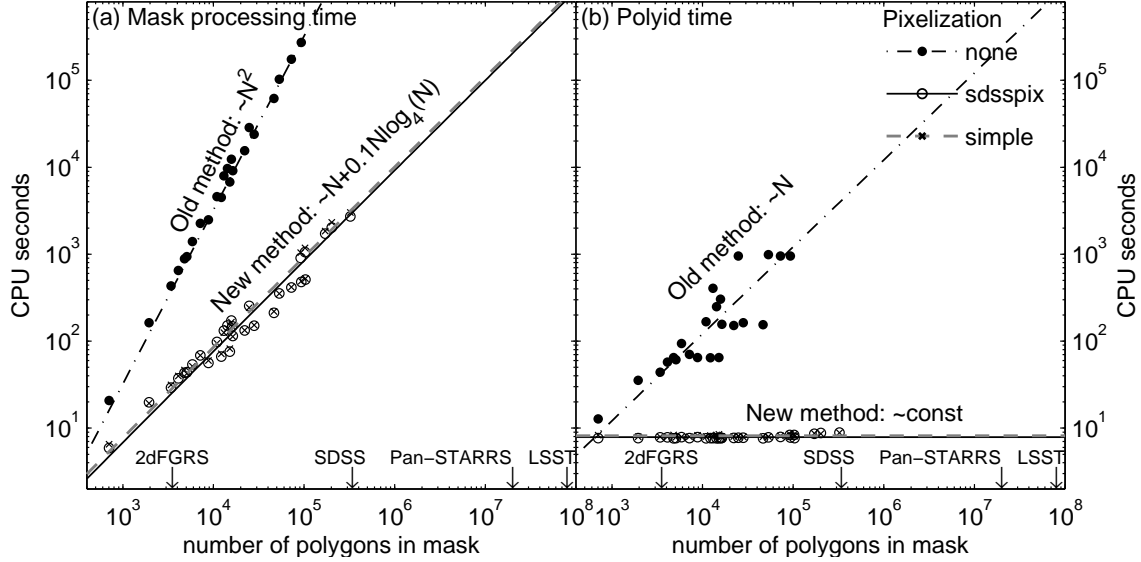


Figure 5-1 Speed trials for a series of portions of the SDSS DR5 mask with and without pixelization. (a) Time required for pixelization, snapping, balkanization and unification of the mask. (b) Time required to identify in which polygon each of the $\sim 400,000$ SDSS DR5 galaxies lies. Each set of trials is fitted with a power law to show how the processing time scales with the number of polygons N . Also shown on the x-axis are the number of polygons in the 2dFGRS mask, the SDSS DR5 mask, and conservative estimates for the Pan-STARRS and LSST large-scale structure masks based on scaling up 2dFGRS.

veys for target selection. The methods we present here are useful for both photometric and spectroscopic surveys – keeping track of factors such as seeing and dust extinction could prove particularly important for photometric redshift determinations (Collister et al. 2007; Oyaizu et al. 2008; Banerji et al. 2007).

The proposed large-scale structure survey to be produced by Pan-STARRS will cover $\sim 30,000$ square degrees in 5 wavelength bands, with each field being observed ~ 50 times such that the images can be co-added. A naive scaling up of the 2dFGRS area and number of polygons gives an estimate of $\sim 2 \times 10^7$ polygons for the final Pan-STARRS mask. Similarly, the LSST large-scale structure survey will cover $\sim 20,000$ square degrees in 6 bands, with ~ 200 co-added images, suggesting $\sim 8 \times 10^7$ polygons for the LSST mask. The need for an improvement in mask processing speed is clearly illustrated in Fig. 5-1: with the old algorithms, the projected processing time for the LSST mask would be over 6000 years. With our new method, this time is reduced by a factor of $\sim 24,000$ to just ten days.

In addition to developing faster algorithms for processing angular masks, we have also integrated the MANGLE utilities with *HEALPix*, a widely used tool for discretizing the celestial sphere (Górski et al. 2005). The methods used by MANGLE are complementary to *HEALPix*: MANGLE is best used for functions that are piecewise-constant in distinct regions of the sky, such as the completeness of a galaxy survey. In contrast, *HEALPix* is optimal for describing functions that are continuously varying across the sky, such as the cosmic microwave background (CMB) or the amount of extinction due to galactic dust. The ability to convert rapidly between these two formats allows for easy comparison of these two types of data without the unnecessary approximation inherent in discretizing an angular mask.

Furthermore, converting a mask into *HEALPix* format allows users to take advantage of pre-existing *HEALPix* tools for rapidly computing spherical harmonics.

The spectacular surveys on the horizon are preparing to generate massive, powerful datasets that will be made publicly available – this in turn necessitates powerful and intuitive general-purpose tools that assist the community to do science with this avalanche of data. We provide a such tools with this new generation of the MANGLE software and describe these new tools here. However, this chapter is not a software manual (a manual is provided on the MANGLE website) but rather a description of the underlying algorithms. These tools have been utilized in recent analyses of SDSS data (Tegmark et al. 2006, discussed in §4.3; Swanson et al. 2008, discussed in Chapter 6); we are now making them public so others can use them as well.

The outline of this chapter is as follows: in §5.2 we give an overview of the terminology we use to describe angular masks and the basic tasks we wish to perform, and in §5.3 we detail our algorithms for accelerating these tasks and quantify their speed. We describe our methods for integrating MANGLE with *HEALPix* in §5.4 and summarize in §5.5.

5.2 Mangle terminology

The process of defining an angular mask of a galaxy survey in a generic way requires a set of standardized terminology. We use the terminology from Hamilton and Tegmark (2004) and present a summary of it here. Our formal definition of an angular mask is a union of an arbitrary number of weighted angular regions bounded by arbitrary numbers of edges. The restrictions on the mask are

1. that each edge must be part of some circle on the sphere (but not necessarily a great circle), and
2. that the weight within each subregion of the mask must be constant.

This definition does not cover every theoretical possibility of how a piecewise-constant function on a sphere could be defined, but in practice it is sufficiently broad to accommodate the design of essentially any galaxy survey. Furthermore, as we discuss in detail in §5.4, a curvilinear angular region (such as a *HEALPix* pixel) can be well-approximated by segments of circles at high resolution. As an example of a typical angular mask, we show a portion of the SDSS angular mask from Data Release 5 (DR5; Adelman-McCarthy et al. 2007) in Fig. 5-2.

The fundamental building block of an angular mask is the spherical polygon, which is defined as a region bounded by edges that are part of a circle on the sphere. An angular mask is thus the union of arbitrarily weighted non-overlapping polygons. For convenience, we provide an updated version of a table from Hamilton and Tegmark (2004) in Table 5.1 containing the definitions of key terms used in this chapter.

The basic procedure used by the MANGLE software to process an angular mask consists of the following steps, which are described in greater detail in Hamilton and Tegmark (2004):

1. Snap
2. Balkanize
3. Weight

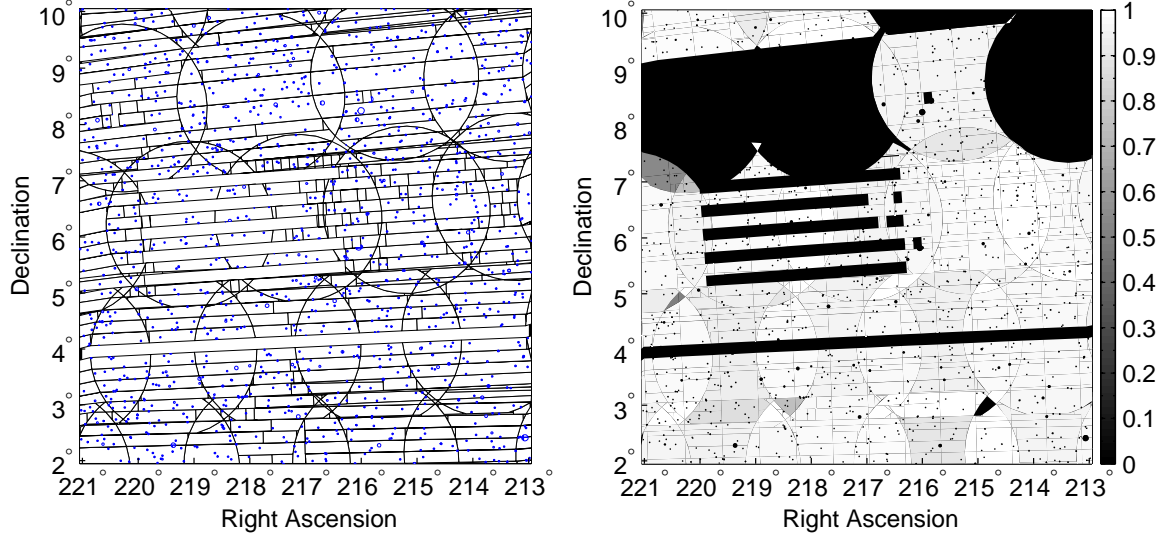


Figure 5-2 A portion of the SDSS DR5 angular mask (Blanton et al. 2005b; Adelman-McCarthy et al. 2007). Left: Polygons defining the mask: spectroscopic plates and lines delineating different scans and spectroscopic plates are shown in black, and holes in the mask are shown in blue/gray. Right: Processed version of the mask, shaded according to survey completeness.

Table 5.1 Definitions of Terms, in Alphabetical Order

Term	Definition
boundary	A set of edges bounding a polygon.
cap	A spherical disk, a region above a circle on the unit sphere.
circle	A line of constant latitude with respect to some arbitrary polar axis on the unit sphere.
edge	An edge is part of a circle. A polygon is enclosed by its edges.
great circle	A line of zero latitude with respect to some arbitrary polar axis on the unit sphere. A great circle is a circle, but a circle is not necessarily a great circle.
mask	The union of an arbitrary number of weighted polygons.
pixel	A special polygon that specifies some predefined region on the sky as part of a scheme for discretizing the unit sphere. Once a mask has been pixelized, each polygon in the mask is guaranteed to overlap with exactly one pixel.
polygon	The intersection of an arbitrary number of caps.
rectangle	A special kind of polygon, a rectangular polygon bounded by lines of constant longitude and latitude.
vertex	A point of intersection of two circles. A vertex of a polygon is a point where two of its edges meet.
weight	The weight assigned to a polygon. The spherical harmonics of a mask are the sum of the spherical harmonics of its polygons, each weighted according to its weight. A weight of 1 is the usual weight. A weight of 0 signifies an empty polygon, a hole. In general the weight may be some arbitrary positive or negative real number.

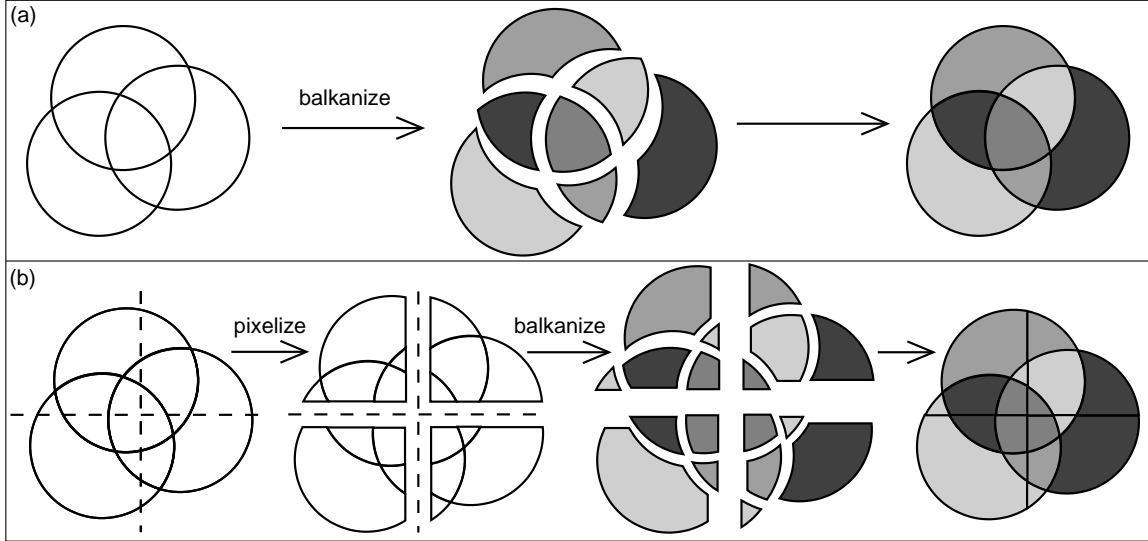


Figure 5-3 A cartoon illustrating the process of balkanization (a) with no pixelization, (b) with pixelization.

4. Unify

The snapping step identifies edges of polygons that are nearly coincident and snaps them together so the edges line up exactly. This is necessary because nearly-coincident edges can cause significant numerical issues in later computations. In practice, this situation occurs when two polygons in a survey are intended to abut perfectly, but are prevented from doing so by roundoff errors or numerical imprecision in the mask definition. There are several tunable tolerances that control how close two edges can be before they get snapped together – these can be adjusted based on how precisely the polygons defining the mask are specified.

Balkanization is the process of resolving a mask into a set of non-overlapping polygons. It checks for overlap between each pair of polygons in the mask, and if the polygons overlap, it fragments them into non-overlapping pieces. After this is completed, it identifies polygons having disconnected geometry and subdivides them into connected parts. The basic concept of balkanization is illustrated in the top panel of Fig. 5-3. The purpose of this procedure is to define all of the distinct regions on the sky in which the piecewise-constant function we are intending to model might take on a different value. For example, the 2dFGRS and SDSS spectroscopic surveys generate masks containing many overlapping circles defining each spectroscopic field observed. The SDSS spectrographs can observe 640 objects in each field, so if there are more than 640 desired target galaxies in the field, they might not all be observed. For example, one field may have spectra for 80 per cent of the targets, and a neighboring field may have 90 per cent, but in the region where they overlap all of the targets may have been observed. This is how the survey completeness is determined and illustrates why balkanization is necessary.

After the mask is balkanized, weights are assigned to each polygon, representing the value of the survey completeness (or any other desired parameter) in that region. The way this is done depends on how this information is provided for a given survey. For example, the 2dFGRS mask software by Peder Norberg and Shaun Cole¹ provides a function that

¹<http://magnum.anu.edu.au/~TDFgg/Public/Release/Masks>

takes an angular position on the sky and returns the completeness, the magnitude limit, the photographic plate number, and the value of the parameter μ (described in Colless et al. 2001) at that location. This information can be imported into MANGLE by producing a list of the midpoints of each of the polygons in the mask, applying the 2dFGRS software to calculate the value of the desired function at each midpoint, and assigning these weights to the appropriate polygon by using the “weight” routine in MANGLE. For the SDSS mask, the files provided by the NYU-VAGC² (Blanton et al. 2005b) already include weights for the survey completeness, so this step is not needed.

The final step of the processing is unification, which discards polygons with zero weight and combines neighboring polygons that have the same weight. While not strictly necessary, this procedure clears out unneeded clutter and makes subsequent calculations more efficient.

After an angular mask has been processed in this fashion, it can be used for function evaluation: i.e., given a point on the sky, determine in which one of the non-overlapping polygons it lies, and then get the weight of that polygon to obtain the value of the function at the input point. It can also be used for creating a random sample of points with the same selection function as the survey, calculating Data-Random $\langle DR \rangle$ and Random-Random $\langle RR \rangle$ angular integrals, and computing the spherical harmonics of the mask. The MANGLE software provides utilities for all of these tasks.

5.3 Speedup: pixelization

The tasks of snapping, balkanization, and unification all require comparing pairs of polygons in the mask. The brute-force method to accomplish this is simply to compare each polygon with every other polygon, which is what the original version of MANGLE did. This naive algorithm is $\mathcal{O}(N^2)$, which is easily sufficient for masks such as the 2dFGRS mask, with an N of a few thousand polygons. However, the SDSS mask has about 100 times as many polygons, and points to the need for a cleverer approach. The method we present here is a divide-and-conquer approach we dub “pixelization,” which processes the mask so that each polygon needs to be compared with only a few nearby polygons.

5.3.1 Pixelization concept

The underlying concept of pixelization is as follows: before performing any snapping, balkanization, or unification, divide the mask into predefined regions called “pixels” and split each polygon along the pixel boundaries such that each polygon is only in one pixel. Then for following tasks, polygons need only be compared with other polygons in the same pixel.

The process of balkanization with and without pixelization is illustrated in Fig. 5-3 for three overlapping polygons. The top panel shows the unpixelized version: balkanization checks for overlap between each pair of polygons, and then fragments it into seven non-overlapping polygons.

The bottom panel shows the same process but using pixelization as a first step. First, each polygon is divided along the pixel boundaries, shown by the dotted lines. At this point, each of the four pixels shown has three polygons in it: the intersections between that pixel and each of the original three polygons. Then balkanization is performed within each pixel: the three polygons in the upper left pixel are split into five non-overlapping polygons, and so forth, yielding a final set of 18 non-overlapping polygons. In this illustrative example,

²<http://sdss.physics.nyu.edu/vagc>

pixelization increases the complexity of the process, but in general it replaces the $\mathcal{O}(N^2)$ algorithm for balkanization with one that is roughly $\mathcal{O}\left(M(N/M)^2\right)$ for N polygons and M pixels, which is roughly $\mathcal{O}(N)$ if $M \sim N$. For large, complicated masks such as SDSS, this speeds up the processing time by a factor of ~ 1200 .

Once a mask has been pixelized, the important task of determining in which polygon(s) a given point lies is sped up greatly as well: one merely has to calculate in which pixel the point lies, and then test if the point is in each polygon within that pixel. For a typical pixelization scheme, the appropriate pixel number for a given point can be found with a simple formula, i.e. an $\mathcal{O}(1)$ calculation, so pixelization reduces the $\mathcal{O}(N)$ algorithm of testing every polygon in the mask to $\mathcal{O}(N/M)$. This means that with pixelization, this task does not depend on the total number of polygons in the mask at all if $M \sim N$.

It is important to note that the pixelization procedure makes no approximations to the original mask – the pixels are used simply as a tool to determine which polygons are close to each other, not as a means of discretizing the mask itself. A mask that has been balkanized after pixelization contains all of the same information as it would without pixelization, except that it took a tiny fraction of the time to produce. Furthermore, unification can be applied across the whole mask rather than within each pixel, which effectively unpixelizes the mask if desired. Thus there are essentially no drawbacks to using our pixelization procedure.

5.3.2 Pixelization schemes

Simple scheme

The most straightforward means of pixelizing the sky is to use lines of equal azimuth and elevation as the pixel boundaries. The azimuth and elevation typically correspond to celestial coordinates – right ascension (RA) and declination (Dec) – in a survey mask. In this scheme, the whole sky is split into quadrants along the equator and prime meridian to form the lowest resolution of pixelization. In MANGLE this is defined as resolution 1.

To pixelize to higher resolutions, each pixel is split into four child pixels, with the boundaries at the midpoints of azimuth and of $\cos(\text{elevation})$ within the pixel. This creates pixels with equal area. Thus resolution 2 consists of each of the four resolution 1 quadrants split into four pixels each, and so forth. This procedure produces a hierarchical pixel structure known in computer science terminology as a quadtree (de Berg et al. 2000): there are 4^r pixels in this scheme at resolution r , and each of these pixels has four child pixels at resolution $r + 1$ and r parent pixels, one at each lower resolution. Resolution 0 is defined as being the whole sky.

In MANGLE, the pixels of the simple scheme are numbered as follows: the whole sky is pixel 0, the four quadrants of resolution 1 are pixels 1, 2, 3, and 4, resolution 2 is pixels 5-20, and so forth. Thus just one number specifies both the resolution and the pixel location. At each resolution, the pixels are numbered in a ring pattern, starting from an elevation of 90° and along increasing azimuth for each ring of equal elevation. The simple scheme pixels at the four lowest resolutions are shown in Fig. 5-4.

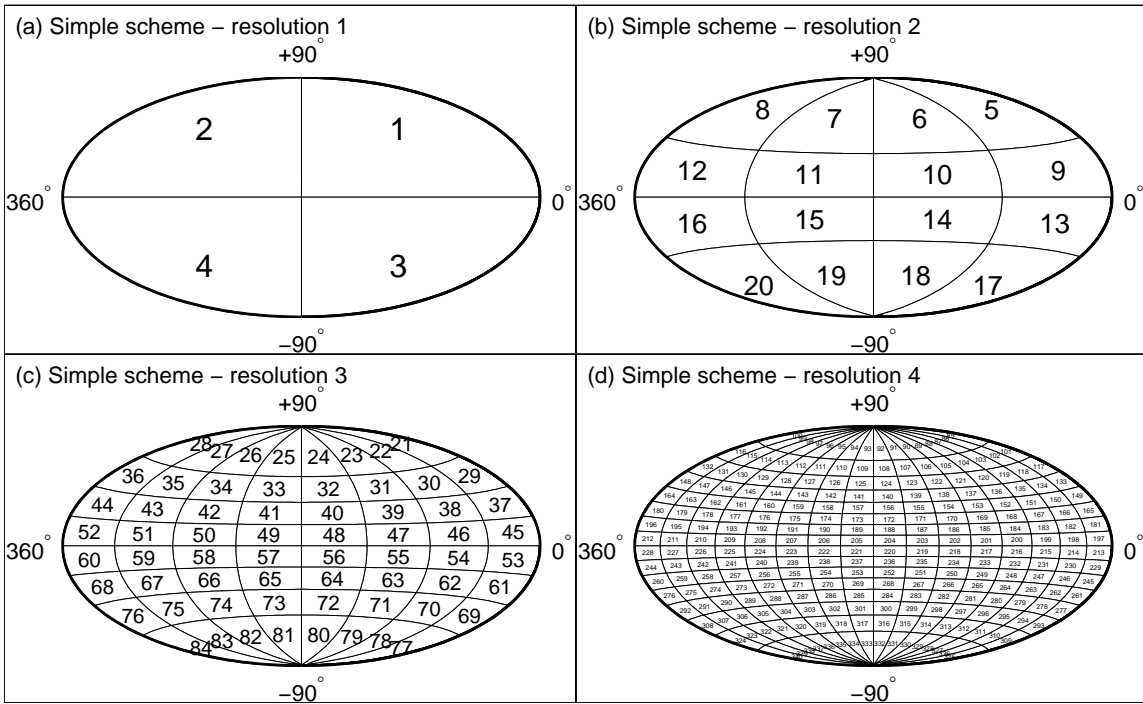


Figure 5-4 The full sky (shown in a Hammer-Aitoff projection in celestial coordinates) pixelized with the simple pixelization scheme at the four lowest resolutions.

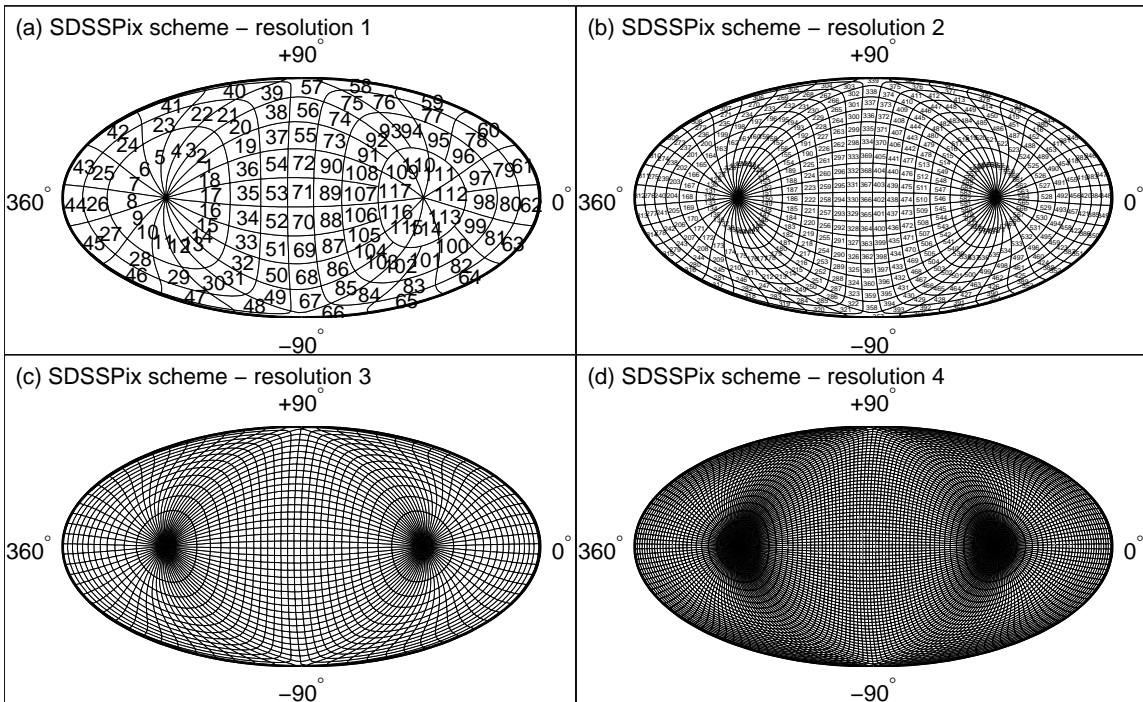


Figure 5-5 The full sky (shown in a Hammer-Aitoff projection in celestial coordinates) pixelized with the SDSSPix pixelization scheme at the four lowest resolutions.

SDSSPix scheme

Alternatively, the pixelization can be done such that it is more closely aligned with the mask of a given survey. In particular, a pixelization scheme called SDSSPix³ has been developed for use with the SDSS geometry. Like the simple scheme, SDSSPix is a hierarchical, equal-area pixelization scheme, and it is based on the SDSS survey coordinates λ and η . As described in Stoughton et al. (2002), SDSS survey coordinates form a spherical coordinate system rotated relative to the celestial coordinate system. The poles are located at $\text{RA} = 95^\circ, \text{Dec} = 0^\circ$ and $\text{RA} = 275^\circ, \text{Dec} = 0^\circ$ (J2000), which are strategically located outside the SDSS covered area and in the galactic plane. η is the azimuthal angle, with lines of constant η being great circles perpendicular to the survey equator, and λ is the elevation angle, with lines of constant λ being small circles parallel to survey equator. $\lambda = 0^\circ, \eta = 0^\circ$ is located at $\text{RA} = 185^\circ, \text{Dec} = 32.5^\circ$ with η increasing northward. This configuration has been chosen such that the stripes produced by the SDSS scanning pattern lie along lines of constant η .

The SDSSPix base resolution is defined by 36 divisions in the η direction (equally spaced in η) and 13 in the λ direction (equally spaced in $\cos \lambda$), for a total of 468 equal-area pixels. These divisions are chosen such that at a special resolution level (called the “superpixel” resolution), there is exactly one pixel across each SDSS stripe. Finally, as in the simple scheme, higher resolutions are achieved by hierarchically subdividing each pixel at a given resolution into four smaller pixels.

SDSSPix has been included in MANGLE by incorporating several routines from the SDSSPix software package available online.³ The numbering scheme in the MANGLE implementation of SDSSPix differs somewhat from the internal SDSSPix numbering: in MANGLE, the entire sky is pixel 0, as in the simple scheme, but it has 117 child pixels (instead of 4), numbered from 1 to 117. These pixels, which comprise resolution 1, are not part of the official SDSSPix scheme, but are created by combining sets of 4 pixels from what is defined as resolution 2 in MANGLE. The resolution 2 pixels are the official SDSSPix base resolution pixels, and are numbered from 118 to 585. Higher resolutions are constructed through the standard SDSSPix hierarchical division of each pixel into 4 child pixels. As in the simple scheme, the pixel number identifies both the resolution and the pixel position. The superpixel resolution described above is defined as resolution 5 in MANGLE and contains a total of 7488 pixels.

MANGLE typically uses RA and Dec as its internal azimuth and elevation coordinates, so the SDSSPix pixels are constructed as rectangles in $\eta - \lambda$ coordinates and then rotated into celestial coordinates. The SDSSPix pixels at the four lowest resolutions are shown in Fig. 5-5.

Other schemes

The implementation of pixelization in MANGLE is designed to be flexible: it is simple for users to add their own scheme as well. The pixelization uses only four basic routines:

1. `get_pixel`: Given a pixel number, return a polygon representing that pixel.
2. `which_pixel`: Given a point on the sky and a resolution, return the pixel number containing the point.

³<http://lahmu.phyast.pitt.edu/~scranton/SDSSPix/>

3. `get_child_pixels`: Given a pixel number, return the numbers of its child pixels.
4. `get_parent_pixels`: Given a pixel number, return the numbers of its parent pixels.

Adding a new pixelization scheme simply requires creating appropriate versions of these four routines. Note that it also requires that the pixels can be represented as polygons – this is *not* strictly the case for the *HEALPix* pixels, as discussed further in §5.4.

5.3.3 Pixelization algorithm

The purpose of pixelization is to speed up the processing of angular masks, which means that the pixelization itself must be done with a clever, speedy algorithm or nothing will be gained. The naive algorithm is to search through all of the polygons in the mask for those that overlap that pixel. This is $\mathcal{O}(NM)$ for N polygons and M pixels, and is not sufficient for our purposes.

Our fast pixelization algorithm is a recursive method that takes advantage of the hierarchical nature of the pixelization schemes. The method works as follows:

1. Start with all the mask polygons that are in pixel i .
2. Create polygons for each child pixel of pixel i at the next resolution level.
3. Split the mask polygons in pixel i along the child pixel boundaries such that each polygon lies within one child pixel.
4. Repeat steps 1-3 for the mask polygons in each child pixel until desired stopping point is reached.

Starting this with pixel $i = 0$, i.e., the whole sky, will pixelize the entire mask in $\mathcal{O}(N \log M)$ time. Thus the pixelization does not add too much overhead time to the overall mask processing.

There are two different methods for choosing the desired stopping point of the pixelization. The simplest method is to stop at a fixed resolution, such that the entire mask is pixelized with pixels of the same size. The example mask from Fig. 5-2 is shown in the left panel of Fig. 5-6 pixelized to a fixed resolution in the simple scheme.

Alternatively, the stopping condition can be chosen to be a maximum number of polygons allowed in each pixel: if there are more than N_{\max} polygons in a given pixel, continue the recursion and divide those polygons into pixels at the next resolution level. This results in an adaptively pixelized mask, where higher resolutions are automatically used in regions of the mask that are more complicated. This method is especially useful for masks with varying degrees of complexity in different areas. The example mask from Fig. 5-2 is shown again in the right panel of Fig. 5-6 pixelized adaptively with $N_{\max} = 30$.

The implementation of pixelization in MANGLE allows users to choose either of these methods and to select values for the fixed resolution level or for N_{\max} .

5.3.4 Speed trials

In order to choose optimal default values for the maximum resolution and N_{\max} as well as to demonstrate the dramatic improvements in speed that pixelization provides, we have conducted a series of speed trials of the new MANGLE software.

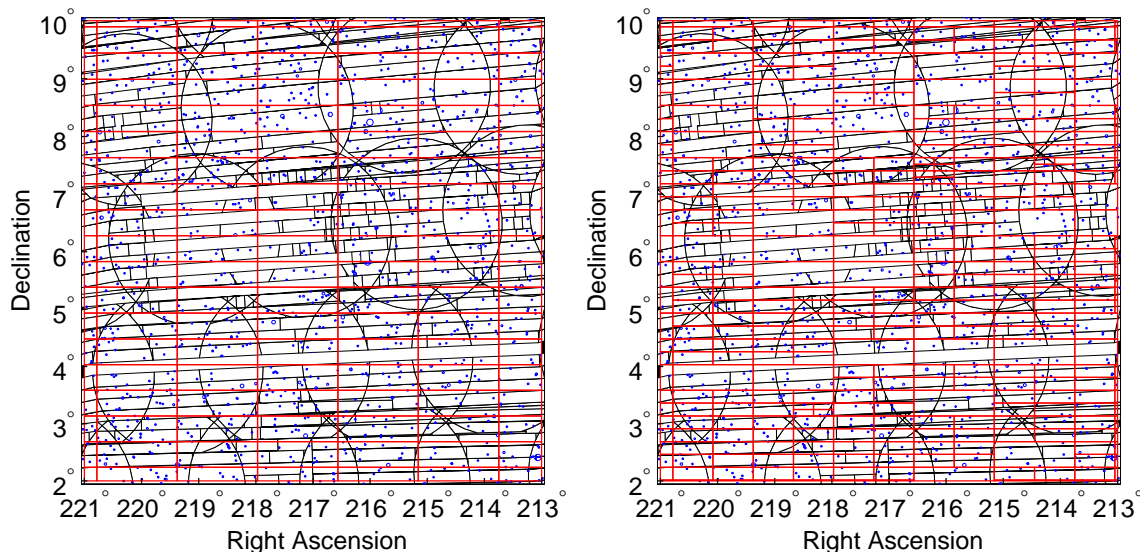


Figure 5-6 Left: portion of SDSS mask from Fig. 5-2 pixelized to resolution 8 (4^8 total pixels on the sky) with the simple pixelization scheme. Pixel boundaries are shown in red/light gray. Right: the same mask pixelized with the simple pixelization scheme using the adaptive resolution method with a maximum of 30 polygons per pixel.

There are two procedures we are interested in optimizing: firstly, basic processing of a mask detailed in §5.2 involving pixelization, snapping, balkanization, and unification, and secondly, the use of the final mask to identify in which polygon a given point lies. We carried out trials of these two procedures using both the simple and SDSSPix pixelization schemes described in §5.3.2. For each of these schemes, we tested both the fixed and adaptive resolution methods for stopping the pixelization algorithm described in §5.3.3. For the fixed resolution method, we measured the time for several different values of the maximum resolution, and for the adaptive resolution method, we measured the time as a function of N_{\max} .

The results are shown in Fig. 5-7. (Note that the overhead time for reading and writing files and doing general setup has been subtracted – the times shown here are just for the primary operations.) From the fixed resolution trials, we see that the optimal resolution choice for the SDSS mask is the one that has approximately 10^5 total pixels on the sky for both the simple and SDSSPix schemes. This corresponds to resolution 9 for the simple scheme and resolution 6 for SDSSPix. When using the adaptive method, the choice for the maximum number of polygons allowed in each pixel that gives the fastest processing is $N_{\max} = 40$ for the simple scheme and $N_{\max} = 46$ for SDSSPix. Overall, the fastest choice (by a slight margin) for the SDSS mask is using the SDSSPix scheme with adaptive resolution. It is also interesting to note that different MANGLE processes have different optimum values – for example, snapping is fastest when there are fewer polygons in each pixel compared to balkanization.

The impact of our pixelization algorithm is most clearly demonstrated by Fig. 5-1. This shows the processing time and polygon identification time for a series of selected portions of the SDSS mask as a function of the total number of polygons, both with and without pixelization – again, overhead time has been subtracted here. Pixelization clearly gives an

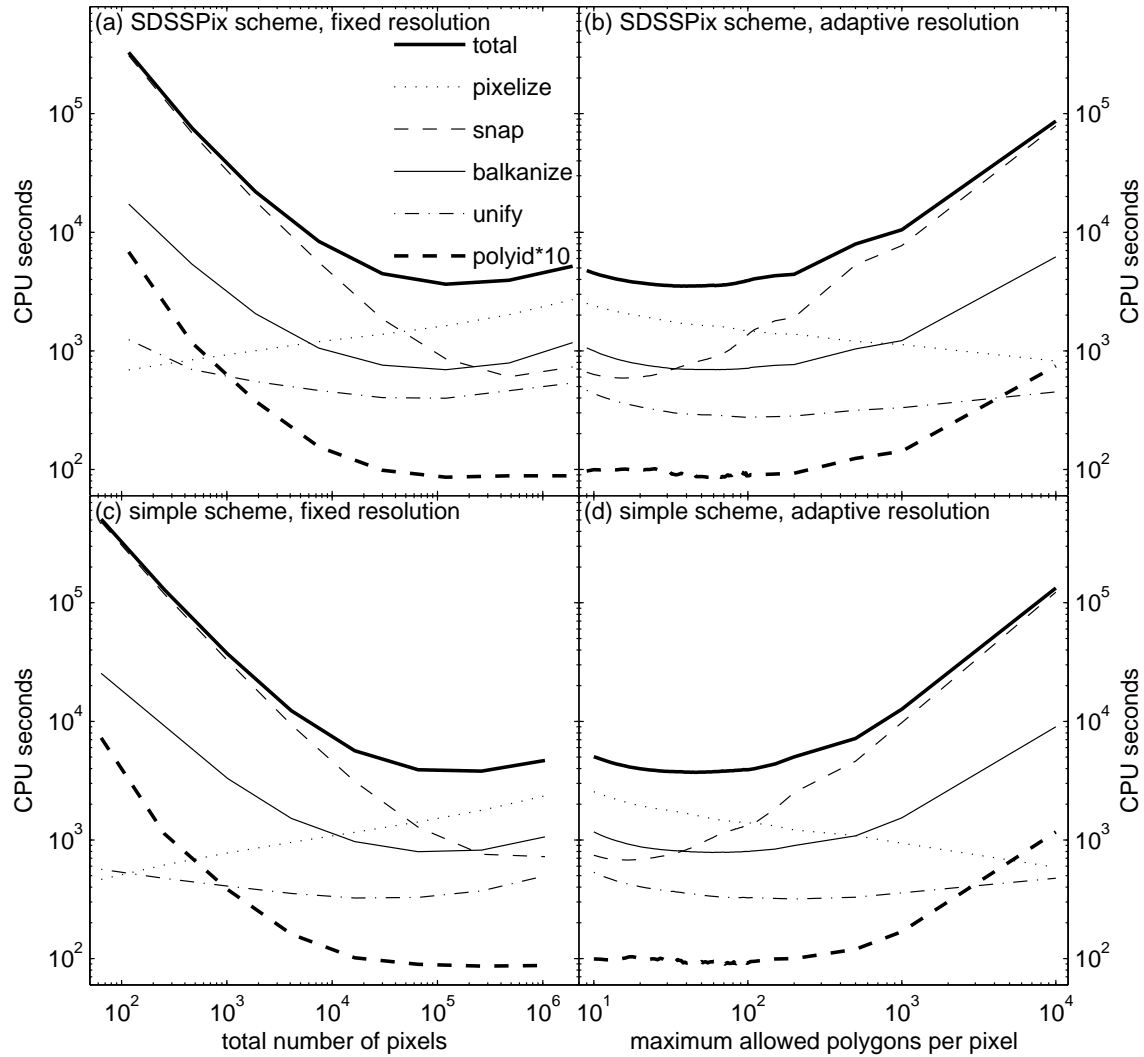


Figure 5-7 Time required to process the full SDSS DR5 mask with different choices of pixelization schemes and methods. The “total” curves are the sum of the pixelization, snapping, balkanization, and unification curves. Also shown is the time required to identify in which polygon each of the $\sim 400,000$ SDSS DR5 galaxies lies (polyid), scaled up by a factor of 10. The plots on the left show time vs. the number of pixels at a fixed resolution. The plots on the right show time vs. N_{\max} , the maximum number of polygons in allowed in each pixel when pixelizing with the adaptive resolution method.

improvement in speed that becomes increasingly significant for larger numbers of polygons.

To quantify this, we fit theoretical models to each series of trials. Without pixelization, the processing time for snapping, balkanization, and unification is well-fitted by AN^2 where A is a free parameter with a best-fitted value of $A = 3.2 \times 10^{-5}$ CPU seconds. With pixelization (and using the adaptive resolution method with the optimal choice for N_{\max}) this is reduced substantially. We fit the times using theoretical models based on the formulas in §5.3.1 assuming $M \sim N$. We fit the pixelization time with $BN \log_4 N$ and the snapping, balkanization, and unification time with CN where B and C are free parameters. The simple scheme gives $(B, C) = (0.0054, 4.7 \times 10^{-4})$ and the SDSSPix scheme gives $(B, C) = (0.0045, 4.8 \times 10^{-4})$ (units are all in CPU seconds) – thus for processing the SDSS mask, the SDSSPix scheme is slightly faster than the simple scheme. Our fits give $C/B = 0.1$, so the overall processing time scales like $\mathcal{O}(N + 0.1N \log_4 N)$.

These fitted curves are shown in Fig. 5-1 and allow us to extrapolate estimates for processing masks with larger numbers of polygons. For the full SDSS DR5 mask containing about 300,000 polygons, pixelization reduces the processing time by a factor of ~ 1200 . The improvement for future surveys will be even more dramatic: the mask for the co-added LSST survey might contain $\sim 10^8$ polygons – pixelization reduces the processing time by a factor of $\sim 24,000$.

The time for identifying in which polygon each SDSS galaxy lies is significantly sped up as well: without pixelization it is fitted by DN where $D = 0.012$ CPU seconds, although the scatter is rather large due to dependence on which polygons are used. With pixelization, it is well-fitted by a constant (8.2 CPU seconds for the simple scheme, 7.9 CPU seconds for the SDSSPix scheme) – thus the time for polygon identification does not depend on how many polygons are in the mask if the number of pixels used is chosen to be roughly proportional to the number of polygons. For the SDSS mask, the time to identify the polygons for all of the SDSS galaxies is reduced by a factor of nearly 500.

5.4 Unification with *HEALPix* and other pixelized tools

HEALPix (Górski et al. 2005; Gorski et al. 1999) is a hierarchical, equal-area, isolatitudinal pixelization scheme for the sphere motivated by computational challenges in analyzing CMB data (Górski et al. 1999; Bond et al. 1999). Its base resolution consists of 12 equal-area pixels; to generate higher resolutions, each pixel at a given resolution is hierarchically subdivided into four smaller pixels, and it represents an interesting class of spherical projections (Calabretta and Roukema 2007). Resolution in *HEALPix* is defined in terms of N_{side} , the number of divisions along the side of a base-resolution pixel required to reach the desired resolution. Because of the hierarchical definition of the higher resolution pixels, N_{side} is always a power of 2, and the total number of pixels at a given resolution is $12N_{\text{side}}^2$.

HEALPix is a very useful scheme in that it allows for fast and accurate astrophysical computations by means of appropriately discretizing functions on the sphere to high resolution (Wandelt et al. 1998; Doré et al. 2001). In particular, *HEALPix* includes routines for fast computations of spherical harmonics (Hivon et al. 2002; Wandelt et al. 2001; Szapudi et al. 2001; Doré et al. 2001). It is widely used in the analysis of cosmic microwave background data from WMAP (Spergel et al. 2007) and has recently been used to approximate galaxy survey masks as well (Percival et al. 2007).

Combining *HEALPix* with MANGLE is useful because it facilitates comparisons between galaxy survey data and the CMB as is done in experiments measuring the integrated Sachs-

Wolfe effect (Padmanabhan et al. 2005; Giannantonio et al. 2006; Rassat et al. 2007), the Sunyaev-Zel’dovich effect (Myers et al. 2004; Reid and Spergel 2006), etc., and can also be used for generating masks that block out regions of high dust extinction from galaxy surveys (Schlegel et al. 1998, dust map available in *HEALPix* format online⁴).

In general, it can be applied to any task requiring comparison between a piecewise-constant function on the sphere to a continuous function sampled on a discretized spherical grid. Converting an angular mask into *HEALPix* format also allows for rapid computations of approximate spherical harmonics of the mask using the existing *HEALPix* tools.

The implementation of the *HEALPix* scheme in MANGLE consists of two components:

1. A new polygon format, “healpix_weight”, which allows the user to input a list of weights corresponding to each *HEALPix* pixel at a given N_{side} parameter;
2. A new utility, “rasterize”, which essentially allows the user to pixelize a mask against the *HEALPix* pixels, by means of a different technique than the pixelization method described in §5.3.

Together, these new features allow effective two-way conversion between the *HEALPix* specifications and those of MANGLE.

5.4.1 Importing *HEALPix* maps into mangle

The structure of the healpix_weight format is quite simple: an input file consists of a list of numbers corresponding to the weight of each *HEALPix* pixel at a given N_{side} parameter, using the nested numbering scheme described in Górski et al. (2005). In addition, the definition of the N_{side} parameter is extended to include 0, which corresponds to a single pixel covering the entire sphere. MANGLE constructs polygons approximately equivalent to the *HEALPix* pixels through the following procedure:

1. The exact azimuth and elevation of each vertex of a given pixel are calculated using the *HEALPix* utility “pix2vec_nest”;
2. The exact azimuth and elevation of each vertex of the four child pixels of the current pixel are calculated using the same utility, four of which are the midpoints of the edges of the current pixel;
3. The four vertices of the given pixel are combined with the four midpoints to construct the current pixel. Each edge is defined by the circle that passes through the two vertices and the midpoint, using the “edges” format described in Hamilton and Tegmark (2004).
4. To eliminate spurious antipodal pieces of the polygon defining the pixel, a fifth cap is constructed whose axis coordinates are the exact center of the current pixel and whose radius is 10^{-6} radians greater than the distance from the center of the pixel to any of the four vertices—this cap thus encloses the entire pixel.

A similar technique could be applied to incorporate other pixelization schemes not exactly described by spherical polygons as well. It is important to note that the pixels constructed in this manner are not exactly equivalent to the actual *HEALPix* pixels – while the hierarchical

⁴http://lambda.gsfc.nasa.gov/product/foreground/ebv_map.cfm

and isolatitudinal properties of the *HEALPix* pixels are preserved, the equal area property is not. For example, at $N_{\text{side}} = 1$, the areas of the approximate pixels differ on average from the actual area by about 0.08%.

However, as the N_{side} parameter increases, this difference decreases rapidly: at $N_{\text{side}} = 512$, the average difference from the actual area is 0.000002%. The boundaries of the both the actual *HEALPix* pixels and our circles approximating them become straight lines in the flat-sky approximation, i.e., when the pixel size is much less than 1 radian. Thus for the resolutions at which *HEALPix* is typically used, the difference is totally negligible.

In applications involving integrations over the sphere, such as calculating spherical harmonics, the slight area differences between the pixels can be corrected for in a straightforward manner since the area of each pixel is known (and can be easily extracted using MANGLE’s “area” format): simply multiply the value of the function in each pixel by the area of that pixel divided by the average pixel area, and then the *HEALPix* spherical harmonics routines will be exact. Furthermore, the paranoid user can get higher precision by rasterizing to a higher resolution and then using the “ud_grade” *HEALPix* utility to obtain results for lower resolutions.

5.4.2 Exporting polygon files as *HEALPix* maps

The idea behind the rasterization method used to convert polygon files into *HEALPix* maps is very similar to that of pixelization: to split up the polygons that comprise a mask using a given set of pixels, such that afterward each polygon lies in only one pixel. However, rasterization is somewhat different, in that afterward the converse statement also holds: each pixel contains only one polygon, namely, itself. In particular, rasterization uses an arbitrary user-defined spherical pixelization as the pre-determined scheme against which to split up the polygons in a given input mask. In general, the user-defined “rasterizer” pixels may be from any pixelization of the sphere, but the method was originally developed for use with the approximate *HEALPix* pixels described in the previous section. From a practical standpoint, it would be simplest to implement any spherical pixelization that can be exactly represented as spherical polygons by following the steps in §5.3.2; however, for pixelization schemes that do not possess this property (such as *HEALPix*), rasterization provides an alternate method of implementation.

The final product of rasterization is a polygon file in which each polygon corresponds to one of the rasterizer pixels (either the approximate *HEALPix* pixels or a user-defined set of pixels) and its weight is the area-averaged weight of the input angular mask within that pixel. This output can easily be converted into a FITS file read by the *HEALPix* software using a simple script provided with MANGLE.

Rasterization consists of the following steps:

1. Calculate the area of each rasterizer pixel;
2. Compute the area of the intersection of each input mask polygon with each rasterizer (e.g., *HEALPix*) pixel;
3. Calculate the area-averaged weight within each rasterizer pixel.

Note that, as with snapping, balkanization, and unification, this procedure is greatly accelerated by pixelizing both the rasterizer polygons and the polygons defining the mask to the same resolution using one of the pixelization schemes described in §5.3.2, e.g. simple

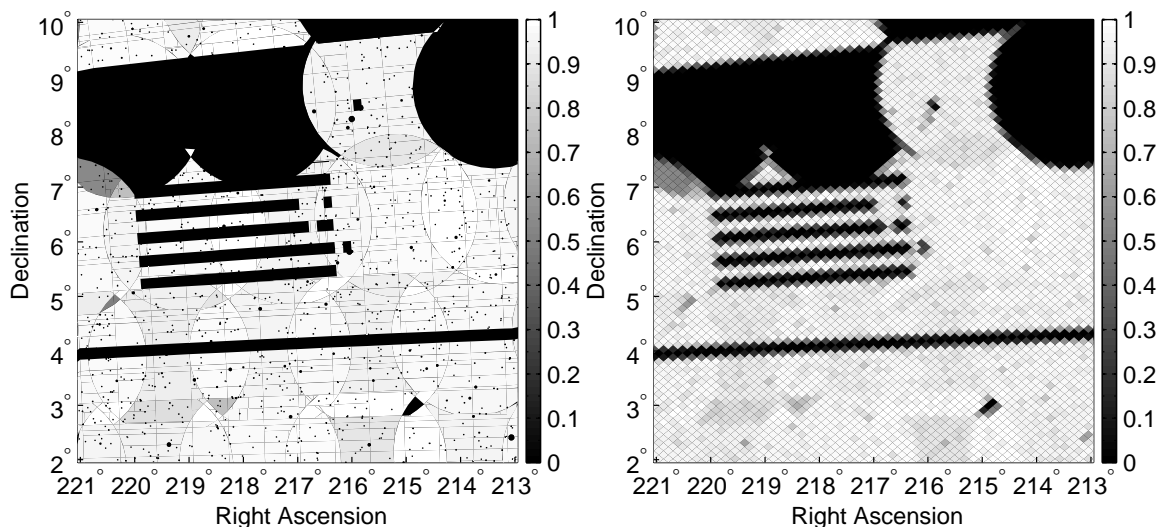


Figure 5-8 Left: Portion of SDSS mask as shown in Fig. 5-2. Right: Portion of SDSS mask from Fig. 5-2 as approximated by *HEALPix* pixels, rasterized to $N_{side} = 512$.

or SDSSPix. Then step (ii) in the above procedure then involves comparing only polygons in the same simple/SDSSPix pixel. Our example mask from Fig. 5-2 (duplicated in the left panel of Fig. 5-8) is shown in the right panel of Fig. 5-8 rasterized with *HEALPix* pixels at $N_{side} = 512$. The ability to convert between MANGLE and *HEALPix* formats allows for straightforward comparisons between different types of functions defined on the sphere, e.g. angular masks of galaxy surveys and the CMB, as illustrated in Fig. 5-9.

5.5 Summary

As technologies for surveying the sky continue to improve, the process of managing the angular masks of galaxy surveys grows ever more complicated. The primary purpose of this chapter has been to present a set of dramatically faster algorithms for completing these tasks.

These algorithms are based on dividing the sky into regions called “pixels” and performing key operations only within each pixel rather than across the entire sky. The pixelization is based on a hierarchical subdivision of the sky – this produces a quadtree data structure that keeps track of which polygons are nearby each other. The preprocessing step of pixelization is $\mathcal{O}(N \log N)$ for a mask with N polygons and $\sim N$ pixels, and it reduces the mask processing time from $\mathcal{O}(N^2)$ to $\mathcal{O}(N)$. Furthermore, it reduces the time required to locate a point within a polygon from $\mathcal{O}(N)$ to $\mathcal{O}(1)$.

This method is exact, i.e., it does not make a discrete approximation to the mask, and it takes only a tiny fraction of the computation time. It accelerates the processing of the SDSS mask by a factor of about 1200 and reduces the time to locate all of the galaxies in the SDSS mask by a factor of nearly 500. It will provide even more dramatic gains for future surveys: processing time for the LSST large-scale structure mask could be reduced by a factor of about 24,000.

We have also described a method for converting between masks described by spherical

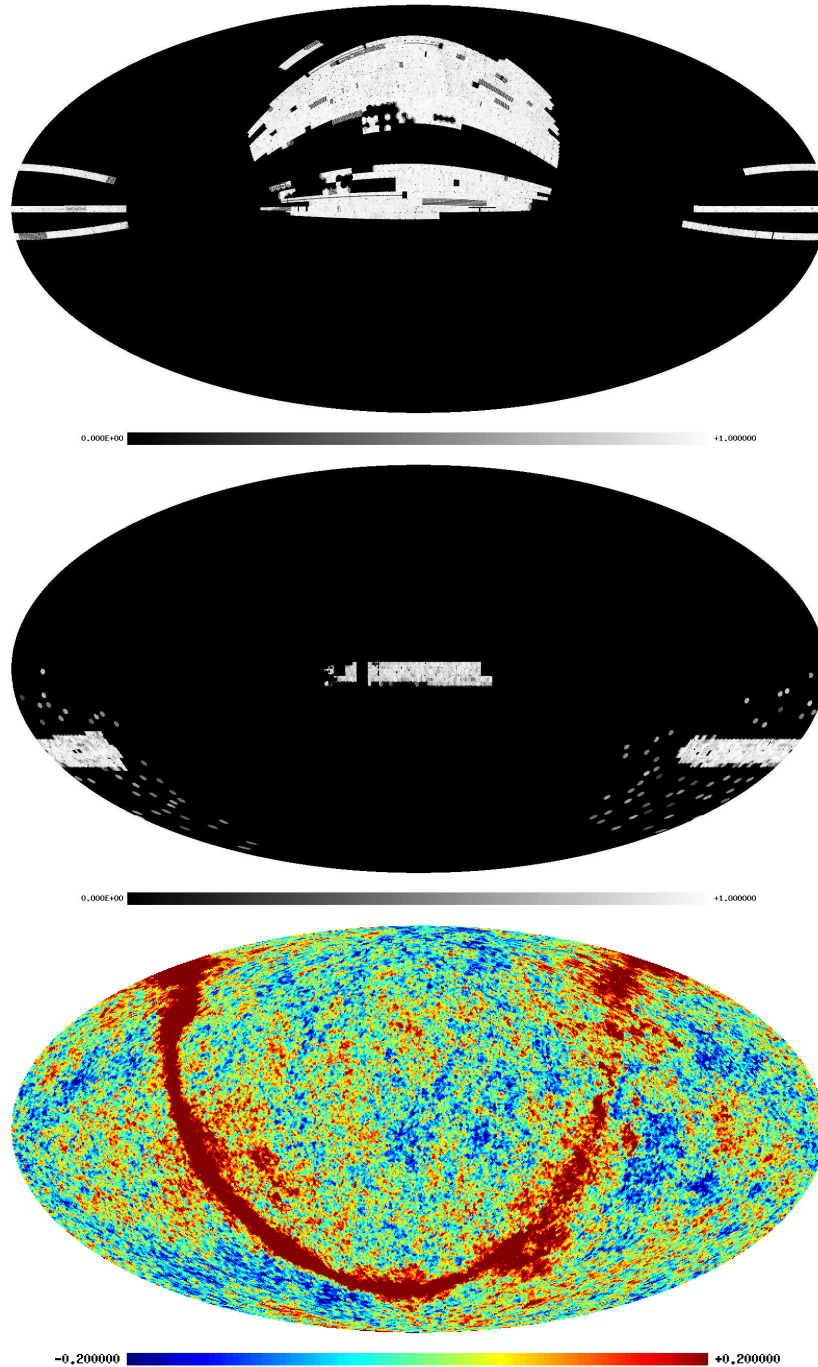


Figure 5-9 The new version of MANGLE can output angular masks in *HEALPix* format, which allows for easy comparisons to CMB and other sky map data and allows users to take advantage of existing *HEALPix* tools. Top: The SDSS DR5 completeness mask, rasterized and plotted using *HEALPix* routines. Middle: The final 2dFGRS completeness mask as determined in Hamilton et al. (2008), rasterized and plotted using *HEALPix* routines. Bottom: CMB temperature difference map measured by WMAP channel 4, with units in mK. Spergel et al. (2007) All three maps are shown at $N_{side} = 512$ in celestial coordinates.

polygons and sky maps in the *HEALPix* format commonly used by CMB and large-scale structure experiments. This provides a convenient way to work with both piecewise-constant functions on the sky such as the completeness of a galaxy survey and continuously varying sky maps such as the CMB temperature. Converting angular masks into *HEALPix* format also allows users to take advantage of existing *HEALPix* tools for rapidly computing spherical harmonics.

All of the new algorithms and features detailed here have been integrated into the MANGLE software suite, which is available for free download at <http://space.mit.edu/home/tegmark/mangle/>. This updated software package should prove increasingly useful in the coming years, especially as next-generation surveys such as DES, WFMOS, Pan-STARRS, and LSST get underway.

Chapter 6

SDSS galaxy clustering: luminosity & color dependence and stochasticity

This chapter is adapted from the paper “SDSS galaxy clustering: luminosity and colour dependence and stochasticity” by Molly E. C. Swanson, Max Tegmark, Michael Blanton, and Idit Zehavi, which was previously published in the *Monthly Notices of the Royal Astronomical Society* 385, pp. 1635-1655 (Swanson et al. 2008).

6.1 Introduction

In order to use galaxy surveys to study the large-scale distribution of matter, the relation between the galaxies and the underlying matter – known as the *galaxy bias* – must be understood. Developing a detailed understanding of this bias is important for two reasons: bias is a key systematic uncertainty in the inference of cosmological parameters from galaxy surveys, and it also has implications for galaxy formation theory.

Since it is difficult to measure the dark matter distribution directly, we can gain insight by studying *relative bias*, i.e., the relation between the spatial distributions of different galaxy subpopulations. There is a rich body of literature on this subject tracing back many decades (see, e.g., Hubble and Humason 1931; Davis and Geller 1976; Hamilton 1988; White et al. 1988; Park et al. 1994; Loveday et al. 1995), and been studied extensively in recent years as well, both theoretically (Seljak 2001; van den Bosch et al. 2003; Cooray 2005; Sheth et al. 2005; Tinker et al. 2007) and observationally. Such studies have established that biasing depends on the type of galaxy under consideration – for example, early-type, red galaxies are more clustered than late-type, blue galaxies (Guzzo et al. 1997; Norberg et al. 2002; Madgwick et al. 2003; Conway et al. 2005; Li et al. 2006; Croton et al. 2007), and luminous galaxies are more clustered than dim galaxies (Willmer et al. 1998; Norberg et al. 2001; Tegmark et al. 2004b; Zehavi et al. 2005; Seljak et al. 2005; Skibba et al. 2006). Since different types of galaxies do not exactly trace each other, it is thus impossible for them all to be exact tracers of the underlying matter distribution.

More quantitatively, the luminosity dependence of bias has been measured in the 2 Degree Field Galaxy Redshift Survey (2dFGRS; Colless et al. 2001) (Norberg et al. 2001, 2002) and in the Sloan Digital Sky Survey (SDSS; York et al. 2000; Stoughton et al. 2002)

(Tegmark et al. 2004b; Zehavi et al. 2005; Li et al. 2006) as well as other surveys, and it is generally found that luminous galaxies are more strongly biased, with the difference becoming more pronounced above L_* , the characteristic luminosity of a galaxy in the Schechter luminosity function (Schechter 1976).

These most recent studies measured the bias from ratios of correlation functions or power spectra. The variances of clustering estimators like correlation functions and power spectra are well-known to be the sum of two physically separate contributions: Poisson shot noise (due to the sampling of the underlying continuous density field with a finite number of galaxies) and sample variance (due to the fact that only a finite spatial volume is probed). On the large scales most relevant to cosmological parameter studies, sample variance dominated the aforementioned 2dFGRS and SDSS measurements, and therefore dominated the error bars on the inferred bias.

This sample variance is easy to understand: if the power spectrum of distant luminous galaxies is measured to be different than that of nearby dim galaxies, then part of this measured bias could be due to the nearby region happening to be more/less clumpy than the distant one. In this chapter, we will eliminate this annoying sample variance by comparing how different galaxies cluster in the *same* region of space, extending the counts-in-cells work of Tegmark and Bromley (1999), Blanton (2000), and Wild et al. (2005) and the correlation function work of Norberg et al. (2001), Norberg et al. (2002), Zehavi et al. (2005), and Li et al. (2006). Here we use the counts-in-cells technique: we divide the survey volume into roughly cubical cells and compare the number of galaxies of each type within each cell. This yields a local, point-by-point measure of the relative bias rather than a global one as in the correlation function method. In other words, by comparing two galaxy density fields directly in real space, including the phase information that correlation function and power spectrum estimators discard, we are able to provide substantially sharper bias constraints.

This local approach also enables us to quantify so-called stochastic bias (Pen 1998; Tegmark and Peebles 1998; Dekel and Lahav 1999; Matsubara 1999). It is well-known that the relation between galaxies and dark matter or between two different types of galaxies is not necessarily deterministic – galaxy formation processes that depend on variables other than the local matter density give rise to stochastic bias as described in Pen (1998), Tegmark and Peebles (1998), Dekel and Lahav (1999), and Matsubara (1999). Evidence for stochasticity in the relative bias between early-type and late-type galaxies has been presented in Wild et al. (2005), Conway et al. (2005), Tegmark and Bromley (1999), and Blanton (2000). Additionally, Simon et al. (2007) finds evidence for stochastic bias between galaxies and dark matter via weak lensing. The time evolution of such stochastic bias has been modeled in Tegmark and Peebles (1998) and was recently updated in Simon (2005). Stochasticity is even predicted in the relative bias between virialized clumps of dark matter (halos) and the linearly-evolved dark matter distribution (Casas-Miranda et al. 2002; Seljak and Warren 2004). Here we aim to test whether stochasticity is necessary for modeling the luminosity-dependent or the color-dependent relative bias.

In this chapter, we study the relative bias as a function of scale using a simple stochastic biasing model by comparing pairs of SDSS galaxy subsamples in cells of varying size. Such a study is timely for two reasons. First of all, the galaxy power spectrum has recently been measured to high precision on large scales with the goal of constraining cosmology (Tegmark et al. 2004b, 2006; Blake et al. 2007; Padmanabhan et al. 2007). As techniques continue to improve and survey volumes continue to grow, it is necessary to reduce systematic uncertainties in order to keep pace with shrinking statistical uncertainties. A detailed understanding of complications due to the dependence of galaxy bias on scale, luminosity,

and color will be essential for making precise cosmological inferences with the next generation of galaxy redshift surveys (Percival et al. 2004; Abazajian et al. 2005; Percival et al. 2007; Zheng and Weinberg 2007; Möller et al. 2007; Kristiansen et al. 2007).

Secondly, a great deal of theoretical progress on models of galaxy formation has been made in recent years, and 2dFGRS and SDSS contain a large enough sample of galaxies that we can now begin to place robust and detailed observational constraints on these models. The framework known as the halo model (Seljak 2000) (see Cooray and Sheth 2002 for a comprehensive review) provides the tools needed to make comparisons between theory and observations. The halo model assumes that all galaxies form in dark matter halos, so the galaxy distribution can be modeled by first determining the halo distribution – either analytically (Catelan et al. 1998; McDonald 2006; Smith et al. 2007) or using N -body simulations (Smith et al. 2003; Kravtsov et al. 2004; Kravtsov 2006) – and then populating the halos with galaxies. This second step can be done using semi-analytical galaxy formation models (Somerville et al. 2001; Berlind et al. 2003; Croton et al. 2006; Baugh 2006) or with a statistical approach using a model for the halo occupation distribution (HOD) (Peacock and Smith 2000; Berlind and Weinberg 2002; Sefusatti and Scoccimarro 2005) or conditional luminosity function (CLF) (Yang et al. 2003; van den Bosch et al. 2003) which prescribes how galaxies populate halos.

Although there are some concerns that the halo model does not capture all of the relevant physics (Yang et al. 2006; Cooray 2006; Gao and White 2007), it has been applied successfully in a number of different contexts (Scranton 2003; Collister and Lahav 2005; Tinker et al. 2006; Skibba et al. 2006). The correlation between a galaxy’s environment (i.e., the local density of surrounding galaxies) and its color and luminosity (Hogg et al. 2004; Blanton et al. 2005a) has been interpreted in the context of the halo model (Berlind et al. 2005; Blanton et al. 2006; Abbas and Sheth 2006), and van den Bosch et al. (2003) and Cooray (2005) make predictions for the bias as a function of galaxy type and luminosity using the CLF formalism. Additionally, Zehavi et al. (2005), Magliocchetti and Porciani (2003), and Abbas and Sheth (2005) use correlation function methods to study the luminosity and color dependence of galaxy clustering, and interpret the results using the Halo Occupation Distribution (HOD) framework. The analysis presented here is complementary to this body of work in that the counts-in-cells method is sensitive to larger scales, uses a different set of assumptions, and compares the two density fields directly in each cell rather than comparing ratios of their second moments. The halo model provides a natural framework in which to interpret the luminosity and color dependence of galaxy biasing statistics we measure here.

The rest of this chapter is organized as follows: §6.2 describes our galaxy data, and §6.3.1 and §6.3.2 describe the construction of our galaxy samples and the partition of the survey volume into cells. In §6.3.3 we outline our relative bias framework, and in §6.3.4 and §6.3.5 we describe our two main analysis methods. We present our results in §6.4 and conclude with a qualitative interpretation of our results in the halo model context in §6.5.

6.2 SDSS Galaxy Data

The SDSS (York et al. 2000; Stoughton et al. 2002) uses a mosaic CCD camera (Gunn et al. 1998) on a dedicated telescope (Gunn et al. 2006) to image the sky in five photometric bandpasses denoted u , g , r , i and z (Fukugita et al. 1996). After astrometric calibration

(Pier et al. 2003), photometric data reduction (Lupton et al. 2001), and photometric calibration (Hogg et al. 2001; Smith et al. 2002; Ivezić et al. 2004; Tucker et al. 2006), galaxies are selected for spectroscopic observations. To a good approximation, the main galaxy sample consists of all galaxies with r -band apparent Petrosian magnitude $r < 17.77$ after correction for reddening as per Schlegel et al. (1998); there are about 90 such galaxies per square degree, with a median redshift of 0.1 and a tail out to $z \sim 0.25$. Galaxy spectra are also measured for the Luminous Red Galaxy sample (Eisenstein et al. 2001), which is not used in this chapter. These targets are assigned to spectroscopic plates of diameter 2.98° by an adaptive tiling algorithm (Blanton et al. 2003b) and observed with a pair of CCD spectrographs (Uomoto et al. 2004), after which the spectroscopic data reduction and redshift determination are performed by automated pipelines. The rms galaxy redshift errors are of order 30 km s^{-1} for main galaxies, hence negligible for the purposes of the present chapter.

Our analysis is based on 380,614 main galaxies (the ‘safe0’ cut) from the 444,189 galaxies in the 5th SDSS data release (‘DR5’) (Adelman-McCarthy et al. 2007), processed via the SDSS data repository at New York University (Blanton et al. 2005b). The details of how these samples were processed and modeled are given in Appendix A of Tegmark et al. (2004b) and in Eisenstein et al. (2005). The bottom line is that each sample is completely specified by three entities:

1. The galaxy positions (RA, Dec, and comoving redshift space distance r for each galaxy) ;
2. The radial selection function $\bar{n}(r)$, which gives the expected (not observed) number density of galaxies as a function of distance ;
3. The angular selection function $\bar{n}(\hat{\mathbf{r}})$, which gives the completeness as a function of direction in the sky, specified in a set of spherical polygons (Hamilton and Tegmark 2004).

The three-dimensional selection functions of our samples are separable, i.e., simply the product $\bar{n}(\mathbf{r}) = \bar{n}(\hat{\mathbf{r}}) \bar{n}(r)$ of an angular and a radial part; here $r \equiv |\mathbf{r}|$ and $\hat{\mathbf{r}} \equiv \mathbf{r}/r$ are the radial comoving distance and the unit vector corresponding to the position \mathbf{r} . The volume-limited samples used in this chapter are constructed so that their radial selection function $\bar{n}(r)$ is constant over a range of r and zero elsewhere. The effective sky area covered is $\Omega \equiv \int \bar{n}(\hat{\mathbf{r}}) d\Omega \approx 5183$ square degrees, and the typical completeness $\bar{n}(\hat{\mathbf{r}})$ exceeds 90 per cent. The conversion from redshift z to comoving distance was made for a flat Λ CDM cosmological model with $\Omega_m = 0.25$. Additionally, we make a first-order correction for redshift space distortions by applying the finger-of-god compression algorithm described in Tegmark et al. (2004b) with a threshold density of $\delta_c = 200$.

6.3 Analysis Methods

6.3.1 Overlapping Volume-Limited Samples

The basic technique used in this chapter is pairwise comparison of the three-dimensional density fields of galaxy samples with different colors and luminosities. As in Zehavi et al. (2005), we focus on these two properties (as opposed to morphological type, spectral type, or surface brightness) for two reasons: they are straightforward to measure from SDSS data, and recent work (Blanton et al. 2005a) has found that luminosity and color is the pair of

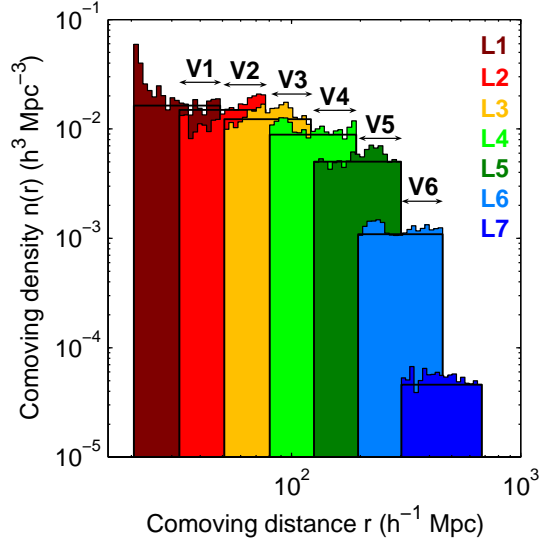


Figure 6-1 Histogram of the comoving number density (after finger-of-god compression) of the volume-limited samples L1-L7. The cuts used to define these samples are shown in Table 6.1. Note that the radial selection function $\bar{n}(r)$ is uniform over the allowed range for each sample. Arrows indicate volumes V1-V6 where neighboring volume-limited samples overlap.

properties that is most predictive of the local overdensity. Since color and spectral type are strongly correlated, our study of the color dependence of bias probes similar physics as studies using spectral type (Tegmark and Bromley 1999; Blanton 2000; Norberg et al. 2002; Wild et al. 2005; Conway et al. 2005).

Our base sample of SDSS galaxies (‘safe0’) has an r -band apparent magnitude range of $14.5 < r < 17.5$. Following the method used in Tegmark et al. (2004b), we created a series of volume-limited samples containing galaxies in different luminosity ranges. These samples are defined by selecting a range of absolute magnitude $M_{\text{luminous}} < M_{0.1r} < M_{\text{dim}}$ and defining a redshift range such that the near limit has $M_{0.1r} = M_{\text{luminous}}$, $r = 14.5$ and the far limit has $M_{0.1r} = M_{\text{dim}}$, $r = 17.5$. Thus by discarding all galaxies outside the redshift range, we are left with a sample with a uniform radial selection function $\bar{n}(r)$ that contains all of the galaxies in the given absolute magnitude range in the volume defined by the redshift limits. Here $M_{0.1r}$ is defined as the absolute magnitude in the r -band shifted to a redshift of $z = 0.1$ (Blanton et al. 2003a).

Our volume-limited samples are labeled L1 through L7, with L1 being the dimmest and L7 being the most luminous. Figure 6-1 shows a histogram of the comoving galaxy density $n(r)$ for L1-L7. The cuts used to make these samples are shown in Table 6.1.

Each sample overlaps spatially only with the samples in neighboring luminosity bins – since the apparent magnitude range spans three magnitudes and the absolute magnitude ranges for each bin span one magnitude, the far redshift limit of a given luminosity bin is approximately equal to the near redshift limit of the bin two notches more luminous. (It is not precisely equal due to evolution and K-corrections.)

The regions where neighboring volume-limited samples overlap provide a clean way to select data for studying the luminosity-dependent bias. By using only the galaxies

Table 6.1 Summary of cuts used to create luminosity-binned volume-limited samples.

Luminosity-binned volume-limited samples	Absolute magnitude	Redshift	Comoving number density \bar{n} ($h^3\text{Mpc}^{-3}$)
L1	$-17 < M_{0.1r} < -16$	$0.007 < z < 0.016$	$(1.63 \pm 0.05) \times 10^{-2}$
L2	$-18 < M_{0.1r} < -17$	$0.011 < z < 0.026$	$(1.50 \pm 0.03) \times 10^{-2}$
L3	$-19 < M_{0.1r} < -18$	$0.017 < z < 0.041$	$(1.23 \pm 0.01) \times 10^{-2}$
L4	$-20 < M_{0.1r} < -19$	$0.027 < z < 0.064$	$(8.86 \pm 0.05) \times 10^{-3}$
L5	$-21 < M_{0.1r} < -20$	$0.042 < z < 0.100$	$(5.02 \pm 0.02) \times 10^{-3}$
L6	$-22 < M_{0.1r} < -21$	$0.065 < z < 0.152$	$(1.089 \pm 0.005) \times 10^{-3}$
L7	$-23 < M_{0.1r} < -22$	$0.101 < z < 0.226$	$(4.60 \pm 0.06) \times 10^{-5}$

Table 6.2 Overlapping volumes in which neighboring luminosity bins are compared.

Pairwise comparison (overlapping) volumes	Overlapping bins	Redshift
V1	L1 & L2	$0.011 < z < 0.016$
V2	L2 & L3	$0.017 < z < 0.026$
V3	L3 & L4	$0.027 < z < 0.041$
V4	L4 & L5	$0.042 < z < 0.064$
V5	L5 & L6	$0.065 < z < 0.100$
V6	L6 & L7	$0.101 < z < 0.152$

in the overlapping region from each of the two neighboring luminosity bins, we obtain two sets of objects (one from the dimmer bin and one from more luminous bin) whose selection is volume-limited and redshift-independent. Furthermore, since they occupy the same volume, they are correlated with the same underlying matter distribution, which eliminates uncertainty due to sample variance and removes potential systematic effects due to sampling different volume sizes (Joyce et al. 2005). We label the overlapping volume regions V1 through V6, where V1 is defined as the overlap between L1 and L2, and so forth. The redshift ranges for V1-V6 are shown Table 6.2.

To study the color dependence of the bias, we further divide each sample into red galaxies and blue galaxies. Figure 6-2 shows the galaxy distribution of our volume-limited samples on a color-magnitude diagram. The sharp boundaries between the different horizontal slices are due to the differences in density and total volume sampled in each luminosity bin. This diagram illustrates the well-known color bimodality, with the redder galaxies falling predominantly in a region commonly known as the E-S0 ridgeline (Balogh et al. 2004; Mateus et al. 2006; Baldry et al. 2006). To separate the E-S0 ridgeline from the rest of the population, we use the same magnitude-dependent color cut as in Zehavi et al. (2005): we define galaxies with $^{0.1}(g-r) < 0.9 - 0.03(M_{0.1r} + 23)$ to be blue and galaxies on the other side of this line to be red.

In each volume V1-V6, we make four separate pairwise comparisons: luminous galaxies vs. dim galaxies, red galaxies vs. blue galaxies, luminous red galaxies vs. dim red galaxies, and luminous blue galaxies vs. dim blue galaxies. The luminous vs. dim comparisons measures the relative bias between galaxies in neighboring luminosity bins, and from this

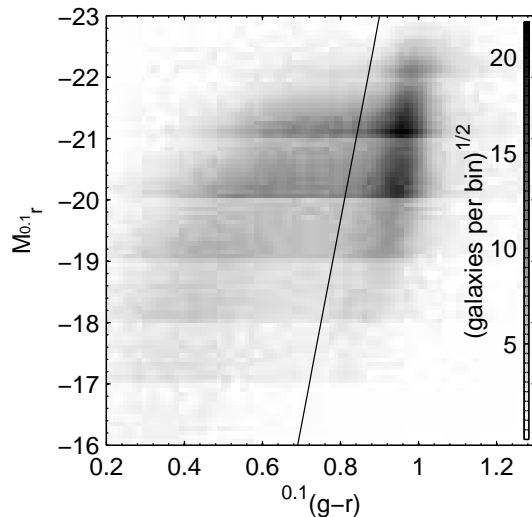


Figure 6-2 Color-magnitude diagram showing the number density distribution of the galaxies in the volume-limited samples. The shading scale has a square-root stretch, with darker areas indicating regions of higher density. The line shows the color cut of $^{0.1}(g-r) = 0.9 - 0.03(M_{0.1,r} + 23)$. We refer to galaxies falling to the left of this line as blue and ones falling to the right of the line as red.

we can extract the luminosity dependence of the bias for all galaxies combined and for red and blue galaxies separately. The red vs. blue comparison measures the color-dependent bias. This set of four different types of pairwise comparisons is illustrated in Fig. 6-3 for V4, and the number of galaxies in each sample being compared is shown in Table 6.3.

6.3.2 Counts-in-Cells Methodology

To compare the different pairs of galaxy samples, we perform a counts-in-cells analysis: we divide each comparison volume into roughly cubical cells and use the number of galaxies of each type in each cell as the primary input to our statistical analysis. This method is complementary to studies based on the correlation function since it involves point-by-point comparison of the two density fields and thus provides a more direct test of the local deterministic linear bias hypothesis. We probe scale dependence by varying the size of the cells.

To create our cells, we first divide the sky into two-dimensional ‘pixels’ at four different angular resolutions using the SDSSPix pixelization scheme¹ as implemented by the updated version of the angular mask processing software MANGLE discussed in Chapter 5 (Hamilton and Tegmark 2004; Swanson et al. 2007). The angular selection function $\bar{n}(\hat{\mathbf{r}})$ is averaged over each pixel to obtain the completeness. To reduce the effects of pixels on the edge of the survey area or in regions affected by internal holes in the survey, we apply a cut on pixel completeness: we only use pixels with a completeness higher than 80 per cent (50 per cent for the lowest angular resolution). Figure 6-4 shows the pixelized SDSS angular mask at our four different resolutions, including only the pixels that pass our completeness

¹See <http://lahmu.phyast.pitt.edu/~scranton/SDSSPix/>

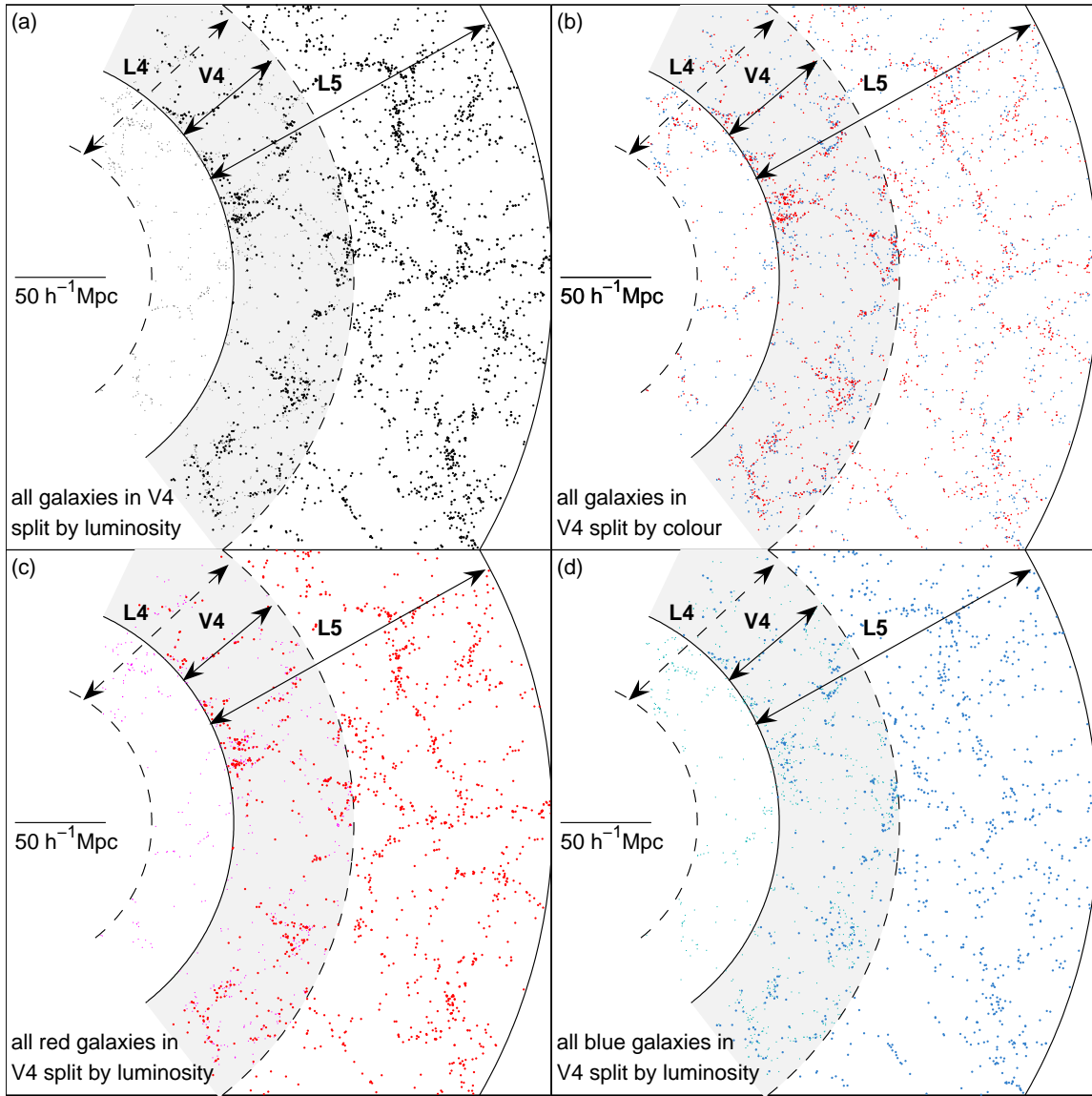


Figure 6-3 Galaxy distributions (after finger-of-god compression) plotted in comoving spatial coordinates for a radial slice of the volume-limited samples L4 (smaller dots, radial boundaries denoted by dashed lines) and L5 (larger dots, radial boundaries denoted by solid lines), which overlap in volume V4. Four different types of pairwise comparisons are illustrated: (a) luminous galaxies (L5) vs. dim galaxies (L4), (b) red galaxies vs. blue galaxies (both in V4), (c) luminous red galaxies (L5) vs. dim red galaxies (L4), and (d) luminous blue galaxies (L5) vs. dim blue galaxies (L4). The shaded regions denote the volume in which the two sets of galaxies are compared. A simple visual inspection shows that the different samples of galaxies being compared generally appear to cluster in the same physical locations – one key question we aim to answer here is if these observed correlations can be described with a simple linear bias model.

Table 6.3 Number of galaxies in each sample being compared.

	All split by luminosity		All split by color	
	Luminous	Dim	Red	Blue
V1	427	651	125	953
V2	2102	2806	1117	3791
V3	6124	8273	5147	9250
V4	12122	23534	17144	18512
V5	11202	53410	37472	27140
V6	1784	38920	27138	13566
	Red split by luminosity		Blue split by luminosity	
	Red luminous	Red dim	Blue luminous	Blue dim
V1	72	53	355	598
V2	620	497	1482	2309
V3	2797	2350	3327	5923
V4	6848	10296	5274	13238
V5	7514	29958	3688	23452
V6	1451	25687	333	13233

cut. The different angular resolutions have 15, 33, 157, and 901 of these angular pixels respectively. At the lowest resolution, each pixel covers 353 square degrees, and the angular area of the pixels decreases by a factor of 1/4 at each resolution level, yielding pixels covering 88, 22, and 5 square degrees at the three higher resolutions.

To produce three-dimensional cells from our pixels, we divide each comparison volume into radial shells of equal volume. We choose the number of radial subdivisions at each angular resolution in each comparison volume such that our cells are approximately cubical, i.e., the radial extent of a cell is approximately equal to its transverse (angular) extent. This procedure makes cells that are not quite perfect cubes – there is some slight variation in the cell shapes, with cells on the near edge of the volume slightly elongated radially and cells on the far edge slightly flattened. We state all of our results as a function of cell size L , defined as the cube root of the cell volume. At the lowest resolution, there is just 1 radial shell for each volume; at the next resolution, we have 3 radial shells for volumes V4 and V5 and 2 radial shells for the other volumes. There are 5 radial shells at the second highest resolution, and 10 at the highest.

Since each comparison volume is at a different distance from us, the angular geometry gives us cells of different physical size in each of the volumes. At the lowest resolution, where there is only one shell in each volume, the cell size is $14 h^{-1}\text{Mpc}$ in V1 and $134 h^{-1}\text{Mpc}$ in V6. At the highest resolution, the cell size is $1.7 h^{-1}\text{Mpc}$ in V1 and $16 h^{-1}\text{Mpc}$ in V6. Figure 6-5 shows the cells in each volume V1-V6 that are closest to a size of $\sim 20 h^{-1}\text{Mpc}$, the range in which the length scales probed by the different volumes overlap. (These are the cells used to produce the results shown in Fig. 6-8.)

6.3.3 Relative Bias Framework

Our task is to quantify the relationship between two fractional overdensity fields $\delta_1(\mathbf{x}) \equiv \rho_1(\mathbf{x})/\bar{\rho}_1 - 1$ and $\delta_2(\mathbf{x}) \equiv \rho_2(\mathbf{x})/\bar{\rho}_2 - 1$ representing two different types of objects. This framework is commonly used with types (1,2) representing (dark matter, galaxies), or as in

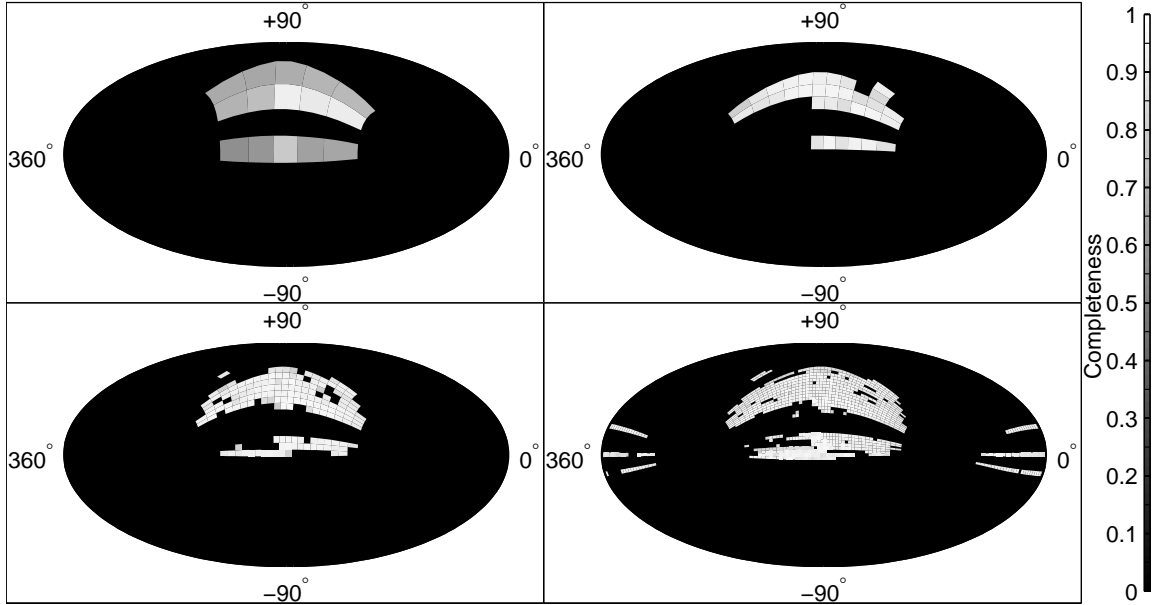


Figure 6-4 The SDSS DR5 angular mask pixelized at the four different resolutions used to partition the survey into cells, shown in Hammer-Aitoff projection in equatorial coordinates. Shading indicates completeness level: 0 per cent is black, 100 per cent is white.

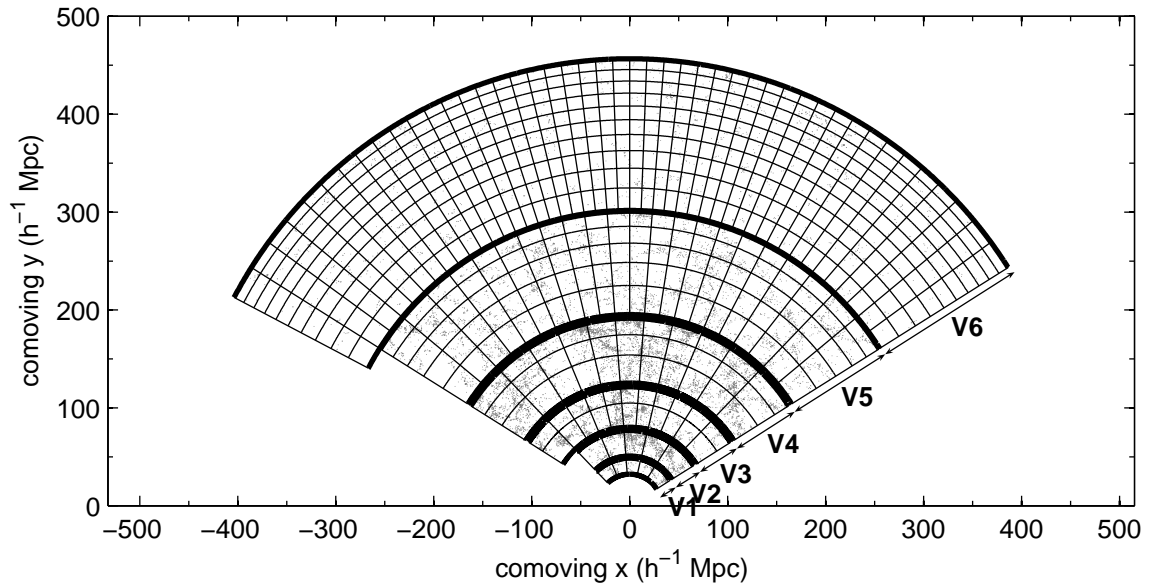


Figure 6-5 A radial slice of the SDSS survey volume divided into cells of size $\sim 20 h^{-1} \text{Mpc}$ with the galaxies in each cell (after finger-of-god compression) shown in grey.

Blanton (2000), Wild et al. (2005), and Conway et al. (2005), (early-type galaxies, late-type galaxies). Here we use it to represent (more luminous galaxies, dimmer galaxies) or (red galaxies, blue galaxies) to compare the samples described in §6.3.1. Galaxies are of course discrete objects, and as customary, we use the continuous field $\rho_\alpha(\mathbf{x})$ (where $\alpha=1$ or 2) to formally refer to the intensity of the Poisson point process involved in distributing the type α galaxies, as described in more detail below.

The simplest (and frequently assumed) relationship between δ_1 and δ_2 is linear deterministic bias:

$$\delta_2(\mathbf{x}) = b_{\text{lin}}\delta_1(\mathbf{x}), \quad (6.1)$$

where b_{lin} is a constant parameter. This model cannot hold in all cases – note that it can give negative densities if $b_{\text{lin}} > 1$ – but is typically a reasonable approximation on cosmologically large length scales where the density fluctuations $\delta_1 \ll 1$, as is the case for the measurements of the large scale power spectrum recently used to constrain cosmological parameters (Tegmark et al. 2004b; Cole et al. 2005; Tegmark et al. 2006). This simple model is likely to break down on length scales small enough to be affected by galaxy formation physics, and such a breakdown could potentially impact the cosmological interpretation of medium- and small-scale power spectrum results from galaxy surveys.

More complicated models allow for non-linearity and stochasticity, as described in detail in Dekel and Lahav (1999):

$$\delta_2(\mathbf{x}) = b[\delta_1(\mathbf{x})]\delta_1(\mathbf{x}) + \epsilon(\mathbf{x}), \quad (6.2)$$

where the bias b is now a (typically slightly non-linear) function of δ_1 . The stochasticity is represented by a random field ϵ – allowing for stochasticity removes the restriction implied by deterministic models that the peaks of δ_1 and δ_2 must coincide spatially. Stochasticity is basically the scatter in the relationship between the two density fields due to physical variables besides the local matter density. Non-local galaxy formation processes can also give rise to stochasticity, as discussed in Matsubara (1999).

The theoretical model we use to describe the galaxy distribution is based on the idea that our universe is one realization drawn from an ensemble of all possible universes that have a given set of cosmological parameters. Any measurement we make in our universe can be described as a random variable over this ensemble of universes. The value we observe is a realization of this random variable. Since we only have one universe to observe, we cannot make repeated observations to draw different values from the distribution. However, we can make theoretical predictions for the probability distribution for a random variable, and then perform statistical tests to see if it is plausible that we would observe the particular value we do if our model is correct. This is the basic idea behind the statistical tests detailed in §6.3.4 and §6.3.5.

Our statistical model is composed of two separate random processes. The first component is the overdensity field $\delta(\mathbf{x})$, which is a realization of a zero-mean random field with a power spectrum predicted by a set of cosmological parameters, as described in §4.1.4. Here, as in §4.1.4, we use regular angle brackets $\langle \rangle$ to denote expectation values over the probability distribution for this random field, e.g., a zero-mean random field $\delta(\mathbf{x})$ has $\langle \delta(\mathbf{x}) \rangle = 0$. The second component is a random point process which describes the locations of galaxies. This is typically taken to be a Poisson point process, which means that the probability of

finding m galaxies in a bounded region A is given by

$$P(m \text{ galaxies in } A) = \frac{[\Lambda(A)]^m}{m!} e^{-\Lambda(A)}, \quad (6.3)$$

where

$$\Lambda(A) \equiv \int_A \lambda(\mathbf{x}) d^3x. \quad (6.4)$$

The function $\lambda(\mathbf{x})$ is the intensity function of the point process. For describing the galaxy distribution, we use $\lambda(\mathbf{x}) = \bar{n}(\mathbf{x})(1 + \delta(\mathbf{x}))$, where $\bar{n}(\mathbf{x})$ is the selection function of the survey as defined in §6.2 – in other words, the expected galaxy density if there were no clustering. Expectation values over this Poisson point process will be denoted by bold angle brackets $\langle \rangle$.

Our basic observational measurement is $\underline{N}_\alpha^{(i)}$, the number of galaxies of type α in cell i observed in our SDSS data sample. We will denote quantities calculated using our SDSS counts-in-cells data – i.e., realizations of random variables in our universe – with underlines. Non-underlined quantities indicate the random variables themselves, for which we compute theoretical expectation values based on the statistical model described above. For example, taking the expectation value over the Poisson point process for type α galaxies in cell i gives

$$\langle N_\alpha^{(i)} \rangle = \bar{N}_\alpha^{(i)} (1 + \delta_\alpha^{(i)}) \quad (6.5)$$

where $\delta_\alpha^{(i)}$ is the volume average of $\delta_\alpha(\mathbf{x})$ over cell i and $\bar{N}_\alpha^{(i)}$ is the integral of the selection function $\bar{n}(\mathbf{x})$ over cell i . Note that aside from slight variations in the angular selection function, $\bar{N}_\alpha^{(i)}$ is the same for all cells i – it is simply the expected number of type α galaxies in cell i in the absence of any clustering. Taking the expectation over the random field realization as well gives

$$\langle \langle N_\alpha^{(i)} \rangle \rangle = \bar{N}_\alpha^{(i)}. \quad (6.6)$$

We estimate the overdensity of galaxies of type α in cell i by

$$\underline{g}_\alpha^{(i)} \equiv \frac{\underline{N}_\alpha^{(i)} - \bar{N}_\alpha^{(i)}}{\bar{N}_\alpha^{(i)}}. \quad (6.7)$$

The n -dimensional vectors

$$\underline{\mathbf{g}}_\alpha \equiv \begin{pmatrix} \underline{g}_\alpha^{(1)} \\ \vdots \\ \underline{g}_\alpha^{(n)} \end{pmatrix} \quad (6.8)$$

contain the counts-in-cells data to which we apply the statistical analyses in §6.3.4 and §6.3.5.

$\underline{\mathbf{g}}_\alpha$ is the realization of the random variable \mathbf{g}_α for our particular universe that we measure from the SDSS data. The covariance matrix of \mathbf{g}_α , which will be the same for any universe drawn from the ensemble defined by our cosmological model, is given by

$$\langle \langle \underline{g}_\alpha^{(i)} \underline{g}_\beta^{(j)} \rangle \rangle = \langle \langle \delta_\alpha^{(i)} \delta_\beta^{(j)} \rangle \rangle + \delta_{\alpha\beta} \mathbf{N}_\alpha^{ij}, \quad (6.9)$$

where $\delta_{\alpha\beta}$ is a Kronecker delta and \mathbf{N}_α is known as the shot noise covariance matrix. The

presence of $\delta_{\alpha\beta}$ implies that we are assuming that type 1 galaxies and type 2 galaxies are distributed via *independent* point processes, so their shot noise is uncorrelated – the correlations between type 1 and type 2 galaxies are encoded in the relationship between $\delta_1(\mathbf{x})$ and $\delta_2(\mathbf{x})$ as in equations (6.1) and (6.2). Although one might expect the fact that the counts of type 1 and type 2 galaxies in a cell is constrained to be equal to the total number of galaxies in the cell could induce correlations in the shot noise, we do not explicitly use the combined total count in our analyses – uncorrelated shot noise is thus a reasonable assumption.

For Poisson point processes, we have

$$\mathbf{N}_\alpha^{ij} \equiv \delta_{ij} / \bar{N}_\alpha^{(i)}. \quad (6.10)$$

For comparing pairs of different types of galaxies, we construct the $2n$ -dimensional data vector

$$\underline{\mathbf{g}} \equiv \begin{pmatrix} \underline{\mathbf{g}}_1 \\ \underline{\mathbf{g}}_2 \end{pmatrix}, \quad (6.11)$$

which, under our theoretical statistical model described above, has covariance matrix

$$\mathbf{C} \equiv \langle \langle \underline{\mathbf{g}} \underline{\mathbf{g}}^T \rangle \rangle = \mathbf{S} + \mathbf{N}, \quad (6.12)$$

with

$$\mathbf{N} \equiv \begin{pmatrix} \mathbf{N}_1 & 0 \\ 0 & \mathbf{N}_2 \end{pmatrix}, \quad \mathbf{S} \equiv \begin{pmatrix} \mathbf{S}_{11} & \mathbf{S}_{12} \\ \mathbf{S}_{12} & \mathbf{S}_{22} \end{pmatrix}, \quad (6.13)$$

and the elements of the matrix \mathbf{S} given by

$$\mathbf{S}_{\alpha\beta}^{ij} = \langle \delta_\alpha^{(i)} \delta_\beta^{(j)} \rangle. \quad (6.14)$$

\mathbf{N} is a diagonal matrix, which indicates that the shot noise is uncorrelated between different cells and also between type 1 and type 2 galaxies within the same cell.

Regarding the matrix \mathbf{S} , other counts-in-cells analyses often assume that the cosmological correlations between different cells can be ignored, i.e., $\langle \delta_\alpha^{(i)} \delta_\beta^{(j)} \rangle = 0$ unless $i = j$. Here we account for cosmological correlations by computing the elements of \mathbf{S} using the best-fitting Λ CDM matter power spectrum as we will now describe in detail. The power spectrum $P_{\alpha\beta}(\mathbf{k})$ is defined as $\langle \hat{\delta}_\alpha(\mathbf{k}) \hat{\delta}_\beta(\mathbf{k}')^\dagger \rangle = (2\pi)^3 \delta^D(\mathbf{k} - \mathbf{k}') P_{\alpha\beta}(\mathbf{k})$, where $\hat{\delta}_\alpha(\mathbf{k}) \equiv \int e^{-i\mathbf{k}\cdot\mathbf{x}} \delta_\alpha(\mathbf{x}) d^3\mathbf{x}$ is the Fourier transform of the overdensity field. $P_{11}(\mathbf{k})$ and $P_{22}(\mathbf{k})$ are the power spectra of type 1 and 2 galaxies respectively, and $P_{12}(\mathbf{k})$ is the cross spectrum between type 1 and 2 galaxies. We assume isotropy and homogeneity, so that $P_{\alpha\beta}(\mathbf{k})$ is a function only of $k \equiv |\mathbf{k}|$, and rewrite the galaxy power spectra in terms of the matter power spectrum $P(k)$:

$$\begin{aligned} P_{11}(k) &= b_1(k)^2 P(k) \\ P_{12}(k) &= b_1(k) b_2(k) r_{12}(k) P(k) \\ P_{22}(k) &= b_2(k)^2 P(k), \end{aligned} \quad (6.15)$$

which defines the functions $b_1(k)$, $b_2(k)$, and $r_{12}(k)$.

To calculate $\langle \delta_\alpha^{(i)} \delta_\beta^{(j)} \rangle$ exactly, we need to convolve $\delta_\alpha(\mathbf{x})$ with a filter representing cell

i and $\delta_\beta(\mathbf{x})$ with a filter representing cell j . This is complicated since our cells, while all roughly cubical, have slightly different shapes. We therefore use an approximation of a spherical top hat smoothing filter with radius R : $w(r, R) \equiv 3/(4\pi R^3)\Theta(R - r)$ with the Fourier transform given by

$$\hat{w}(k, R) = \frac{3}{(kR)^3} [\sin(kR) - kR \cos(kR)]. \quad (6.16)$$

R is chosen so that the effective scale corresponds to cubes with side length L : $R = \sqrt{5/12}L$, where L is the cell size defined in §6.3.2. (See p. 500 in Peacock 1999 for derivation of the $\sqrt{5/12}$ factor.) This gives

$$\langle \delta_\alpha^{(i)} \delta_\beta^{(j)} \rangle = \frac{1}{2\pi^2} \int_0^\infty \frac{\sin(kr_{ij})}{kr_{ij}} P_{\alpha\beta}(k) |\hat{w}(k, R)|^2 k^2 dk, \quad (6.17)$$

where r_{ij} is the distance between the centers of cells i and j . The kernel of this integrand – meaning everything besides $P_{\alpha\beta}(k)$ here – typically peaks at $k \sim 1/R$ and is only non-negligible in a range of $\Delta \log_{10} k \sim 1$. Assuming that the functions $b_1(k)$, $b_2(k)$, and $r_{12}(k)$ vary slowly with k over this range, they can be approximated by their values at $k_{\text{peak}} \equiv 1/R = \sqrt{12/5}/L$ and pulled outside the integral, allowing us to write

$$\mathbf{S} = \sigma_1^2(L) \begin{bmatrix} \mathbf{S}_M & b_{\text{rel}}(L) r_{\text{rel}}(L) \mathbf{S}_M \\ b_{\text{rel}}(L) r_{\text{rel}}(L) \mathbf{S}_M & b_{\text{rel}}(L)^2 \mathbf{S}_M \end{bmatrix} \quad (6.18)$$

where $\sigma_1^2(L) \equiv b_1(k_{\text{peak}})^2$, $b_{\text{rel}}(L) \equiv b_2(k_{\text{peak}})/b_1(k_{\text{peak}})$, $r_{\text{rel}}(L) \equiv r_{12}(k_{\text{peak}})$, and \mathbf{S}_M is the correlation matrix for the underlying matter density:

$$\mathbf{S}_M^{ij} = \frac{1}{2\pi^2} \int_0^\infty \frac{\sin(kr_{ij})}{kr_{ij}} P(k) |\hat{w}(k, R)|^2 k^2 dk. \quad (6.19)$$

For the matter power spectrum $P(k)$, we use the fitting formula from Novosyadlyj et al. (1999) with the best-fitting ‘vanilla’ parameters from Tegmark et al. (2004a) and apply the non-linear transformation of Smith et al. (2003). In principle, using $P(k)$ as determined previously from SDSS data could introduce some model dependence in our results. However, our tests in §6.A.1 using an uncorrelated (i.e., diagonal) signal matrix indicate that the particular choice of the matter power spectrum has no significant effect on the results, so this is not a problem in practice.

Our primary parameters are the relative bias factor $b_{\text{rel}}(L)$, the relative cross-correlation coefficient $r_{\text{rel}}(L)$, and the overall normalization $\sigma_1^2(L)$. The only assumptions we have made in defining these parameters are homogeneity, isotropy, and that $b_1(k)$, $b_2(k)$, and $r_{12}(k)$ vary slowly in k . These parameters are closely related to those in the biasing models specified in equations (6.1) and (6.2): If linear deterministic biasing holds, then $b_{\text{rel}} = b_{\text{lin}}$ and $r_{\text{rel}} = 1$, and the addition of either non-linearity or stochasticity will give $r_{\text{rel}} < 1$. As discussed in Matsubara (1999), stochasticity is expected to vanish in Fourier space (i.e., $r_{12}(k) = 1$) on large scales where the density fluctuations are small, but scale dependence of $b_1(k)$ and $b_2(k)$ can still give rise to stochasticity in real space. We will measure the parameters $b_{\text{rel}}(L)$ and $r_{\text{rel}}(L)$ as a function of scale, thus testing whether the bias is scale dependent and determining the range of scales on which linear biasing holds.

6.3.4 The Null-buster Test

Can the relative bias between dim and luminous galaxies or between red and blue galaxies be explained by simple linear deterministic biasing? To address this question, we use the so-called null-buster test described in Tegmark and Bromley (1999). For a pair of different types of galaxies, we calculate an n -dimensional difference map vector

$$\underline{\mathbf{g}}_{\Delta} \equiv \underline{\mathbf{g}}_2 - f \underline{\mathbf{g}}_1 \quad (6.20)$$

for a range of values of f . (Note that $\underline{\mathbf{g}}_{\Delta}$ contains a model parameter f even though it is constructed from observed quantities.) If equation (6.1) holds and $f = b_{\text{lin}}$, then the density fluctuations cancel and $\underline{\mathbf{g}}_{\Delta}$ will contain only shot noise, with a covariance matrix $\langle \langle \underline{\mathbf{g}}_{\Delta} \underline{\mathbf{g}}_{\Delta}^T \rangle \rangle = \mathbf{N}_{\Delta} \equiv \mathbf{N}_2 + f^2 \mathbf{N}_1$ – this is our null hypothesis. Alternatively, if equation (6.1) does not hold, the covariance matrix is instead given by $\langle \langle \underline{\mathbf{g}}_{\Delta} \underline{\mathbf{g}}_{\Delta}^T \rangle \rangle = \mathbf{N}_{\Delta} + \mathbf{S}_{\Delta}$, where \mathbf{S}_{Δ} is some residual signal. We want to construct a test to confirm or refute the null hypothesis of deterministic linear bias. We aim to distinguish between the following two cases:

- Null hypothesis H_0 : $\langle \langle \underline{\mathbf{g}}_{\Delta} \underline{\mathbf{g}}_{\Delta}^T \rangle \rangle = \mathbf{N}_{\Delta}$ for some value of f .
- Alternate hypothesis H_1 : $\langle \langle \underline{\mathbf{g}}_{\Delta} \underline{\mathbf{g}}_{\Delta}^T \rangle \rangle = \mathbf{N}_{\Delta} + \mathbf{S}_{\Delta}$ even when f is chosen to minimize the contribution of \mathbf{S}_{Δ} .

One valid test of H_0 would be a χ^2 test – that is, compute a χ^2 statistic assuming H_0 is true (so $\underline{\chi}^2 \equiv \underline{\mathbf{g}}_{\Delta}^T \mathbf{N}_{\Delta}^{-1} \underline{\mathbf{g}}_{\Delta}$), minimize χ^2 with respect to the parameter f , and then check to see whether $\underline{\chi}_{\text{min}}^2$, the value of $\underline{\chi}^2$ at the minimum point, indicates a good model fit. For a system with N degrees of freedom where $N \gg 1$, the distribution of χ^2 can be approximated as a Gaussian distribution with mean N and variance $2N$ – here $N = n - 1$ (the number of cells n minus 1 fitted parameter f). Thus $(\underline{\chi}_{\text{min}}^2 - N) / \sqrt{2N}$ is a measure of the number of ‘sigmas’ the observed $\underline{\chi}_{\text{min}}^2$ value lies away from the mean expected value if H_0 is true. The usual convention is to consider the model a good fit if $\left| (\underline{\chi}_{\text{min}}^2 - N) / \sqrt{2N} \right| < 2$, i.e., the data is consistent with the null hypothesis at the 2σ level.

However, if we have some knowledge of the form that a deviation from the null hypothesis is likely to take (that is, a model for the residual signal \mathbf{S}_{Δ}), we can construct a statistic that is more sensitive than χ^2 for ruling out the null hypothesis H_0 in the event that the alternate hypothesis H_1 is true. Here we follow Tegmark and Peebles (1998) and Tegmark (1999) and generalize the χ^2 test statistic by constructing a quadratic test statistic $q \equiv \underline{\mathbf{g}}_{\Delta}^T \mathbf{E} \underline{\mathbf{g}}_{\Delta}$ for some matrix \mathbf{E} . We want to choose \mathbf{E} such that our test will rule out H_0 with maximum significance if H_1 is true. Our generalized version of $(\underline{\chi}_{\text{min}}^2 - N) / \sqrt{2N}$, the significance level (i.e. the number of ‘sigmas’) at which we can rule out H_0 , is given by

$$\underline{\nu} \equiv \frac{q - \langle \langle q | H_0 \rangle \rangle}{\Delta q} \quad (6.21)$$

where $(\Delta q)^2 \equiv \langle \langle q^2 | H_0 \rangle \rangle - \langle \langle q | H_0 \rangle \rangle^2$ is the variance of q given that H_0 is true. The desired matrix \mathbf{E} maximizes

$$\langle \langle \nu | H_1 \rangle \rangle = \frac{\langle \langle q | H_1 \rangle \rangle - \langle \langle q | H_0 \rangle \rangle}{\Delta q}, \quad (6.22)$$

the expected value of ν if the alternate hypothesis H_1 holds. The matrix \mathbf{E} satisfying this requirement is derived in Tegmark (1999) to be $\mathbf{E} \propto \mathbf{N}_\Delta^{-1} \mathbf{S}_\Delta \mathbf{N}_\Delta^{-1}$, which we insert into equation (6.21) to give our null-buster statistic:

$$\underline{\nu} = \frac{\underline{\mathbf{g}}_\Delta^T \mathbf{N}_\Delta^{-1} \mathbf{S}_\Delta \mathbf{N}_\Delta^{-1} \underline{\mathbf{g}}_\Delta - \text{Tr}(\mathbf{N}_\Delta^{-1} \mathbf{S}_\Delta)}{[2 \text{Tr}(\mathbf{N}_\Delta^{-1} \mathbf{S}_\Delta \mathbf{N}_\Delta^{-1} \mathbf{S}_\Delta)]^{1/2}}. \quad (6.23)$$

This can be interpreted as the significance level (i.e. the number of ‘sigmas’) at which we can rule out the null hypothesis H_0 of deterministic linear bias. As detailed in Tegmark (1999), this test assumes that the Poisson shot noise contribution can be approximated as Gaussian but makes no other assumptions about the probability distribution of $\underline{\mathbf{g}}_\Delta$. It is a valid test for any choice of \mathbf{S}_Δ and reduces to a standard χ^2 test if $\mathbf{S}_\Delta = \mathbf{N}_\Delta$, but it rules out H_0 with maximum significance in the case where H_1 is true, i.e., where \mathbf{S}_Δ is the true residual signal.

Using equations (6.13), (6.14), and (6.18), the covariance matrix of $\underline{\mathbf{g}}_\Delta$ can be written as

$$\langle \underline{\mathbf{g}}_\Delta \underline{\mathbf{g}}_\Delta^T \rangle = \sigma_1^2 (f^2 - 2b_{\text{rel}} r_{\text{rel}} f + b_{\text{rel}}^2) \mathbf{S}_M + \mathbf{N}_\Delta, \quad (6.24)$$

where \mathbf{S}_M is given by equation (6.19). We use $\mathbf{S}_\Delta = \mathbf{S}_M$ in equation (6.23) (note that ν is independent of the normalization of \mathbf{S} , which scales out) since deviations from linear deterministic bias are likely to be correlated with large-scale structure.

To apply the null-buster test, we compute $\underline{\nu}$ as a function of f and then minimize it. If the minimum value $\underline{\nu}_{\text{min}} > 2$, we rule out linear deterministic bias at $> 2\sigma$. If the null hypothesis cannot be ruled out and we choose to accept it as an accurate description of the data, we can take r_{rel} to be equal to unity and then use the value of f that gives $\underline{\nu}_{\text{min}}$ as a measure of b_{rel} .

We calculate the uncertainty on b_{rel} using two different methods. The first method makes use of the fact that ν is generalized χ^2 statistic: the uncertainty on b_{rel} , is given by the range in f that gives $\sqrt{2N} (\underline{\nu} - \underline{\nu}_{\text{min}}) \leq 1$, where N is the number of degrees of freedom (equal to the number of cells minus 1 fitted parameter). This is a generalization of the standard $\Delta\chi^2 = 1$ uncertainty since ν is a generalization of $(\chi_{\text{min}}^2 - N) / \sqrt{2N}$. The second method uses jackknife resampling, which is described in §6.B.1 along with a comparison of the two methods. We present all of our results derived from the null-buster test using the uncertainties from the jackknife method.

6.3.5 Maximum Likelihood Method

In addition to the null-buster test, we use a maximum likelihood analysis to determine the parameters b_{rel} and r_{rel} . Our method is a generalization of the maximum likelihood method used in previous work, accounting for correlations between different cells but making a somewhat different set of assumptions.

In Blanton (2000), Wild et al. (2005), Conway et al. (2005), the probability of observing N_1 galaxies of type 1 and N_2 galaxies of type 2 in a given cell is expressed as

$$P(N_1, N_2) = \int_{-1}^{\infty} \int_{-1}^{\infty} \text{Pois} [N_1, \bar{N}_1 (1 + \delta_1)] \times \text{Pois} [N_2, \bar{N}_2 (1 + \delta_2)] f(\delta_1, \delta_2, \alpha) d\delta_1 d\delta_2, \quad (6.25)$$

where $f(\delta_1, \delta_2, \alpha)$ is the joint probability distribution of δ_1 and δ_2 in one cell, α represents a set of parameters which depend on the biasing model, and $\text{Poiss}(N, \lambda) \equiv \lambda^N e^{-\lambda}/N!$ is the Poisson probability to observe N objects given a mean value λ . The likelihood function for n cells is given a set of observations $\underline{N}_1^{(i)}$ and $\underline{N}_2^{(i)}$ is then given by

$$\mathcal{L}(\alpha) \equiv \prod_{i=1}^n P\left(\underline{N}_1^{(i)}, \underline{N}_2^{(i)}\right), \quad (6.26)$$

which is minimized with respect to the parameters α . This treatment makes two assumptions: it neglects correlations between different cells and it assumes that the galaxy discreteness is Poissonian. These assumptions greatly simplify the computation of \mathcal{L} , but are understood to be approximations to the true process. Cosmological correlations are known to exist on large scales, although their impact on counts-in-cells analyses has been argued to be small (Broadhurst et al. 1995; Conway et al. 2005). Semi-analytical modeling (Sheth and Diaferio 2001; Berlind and Weinberg 2002), N -body simulation (Casas-Miranda et al. 2002; Kravtsov et al. 2004), and smoothed particle hydrodynamic simulation (Berlind et al. 2003) investigations suggest that the probability distribution for galaxies/halos is sub-Poissonian in some regimes, and in fact non-Poissonian behavior is implied by observations as well (Yang et al. 2003; Wild et al. 2005).

Dropping these two assumptions, we can write a more general expression for the likelihood function for n cells:

$$\begin{aligned} \mathcal{L}(\alpha, \beta) &\equiv P\left(\underline{N}_1^{(1)}, \dots, \underline{N}_1^{(n)}, \underline{N}_2^{(1)}, \dots, \underline{N}_2^{(n)}\right) = \\ &\int_{-1}^{\infty} \dots \int_{-1}^{\infty} \left[\prod_{i=1}^n P_g\left(\underline{N}_1^{(i)}, \bar{N}_1^{(i)}(1 + \delta_1^{(i)}), \beta\right) \right] \\ &\times \left[\prod_{j=1}^n P_g\left(\underline{N}_2^{(j)}, \bar{N}_2^{(j)}(1 + \delta_2^{(j)}), \beta\right) \right] \\ &\times f\left(\delta_1^{(1)}, \dots, \delta_1^{(n)}, \delta_2^{(1)}, \dots, \delta_2^{(n)}, \alpha\right) \\ &\times d\delta_1^{(1)} \dots d\delta_1^{(n)} d\delta_2^{(1)} \dots d\delta_2^{(n)}, \end{aligned} \quad (6.27)$$

where $\text{Poiss}(N, \lambda)$ has been replaced with a generic probability $P_g(N, \lambda, \beta)$ for the galaxy distribution parameterized by some parameters β and $f\left(\delta_1^{(1)}, \dots, \delta_1^{(n)}, \delta_2^{(1)}, \dots, \delta_2^{(n)}, \alpha\right)$ is a joint probability distribution relating δ_1 and δ_2 in all cells. In practice, this would be prohibitively difficult to calculate as it involves $2n$ integrations (Dodelson et al. 1997), and would require a reasonable parameterized form for $P_g(N, \lambda, \beta)$ as well as $f\left(\delta_1^{(1)}, \dots, \delta_1^{(n)}, \delta_2^{(1)}, \dots, \delta_2^{(n)}, \alpha\right)$.

In this chapter, we take a simpler approach and approximate the probability distribution for our data vector \mathbf{g} to be Gaussian with the covariance matrix \mathbf{C} as defined by equations (6.12), (6.13) and (6.18), and use this to define our likelihood function in terms of the parameters σ_1^2 , b_{rel} , and r_{rel} :

$$\begin{aligned} \mathcal{L}(\sigma_1^2, b_{\text{rel}}, r_{\text{rel}}) &\equiv P(\underline{g}_1^{(1)}, \dots, \underline{g}_1^{(n)}, \underline{g}_2^{(1)}, \dots, \underline{g}_2^{(n)}) \\ &= \frac{1}{(2\pi)^n |\mathbf{C}|^{1/2}} \exp\left(-\frac{1}{2} \underline{\mathbf{g}}^\dagger \mathbf{C}^{-1} \underline{\mathbf{g}}\right). \end{aligned} \quad (6.28)$$

Note that this includes the shot noise since $\mathbf{C} = \mathbf{S} + \mathbf{N}$, and is not precisely equivalent to assuming that P_g and f in equation (6.27) are Gaussian.

For r_{rel} values of $|r_{\text{rel}}| > 1$, the matrix \mathbf{C} is singular, and thus the likelihood function cannot be computed. Hence this analysis method automatically incorporates the constraint that $|r_{\text{rel}}| \leq 1$, which is physically expected for a cross-correlation coefficient.

To determine the best fit values of our parameters for each pairwise comparison, we maximize $2 \ln \mathcal{L}(\sigma_1^2, b_{\text{rel}}, r_{\text{rel}})$ with respect to σ_1^2 , b_{rel} , and r_{rel} . Since our method of comparing pairs of galaxy samples primarily probes the relative biasing between the two types of galaxies, it is not particularly sensitive to σ_1^2 , which represents the bias of type 1 galaxies relative to the dark matter power spectrum used in equation (6.19). Thus we marginalize over σ_1^2 and calculate the uncertainty on b_{rel} and r_{rel} using the $\Delta(2 \ln \mathcal{L}) = 1$ contour in the $b_{\text{rel}}-r_{\text{rel}}$ plane. This procedure is discussed in more detail in §6.B.2.

6.4 Results

6.4.1 Null-buster Results

To test the deterministic linear bias model, we apply the null-buster test described in §6.3.4 to the pairs of galaxy samples described in §6.3.1. For studying the luminosity-dependent bias, we use the galaxies in the more luminous bin as the type 1 galaxies and the dimmer bin as the type 2 galaxies for each pair of neighboring luminosity bins, and repeat this in each volume V1-V6. We do this for all galaxies and also for red and blue galaxies separately. For the color dependence, we use red galaxies as type 1 and blue galaxies as type 2, and again repeat this in each volume. To determine the scale dependence, we repeat all of these tests for four different values of the cell size L as described in §6.3.2.

Is the bias linear and deterministic?

The results are plotted in Fig. 6-6, which shows the minimum value of the null-buster test statistic $\underline{\nu}_{\text{min}}$ vs. cell size L . According to this test, deterministic linear biasing is in fact an excellent fit for the luminosity-dependent bias: nearly all $\underline{\nu}_{\text{min}}$ fall within $|\underline{\nu}_{\text{min}}| < 2$, indicating consistency with the null hypothesis at the 2σ level. (There are a few exceptions in the case of the red galaxies, the largest being $\underline{\nu}_{\text{min}} \sim 5$ for the smallest cell size in V3.) For color-dependent bias, however, deterministic linear biasing is ruled out quite strongly, especially at smaller scales.

The cases where the null hypothesis survives are quite noteworthy, since this implies that essentially all of the large clustering signal that is present in the data (and is visually apparent in Fig. 6-3) is common to the two galaxy samples and can be subtracted out. For example, for the V5 luminosity split at the highest angular resolution ($L = 10 h^{-1} \text{Mpc}$), clustering signal is detected at 953σ in the faint sample ($\underline{\nu}(f) \approx 953$ for $f = 0$) and at 255σ in the bright sample ($\underline{\nu}(f) \approx 255$ for $f = \infty$), yet the weighted difference of the

two maps is consistent with mere shot noise ($\underline{\nu}(0.88) \approx -0.63$). This also shows that no luminosity-related systematic errors afflict the sample selection even at that low level.

Is the bias independent of scale?

For the luminosity-dependent bias, we use the value of f that gives $\underline{\nu}_{\min}$ as a measure of b_{rel} , the relative bias between two neighboring luminosity bins. Since deterministic linear bias is ruled out in the case of the color-dependent bias, we instead use the value of b_{rel} from the likelihood analysis here. We find that although the value of b_{rel} depends on luminosity, it does not appear to depend strongly on scale, as can be seen in Fig. 6-7: in all plots the curves appear roughly horizontal. To test this ‘chi-by-eye’ inference of scale independence quantitatively, we applied a simple χ^2 fit on the four data points (or three in the color-dependent case) in each volume using a one-parameter model: a horizontal line with a constant value of b_{rel} . For this fit we use covariance matrices derived from jackknife resampling, as discussed in §6.B.1. We define this model to be a good fit if the goodness-of-fit value (the probability that a χ^2 as poor as the value calculated should occur by chance, as defined in Press et al. 1992) exceeds 0.01.

We find that this model of no scale dependence is a good fit for all data sets plotted in Fig. 6-7. We therefore find no evidence that the luminosity- or color-dependent bias is scale-dependent on the scales we probe here ($2 - 160 h^{-1}\text{Mpc}$). This implies that recent cosmological parameter analyses which use only measurements on scales $\gtrsim 60 h^{-1}\text{Mpc}$ (e.g., Sánchez et al. 2006; Tegmark et al. 2006; Spergel et al. 2007) are probably justified in assuming scale independence of luminosity-dependent bias.

In comparison to previous work (Zehavi et al. 2005; Li et al. 2006), it is perhaps surprising to see as little scale dependence as we do – Li et al. (2006) find the luminosity-dependent bias to vary with scale (see their fig. 4), in contrast to what we find here. The measurement of luminosity-dependent bias in Zehavi et al. (2005) agrees more closely with our observation of scale independence, but their fig. 10 indicates that we might expect to see scale dependence of the luminosity-dependent bias in the most luminous samples. However, we measure the bias in our most luminous samples (in V6) at $16 - 134 h^{-1}\text{Mpc}$, well above the range probed in Zehavi et al. (2005), so there is no direct conflict here. Additionally, fig. 13 of Zehavi et al. (2005) and fig. 10 of Li et al. (2006) show that correlation functions of red and blue galaxies have significantly different slopes, implying that the color-dependent bias should be strongly scale-dependent on $0.1 - 10 h^{-1}\text{Mpc}$ scales. However, the points $> 1 h^{-1}\text{Mpc}$ in these plots (the range comparable to the scales we probe here) do not appear strongly scale dependent, so our results are not inconsistent with these correlation function measurements. This interpretation is further supported by recent work (Wang et al. 2007) that finds correlation functions for different luminosities and colors to be roughly parallel above $\sim 1 h^{-1}\text{Mpc}$.

How bias depends on luminosity

Our next step is to calculate the relative bias parameter b/b_* (the bias relative to L_* galaxies) as a function of luminosity by combining the measured values of b_{rel} between the different pairs of luminosity bins. This function has been measured previously using SDSS power spectra (Tegmark et al. 2004b) at length scales of $\sim 60 h^{-1}\text{Mpc}$ as well as SDSS (Zehavi et al. 2005; Li et al. 2006; Wang et al. 2007) and 2dFGRS (Norberg et al. 2001) correlation functions at length scales of $\sim 1 h^{-1}\text{Mpc}$ – here we measure it at length scales

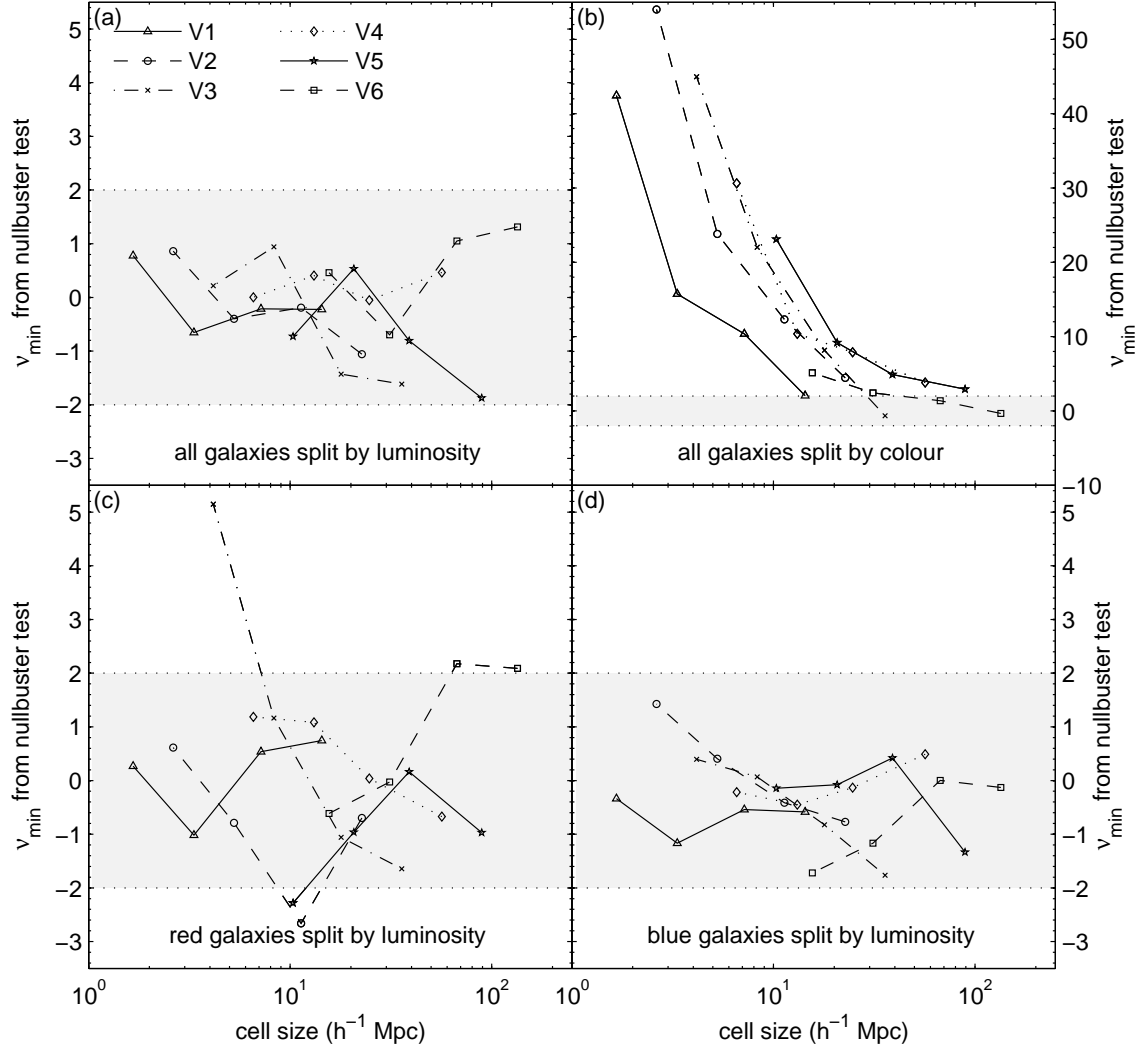


Figure 6-6 Null-buster results for pairwise comparisons. ν_{\min} measures the number of sigmas at which deterministic linear biasing can be ruled out as a model of relative bias between the two samples being compared. Shaded areas indicate $|\nu_{\min}| < 2$, where data is consistent with the null hypothesis at the 2σ level. Four different types of pairwise comparison are illustrated: (a) luminous vs. dim, (b) red vs. blue, (c) luminous red vs. dim red, and (d) luminous blue vs. dim blue. The different symbols denote the different comparison volumes V1-V6. The luminosity-dependent bias (a, c, d) is consistent with deterministic linear biasing but color-dependent bias (b) is not.

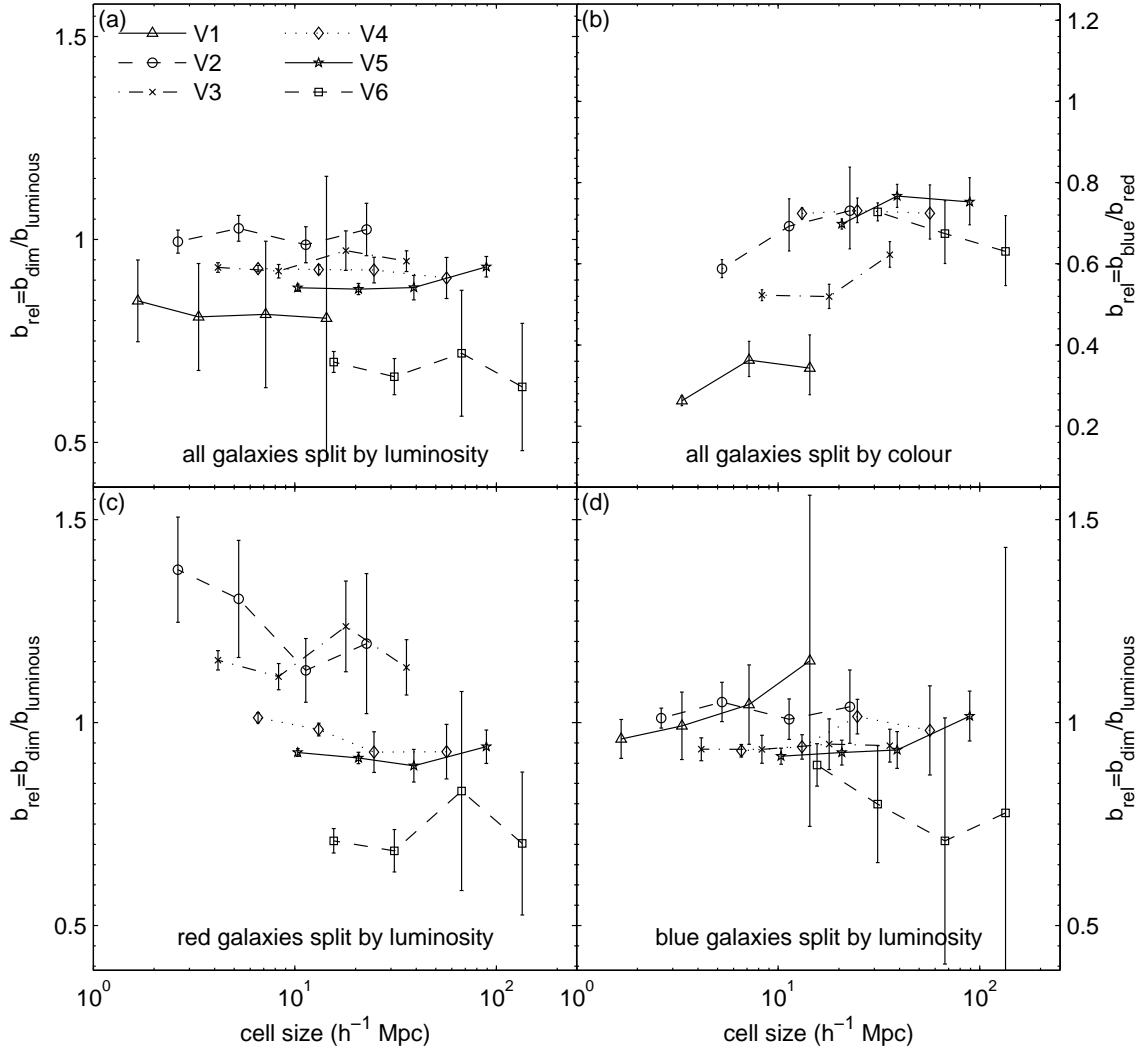


Figure 6-7 Relative bias b_{rel} between pairwise samples. (a) luminous vs. dim, (b) red vs. blue, (c) luminous red vs. dim red, and (d) luminous blue vs. dim blue, revealing no significant scale dependence of luminosity- or color-dependent bias. The b_{rel} values shown for luminosity dependent splittings (a), (c), and (d) were computed with the null-buster analysis, those shown for the color-dependent splitting (b) were computed with the likelihood analysis. The different symbols denote the different comparison volumes V1-V6.

of $\sim 20 h^{-1}\text{Mpc}$.

The bias of each luminosity bin relative to the central bin L4 is given by

$$\begin{aligned} \frac{b_1}{b_4} &= b_{12}b_{23}b_{34}, & \frac{b_2}{b_4} &= b_{23}b_{34}, & \frac{b_3}{b_4} &= b_{34}, \\ \frac{b_7}{b_4} &= \frac{1}{b_{45}b_{56}b_{67}}, & \frac{b_6}{b_4} &= \frac{1}{b_{45}b_{56}}, & \frac{b_5}{b_4} &= \frac{1}{b_{45}}, \end{aligned} \quad (6.29)$$

where $b_{\alpha\beta}$ denotes the measured value of b_{rel} between luminosity bins $L\alpha$ and $L\beta$ using all galaxies and b_α denotes the bias of galaxies in luminosity bin $L\alpha$ relative to the dark matter. For each pairwise comparison, we choose the value of b_{rel} calculated at the resolution where the cell size is closest to $20 h^{-1}\text{Mpc}$, as illustrated in Fig. 6-5. (Since we see no evidence for scale dependence of b_{rel} for the luminosity-dependent bias, this choice does not strongly influence the results.)

To compute the error bars on b_α/b_4 , we rewrite equation (6.29) as a linear matrix equation using the logs of the bias values:

$$\begin{pmatrix} 1 & -1 & 0 & 0 & 0 & 0 \\ 0 & 1 & -1 & 0 & 0 & 0 \\ 0 & 0 & 1 & 0 & 0 & 0 \\ 0 & 0 & 0 & -1 & 0 & 0 \\ 0 & 0 & 0 & 1 & -1 & 0 \\ 0 & 0 & 0 & 0 & 1 & -1 \end{pmatrix} \begin{pmatrix} \log b_1/b_4 \\ \log b_2/b_4 \\ \log b_3/b_4 \\ \log b_5/b_4 \\ \log b_6/b_4 \\ \log b_7/b_4 \end{pmatrix} = \begin{pmatrix} \log b_{12} \\ \log b_{23} \\ \log b_{34} \\ \log b_{45} \\ \log b_{56} \\ \log b_{67} \end{pmatrix}, \quad (6.30)$$

or $\mathbf{A}\mathbf{b}_{\text{log}} = \mathbf{b}_{\text{log,rel}}$, where $\mathbf{b}_{\text{log,rel}}$ is a vector of the log of our relative bias measurements $b_{\alpha\beta}$, \mathbf{b}_{log} is a vector of the log of the bias values b_α/b_4 , and \mathbf{A} is the matrix relating them. We determine the covariance matrix Σ_{rel} of \mathbf{b}_{rel} (a vector of the relative bias measurements $b_{\alpha\beta}$) from the jackknife resampling described in §6.B.1, and then compute the covariance matrix $\Sigma_{\text{log,rel}}$ of $\mathbf{b}_{\text{log,rel}}$ by

$$\Sigma_{\text{log,rel}} = (\mathbf{B}_{\text{rel}}^T)^{-1} \Sigma_{\text{rel}} \mathbf{B}_{\text{rel}}^{-1} \quad (6.31)$$

where $\mathbf{B}_{\text{rel}} \equiv \text{diag}(\mathbf{b}_{\text{rel}})$. We invert equation (6.30) to give \mathbf{b}_{log} :

$$\mathbf{b}_{\text{log}} = \mathbf{A}^{-1} \mathbf{b}_{\text{log,rel}}, \quad (6.32)$$

with the covariance matrix for \mathbf{b}_{log} given by

$$\Sigma_{\text{log}} = (\mathbf{A}^T \Sigma_{\text{log,rel}}^{-1} \mathbf{A})^{-1}. \quad (6.33)$$

We then fit our data with the model used in Norberg et al. (2001): $b(M)/b_* = a_1 + a_2(L/L_*)$, parameterized by $\mathbf{a} \equiv (a_1, a_2)$. Here M is the central absolute magnitude of the bin, L is the corresponding luminosity, and $M_* = -20.83$. We use a weighted least-squares

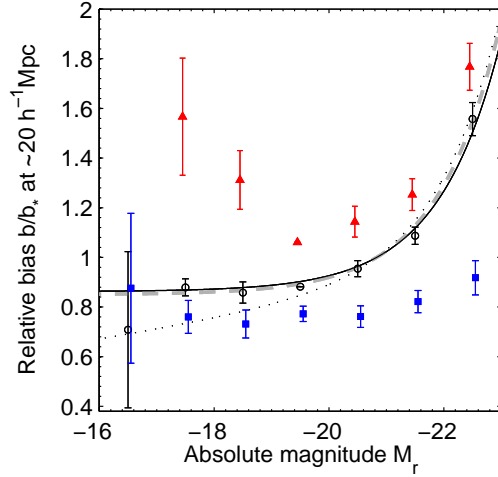


Figure 6-8 Luminosity dependence of bias for all (open circles), red (solid triangles), and blue (solid squares) galaxies at a cell size of $\sim 20 h^{-1}\text{Mpc}$ from null-buster results. The solid line is a model fit to the all-galaxy data points, the dotted line shows the model from Tegmark et al. (2004b), and the grey dashed line shows the model from Norberg et al. (2001). The Norberg et al. (2001) model has been computed using the SDSS r -band value of $M_* = -20.83$.

fit that is linear in the parameters (a_1, a_2) – that is, we solve the matrix equation

$$\begin{pmatrix} b_1/b_4 \\ b_2/b_4 \\ b_3/b_4 \\ b_4/b_4 \\ b_5/b_4 \\ b_6/b_4 \end{pmatrix} = \begin{pmatrix} 1 & L_1/L_4 \\ 1 & L_2/L_4 \\ 1 & L_3/L_4 \\ 1 & L_4/L_4 \\ 1 & L_5/L_4 \\ 1 & L_6/L_4 \end{pmatrix} \begin{pmatrix} a_1 \\ a_2 \end{pmatrix}, \quad (6.34)$$

or $\mathbf{b} = \mathbf{X}\mathbf{a}$, where \mathbf{b} is a vector of the bias values b_α/b_4 and \mathbf{X} is the matrix representing our model. We solve for \mathbf{a} using

$$\mathbf{a} = (\mathbf{X}^T \boldsymbol{\Sigma}^{-1} \mathbf{X})^{-1} \mathbf{X}^T \boldsymbol{\Sigma}^{-1} \mathbf{b}. \quad (6.35)$$

Here $\boldsymbol{\Sigma}$ is the covariance matrix of \mathbf{b} , given by

$$\boldsymbol{\Sigma} = \mathbf{B} \boldsymbol{\Sigma}_{\log} \mathbf{B}^T, \quad (6.36)$$

where $\boldsymbol{\Sigma}_{\log}$ is given by equation (6.33) and $\mathbf{B} \equiv \text{diag}(\mathbf{b})$. This procedure gives us the best-fitting values for the parameters a_1 and a_2 , accounting for the correlations between the data points that are induced we compute the bias values \mathbf{b} from our relative bias measurements. We then normalize the model such that $b(M_*)/b_* = 1$.

Figure 6-8 shows a plot of b/b_* vs. M : results for all galaxies are plotted with black open circles, our best-fitting model is shown by the solid line, the best-fitting model from

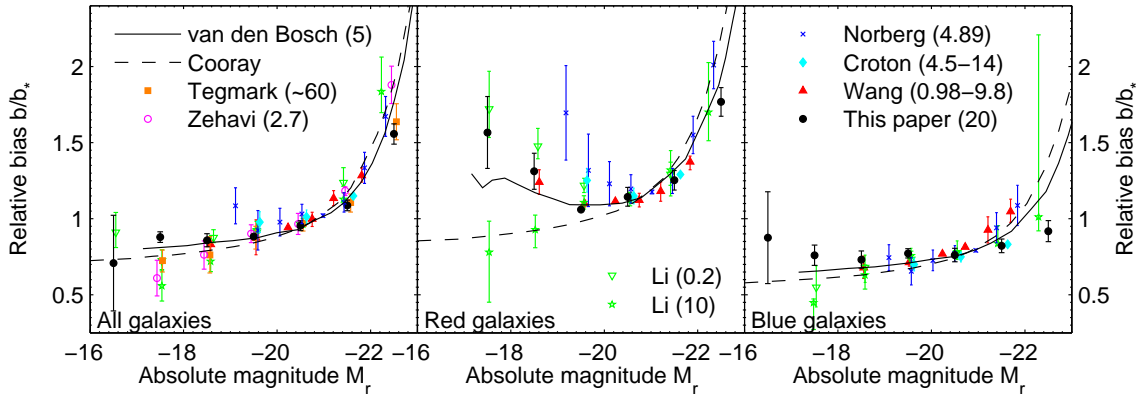


Figure 6-9 Comparison to previous results for the luminosity dependence of bias for all, red, and blue galaxies. Norberg et al. (2002); Zehavi et al. (2005); Li et al. (2006), and Wang et al. (2007) use correlation function measurements, Tegmark et al. (2004b) use the power spectrum, and Croton et al. (2007) use counts in cells. To better illustrate the similarities and differences in the trends as a function of luminosity, we have normalized all measurements to match our results using the bin closest to $M_* = -20.83$. The error bars shown are all relative: they do not include uncertainties due to the normalization. Numbers in parentheses denote the scale in $h^{-1}\text{Mpc}$ at which the measurements were done. Also shown are theoretical models from van den Bosch et al. (2003) (we show their model B as a representative example) and Cooray (2005) – these are also normalized to match our results at M_* .

Norberg et al. (2001) is shown by the grey dashed line, and the best-fitting model from Tegmark et al. (2004b) is shown by the dotted line. The error bars represent the diagonal elements of Σ from equation (6.36). Our model, with $(a_1, a_2) = (0.862, 0.138)$, agrees extremely well with the model from Norberg et al. (2001), with $(a_1, a_2) = (0.85, 0.15)$. This agreement is quite remarkable since we use data from a different survey and analyze it with a completely different technique.

A comparison of our results with previous measurements is shown in Fig. 6-9 in the left panel. In order to compare our SDSS results with results from 2dFGRS (Norberg et al. 2002; Croton et al. 2007), we have added a constant factor of -1.13 to their quoted values for $M_{b_J} - 5 \log_{10} h$ in order to line up the value of M_* used in Norberg et al. (2002) ($M_{b_J} - 5 \log_{10} h = -19.7$) with the value used here ($M_{01.r} = -20.83$). Note that this is necessarily a rough correction since the magnitude in the different bands varies depending on the spectrum of each galaxy, but this method provides a reasonable means of comparing the different results. This plot shows excellent agreement over a wide range of scales, lending further support to our conclusion that the luminosity-dependent bias is independent of scale.

We also use equation (6.32) to calculate b/b_* vs. M for red and blue galaxies separately. To plot the points for red, blue, and all galaxies on the same b/b_* vs. M plot, we need to determine their relative normalizations. Applying equation (6.32) to the red and blue galaxies gives $b_{\alpha,\text{red}}/b_{4,\text{red}}$ and $b_{\alpha,\text{blue}}/b_{4,\text{blue}}$, so to normalize the red-galaxy and blue-galaxy

data points to the all-galaxy data points in Fig. 6-8, we need to calculate

$$\frac{b_{\alpha,\text{red}}}{b_{*,\text{all}}} = \frac{b_{4,\text{all}}}{b_{*,\text{all}}} \frac{b_{4,\text{red}}}{b_{4,\text{all}}} \frac{b_{\alpha,\text{red}}}{b_{4,\text{red}}} \quad (6.37)$$

and

$$\frac{b_{\alpha,\text{blue}}}{b_{*,\text{all}}} = \frac{b_{4,\text{all}}}{b_{*,\text{all}}} \frac{b_{4,\text{red}}}{b_{4,\text{all}}} \frac{b_{4,\text{blue}}}{b_{4,\text{red}}} \frac{b_{\alpha,\text{blue}}}{b_{4,\text{blue}}}. \quad (6.38)$$

The factor $b_{4,\text{all}}/b_{*,\text{all}}$ is simply the normalization factor chosen for the above model to give $b(M_*)/b_* = 1$. To determine $b_{4,\text{red}}/b_{4,\text{all}}$, we use best-fitting values of σ_1^2 from the likelihood analysis described in §6.3.5 at the resolution with cell sizes closest to $20 h^{-1}\text{Mpc}$: σ_1 from the comparison of dimmer and more luminous galaxies in V3 gives $b_{4,\text{all}}$, and similarly σ_1 from the comparison of blue and red galaxies in L4 gives $b_{4,\text{red}}$, so

$$\frac{b_{4,\text{red}}}{b_{4,\text{all}}} = \left(\frac{\sigma_{1,\text{red vs. blue L4}}^2}{\sigma_{1,\text{lum vs. dim V3}}^2} \right)^{1/2}. \quad (6.39)$$

The blue points are then normalized relative to the red points using $b_{4,\text{blue}}/b_{4,\text{red}}$ equal to the measured value of b_{rel} from the likelihood comparison of blue and red galaxies in L4. Thus the shapes of the red and blue curves are determined using the luminosity-dependent bias from the null-buster analysis, but their normalization uses information from the likelihood analysis as well.

Splitting the luminosity dependence of the bias by color reveals some interesting features. The bias of the blue galaxies shows only a weak dependence on luminosity, and both luminous ($M \sim -22$) and dim ($M \sim -17$) red galaxies have slightly higher bias than moderately bright ($M \sim -20 \sim M_*$) red galaxies. The previously observed luminosity dependence of bias, with a weak dependence dimmer than L_* and a strong increase above L_* , is thus quite sensitive to the color selection: the lower luminosity bins contain mostly blue galaxies and thus show weak luminosity dependence, whereas the more luminous bins are dominated by red galaxies which drive the observed trend of more luminous galaxies being more strongly biased. It is instructive to compare these results with the mean local overdensity in color-magnitude space, as in fig. 2 of Blanton et al. (2005a). Although our bias measurements are necessarily much coarser, it can be seen that the bias is strongest where the overdensity is largest, as has been seen previously (Abbas and Sheth 2006).

Comparisons of our results to other measurements of luminosity-dependent bias for red and blue galaxies are shown in Fig. 6-9 in the middle and right panels. Indications of the differing trends for red and blue galaxies have been observed in previous work: an early hint of the upturn in the bias for dim red galaxies was seen in Norberg et al. (2002), and recent results (Wang et al. 2007) also indicate higher bias for dim red galaxies at scales $> 1 h^{-1}\text{Mpc}$. However, there is some inconsistency between these results compared to Zehavi et al. (2005) and Li et al. (2006) regarding the dim red galaxies: they find that dim red galaxies exhibit the strongest clustering on scales $< 1 h^{-1}\text{Mpc}$ and luminous red galaxies exhibit the strongest clustering on larger scales, as can be seen from the green points in Fig. 6-9. This is shown in fig. 14 of Zehavi et al. (2005) and fig. 11 of Li et al. (2006). However, we find the dim red galaxies to have higher bias than L_* red galaxies at all the scales we probe ($2-40 h^{-1}\text{Mpc}$ in this case). This upturn of the bias for dim red galaxies is present in the halo model-based theoretical curves from van den Bosch et al. (2003), although not

in the theoretical curves from Cooray (2005). Note also that van den Bosch et al. (2003) use the data from Norberg et al. (2002) to constrain their models so the agreement between the theory and data should be interpreted with some caution.

Recent measurements of higher order clustering statistics (Croton et al. 2007) find the same trends in the clustering strengths of red and blue galaxies, although they indicate that their linear bias measurement (which should be comparable to ours) shows the opposite trends – little luminosity dependence for red galaxies and a slight monotonic increase for blue galaxies. However, their luminosity range is much narrower than ours so the trends are less clear, and placing their data points on Fig. 6-9 shows that they are in good agreement with our results.

Previous studies (Norberg et al. 2002; Li et al. 2006; Wang et al. 2007) have also reported a somewhat stronger luminosity dependence of blue galaxy clustering than we have measured here. As can be seen in Fig. 6-9, Norberg et al. (2002) and Wang et al. (2007) measure slightly higher bias for luminous blue galaxies, and (Li et al. 2006) measure slightly lower bias for dim blue galaxies. Although the quantitative disagreement is fairly small, the qualitative trends of the previous studies imply that the bias of blue galaxies increases with luminosity, as opposed to our measurement which indicates a lack of luminosity dependence.

6.4.2 Likelihood Results

To study the luminosity dependence, color dependence and stochasticity of bias in more detail, we also apply the maximum likelihood method described in §6.3.5 to all of the same pairs of samples used in the null-buster test. Due to constraints on computing power and memory, we perform these calculations for only three values of the cell size L rather than four, dropping the highest resolution (smallest cell size) shown in Fig. 6-4. The likelihood analysis makes a few additional assumptions, but provides a valuable cross-check and also a measurement of the parameter r_{rel} which encodes the stochasticity and non-linearity of the relative bias.

For each pair of samples, the likelihood function given in equation (6.28) is maximized with respect to the parameters σ_1^2 , b_{rel} , and r_{rel} and marginalized over σ_1^2 to determine the best-fitting values of b_{rel} and r_{rel} , with uncertainties defined by the $\Delta(2 \ln \mathcal{L}) = 1$ contour in the $b_{\text{rel}}-r_{\text{rel}}$ plane. As we discuss in §6.B.2, the values of b_{rel} found here are consistent with those determined using the null-buster test.

Figure 6-10 shows the best-fitting values of r_{rel} as a function of cell size L . For the comparisons between neighboring luminosity bins, the results are consistent with $r_{\text{rel}} = 1$. On the other hand, the comparisons between red and blue galaxies give $r_{\text{rel}} < 1$, with smaller cell sizes L giving smaller values of r_{rel} . This confirms the null-buster result that the luminosity-dependent bias can be accurately modeled using simple deterministic linear bias but color-dependent bias demands a more complicated model. Also, r_{rel} for the color-dependent bias is seen to depend on scale but not strongly on luminosity. In contrast, b_{rel} (both in the null-buster and likelihood analyses) depends on luminosity but not on scale.

To summarize, we find that the simple, deterministic model is a good fit for the luminosity-dependent bias, but the color-dependent bias shows evidence for stochasticity and/or non-linearity which increases in strength towards smaller scales. These results are consistent with previous detections of stochasticity/non-linearity in spectral-type-dependent bias (Tegmark and Bromley 1999; Blanton 2000; Conway et al. 2005), and also agree with (Wild et al. 2005) which measures significant stochasticity between galaxies of different color or spectral type, but not between galaxies of different luminosities.

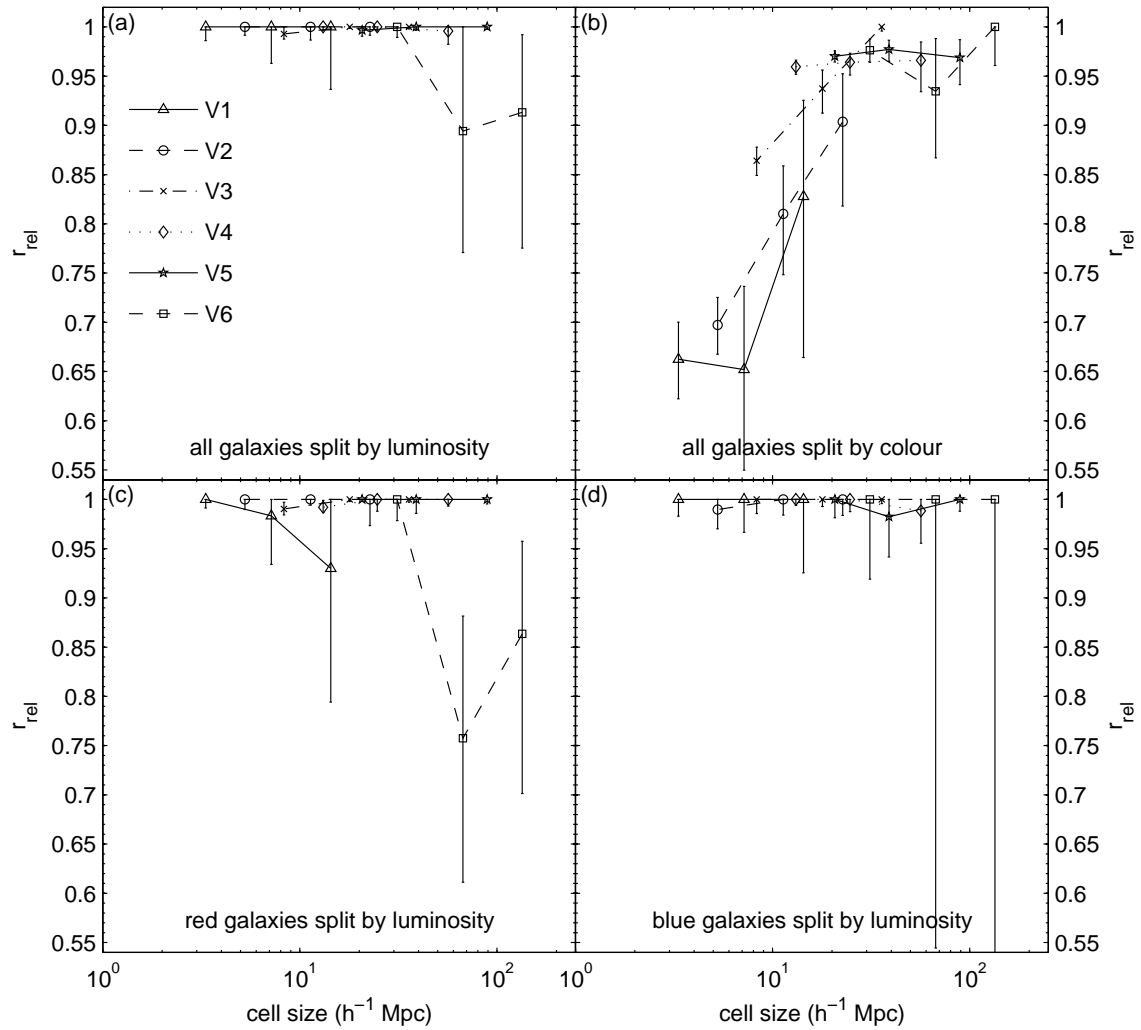


Figure 6-10 The best-fitting values of the relative cross-correlation coefficient r_{rel} between pairwise samples. Four different types of pairwise comparison are illustrated: (a) luminous vs. dim, (b) red vs. blue, (c) luminous red vs. dim red, and (d) luminous blue vs. dim blue. The different symbols denote the different comparison volumes V1-V6.

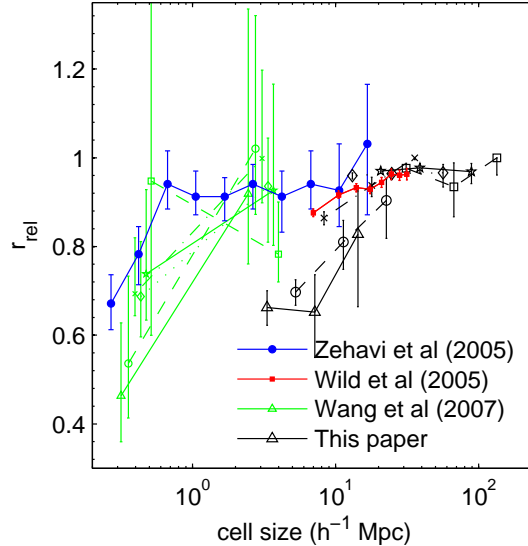


Figure 6-11 Comparison of relative cross-correlation coefficient r_{rel} between red and blue galaxies as measured with different techniques. The points from Zehavi et al. (2005) are extracted from cross-correlation measurements between red and blue galaxies in SDSS with $M_{0.1r} < -21$, and the Wild et al. (2005) points are from a counts-in-cells analysis using all 2dFGRS galaxies. Our results and the Wang et al. (2007) results (also from SDSS) are separated by luminosity – symbols are the same as in Fig. 6-10, and for the Wang et al. (2007) results, open triangles denote their dimmest bin ($-19 < M_{0.1r} < -18$) and open squares denote their most luminous bin ($-23 < M_{0.1r} < -21.5$). The length scales used in Wang et al. (2007) are averages over small scales ($0.16 - 0.98 h^{-1}\text{Mpc}$) and large scales ($0.98 - 9.8 h^{-1}\text{Mpc}$) – points here are shown in the middle of these ranges and offset for clarity.

We compare our results for r_{rel} for red and blue galaxies to previous results in Fig. 6-11. This shows good agreement between our results and those of Wild et al. (2005) (r_{lin} from their fig. 11), implying that these results are quite robust since our analysis uses a different data set, employs different methods, and makes different assumptions.

For the results from cross-correlation measurements, however, the agreement is not as clear. Zehavi et al. (2005) find that the cross-correlation between red and blue galaxies (their fig. 24), indicates that r_{rel} is consistent with 1 on scales $> 1 h^{-1}\text{Mpc}$. However, it is not clear that this result disagrees with ours, as their result is for luminous galaxies ($M_{0.1r} < -21$) and we do not see a strong indication of $r_{\text{rel}} < 1$ for our V6 sample ($23 < M_{0.1r} < -21$).

More recent cross-correlation measurements (Wang et al. 2007) do find evidence for stochasticity/non-linearity between red and blue galaxies at scales $< 1 h^{-1}\text{Mpc}$ and also show an indication that dimmer galaxies have slightly lower values of r_{rel} . Note also that the method of calculating r_{rel} by taking ratios of cross- and auto-correlation functions as used for Zehavi et al. (2005) and Wang et al. (2007) does not automatically incorporate the constraint that $|r_{\text{rel}}| \leq 1$ as our analysis does, so their error bars are allowed to extend above $r_{\text{rel}} = 1$ in Fig. 6-11.

Overall, the counts-in-cells measurements (this chapter, Wild et al. 2005) show stronger

evidence for stochasticity/non-linearity at larger scales than the cross-correlation measurements (Zehavi et al. 2005; Wang et al. 2007), indicating either that there might be some slight systematic variation between the two methods or that the counts-in-cells method is more sensitive to these effects.

6.5 Conclusions

To shed further light on how galaxies trace matter, we have quantified how different types of galaxies trace each other. We have analyzed the relative bias between pairs of volume-limited galaxy samples of different luminosities and colors using counts-in-cells at varying length scales. This method is most sensitive to length scales between those probed by correlation function and power spectrum methods, and makes point-by-point comparisons of the density fields rather than using ratios of moments, thereby eliminating sample variance and obtaining a local rather than global measure of the bias. We applied a null-buster test on each pair of subsamples to determine if the relative bias was consistent with deterministic linear biasing, and we also performed a maximum-likelihood analysis to find the best-fitting parameters for a simple stochastic biasing model.

6.5.1 Biasing results

Our primary results are:

1. The luminosity-dependent bias for red galaxies is significantly different from that of blue galaxies: the bias of blue galaxies shows only a weak dependence on luminosity, whereas both luminous and dim red galaxies have higher bias than moderately bright (L_*) red galaxies.
2. Both of our analysis methods indicate that the simple, deterministic model is a good fit for the luminosity-dependent bias, but that the color-dependent bias is more complicated, showing strong evidence for stochasticity and/or non-linearity on scales $\lesssim 10h^{-1}$ Mpc.
3. The luminosity-dependent bias is consistent with being scale-independent over the range of scales probed here ($2 - 160 h^{-1}$ Mpc). The color-dependent bias depends on luminosity but not on scale, while the cross-correlation coefficient r_{rel} depends on scale but not strongly on luminosity, giving smaller r_{rel} values at smaller scales.

These results are encouraging from the perspective of using galaxy clustering to measure cosmological parameters: simple scale-independent linear biasing appears to be a good approximation on the $\gtrsim 60 h^{-1}$ Mpc scales used in many recent cosmological studies (e.g., Sánchez et al. (2006); Tegmark et al. (2006); Spergel et al. (2007)). However, further quantification of small residual effects will be needed to do full justice to the precision of next-generation data sets on the horizon. Moreover, our results regarding color sensitivity suggest that more detailed bias studies are worthwhile for luminous red galaxies, which have emerged a powerful cosmological probe because of their visibility at large distances and near-optimal number density (Eisenstein et al. 2001, 2005; Tegmark et al. 2006), since color cuts are involved in their selection.

6.5.2 Implications for galaxy formation

What can these results tell us about galaxy formation in the context of the halo model? First of all, as discussed in Zehavi et al. (2005), the large bias of the faint red galaxies can be explained by the fact that such galaxies tend to be satellites in high mass halos, which are more strongly clustered than low mass halos. Previous studies have found that central galaxies in low-mass halos are preferentially blue, central galaxies in high mass halos tend to be red, and that the luminosity of the central galaxy is strongly correlated with the halo mass (Yang et al. 2005; Zheng et al. 2005). Our observed lack of luminosity dependence of the bias for blue galaxies would then be a reflection of the correlation between luminosity and halo mass being weaker for blue galaxies than for red ones. Additional work is needed to study this quantitatively and compare it with theoretical predictions from galaxy formation models.

The detection of stochasticity between red and blue galaxies may imply that red and blue galaxies tend to live in different halos – a study of galaxy groups in SDSS (Weinmann et al. 2006) recently presented evidence supporting this, but this is at odds with the cross-correlation measurement in Zehavi et al. (2005), which implies that blue and red galaxies are well-mixed within halos. The fact that the stochasticity is strongest at small scales suggests that this effect is due to the 1-halo term, i.e., arising from pairs of galaxies in the same halo, although some amount of stochasticity persists even for large scales. However, the halo model implications for stochasticity have not been well-studied to date.

In summary, our results on galaxy biasing and future work along these lines should be able to deepen our understanding of both cosmology (by quantifying systematic uncertainties) and galaxy formation.

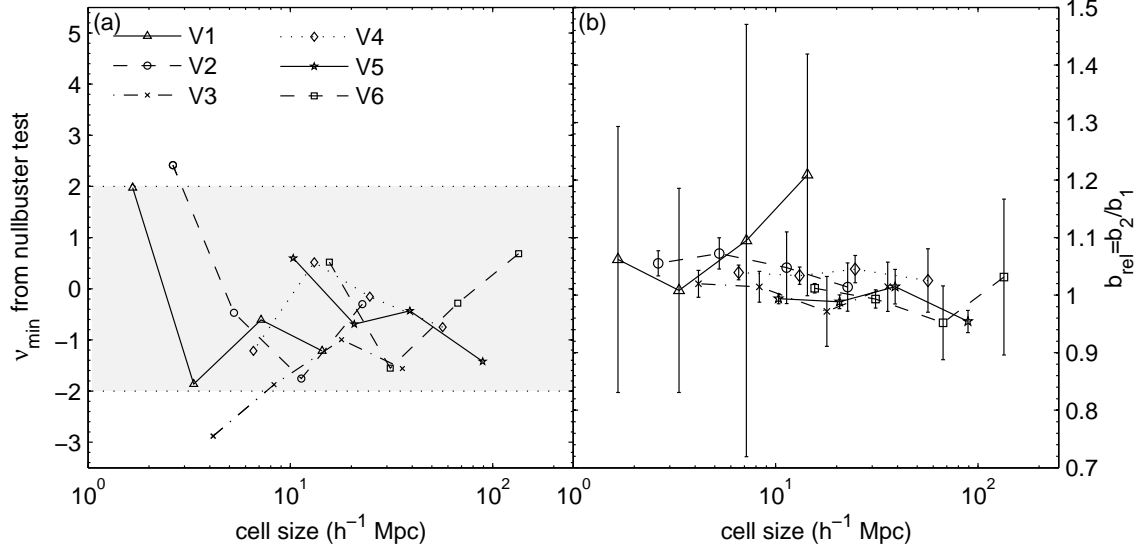


Figure 6-12 Null-buster results for randomly split samples.

6.A Consistency Checks

6.A.1 Alternate null-buster analyses

In order to test the robustness of our results against various systematic effects, we have repeated the null-buster analysis with four different modifications: splitting the galaxy samples randomly, offsetting the pixel positions, using galaxy positions without applying the finger-of-god compression algorithm, and ignoring the cosmological correlations between neighboring cells.

Randomly split samples

The null-buster test assumes that the Poissonian shot noise for each type of galaxy in each pixel is uncorrelated – i.e., that the matrix \mathbf{N} in equation (6.13) is diagonal – and that this shot noise can be approximated as Gaussian. To test the impact of these assumptions on our results, we repeated the null-buster analysis using randomly split galaxy samples rather than splitting by luminosity or color. For each volume V1-V6, we created two samples by generating a uniformly distributed random number for each galaxy and assigning it to sample 1 for numbers > 0.5 and sample 2 otherwise.

If the null-buster test is accurate, we expect the pairwise comparison for the randomly split samples to be consistent with deterministic linear bias with $b_{\text{rel}} = 1$. The results are shown in Fig. 6-12 – we find that, indeed, deterministic linear bias is not ruled out, with nearly all of the ν_{\min} points falling within ± 2 . Furthermore, the measured values of b_{rel} are seen to be consistent with 1. Thus, we detect no systematic effects due to the null-buster assumptions.

Offset pixel positions

To test if our results are stable against the pixelization chosen, particularly at large scales where we have a small number of cells, we shifted the locations on the sky of the angular

pixels defining the cells by half a pixel width in declination. Applying the null-buster analysis to the offset pixels reveals no significant differences from the original analysis: the luminosity-dependent comparisons for all, red, and blue galaxies are still consistent with deterministic linear bias, and the color-dependent comparison still shows strong evidence for stochasticity and/or nonlinearity, especially at smaller scales.

For the all-, red-, and blue-galaxy, luminosity-dependent comparisons, we also compared the measured values of b_{rel} from the offset analysis with the original analysis: we took the difference between the two measured values in each volume at each resolution and divided this by the larger of the error bars on the two analyses to determine the number of sigmas by which the two analyses differ. In order to be conservative, we did not add the error bars from the two analyses in quadrature, since this would overestimate the error on the difference if they are correlated and this would make our test less robust. Note that a fully proper treatment would necessitate accounting for the correlations between the errors from each analysis, which we have not done – the discussions in the this and the following sections are meant only to serve as a crude reality check.

For the error bars on the original analysis, we used the jackknife uncertainties described in §6.B.1, and for the offset analysis error bars we use the generalized χ^2 uncertainties described in §6.3.4 computed from the offset results. (This is because we did not perform jackknife resampling for the offset case or the other modified analyses.)

The results show good agreement: out of a total of 72 measured b_{rel} values, only 4 differ by more than 2σ (all galaxies in V3 and V5 at the second-smallest cell size, at 2.6σ and 3.2σ respectively, and the red galaxies in V3 and V5 at the second-smallest cell size, at 2.2σ and 3.3σ respectively). As a rough test for systematic trends, we also counted the number of measurements for which the measured value of b_{rel} is larger in each analysis. We found that in 38 cases the value from the offset analysis was larger, and in 34 cases the value from the original analysis was larger, indicating no systematic trends in the deviations.

No finger-of-god compression

Our analysis used the finger-of-god compression algorithm from Tegmark et al. (2004b) with a threshold density of $\delta_c = 200$. This gives a first-order correction for redshift space distortions, but it complicates comparisons to other analyses which work purely in redshift space (e.g. Wild et al. 2005) or use projected correlation functions (e.g. Zehavi et al. 2005), particularly at small scales ($\lesssim 10 h^{-1}\text{Mpc}$) where the effects of virialized galaxy clusters could be significant. To test the sensitivity of our results to this correction, we repeated the null-buster analysis with no finger-of-god compression.

The results show excellent agreement with the original analysis – the smallest-scale measurements for the color-dependent comparison only rule out deterministic linear bias at 30 sigma rather than 40, but the conclusions remain the same. Additionally, we compared the measured b_{rel} values to the original analysis as in §6.A.1 and find all 72 measurements to be within 2σ . In 25 cases, the analysis without finger-of-god compression gave a larger b_{rel} value, and in 47 cases the original analysis gave a larger value. This indicates that there might be a very slight tendency to underestimate b_{rel} if fingers-of-god are not accounted for, but the effect is quite small and well within our error bars. Thus, the finger-of-god compression has no substantial impact on our results.

Uncorrelated signal matrix

The null-buster test requires a choice of residual signal matrix \mathbf{S}_Δ – our analysis uses a signal matrix derived from the matter power spectrum, thus accounting for cosmological correlations between neighboring cells. However, these correlations are commonly assumed to be negligible in other counts-in-cells analyses (Blanton 2000; Wild et al. 2005; Conway et al. 2005). To test the sensitivity to the choice of \mathbf{S}_Δ , we repeated the analysis using \mathbf{S}_Δ equal to the identity matrix.

Again, we find the results to agree well with the original analysis and lead to the same conclusions. When comparing the measured b_{rel} values to the original analysis as in §6.A.1, we find only 4 out of 72 points differing by more than 2σ (all galaxies in V5 at the smallest cell size, at -2.6σ , red galaxies in V4 at the second-smallest and smallest cell size, at 2.2σ and 2.8σ respectively, and blue galaxies in V4 at the smallest cell size, at -3.1σ). In 39 cases the value of b_{rel} is larger with the uncorrelated signal matrix, and in 33 cases b_{rel} is larger in the original analysis, indicating no strong systematic effects. Thus we expect our results to be directly comparable to other counts-in-cells analyses done without accounting for cosmological correlations.

6.B Uncertainty Calculations

6.B.1 Jackknife uncertainties for null-buster analysis

We use jackknife resampling to calculate the uncertainties for the null-buster analysis. The concept is as follows: divide area covered on the sky into N spatially contiguous regions, and then repeat the analysis N times, omitting each of the N regions in turn. The covariance matrix for the measured parameters is then estimated by

$$\Sigma_{\text{rel}}^{ij} = \frac{N-1}{N} \sum_{k=1}^N \left(b_{\text{rel},k}^i - \overline{b_{\text{rel}}^i} \right) \left(b_{\text{rel},k}^j - \overline{b_{\text{rel}}^j} \right) \quad (6.40)$$

where superscripts i and j denote measurements of b_{rel} in different volumes and at different scales, $b_{\text{rel},k}^i$ denotes the value of b_{rel}^i with the k th jackknife region omitted, and $\overline{b_{\text{rel}}^i}$ is the average over all N values of $b_{\text{rel},k}^i$.

For our analysis, we use the 15 pixels at our lowest resolution (upper left panel in Fig. 6-4) as the jackknife regions. However, since we use a looser completeness cut at the lowest resolution, two of these pixels cover an area that is not used at higher resolutions. Thus we chose not to include these two pixels in our jackknives since they do not omit much (or any) area at the higher resolutions. Thus our jackknife resampling has $N = 13$. This technique allows us to estimate the uncertainties on all of our b_{rel} measurements as well as the covariance matrix quantifying the correlations between them. We use these covariances in the model-fitting done in §6.4.1 and §6.4.1.

Figure 6-13 shows the uncertainties on b_{rel} as calculated from jackknife resampling compared to those calculated with the generalized χ^2 method described in §6.3.4. Overall, the two methods agree well, but the jackknife method gives larger uncertainties at the smallest scales and in volume V1. The reason for the large jackknife uncertainties in volume V1 is because it is significantly smaller than the other volumes, and it is small enough that omitting a cell containing just one large cluster can have a substantial effect on the measured value of b_{rel} . Thus the large uncertainties in V1 reflect the effects of sampling a small

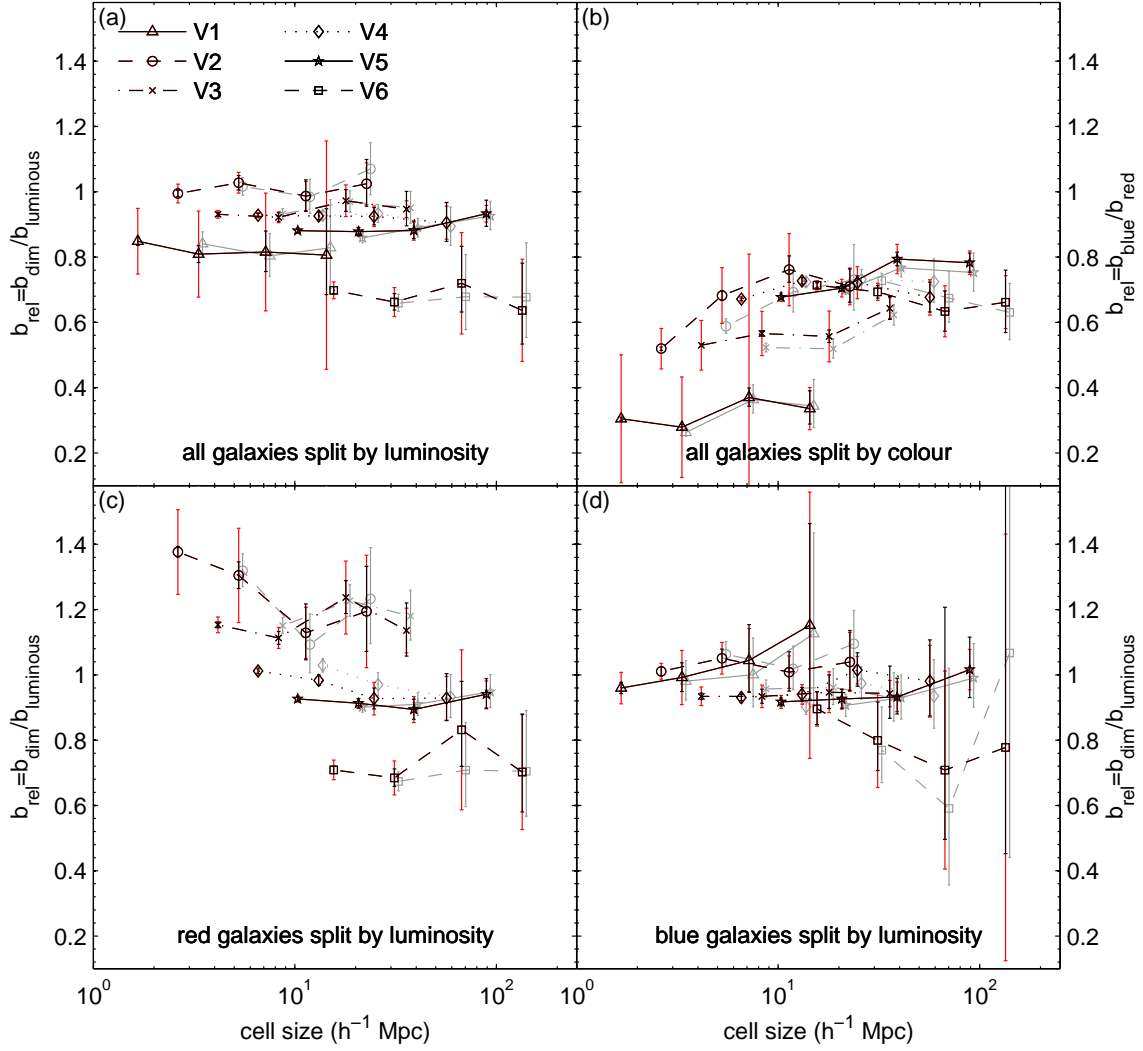


Figure 6-13 Comparison of two methods for calculating uncertainties on b_{rel} from the null-buster analysis: jackknife resampling (red) and the generalized χ^2 method (black). Also shown are the results for b_{rel} from the likelihood analysis (grey).

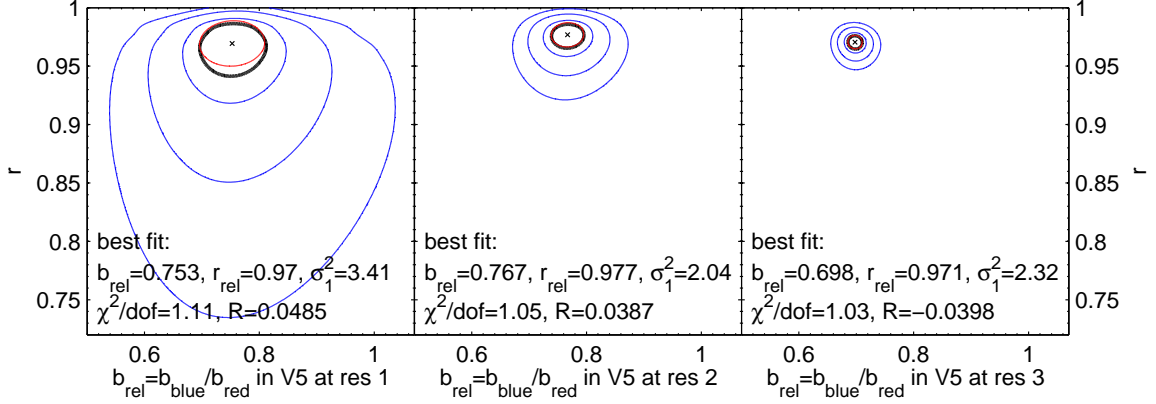


Figure 6-14 Typical contour plots of $\Delta(2 \ln \mathcal{L})$ for volume V5 for three different resolutions corresponding (from left- to right-hand-side) to cell sizes of 89, 39, and 21 h^{-1} Mpc. Blue contours denote the 1, 2 and 3 σ two-dimensional confidence regions, and black contours denote the 1 σ one-dimensional confidence region used for computing error bars on b_{rel} and r_{rel} . The red contours denote the error ellipse calculated from the second-order approximation to $2 \ln \mathcal{L}$ at the best-fit point, marked with a \times .

volume. Since there are so few dim red galaxies, these effects are particularly egregious for the measurements of luminosity-dependent bias of red galaxies in V1. Thus, based on the jackknife results, we elected to not use V1 in our analysis of the red galaxies.

6.B.2 Likelihood uncertainties

Likelihood contours

As described in §6.3.5, we calculate the uncertainty on b_{rel} and r_{rel} for the likelihood method using the $\Delta(2 \ln \mathcal{L}) = 1$ contour in the $b_{\text{rel}}-r_{\text{rel}}$ plane after marginalizing over σ_1^2 . This means that for each comparison volume and at each resolution, we calculate \mathcal{L} from equation (6.28) over a grid of b_{rel} and r_{rel} values and maximize $2 \ln \mathcal{L}$ with respect to σ_1^2 at each grid point. This gives us a 2-dimensional likelihood function, which we then maximize to find the best-fit values for b_{rel} and r_{rel} . Uncertainties are calculated using the function

$$\Delta(2 \ln \mathcal{L}(b_{\text{rel}}, r_{\text{rel}})) \equiv 2 \ln \mathcal{L}(b_{\text{rel}}^{\text{max}}, r_{\text{rel}}^{\text{max}}) - 2 \ln \mathcal{L}(b_{\text{rel}}, r_{\text{rel}}). \quad (6.41)$$

Typical contour plots of this function for volume V5 at each of the three cell sizes used are shown in Fig. 6-14.

We define 1- and 2-dimensional confidence regions using the standard procedures detailed in Press et al. (1992), using $\Delta(2 \ln \mathcal{L})$ as an equivalent to $\Delta\chi^2$: the 1 σ (68.3%) 1-dimensional confidence region is given by $\Delta(2 \ln \mathcal{L}) = 1$, so we define our error bars on b_{rel} and r_{rel} by projecting the $\Delta(2 \ln \mathcal{L}) = 1$ contour (shown in black in Fig. 6-14) onto the b_{rel} and r_{rel} axes. For illustrative purposes we also show the 1 σ , 2 σ , and 3 σ (68.3%, 95.4%, and 99.73%) 2-dimensional confidence regions in these plots, given by $\Delta(2 \ln \mathcal{L}) = 2.30$, 6.17, and 11.8 respectively.

To check the goodness of fit, we also compute an effective value of χ^2 :

$$\chi_{\text{eff}}^2 \equiv -2 \ln \mathcal{L} - \ln |\mathbf{C}| - 2n \ln(2\pi), \quad (6.42)$$

where \mathbf{C} is given by equation (6.12) and n is the number of cells. If our model is a good fit, the value of χ_{eff}^2 at the best fit parameter values should be close to the number of degrees of freedom, given by $\text{dof} = 2n - 2$ ($2n$ data points for type 1 and 2 galaxies in each cell minus 2 parameters b_{rel} and r_{rel}). We calculated $\chi_{\text{eff}}^2/\text{dof}$ for each volume and resolution and found they all lie quite close to 1, ranging from a minimum value of 0.678 to a maximum value of 1.11. Thus this test indicates our model is a good fit.

The uncertainties on b_{rel} and r_{rel} could perhaps be calculated more accurately using jackknife resampling as we did for the null-buster case; however, repeating the analysis for each jackknife sample is computationally prohibitive since performing all the calculations for just one likelihood analysis took several months of CPU time.

$b_{\text{rel}}-r_{\text{rel}}$ covariance matrices

Alternatively, we can calculate the uncertainties using the parameter covariance matrix at the best fit parameter values, as is commonly done in χ^2 analyses. The Hessian matrix of second derivatives is given by

$$\mathbf{H} \equiv \begin{pmatrix} \frac{d^2(2 \ln \mathcal{L})}{db_{\text{rel}}^2} & \frac{d^2(2 \ln \mathcal{L})}{db_{\text{rel}} dr_{\text{rel}}} \\ \frac{d^2(2 \ln \mathcal{L})}{db_{\text{rel}} dr_{\text{rel}}} & \frac{d^2(2 \ln \mathcal{L})}{dr_{\text{rel}}^2} \end{pmatrix} \quad (6.43)$$

and the parameter covariance matrix is given by

$$\mathbf{C}_{\text{param}} \equiv 2\mathbf{H}^{-1} = \begin{pmatrix} \sigma_{b_{\text{rel}}}^2 & \sigma_{b_{\text{rel}} r_{\text{rel}}}^2 \\ \sigma_{b_{\text{rel}} r_{\text{rel}}}^2 & \sigma_{r_{\text{rel}}}^2 \end{pmatrix}. \quad (6.44)$$

Thus the uncertainties are given by $\sigma_{b_{\text{rel}}}^2$ and $\sigma_{r_{\text{rel}}}^2$ with this method. This is equivalent to approximating the likelihood function $2 \ln \mathcal{L}$ with its second-order Taylor series about the best-fit point, and it defines an error ellipse that approximates the $\Delta(2 \ln \mathcal{L}) = 1$ contour. These error ellipses are shown in Fig. 6-14 in red, and are seen to be in close agreement with the true $\Delta(2 \ln \mathcal{L}) = 1$ contours.

This method also allows us to measure the correlation between b_{rel} and r_{rel} by calculating the correlation coefficient, given by

$$R \equiv \frac{\sigma_{b_{\text{rel}} r_{\text{rel}}}^2}{\left(\sigma_{b_{\text{rel}}}^2 \sigma_{r_{\text{rel}}}^2\right)^{1/2}}. \quad (6.45)$$

R will fall between -1 (perfectly anti-correlated) and 1 (perfectly correlated). Effectively this measures the tilt of the error ellipse in the $b_{\text{rel}}-r_{\text{rel}}$ plane. Overall we find the values of R to be quite small – typically $|R| \sim 0.05$ – indicating no large correlations between b_{rel} and r_{rel} . Out of the 72 points we calculate, only 6 have $|R| > 0.3$. The cases with the largest R values are for blue galaxies in volume V6, where the uncertainties are quite large due to the small number of bright blue galaxies and the error ellipses are not good approximations to the likelihood contours anyway – thus these few cases with large R are not overly concerning.

Comparison with null-buster results

Finally, we compare the results for b_{rel} from the likelihood method to the results from the null-buster analysis in Fig. 6-13, with the likelihood points shown in grey. As can be seen in this plot, the likelihood and null-buster values for b_{rel} agree within the uncertainties, even for the color-dependent bias where the null-buster values are not necessarily accurate since deterministic linear bias is ruled out. Thus our two analysis methods are in excellent agreement with each other.

Chapter 7

Conclusions

We set out in this thesis to explore the connections between particle physics and astrophysics by using the tools of particle physics to do astronomy, a.k.a. “Astrophysics Underground,” and by using the tools of astronomy to do particle physics, a.k.a. “Particle Physics in the Sky.” What have we accomplished in these endeavors?

In “Astrophysics Underground,” we performed a search for extremely high-energy upward-going muons in the Super-K neutrino detector and set an upper limit on the flux of neutrinos coming from astrophysical sources such as AGNs. Have we really learned anything about astrophysics here? Yes, albeit rather indirectly – our upper limit on the astrophysical neutrino flux tells us that AGNs are not producing an unexpectedly large amount of neutrinos. However, much more time and energy was devoted to thinking about the particle physics technical issues than about the primary astrophysical science goal. We developed a way to use previously ignored information from the Super-K detector, studied how muons propagate through rock and water, and did a detailed analysis of various particle physics phenomena contributing to the background flux. Ultimately, most of what we learned was really about particle physics.

This same effect was even more true in “Particle Physics in the Sky.” Here we developed a powerful software tool to manage angular masks of the next generation of galaxy surveys and analyzed the details of relative bias between galaxies of different luminosities and colors. These projects contribute to cosmology by providing techniques to better use galaxy surveys as a cosmological tool. In particular, gaining a better understanding of bias is key for reducing the systematic uncertainties inherent in galaxy survey cosmology. Have we learned any particle physics? Again, yes, though again rather indirectly, in that we have contributed to the overall cosmological programs to understand dark matter and dark energy. What we really learned about is the physics of galaxies – our results on how different types of galaxies cluster differently most directly shed light on the complex physical processes governing galaxy formation and evolution. It may appear overly optimistic to claim that we have really done any particle physics here, but it is important to remember that our understanding of cosmology from galaxy surveys is only as good as our understanding of bias, and if we hope to gain further insight about particle physics from the next generation of cosmological measurements, it is essential that we understand the physics of galaxies at a deeper level.

One particularly interesting direction for future research is to use relative bias measurements as a guide for refining halo model methods for putting galaxies in dark matter halos, as discussed in §4.1.5. This can help us gain a better understanding of the physics that

links galaxy properties to halo mass, and provide a better way of modeling of complicated bias. Furthermore, we can combined this with advances in nonlinear modeling of structure formation in order to further refine galaxy surveys as a tool for doing cosmology. This makes the biggest difference at length scales slightly smaller than where the power spectrum is typically measured, a regime which is particularly important for setting cosmological bounds on the neutrino mass. Such investigations will also help reduce systematic uncertainties on measuring the baryon oscillation length scale as a standard ruler for studying dark energy. Thus, even if we have not addressed them directly, the particle physics science goals are clearly in sight.

It is perhaps a natural outcome of studying the science questions of one field with the techniques of another that one gets more immersed in the area of the technique. This is borne out in the traditional physics department divisions as well – the work on neutrino astrophysics presented here was done within a particle physics division, and in general is done by scientists who call themselves particle physicists rather than astronomers. Likewise, the work on cosmology was done within an astrophysics division and is more often grouped with astronomy, not high energy physics. In many ways this makes sense – after all, if a scientist at such an interface spends most of their time thinking about the physics of the techniques they are using, it is perfectly logical to surround oneself with experts in that area. However, more direct interaction between scientists on either side of the fence can potentially be extremely beneficial, as is happening at new interdisciplinary research centers across the world.

In conclusion, we have hopefully provided valuable tools for upcoming experiments in both neutrino astronomy and cosmology. These lines of research represent areas where the traditionally separate fields of particle physics and astrophysics overlap and have produced much fruitful interaction between physicists exploring the largest and smallest scales in our universe. The work in this thesis makes contributions to the exciting research in progress at the interface of these two rich fields.

Bibliography

- Abazajian, K. et al. (2005). Cosmology and the Halo Occupation Distribution from Small-Scale Galaxy Clustering in the Sloan Digital Sky Survey. *ApJ* 625, 613–620.
- Abbas, U. and R. K. Sheth (2005). The environmental dependence of clustering in hierarchical models. *MNRAS* 364, 1327–1336.
- Abbas, U. and R. K. Sheth (2006). The environmental dependence of galaxy clustering in the Sloan Digital Sky Survey. *MNRAS* 372, 1749–1754.
- Abe, K. et al. (2006). High-Energy Neutrino Astronomy Using Upward-going Muons in Super-Kamiokande I. *ApJ* 652, 198–205.
- Abell, G. O. (1959). The National Geographic Society-Palomar Observatory Sky Survey. Leaflet of the Astronomical Society of the Pacific 8, 121–+.
- Abell, G. O. (1961). Evidence regarding second-order clustering of galaxies and interactions between clusters of galaxies. *AJ* 66, 607–+.
- Abraham, J. et al. (2007). Correlation of the Highest-Energy Cosmic Rays with Nearby Extragalactic Objects. *Science* 318, 938–943.
- Achterberg, A. et al. (2007). Multiyear search for a diffuse flux of muon neutrinos with AMANDA-II. *Phys. Rev. D* 76(4), 042008–+.
- Adelman-McCarthy, J. K. et al. (2006). The Fourth Data Release of the Sloan Digital Sky Survey. *ApJS* 162, 38–48.
- Adelman-McCarthy, J. K. et al. (2007). The Fifth Data Release of the Sloan Digital Sky Survey. *ApJS* 172, 634–644.
- Aggouras, G. et al. (2005). Operation, Performance and Measurements with the NESTOR Test Detector. Volume 5 of Proceedings of the 29th International Cosmic Ray Conference, 91–+.
- Ahrens, J. et al. (2004). Muon track reconstruction and data selection techniques in AMANDA. *Nuclear Instruments and Methods in Physics Research A* 524, 169–194.
- Albrecht, A., G. Bernstein, R. Cahn, W. L. Freedman, J. Hewitt, W. Hu, J. Huth, M. Kamionkowski, E. W. Kolb, L. Knox, J. C. Mather, S. Staggs, and N. B. Suntzeff (2006). Report of the Dark Energy Task Force. [astro-ph/0609591](https://arxiv.org/abs/astro-ph/0609591).
- Ambrosio, M. et al. (2003). Search for diffuse neutrino flux from astrophysical sources with MACRO. *Astropart. Phys.* 19, 1–13.

- Ashie, Y. et al. (2005). Measurement of atmospheric neutrino oscillation parameters by Super-Kamiokande I. *Phys. Rev. D* 71(11), 112005–+.
- Baldry, I. K., M. L. Balogh, R. G. Bower, K. Glazebrook, R. C. Nichol, S. P. Bamford, and T. Budavari (2006). Galaxy bimodality versus stellar mass and environment. *MNRAS* 373, 469–483.
- Balogh, M. L., I. K. Baldry, R. Nichol, C. Miller, R. Bower, and K. Glazebrook (2004). The Bimodal Galaxy Color Distribution: Dependence on Luminosity and Environment. *ApJ* 615, L101–L104.
- Banerji, M., F. B. Abdalla, O. Lahav, and H. Lin (2007). Photometric Redshifts for the Dark Energy Survey and VISTA and Implications for Large Scale Structure. [arXiv:0711.1059](https://arxiv.org/abs/0711.1059).
- Barwick, S. W. et al. (2006). Constraints on Cosmic Neutrino Fluxes from the Antarctic Impulsive Transient Antenna Experiment. *Physical Review Letters* 96(17), 171101–+.
- Baugh, C. M. (2006). A primer on hierarchical galaxy formation: the semi-analytical approach. *Reports of Progress in Physics* 69, 3101–3156.
- Benabed, K. and L. van Waerbeke (2004). Constraining dark energy evolution with gravitational lensing by large scale structures. *Phys. Rev. D* 70(12), 123515–+.
- Berghaus, P. et al. (2007). Status and Results from AMANDA/IceCube. [arXiv:0712.4406](https://arxiv.org/abs/0712.4406).
- Berlind, A. A., M. R. Blanton, D. W. Hogg, D. H. Weinberg, R. Davé, D. J. Eisenstein, and N. Katz (2005). Interpreting the Relationship between Galaxy Luminosity, Color, and Environment. *ApJ* 629, 625–632.
- Berlind, A. A. and D. H. Weinberg (2002). The Halo Occupation Distribution: Toward an Empirical Determination of the Relation between Galaxies and Mass. *ApJ* 575, 587–616.
- Berlind, A. A., D. H. Weinberg, A. J. Benson, C. M. Baugh, S. Cole, R. Davé, C. S. Frenk, A. Jenkins, N. Katz, and C. G. Lacey (2003). The Halo Occupation Distribution and the Physics of Galaxy Formation. *ApJ* 593, 1–25.
- Bionta, R. M., G. Blewitt, C. B. Bratton, D. Caspere, and A. Ciocio (1987). Observation of a neutrino burst in coincidence with supernova 1987A in the Large Magellanic Cloud. *Physical Review Letters* 58, 1494–1496.
- Biviano, A. (2000). From Messier to Abell: 200 Years of Science with Galaxy Clusters. [astro-ph/0010409](https://arxiv.org/abs/astro-ph/0010409).
- Blake, C., A. Collister, S. Bridle, and O. Lahav (2007). Cosmological baryonic and matter densities from 600000 SDSS luminous red galaxies with photometric redshifts. *MNRAS* 374, 1527–1548.
- Blanton, M. (2000). How Stochastic Is the Relative Bias between Galaxy Types? *ApJ* 544, 63–80.
- Blanton, M. R. et al. (2005b). New York University Value-Added Galaxy Catalog: A Galaxy Catalog Based on New Public Surveys. *AJ* 129, 2562–2578.

- Blanton, M. R., J. Brinkmann, I. Csabai, M. Doi, D. Eisenstein, M. Fukugita, J. E. Gunn, D. W. Hogg, and D. J. Schlegel (2003a). Estimating Fixed-Frame Galaxy Magnitudes in the Sloan Digital Sky Survey. *AJ* 125, 2348–2360.
- Blanton, M. R., D. Eisenstein, D. W. Hogg, D. J. Schlegel, and J. Brinkmann (2005a). Relationship between Environment and the Broadband Optical Properties of Galaxies in the Sloan Digital Sky Survey. *ApJ* 629, 143–157.
- Blanton, M. R., D. Eisenstein, D. W. Hogg, and I. Zehavi (2006). The Scale Dependence of Relative Galaxy Bias: Encouragement for the “Halo Model” Description. *ApJ* 645, 977–985.
- Blanton, M. R., H. Lin, R. H. Lupton, F. M. Maley, N. Young, I. Zehavi, and J. Loveday (2003b). An Efficient Targeting Strategy for Multiobject Spectrograph Surveys: the Sloan Digital Sky Survey “Tiling” Algorithm. *AJ* 125, 2276–2286.
- Bond, J. R., S. Cole, G. Efstathiou, and N. Kaiser (1991). Excursion set mass functions for hierarchical Gaussian fluctuations. *ApJ* 379, 440–460.
- Bond, J. R., R. G. Crittenden, A. H. Jaffe, and L. Knox (1999). Computing challenges of the cosmic microwave background. *Comput. Sci. Eng.* 1, 21–35.
- Bottai, S. and L. Perrone (2001). Simulation of UHE muons propagation for GEANT3. *Nucl. Instrum. Methods Phys. Res., Sect. A* 459, 319–325.
- Bowman, J. D., M. F. Morales, and J. N. Hewitt (2007). Constraints on Fundamental Cosmological Parameters with Upcoming Redshifted 21 cm Observations. *ApJ* 661, 1–9.
- Broadhurst, T. J., A. N. Taylor, and J. A. Peacock (1995). Mapping cluster mass distributions via gravitational lensing of background galaxies. *ApJ* 438, 49–61.
- Bugaev, E. V., V. A. Naumov, S. I. Sinegovskii, and E. S. Zaslavskaja (1989). Prompt leptons in cosmic rays. *Nuovo Cimento C* 12, 41–73.
- Bullock, J. S., T. S. Kolatt, Y. Sigad, R. S. Somerville, A. V. Kravtsov, A. A. Klypin, J. R. Primack, and A. Dekel (2001). Profiles of dark haloes: evolution, scatter and environment. *MNRAS* 321, 559–575.
- Calabretta, M. R. and B. F. Roukema (2007). Mapping on the HEALPix grid. *MNRAS* 381, 865–872.
- Carpenter, E. F. (1938). Some Characteristics of Associated Galaxies. I. a. Density Restriction in the Metagalaxy. *ApJ* 88, 344–+.
- Casas-Miranda, R., H. J. Mo, R. K. Sheth, and G. Boerner (2002). On the distribution of haloes, galaxies and mass. *MNRAS* 333, 730–738.
- Catelan, P., F. Lucchin, S. Matarrese, and C. Porciani (1998). The bias field of dark matter haloes. *MNRAS* 297, 692–712.
- Christensen, N., R. Meyer, L. Knox, and B. Luey (2001). Bayesian methods for cosmological parameter estimation from cosmic microwave background measurements. *Classical and Quantum Gravity* 18, 2677–2688.

- Coil, A. L. et al. (2008). The DEEP2 Galaxy Redshift Survey: Color and Luminosity Dependence of Galaxy Clustering at $z \sim 1$. *ApJ* 672, 153–176.
- Cole, S. et al. (2005). The 2dF Galaxy Redshift Survey: power-spectrum analysis of the final data set and cosmological implications. *MNRAS* 362, 505–534.
- Colless, M. et al. (2001). The 2dF Galaxy Redshift Survey: spectra and redshifts. *MNRAS* 328, 1039–1063.
- Colless, M. et al. (2003). The 2dF Galaxy Redshift Survey: Final Data Release. *astro-ph/0306581*.
- Collister, A. et al. (2007). MegaZ-LRG: a photometric redshift catalogue of one million SDSS luminous red galaxies. *MNRAS* 375, 68–76.
- Collister, A. A. and O. Lahav (2005). Distribution of red and blue galaxies in groups: an empirical test of the halo model. *MNRAS* 361, 415–427.
- Conrad, J., O. Botner, A. Hallgren, and C. Pérez de Los Heros (2003). Including systematic uncertainties in confidence interval construction for Poisson statistics. *Phys. Rev. D* 67(1), 012002–+.
- Conroy, C., A. L. Coil, M. White, J. A. Newman, R. Yan, M. C. Cooper, B. F. Gerke, M. Davis, and D. C. Koo (2005). The DEEP2 Galaxy Redshift Survey: The Evolution of Void Statistics from $z \sim 1$ to $z \sim 0$. *ApJ* 635, 990–1005.
- Conway, E. et al. (2005). The 2dF Galaxy Redshift Survey: the nature of the relative bias between galaxies of different spectral type. *MNRAS* 356, 456–474.
- Conway, J. (2002). Efficiency Uncertainties: A Bayesian Prescription. Technical Report CDF/PUB/5894, CDF, Batavia, IL. http://www-cdf.fnal.gov/physics/statistics/statistics_recommendations.html.
- Cooray, A. (2005). A divided Universe: red and blue galaxies and their preferred environments. *MNRAS* 363, 337–352.
- Cooray, A. (2006). Are galaxy properties only determined by the dark matter halo mass? *astro-ph/0601090*.
- Cooray, A. and R. Sheth (2002). Halo models of large scale structure. *Phys. Rep.* 372, 1–129.
- Cousins, R. D. and V. L. Highland (1992). Incorporating systematic uncertainties into an upper limit. *Nucl. Instrum. Methods Phys. Res., Sect. A* 320, 331–335.
- Crocce, M. and R. Scoccimarro (2008). Nonlinear evolution of baryon acoustic oscillations. *Phys. Rev. D* 77(2), 023533–+.
- Crook, A. C., J. P. Huchra, N. Martimbeau, K. L. Masters, T. Jarrett, and L. M. Macri (2007). Groups of Galaxies in the Two Micron All Sky Redshift Survey. *ApJ* 655, 790–813.
- Croton, D. J., P. Norberg, E. Gaztañaga, and C. M. Baugh (2007). Statistical analysis of galaxy surveys - III. The non-linear clustering of red and blue galaxies in the 2dFGRS. *MNRAS* 379, 1562–1570.

- Croton, D. J., V. Springel, S. D. M. White, G. De Lucia, C. S. Frenk, L. Gao, A. Jenkins, G. Kauffmann, J. F. Navarro, and N. Yoshida (2006). The many lives of active galactic nuclei: cooling flows, black holes and the luminosities and colours of galaxies. *MNRAS* 365, 11–28.
- da Costa, L. (1999). Galaxy redshift surveys: 20 years later (invited review). In A. J. Banday, R. K. Sheth, and L. N. da Costa (Eds.), *Evolution of Large Scale Structure: From Recombination to Garching*, 87–+.
- da Costa, L. N., P. S. Pellegrini, M. Davis, A. Meiksin, W. L. W. Sargent, and J. L. Tonry (1991). Southern Sky Redshift Survey - The catalog. *ApJS* 75, 935–964.
- Dark Energy Survey Collaboration (2005). The Dark Energy Survey. [astro-ph/0510346](https://arxiv.org/abs/astro-ph/0510346).
- Davis, M. et al. (2003). Science Objectives and Early Results of the DEEP2 Redshift Survey. In P. Guhathakurta (Ed.), *Discoveries and Research Prospects from 6- to 10-Meter-Class Telescopes II*, Volume 4834 of *Proceedings of the SPIE*, 161–172.
- Davis, M. and M. J. Geller (1976). Galaxy Correlations as a Function of Morphological Type. *ApJ* 208, 13–19.
- Davis, R. (1996). A review of measurements of the solar neutrino flux and their variation. *Nuclear Physics B Proceedings Supplements* 48, 284–298.
- Davis, R. (2003). Nobel Lecture: A half-century with solar neutrinos. *Rev. Mod. Phys.* 75, 985–994.
- de Berg, M., M. van Kreveld, M. Overmars, and O. Schwarzkopf (2000). *Computational Geometry: Algorithms and Applications*, Chapter 14, 291–298. New York: Springer.
- de Oliveira-Costa, A. (2005). The Cosmic Microwave Background and its Polarization. In A. Adamson, C. Aspin, C. Davis, and T. Fujiyoshi (Eds.), *Astronomical Polarimetry: Current Status and Future Directions*, Volume 343 of *Astronomical Society of the Pacific Conference Series*, 485–+.
- de Vaucouleurs, G. (1958). Further evidence for a local super-cluster of galaxies: rotation and expansion. *AJ* 63, 253–+.
- Dekel, A. and O. Lahav (1999). Stochastic Nonlinear Galaxy Biasing. *ApJ* 520, 24–34.
- Desai, S. et al. (2003). Study of Upward Showering Muons in Super-Kamiokande. Volume 3 of *Proceedings of the 28th International Cosmic Ray Conference*, 1673.
- Desai, S. et al. (2004). Search for dark matter WIMPs using upward through-going muons in Super-Kamiokande. *Phys. Rev. D* 70(8), 083523–+.
- Desai, S. et al. (2008). Study of TeV neutrinos with upward showering muons in Super-Kamiokande. *Astroparticle Physics* 29, 42–54.
- Dodelson, S. (2003). *Modern cosmology*. Amsterdam: Academic Press.
- Dodelson, S., L. Hui, and A. Jaffe (1997). Likelihood Analysis of Galaxy Surveys. [astro-ph/9712074](https://arxiv.org/abs/astro-ph/9712074).

- Dolag, K., S. Borgani, S. Schindler, A. Diaferio, and A. M. Bykov (2008). Simulation Techniques for Cosmological Simulations. *Space Science Reviews* 134, 229–268.
- Doré, O., L. Knox, and A. Peel (2001). CMB power spectrum estimation via hierarchical decomposition. *Phys. Rev. D* 64(8), 083001–+.
- Doré, O., R. Teyssier, F. R. Bouchet, D. Vibert, and S. Prunet (2001). MAPCUMBA: A fast iterative multi-grid map-making algorithm for CMB experiments. *A&A* 374, 358–370.
- Doughty, N. A., C. D. Shane, and F. B. Wood (1974). The all-sky sixteenth magnitude photographic sky surveys of Mount John University Observatory and Lick Observatory. *Southern Stars* 25, 107–127.
- Dziewonski, A. (1989). The Encyclopedia of Solid Earth Geophysics, Chapter “Earth Structure, Global”, 331. New York: Van Nostrand Reinhold.
- Eisenstein, D. J. et al. (2001). Spectroscopic Target Selection for the Sloan Digital Sky Survey: The Luminous Red Galaxy Sample. *AJ* 122, 2267–2280.
- Eisenstein, D. J. et al. (2005). Detection of the Baryon Acoustic Peak in the Large-Scale Correlation Function of SDSS Luminous Red Galaxies. *ApJ* 633, 560–574.
- Eisenstein, D. J. and W. Hu (1999). Power Spectra for Cold Dark Matter and Its Variants. *ApJ* 511, 5–15.
- Eisenstein, D. J., H.-J. Seo, and M. White (2007). On the Robustness of the Acoustic Scale in the Low-Redshift Clustering of Matter. *ApJ* 664, 660–674.
- Elgarøy, Ø. and O. Lahav (2006). Sub-eV upper limits on neutrino masses from cosmology. *Physica Scripta Volume T* 127, 105–106.
- Falcke, H. D. et al. (2007). A very brief description of LOFAR the Low Frequency Array. *Highlights of Astronomy* 14, 386–387.
- Feldman, G. J. and R. D. Cousins (1998). Unified approach to the classical statistical analysis of small signals. *Phys. Rev. D* 57, 3873–3889.
- Feng, J. L. (2008). Collider Physics and Cosmology. arXiv:0801.1334.
- Fermi, E. (1949). On the Origin of Cosmic Acceleration. *Phys. Rev.* 75, 1169–1174.
- Frieman, J., M. Turner, and D. Huterer (2008). Dark Energy and the Accelerating Universe. arXiv:0803.0982.
- Fukuda, S. et al. (2003). The Super-Kamiokande detector. *Nucl. Instrum. Methods Phys. Res., Sect. A* 501, 418–462.
- Fukuda, Y. et al. (1998). Evidence for Oscillation of Atmospheric Neutrinos. *Phys. Rev. Lett.* 81, 1562–1567.
- Fukuda, Y. et al. (1999). Measurement of the Flux and Zenith-Angle Distribution of Upward Throughgoing Muons by Super-Kamiokande. *Phys. Rev. Lett.* 82, 2644–2648.
- Fukugita, M., T. Ichikawa, J. E. Gunn, M. Doi, K. Shimasaku, and D. P. Schneider (1996). The Sloan Digital Sky Survey Photometric System. *AJ* 111, 1748–+.

- Gaisser, T. K. (1990). *Cosmic rays and particle physics*. New York: Cambridge University Press.
- Gaisser, T. K., F. Halzen, and T. Stanev (1995). Particle astrophysics with high energy neutrinos. *Phys. Rep.* 258, 173–236.
- Gandhi, R., C. Quigg, M. H. Reno, and I. Sarcevic (1996). Ultrahigh-energy neutrino interactions. *Astropart. Phys.* 5, 81–110.
- Gao, L. and S. D. M. White (2007). Assembly bias in the clustering of dark matter haloes. *MNRAS* 377, L5–L9.
- Gelmini, G., P. Gondolo, and G. Varieschi (2000a). Prompt atmospheric neutrinos and muons: Dependence on the gluon distribution function. *Phys. Rev. D* 61(5), 056011–+.
- Gelmini, G., P. Gondolo, and G. Varieschi (2000b). Prompt atmospheric neutrinos and muons: NLO versus LO QCD predictions. *Phys. Rev. D* 61(3), 036005–+.
- Gelmini, G., P. Gondolo, and G. Varieschi (2003). Measuring the prompt atmospheric neutrino flux with down-going muons in neutrino telescopes. *Phys. Rev. D* 67(1), 017301–+.
- Giannantonio, T., R. G. Crittenden, R. C. Nichol, R. Scranton, G. T. Richards, A. D. Myers, R. J. Brunner, A. G. Gray, A. J. Connolly, and D. P. Schneider (2006). High redshift detection of the integrated Sachs-Wolfe effect. *Phys. Rev. D* 74(6), 063520–+.
- Gilks, W. R., S. Richardson, and D. J. Spiegelhalter (1996). *Markov Chain Monte Carlo in Practice*. London: Chapman & Hall.
- Glazebrook, K. et al. (2006). Wfmos detf white paper. <http://home.fnal.gov/~rocky/DETF/Dey.pdf>.
- Gluck, M., E. Reya, and A. Vogt (1995). Dynamical Parton Distributions of the Proton and Small X Physics. *Z. Phys., C* 67, 433–+.
- Gondolo, P. (2004). Introduction to Non-Baryonic Dark Matter. *astro-ph/0403064*.
- Goodman, J. E. and J. O’Rourke (Eds.) (2004). *Handbook of Discrete and Computational Geometry*, 778 and 871–872. New York: Chapman & Hall/CRC.
- Górski, K. M. et al. (1999). Analysis issues for large CMB data sets. In A. J. Banday, R. K. Sheth, and L. N. da Costa (Eds.), *Evolution of Large Scale Structure: From Recombination to Garching*, 37–+.
- Górski, K. M., E. Hivon, A. J. Banday, B. D. Wandelt, F. K. Hansen, M. Reinecke, and M. Bartelmann (2005). HEALPix: A Framework for High-Resolution Discretization and Fast Analysis of Data Distributed on the Sphere. *ApJ* 622, 759–771.
- Gorski, K. M., B. D. Wandelt, F. K. Hansen, E. Hivon, and A. J. Banday (1999). The HEALPix Primer. *astro-ph/9905275*.
- Greisen, K. (1966). End to the Cosmic-Ray Spectrum? *Phys. Rev. Lett.* 16, 748–750.

- Gunn, J. E. et al. (1998). The Sloan Digital Sky Survey Photometric Camera. *AJ* 116, 3040–3081.
- Gunn, J. E. et al. (2006). The 2.5 m Telescope of the Sloan Digital Sky Survey. *AJ* 131, 2332–2359.
- Guzzo, L., M. A. Strauss, K. B. Fisher, R. Giovanelli, and M. P. Haynes (1997). Redshift-Space Distortions and the Real-Space Clustering of Different Galaxy Types. *ApJ* 489, 37–+.
- Haiman, Z. et al. (2005). An X-ray Galaxy Cluster Survey for Investigations of Dark Energy. [astro-ph/0507013](https://arxiv.org/abs/astro-ph/0507013).
- Halzen, F. and D. Hooper (2002). High-energy neutrino astronomy: the cosmic ray connection. *Reports of Progress in Physics* 65, 1025–1078.
- Halzen, F. and A. O’Murchadha (2008). Neutrinos from Auger Sources. [arXiv:0802.0887](https://arxiv.org/abs/0802.0887).
- Hamilton, A. J. S. (1988). Evidence for biasing in the CfA survey. *ApJ* 331, L59–L62.
- Hamilton, A. J. S. (1993a). Omega from the anisotropy of the redshift correlation function in the IRAS 2 Jansky survey. *ApJ* 406, L47–L50.
- Hamilton, A. J. S. (1993b). Toward Better Ways to Measure the Galaxy Correlation Function. *ApJ* 417, 19–+.
- Hamilton, A. J. S. (1998). Linear Redshift Distortions: a Review. In D. Hamilton (Ed.), *The Evolving Universe*, Volume 231 of *Astrophysics and Space Science Library*, 185–+.
- Hamilton, A. J. S. and M. Tegmark (2004). A scheme to deal accurately and efficiently with complex angular masks in galaxy surveys. *MNRAS* 349, 115–128.
- Hamilton, A. J. S., M. Tegmark, and M. E. C. Swanson (2008). in preparation.
- Hannestad, S., A. Mirizzi, G. G. Raffelt, and Y. Y. Y. Wong (2008). Cosmological constraints on neutrino plus axion hot dark matter: Update after WMAP-5. [arXiv:0803.1585](https://arxiv.org/abs/0803.1585).
- Hastings, W. K. (1970). Monte Carlo sampling methods using Markov chains and their applications. *Biometrika* 57, 97.
- Hikage, C., T. Matsubara, Y. Suto, C. Park, A. S. Szalay, and J. Brinkmann (2005). Fourier Phase Analysis of SDSS Galaxies. *PASJ* 57, 709–718.
- Hill, G. C. (2003). Comment on “Including systematic uncertainties in confidence interval construction for Poisson statistics”. *Phys. Rev. D* 67(11), 118101–+.
- Hinshaw, G. et al. (2008). Five-Year Wilkinson Microwave Anisotropy Probe (WMAP) Observations: Data Processing, Sky Maps, and Basic Results. [arXiv:0803.0732](https://arxiv.org/abs/0803.0732).
- Hirata, K., T. Kajita, M. Koshiba, M. Nakahata, and Y. Oyama (1987). Observation of a neutrino burst from the supernova SN1987A. *Physical Review Letters* 58, 1490–1493.

- Hivon, E., K. M. Górski, C. B. Netterfield, B. P. Crill, S. Prunet, and F. Hansen (2002). MASTER of the Cosmic Microwave Background Anisotropy Power Spectrum: A Fast Method for Statistical Analysis of Large and Complex Cosmic Microwave Background Data Sets. *ApJ* 567, 2–17.
- Hogg, D. W. et al. (2004). The Dependence on Environment of the Color-Magnitude Relation of Galaxies. *ApJ* 601, L29–L32.
- Hogg, D. W., D. P. Finkbeiner, D. J. Schlegel, and J. E. Gunn (2001). A Photometricity and Extinction Monitor at the Apache Point Observatory. *AJ* 122, 2129–2138.
- Honda, M., T. Kajita, K. Kasahara, and S. Midorikawa (2004). New calculation of the atmospheric neutrino flux in a three-dimensional scheme. *Phys. Rev. D* 70(4), 043008–+.
- Hu, W. (2005). Dark Energy Probes in Light of the CMB. In S. C. Wolff and T. R. Lauer (Eds.), *Observing Dark Energy*, Volume 339 of *Astronomical Society of the Pacific Conference Series*, 215–+.
- Hu, W., S. DeDeo, and C. Vale (2007). Cluster mass estimators from CMB temperature and polarization lensing. *New Journal of Physics* 9, 441–+.
- Hu, W., M. Fukugita, M. Zaldarriaga, and M. Tegmark (2001). Cosmic Microwave Background Observables and Their Cosmological Implications. *ApJ* 549, 669–680.
- Hubble, E. (1934). No. 485. The distribution of extra-galactic nebulae. *Contributions from the Mount Wilson Observatory / Carnegie Institution of Washington* 485, 1–69.
- Hubble, E. and M. L. Humason (1931). The Velocity-Distance Relation among Extra-Galactic Nebulae. *ApJ* 74, 43–+.
- Huchra, J. et al. (2005). The 2MASS Redshift Survey and Low Galactic Latitude Large-Scale Structure. In *Nearby Large-Scale Structures and the Zone of Avoidance*, *Astronomical Society of the Pacific Conference Series*, Volume 329, 135–+.
- Huchra, J., M. Davis, D. Latham, and J. Tonry (1983). A survey of galaxy redshifts. IV - The data. *ApJS* 52, 89–119.
- Humason, M. L., N. U. Mayall, and A. R. Sandage (1956). Redshifts and magnitudes of extragalactic nebulae. *AJ* 61, 97–162.
- IceCube Collaboration (2007). The IceCube Collaboration: contributions to the 30th International Cosmic Ray Conference (ICRC 2007). *arXiv:0711.0353*.
- Ikedda, M. et al. (2007). Search for Supernova Neutrino Bursts at Super-Kamiokande. *ApJ* 669, 519–524.
- Ivezić, Ž. et al. (2004). SDSS data management and photometric quality assessment. *Astronomische Nachrichten* 325, 583–589.
- Joyce, M., F. Sylos Labini, A. Gabrielli, M. Montuori, and L. Pietronero (2005). Basic properties of galaxy clustering in the light of recent results from the Sloan Digital Sky Survey. *A&A* 443, 11–16.

- Kaiser, N. (2004). Pan-STARRS: a wide-field optical survey telescope array. In J. M. Oschmann, Jr. (Ed.), *Ground-based Telescopes*, Volume 5489 of *Proceedings of the SPIE*, 11–22.
- Kappes, A. et al. (2007). KM3NeT: A Next Generation Neutrino Telescope in the Mediterranean Sea. [arXiv:0711.0563](https://arxiv.org/abs/0711.0563).
- Katz, U. F. (2004). Status of the ANTARES project. *Eur. Phys. J. C* 33, 971–974.
- Katz, U. F. (2006). KM3NeT: Towards a km³ Mediterranean neutrino telescope. *Nuclear Instruments and Methods in Physics Research A* 567, 457–461.
- Kernan, P. J. and L. M. Krauss (1995). Updated limits on the electron neutrino mass and large angle oscillations from SN 1987A. *Nuclear Physics B* 437, 243–256.
- Kolb, E. W. and M. S. Turner (1990). *The Early Universe*. New York: Addison-Wesley.
- Kolb, R. (2007). A thousand invisible cords binding astronomy and high-energy physics. *Reports of Progress in Physics* 70, 1583–1595.
- Komatsu, E. et al. (2008). Five-Year Wilkinson Microwave Anisotropy Probe (WMAP) Observations: Cosmological Interpretation. [arXiv:0803.0547](https://arxiv.org/abs/0803.0547).
- Koshiaba, M. (2003). Nobel Lecture: Birth of neutrino astrophysics. *Rev. Mod. Phys.* 75, 1011–1020.
- Kravtsov, A. V. (2006). Modeling Galaxy Clustering with Cosmological Simulations. [astro-ph/0607463](https://arxiv.org/abs/astro-ph/0607463).
- Kravtsov, A. V., A. A. Berlind, R. H. Wechsler, A. A. Klypin, S. Gottlöber, B. Allgood, and J. R. Primack (2004). The Dark Side of the Halo Occupation Distribution. *ApJ* 609, 35–49.
- Kristiansen, J. R., Ø. Elgarøy, and H. Dahle (2007). Using the cluster mass function from weak lensing to constrain neutrino masses. *Phys. Rev. D* 75(8), 083510–+.
- Lesgourgues, J. and S. Pastor (2006). Massive neutrinos and cosmology. *Phys. Rep.* 429, 307–379.
- Lewis, A. and S. Bridle (2002). Cosmological parameters from CMB and other data: A Monte Carlo approach. *Phys. Rev. D* 66(10), 103511–+.
- Li, C., G. Kauffmann, Y. P. Jing, S. D. M. White, G. Börner, and F. Z. Cheng (2006). The dependence of clustering on galaxy properties. *MNRAS* 368, 21–36.
- Lipari, P. and T. Stanev (1991). Propagation of multi-TeV muons. *Phys. Rev. D* 44, 3543–3554.
- Lobashev, V. M. (2003). The search for the neutrino mass by direct method in the tritium beta-decay and perspectives of study it in the project KATRIN. *Nuclear Physics A* 719, 153–160.
- Loveday, J., S. J. Maddox, G. Efstathiou, and B. A. Peterson (1995). The Stromlo-APM redshift survey. 2: Variation of galaxy clustering with morphology and luminosity. *ApJ* 442, 457–468.

- LSST Collaboration (2006). LSST DETF White Paper. http://www.lsst.org/Science/docs/LSST_DETF_Whitepaper.pdf.
- Lupton, R., J. E. Gunn, Z. Ivezić, G. R. Knapp, and S. Kent (2001). Astronomical Data Analysis Software and Systems X. In F. R. Harnden, Jr., F. A. Primini, and H. E. Payne (Eds.), ASP Conf. Ser., Volume 238, San Francisco, 269–+. Astron. Soc. Pac.
- Maddox, S. J., G. Efstathiou, and W. J. Sutherland (1990a). The APM Galaxy Survey - Part Two - Photometric Corrections. MNRAS 246, 433–+.
- Maddox, S. J., G. Efstathiou, and W. J. Sutherland (1996). The APM Galaxy Survey - III. an analysis of systematic errors in the angular correlation function and cosmological implications. MNRAS 283, 1227–1263.
- Maddox, S. J., G. Efstathiou, W. J. Sutherland, and J. Loveday (1990b). The APM galaxy survey. I - APM measurements and star-galaxy separation. MNRAS 243, 692–712.
- Madgwick, D. S. et al. (2003). The 2dF Galaxy Redshift Survey: galaxy clustering per spectral type. MNRAS 344, 847–856.
- Magliocchetti, M. and C. Porciani (2003). The halo distribution of 2dF galaxies. MNRAS 346, 186–198.
- Mandelbaum, R., C. M. Hirata, U. Seljak, J. Guzik, N. Padmanabhan, C. Blake, M. R. Blanton, R. Lupton, and J. Brinkmann (2005). Systematic errors in weak lensing: application to SDSS galaxy-galaxy weak lensing. MNRAS 361, 1287–1322.
- Mannheim, K., R. J. Protheroe, and J. P. Rachen (2001). Cosmic ray bound for models of extragalactic neutrino production. Phys. Rev. D 63(2), 023003–+.
- Martínez, V. J. and E. Saar (2002). Statistics of the Galaxy Distribution. New York: Chapman & Hall/CRC.
- Mateus, A., L. Sodré, R. Cid Fernandes, G. Stasińska, W. Schoenell, and J. M. Gomes (2006). Semi-empirical analysis of Sloan Digital Sky Survey galaxies - II. The bimodality of the galaxy population revisited. MNRAS 370, 721–737.
- Mather, J. C. et al. (1994). Measurement of the cosmic microwave background spectrum by the COBE FIRAS instrument. ApJ 420, 439–444.
- Matsubara, T. (1999). Stochasticity of Bias and Nonlocality of Galaxy Formation: Linear Scales. ApJ 525, 543–553.
- McDonald, P. (2006). Clustering of dark matter tracers: Renormalizing the bias parameters. Phys. Rev. D 74(10), 103512–+.
- Metropolis, N., A. W. Rosenbluth, M. N. Rosenbluth, A. H. Teller, and E. Teller (1953). Equation of State Calculations by Fast Computing Machines. J. Chem. Phys. 21, 1087–1092.
- Mo, H. J. and S. D. M. White (1996). An analytic model for the spatial clustering of dark matter haloes. MNRAS 282, 347–361.

- Möller, O., M. Kitzbichler, and P. Natarajan (2007). Strong lensing statistics in large, $z \lesssim 0.2$, surveys: bias in the lens galaxy population. *MNRAS* 379, 1195–1208.
- Myers, A. D., T. Shanks, P. J. Outram, W. J. Frith, and A. W. Wolfendale (2004). Evidence for an extended Sunyaev-Zel’dovich effect in WMAP data. *MNRAS* 347, L67–L72.
- Navarro, J. F., C. S. Frenk, and S. D. M. White (1996). The Structure of Cold Dark Matter Halos. *ApJ* 462, 563–+.
- Neyman, J. and E. L. Scott (1952). A Theory of the Spatial Distribution of Galaxies. *ApJ* 116, 144–+.
- Nishimichi, T., I. Kayo, C. Hikage, K. Yahata, A. Taruya, Y. P. Jing, R. K. Sheth, and Y. Suto (2007). Bispectrum and Nonlinear Biasing of Galaxies: Perturbation Analysis, Numerical Simulation, and SDSS Galaxy Clustering. *PASJ* 59, 93–106.
- Norberg, P. et al. (2001). The 2dF Galaxy Redshift Survey: luminosity dependence of galaxy clustering. *MNRAS* 328, 64–70.
- Norberg, P. et al. (2002). The 2dF Galaxy Redshift Survey: the dependence of galaxy clustering on luminosity and spectral type. *MNRAS* 332, 827–838.
- Novosyadlyj, B., R. Durrer, and V. N. Lukash (1999). An analytic approximation of MDM power spectra in four dimensional parameter space. *A&A* 347, 799–808.
- Oyaizu, H., M. Lima, C. E. Cunha, H. Lin, J. Frieman, and E. S. Sheldon (2008). A Galaxy Photometric Redshift Catalog for the Sloan Digital Sky Survey Data Release 6. *ApJ* 674, 768–783.
- Padmanabhan, N. et al. (2007). The clustering of luminous red galaxies in the Sloan Digital Sky Survey imaging data. *MNRAS* 378, 852–872.
- Padmanabhan, N., C. M. Hirata, U. Seljak, D. J. Schlegel, J. Brinkmann, and D. P. Schneider (2005). Correlating the CMB with luminous red galaxies: The integrated Sachs-Wolfe effect. *Phys. Rev. D* 72(4), 043525–+.
- Padmanabhan, T. (1993). *Structure Formation in the Universe*. New York: Cambridge University Press.
- Park, C., Y.-Y. Choi, M. S. Vogeley, J. R. I. Gott, and M. R. Blanton (2007). Environmental Dependence of Properties of Galaxies in the Sloan Digital Sky Survey. *ApJ* 658, 898–916.
- Park, C., Y.-Y. Choi, M. S. Vogeley, J. R. I. Gott, J. Kim, C. Hikage, T. Matsubara, M.-G. Park, Y. Suto, and D. H. Weinberg (2005). Topology Analysis of the Sloan Digital Sky Survey. I. Scale and Luminosity Dependence. *ApJ* 633, 11–22.
- Park, C., M. S. Vogeley, M. J. Geller, and J. P. Huchra (1994). Power spectrum, correlation function, and tests for luminosity bias in the CfA redshift survey. *ApJ* 431, 569–585.
- Pasquali, L., M. H. Reno, and I. Sarcevic (1999). Lepton fluxes from atmospheric charm. *Phys. Rev. D* 59(3), 034020–+.
- Peacock, J. A. (1999). *Cosmological Physics*. New York: Cambridge University Press.

- Peacock, J. A. and S. J. Dodds (1994). Reconstructing the Linear Power Spectrum of Cosmological Mass Fluctuations. *MNRAS* 267, 1020–+.
- Peacock, J. A. and A. F. Heavens (1990). Alternatives to the Press-Schechter cosmological mass function. *MNRAS* 243, 133–143.
- Peacock, J. A. and R. E. Smith (2000). Halo occupation numbers and galaxy bias. *MNRAS* 318, 1144–1156.
- Pen, U.-L. (1998). Reconstructing Nonlinear Stochastic Bias from Velocity Space Distortions. *ApJ* 504, 601–+.
- Percival, W. J. et al. (2007). The Shape of the Sloan Digital Sky Survey Data Release 5 Galaxy Power Spectrum. *ApJ* 657, 645–663.
- Percival, W. J., S. Cole, D. J. Eisenstein, R. C. Nichol, J. A. Peacock, A. C. Pope, and A. S. Szalay (2007). Measuring the Baryon Acoustic Oscillation scale using the Sloan Digital Sky Survey and 2dF Galaxy Redshift Survey. *MNRAS* 381, 1053–1066.
- Percival, W. J., L. Verde, and J. A. Peacock (2004). Fourier analysis of luminosity-dependent galaxy clustering. *MNRAS* 347, 645–653.
- Perlmutter, S. et al. (1999). Measurements of Omega and Lambda from 42 High-Redshift Supernovae. *ApJ* 517, 565–586.
- Peskin, M. E. (2008). Supersymmetry in Elementary Particle Physics. arXiv:0801.1928.
- Pier, J. R., J. A. Munn, R. B. Hindsley, G. S. Hennessy, S. M. Kent, R. H. Lupton, and Ž. Ivezić (2003). Astrometric Calibration of the Sloan Digital Sky Survey. *AJ* 125, 1559–1579.
- Press, W. H. and P. Schechter (1974). Formation of Galaxies and Clusters of Galaxies by Self-Similar Gravitational Condensation. *ApJ* 187, 425–438.
- Press, W. H., S. A. Teukolsky, W. T. Vetterling, and B. P. Flannery (1992) Numerical recipes in C. The art of scientific computing (2nd ed.). New York: Cambridge University Press.
- Rassat, A., K. Land, O. Lahav, and F. B. Abdalla (2007). Cross-correlation of 2MASS and WMAP 3: implications for the integrated Sachs-Wolfe effect. *MNRAS* 377, 1085–1094.
- Reid, B. A. and D. N. Spergel (2006). Sunyaev-Zel’dovich Effect Signals in Cluster Models. *ApJ* 651, 643–657.
- Riess, A. G. et al. (1998). Observational Evidence from Supernovae for an Accelerating Universe and a Cosmological Constant. *AJ* 116, 1009–1038.
- Romeo, A. B., O. Agertz, B. Moore, and J. Stadel (2008). Discreteness Effects in Lambda Cold Dark Matter Simulations: A Wavelet-Statistical View. arXiv:0804.0294.
- Ryazhskaya, O. G., L. V. Volkova, and O. Saavedra (2002). A limit on charm produced cosmic ray muon and atmospheric neutrino fluxes. *Nucl. Phys. Proc. Suppl.* 110, 531–533.

- Sánchez, A. G., C. M. Baugh, W. J. Percival, J. A. Peacock, N. D. Padilla, S. Cole, C. S. Frenk, and P. Norberg (2006). Cosmological parameters from cosmic microwave background measurements and the final 2dF Galaxy Redshift Survey power spectrum. *MNRAS* 366, 189–207.
- Sandage, A. R. (1970). Cosmology: a search for two numbers. *Physics Today* 23, 34–41.
- Sapienza, P. (2006). Status of the NEMO Project. *astro-ph/0611105*.
- Saunders, W. et al. (2000). The PSCz catalogue. *MNRAS* 317, 55–63.
- Schechter, P. (1976). An analytic expression for the luminosity function for galaxies. *ApJ* 203, 297–306.
- Schlegel, D. J., D. P. Finkbeiner, and M. Davis (1998). Maps of Dust Infrared Emission for Use in Estimation of Reddening and Cosmic Microwave Background Radiation Foregrounds. *ApJ* 500, 525–+.
- Schlickeiser, R. (2002). *Cosmic Ray Astrophysics*. Berlin: Springer.
- Scoccimarro, R., R. K. Sheth, L. Hui, and B. Jain (2001). How Many Galaxies Fit in a Halo? Constraints on Galaxy Formation Efficiency from Spatial Clustering. *ApJ* 546, 20–34.
- Scott, E. L., C. D. Shane, and M. D. Swanson (1954). Comparison of the Synthetic and Actual Distribution of Galaxies on a Photographic Plate. *ApJ* 119, 91–+.
- Scranton, R. (2003). Testing the halo model against the SDSS photometric survey. *MNRAS* 339, 410–426.
- SDSS Collaboration (2007). After SDSS-II White Paper. http://cosmology.lbl.gov/BOSS/as2_proposal.pdf.
- Sefusatti, E. and R. Scoccimarro (2005). Galaxy bias and halo-occupation numbers from large-scale clustering. *Phys. Rev. D* 71(6), 063001–+.
- Seljak, U. (2000). Analytic model for galaxy and dark matter clustering. *MNRAS* 318, 203–213.
- Seljak, U. (2001). Redshift-space bias and β from the halo model. *MNRAS* 325, 1359–1364.
- Seljak, U., A. Makarov, R. Mandelbaum, C. M. Hirata, N. Padmanabhan, P. McDonald, M. R. Blanton, M. Tegmark, N. A. Bahcall, and J. Brinkmann (2005). SDSS galaxy bias from halo mass-bias relation and its cosmological implications. *Phys. Rev. D* 71(4), 043511–+.
- Seljak, U. and M. S. Warren (2004). Large-scale bias and stochasticity of haloes and dark matter. *MNRAS* 355, 129–136.
- Seljak, U. and M. Zaldarriaga (1996). A Line-of-Sight Integration Approach to Cosmic Microwave Background Anisotropies. *ApJ* 469, 437–+.
- Shectman, S. A., S. D. Landy, A. Oemler, D. L. Tucker, H. Lin, R. P. Kirshner, and P. L. Schechter (1996). The Las Campanas Redshift Survey. *ApJ* 470, 172–+.

- Shen, Y. et al. (2007). Clustering of High-Redshift ($z \geq 2.9$) Quasars from the Sloan Digital Sky Survey. *AJ* 133, 2222–2241.
- Sheth, R. K., A. J. Connolly, and R. Skibba (2005). Marked correlations in galaxy formation models. *astro-ph/0511773*.
- Sheth, R. K. and A. Diaferio (2001). Peculiar velocities of galaxies and clusters. *MNRAS* 322, 901–917.
- Sheth, R. K., H. J. Mo, and G. Tormen (2001). Ellipsoidal collapse and an improved model for the number and spatial distribution of dark matter haloes. *MNRAS* 323, 1–12.
- Sheth, R. K. and G. Tormen (1999). Large-scale bias and the peak background split. *MNRAS* 308, 119–126.
- Simon, P. (2005). Time evolution of the stochastic linear bias of interacting galaxies on linear scales. *A&A* 430, 827–842.
- Simon, P., M. Hettterscheidt, M. Schirmer, T. Erben, P. Schneider, C. Wolf, and K. Meisenheimer (2007). GaBoDS: The Garching-Bonn Deep Survey. VI. Probing galaxy bias using weak gravitational lensing. *A&A* 461, 861–879.
- Skibba, R., R. K. Sheth, A. J. Connolly, and R. Scranton (2006). The luminosity-weighted or ‘marked’ correlation function. *MNRAS* 369, 68–76.
- Slosar, A. and M. Hobson (2003). An improved Markov-chain Monte Carlo sampler for the estimation of cosmological parameters from CMB data. *astro-ph/0307219*.
- Smith, J. A. et al. (2002). The u’g’r’i’z’ Standard-Star System. *AJ* 123, 2121–2144.
- Smith, R. E., J. A. Peacock, A. Jenkins, S. D. M. White, C. S. Frenk, F. R. Pearce, P. A. Thomas, G. Efstathiou, and H. M. P. Couchman (2003). Stable clustering, the halo model and non-linear cosmological power spectra. *MNRAS* 341, 1311–1332.
- Smith, R. E., R. Scoccimarro, and R. K. Sheth (2007). Scale dependence of halo and galaxy bias: Effects in real space. *Phys. Rev. D* 75(6), 063512–+.
- Smith, R. E., R. Scoccimarro, and R. K. Sheth (2008). Motion of the acoustic peak in the correlation function. *Phys. Rev. D* 77(4), 043525–+.
- Sokolsky, P. and G. B. Thomson (2007). TOPICAL REVIEW: Highest energy cosmic-rays and results from the HiRes experiment. *Journal of Physics G Nuclear Physics* 34, 401–+.
- Somerville, R. S., G. Lemson, Y. Sigad, A. Dekel, G. Kauffmann, and S. D. M. White (2001). Non-linear stochastic galaxy biasing in cosmological simulations. *MNRAS* 320, 289–306.
- Spergel, D. N. et al. (2003). First-Year Wilkinson Microwave Anisotropy Probe (WMAP) Observations: Determination of Cosmological Parameters. *ApJS* 148, 175–194.
- Spergel, D. N. et al. (2007). Three-Year Wilkinson Microwave Anisotropy Probe (WMAP) Observations: Implications for Cosmology. *ApJS* 170, 377–408.

- Springel, V. et al. (2005). Simulations of the formation, evolution and clustering of galaxies and quasars. *Nature* 435, 629–636.
- Staśto, A. M. (2004). Ultrahigh Energy Neutrino Physics. *Int. J. Mod. Phys. A* 19, 317–340.
- Stecker, F. W. and M. H. Salamon (1996). High Energy Neutrinos from Quasars. *Space Sci. Rev.* 75, 341–355.
- Steigman, G. (2007). Primordial Nucleosynthesis in the Precision Cosmology Era. *Annual Review of Nuclear and Particle Science* 57, 463–491.
- Stoughton, C. et al. (2002). Sloan Digital Sky Survey: Early Data Release. *AJ* 123, 485–548.
- Strauss, M. A., J. P. Huchra, M. Davis, A. Yahil, K. B. Fisher, and J. Tonry (1992). A redshift survey of IRAS galaxies. VII - The infrared and redshift data for the 1.936 Jansky sample. *ApJS* 83, 29–63.
- Stubbs, C. W., D. Sweeney, J. A. Tyson, and the LSST Collaboration (2004). An Overview of the Large Synoptic Survey Telescope (LSST) System. In *Bulletin of the American Astronomical Society*, Volume 36, 1527–+.
- Swanson, M. E. C. et al. (2006). Search for Diffuse Astrophysical Neutrino Flux Using Ultra-High-Energy Upward-going Muons in Super-Kamiokande I. *ApJ* 652, 206–215.
- Swanson, M. E. C., M. Tegmark, M. Blanton, and I. Zehavi (2008). SDSS galaxy clustering: luminosity and colour dependence and stochasticity. *MNRAS* 385, 1635–1655.
- Swanson, M. E. C., M. Tegmark, A. J. S. Hamilton, and J. C. Hill (2007). Methods for Rapidly Processing Angular Masks of Next-Generation Galaxy Surveys. [arXiv:0711.4352](https://arxiv.org/abs/0711.4352).
- Szapudi, I., S. Prunet, and S. Colombi (2001). Fast Analysis of Inhomogenous Megapixel Cosmic Microwave Background Maps. *ApJ* 561, L11–L14.
- Taruya, A. and T. Hiramatsu (2008). A Closure Theory for Nonlinear Evolution of Cosmological Power Spectra. *ApJ* 674, 617–635.
- Tasitsiomi, A., A. V. Kravtsov, R. H. Wechsler, and J. R. Primack (2004). Modeling Galaxy-Mass Correlations in Dissipationless Simulations. *ApJ* 614, 533–546.
- Tegmark, M. (1997). Measuring Cosmological Parameters with Galaxy Surveys. *Physical Review Letters* 79, 3806–3809.
- Tegmark, M. (1999). Comparing and Combining Cosmic Microwave Background Data Sets. *ApJ* 519, 513–517.
- Tegmark, M. et al. (2004a). Cosmological parameters from SDSS and WMAP. *Phys. Rev. D* 69(10), 103501–+.
- Tegmark, M. et al. (2004b). The Three-Dimensional Power Spectrum of Galaxies from the Sloan Digital Sky Survey. *ApJ* 606, 702–740.
- Tegmark, M. et al. (2006). Cosmological constraints from the SDSS luminous red galaxies. *Phys. Rev. D* 74(12), 123507–+.

- Tegmark, M. and B. C. Bromley (1999). Observational Evidence for Stochastic Biasing. *ApJ* 518, L69–L72.
- Tegmark, M., A. J. S. Hamilton, and Y. Xu (2002). The power spectrum of galaxies in the 2dF 100k redshift survey. *MNRAS* 335, 887–908.
- Tegmark, M. and P. J. E. Peebles (1998). The Time Evolution of Bias. *ApJ* 500, L79+.
- Tegmark, M. and M. J. Rees (1998). Why is the Cosmic Microwave Background Fluctuation Level 10^{-5} ? *ApJ* 499, 526+.
- Tegmark, M., J. Silk, and A. Blanchard (1994). On the inevitability of reionization: Implications for cosmic microwave background fluctuations. *ApJ* 420, 484–496.
- Tegmark, M., A. Vilenkin, and L. Pogosian (2005). Anthropic predictions for neutrino masses. *Phys. Rev. D* 71(10), 103523+.
- Terzian, Y. and J. Lazio (2006). The Square Kilometre Array. Volume 6267 of Proceedings of the SPIE.
- Thunman, M., G. Ingelman, and P. Gondolo (1996). Charm production and high energy atmospheric muon and neutrino fluxes. *Astropart. Phys.* 5, 309–332.
- Tinker, J. L., C. Conroy, P. Norberg, S. G. Patiri, D. H. Weinberg, and M. S. Warren (2007). Void Statistics in Large Galaxy Redshift Surveys: Does Halo Occupation of Field Galaxies Depend on Environment? [arXiv:0707.3445](https://arxiv.org/abs/0707.3445).
- Tinker, J. L., P. Norberg, D. H. Weinberg, and M. S. Warren (2007). On the Luminosity Dependence of the Galaxy Pairwise Velocity Dispersion. *ApJ* 659, 877–889.
- Tinker, J. L., D. H. Weinberg, and M. S. Warren (2006). Cosmic Voids and Galaxy Bias in the Halo Occupation Framework. *ApJ* 647, 737–752.
- Tinker, J. L., D. H. Weinberg, Z. Zheng, and I. Zehavi (2005). On the Mass-to-Light Ratio of Large-Scale Structure. *ApJ* 631, 41–58.
- Tucker, D. L. et al. (2006). The Sloan Digital Sky Survey monitor telescope pipeline. *Astronomische Nachrichten* 327, 821+.
- Tyson, J. A. (2002). Large Synoptic Survey Telescope: Overview. In J. A. Tyson and S. Wolff (Eds.), *Survey and Other Telescope Technologies and Discoveries*, Volume 4836 of Proceedings of the SPIE, 10–20.
- Tyson, J. A. (2006). Precision Studies of Dark Energy with LSST. In T. M. Liss (Ed.), *Intersections of Particle and Nuclear Physics: 9th Conference CIPAN2006*, Volume 870 of American Institute of Physics Conference Series, 44–52.
- Tytler, D., X.-M. Fan, and S. Burles (1996). Cosmological baryon density derived from the deuterium abundance at redshift $z = 3.57$. *Nature* 381, 207–209.
- Uomoto, A., S. A. Smee, and R. H. Barkhouser (2004). A high-efficiency near-infrared spectrograph for the Apache Point 3.5 m telescope. In A. F. M. Moorwood and M. Iye (Eds.), *Ground-based Instrumentation for Astronomy*, Volume 5492 of Proceedings of the SPIE, 1411–1422.

- van den Bosch, F. C., X. Yang, and H. J. Mo (2003). Linking early- and late-type galaxies to their dark matter haloes. *MNRAS* 340, 771–792.
- Verde, L. et al. (2003). First-Year Wilkinson Microwave Anisotropy Probe (WMAP) Observations: Parameter Estimation Methodology. *ApJS* 148, 195–211.
- Volkova, L. V. (1980). Energy Spectra and Angular Distributions of Atmospheric Neutrinos. *Sov. J. Nucl. Phys.* 31, 784–+.
- Wandelt, B. D., E. Hivon, and K. M. Gorski (1998). Topological Analysis of High-Resolution CMB Maps. *astro-ph/9803317*.
- Wandelt, B. D., E. Hivon, and K. M. Górski (2001). Cosmic microwave background anisotropy power spectrum statistics for high precision cosmology. *Phys. Rev. D* 64(8), 083003–+.
- Wang, Y., X. Yang, H. J. Mo, and F. C. van den Bosch (2007). The Cross-Correlation between Galaxies of Different Luminosities and Colors. *ApJ* 664, 608–632.
- Waxman, E. and J. Bahcall (1999). High energy neutrinos from astrophysical sources: An upper bound. *Phys. Rev. D* 59(2), 023002–+.
- Weinberg, D. H., R. Davé, N. Katz, and J. A. Kollmeier (2003). The Lyman- α Forest as a Cosmological Tool. In S. H. Holt and C. S. Reynolds (Eds.), *The Emergence of Cosmic Structure*, Volume 666 of American Institute of Physics Conference Series, 157–169.
- Weinmann, S. M., F. C. van den Bosch, X. Yang, and H. J. Mo (2006). Properties of galaxy groups in the Sloan Digital Sky Survey - I. The dependence of colour, star formation and morphology on halo mass. *MNRAS* 366, 2–28.
- White, S. D. M. (2007). Fundamental physics: why Dark Energy is bad for astronomy. *Reports of Progress in Physics* 70, 883–897.
- White, S. D. M., G. Efstathiou, and C. S. Frenk (1993). The amplitude of mass fluctuations in the universe. *MNRAS* 262, 1023–1028.
- White, S. D. M., R. B. Tully, and M. Davis (1988). Clustering bias in the nearby galaxies catalog and in cold dark matter models. *ApJ* 333, L45–L49.
- Wild, V. et al. (2005). The 2dF Galaxy Redshift Survey: stochastic relative biasing between galaxy populations. *MNRAS* 356, 247–269.
- Willmer, C. N. A., L. N. da Costa, and P. S. Pellegrini (1998). Southern Sky Redshift Survey: Clustering of Local Galaxies. *AJ* 115, 869–884.
- Yadav, J., S. Bharadwaj, B. Pandey, and T. R. Seshadri (2005). Testing homogeneity on large scales in the Sloan Digital Sky Survey Data Release One. *MNRAS* 364, 601–606.
- Yamamoto, K., B. A. Bassett, R. C. Nichol, Y. Suto, and K. Yahata (2006). Searching for modified gravity with baryon oscillations: From SDSS to wide field multiobject spectroscopy (WFMOS). *Phys. Rev. D* 74(6), 063525–+.
- Yang, X., H. J. Mo, Y. P. Jing, and F. C. van den Bosch (2005). Galaxy occupation statistics of dark matter haloes: observational results. *MNRAS* 358, 217–232.

- Yang, X., H. J. Mo, and F. C. van den Bosch (2003). Constraining galaxy formation and cosmology with the conditional luminosity function of galaxies. *MNRAS* 339, 1057–1080.
- Yang, X., H. J. Mo, and F. C. van den Bosch (2006). Observational Evidence for an Age Dependence of Halo Bias. *ApJ* 638, L55–L58.
- Yang, X., H. J. Mo, and F. C. van den Bosch (2008). Galaxy Groups in the SDSS DR4. II. Halo Occupation Statistics. *ApJ* 676, 248–261.
- York, D. G. et al. (2000). The Sloan Digital Sky Survey: Technical Summary. *AJ* 120, 1579–1587.
- Zas, E., F. Halzen, and R. A. Vázquez (1993). High energy neutrino astronomy: Horizontal air shower arrays versus underground detectors. *Astropart. Phys.* 1, 297–315.
- Zatsepin, G. T. and V. A. Kuzmin (1966). Upper Limit of the Spectrum of Cosmic Rays. *JTEP Letters* 4, 79.
- Zehavi, I. et al. (2005). The Luminosity and Color Dependence of the Galaxy Correlation Function. *ApJ* 630, 1–27.
- Zentner, A. R. (2007). The Excursion Set Theory of Halo Mass Functions, Halo Clustering, and Halo Growth. *International Journal of Modern Physics D* 16, 763–815.
- Zheng, Z., A. A. Berlind, D. H. Weinberg, A. J. Benson, C. M. Baugh, S. Cole, R. Davé, C. S. Frenk, N. Katz, and C. G. Lacey (2005). Theoretical Models of the Halo Occupation Distribution: Separating Central and Satellite Galaxies. *ApJ* 633, 791–809.
- Zheng, Z. and D. H. Weinberg (2007). Breaking the Degeneracies between Cosmology and Galaxy Bias. *ApJ* 659, 1–28.
- Zwicky, F. (1952). Dispersion in the Large-Scale Distribution of Galaxies. *PASP* 64, 247–+.